



HAL
open science

Topics in 21-cm cosmology: foreground models and their subtraction, map reconstruction for wide field of view interferometers and PAON-4 data analysis

Qizhi Huang

► **To cite this version:**

Qizhi Huang. Topics in 21-cm cosmology: foreground models and their subtraction, map reconstruction for wide field of view interferometers and PAON-4 data analysis. *Cosmology and Extra-Galactic Astrophysics [astro-ph.CO]*. Université Paris-Saclay; University of Chinese academy of sciences, 2019. English. NNT: 2019SACLS373 . tel-02374109

HAL Id: tel-02374109

<https://theses.hal.science/tel-02374109>

Submitted on 21 Nov 2019

HAL is a multi-disciplinary open access archive for the deposit and dissemination of scientific research documents, whether they are published or not. The documents may come from teaching and research institutions in France or abroad, or from public or private research centers.

L'archive ouverte pluridisciplinaire **HAL**, est destinée au dépôt et à la diffusion de documents scientifiques de niveau recherche, publiés ou non, émanant des établissements d'enseignement et de recherche français ou étrangers, des laboratoires publics ou privés.

Topics in 21-cm cosmology: Foreground models and their subtraction, map reconstruction for wide field of view interferometers and PAON-4 data analysis

Thèse de doctorat de l'Université Paris-Saclay et
University of Chinese Academy of Sciences
préparée à l'Université Paris-Sud

École doctorale n°576: particules hadrons énergie et noyau:
instrumentation, image, cosmos et simulation (Pheniics)
Spécialité de doctorat: Astroparticules et Cosmologie

Thèse présentée et soutenue à Orsay, le 18 octobre 2019, par

Qizhi HUANG

Composition du Jury :

Fabien Cavalier DR — LAL, CNRS/IN2P3; Université Paris-Sud	Président
Yannick Giraud-Héraud DR — APC, CNRS/IN2P3; Université Paris-Diderot	Rapporteur
Yi Mao PR Ass — Université de Tsinghua (Pékin)	Rapporteur
Jean-Michel Martin Astr. Adj — GEPI, Observatoire de Paris	Examineur
Réza Ansari PR — Université Paris-Sud; LAL, CNRS/IN2P3	Directeur de thèse
Xuelei Chen PR — NAOC, Chinese Academy of Sciences (Pékin)	Co-Directeur de thèse

Abstract

Some aspects of extracting cosmological 21-cm signal from radio observations, as well as interferometric data processing for ground observation and space mission have been studied and discussed in this dissertation. We constructed a high-resolution self-consistent radio foreground model, and explored a method of extracting the 21-cm signal, through filtering in frequency and angular domains. We developed and tested also an imaging algorithm for lunar orbit satellite interferometer with time-varying all-sky response and time-varying noncoplanar baselines. Finally, we performed a first analysis of PAON-4 prototype transit interferometer observations.

It is difficult to extract the neutral hydrogen signal from the 21-cm experimental data, first of all because the astrophysical foregrounds and the receiver noise are 5–6 orders of magnitude higher than the 21-cm signal. In addition, there is no foreground model with sufficiently high resolution to match the performance of modern radio interferometers to assist foreground subtraction. In this dissertation, we present a high-resolution foreground model at mid- and low-frequencies, which includes a point source model and a diffuse emission model. Our model can generate the radio foregrounds in the frequency band from 10 MHz to 2.3 GHz and with a resolution of 1 arcminute. The model can provide a matching input sky map for the simulation of observations with modern large interferometric arrays.

We have carried out a first evaluation of an algorithm for 21-cm signal extraction based on a two-stage filtering, in frequency and then, in angular domain. In frequency, along the direction of a line of sight, the foreground is considered to be smooth while the 21-cm signal and noise have fast varying fluctuations. The smooth foreground can then be filtered out from the data in frequency domain. In angular domain, the receiver noise should be nearly uncorrelated between different directions, while the 21-cm signal follows the large scale structure of the Universe and present correlations at various scales. The difference in angular correlation properties of noise and 21-cm signal is then used to filter out the noise. The Wiener filter, which is widely used in signal processing, has been studied for such two-stage filtering.

Long radio waves, below 30 MHz frequency are strongly reflected and refracted by the Earth's ionosphere, and are also seriously contaminated by RFI. So far, observations from the ground remains difficult at these long wavelengths, while a satellite interferometer in orbit around the Moon can make an excellent observation in this band, as observations would not be affected by the atmosphere, and the Moon would shield the strong RFI from the Earth. However, the satellite interferometric imaging in a fixed orbit will result in a mirror symmetric image with respect to the orbital plane. In addition, the time-varying shadow of the Moon on the sky makes widely used large field of view imaging algorithms such as W-Projection and W-Stacking not applicable. In the method we have developed, the precession of satellite orbital plane is used to solve the mirror symmetry, and an imaging algorithm based on the linear mapping between the sky map and the visibilities, both in angular space and spherical harmonic space is used to solve the imaging problem. In addition, the impact of various baseline distributions on imaging performance is also discussed.

Finally, we perform a first analysis of the observational data from the PAON-4 prototype transit interferometer. Starting from the raw data, the RFI have been removed. We have evaluated the overall performance of the array, in term of system temperature and antenna response. Using the standard calibrators as well as the publicly available observational sky maps such as the 21-cm LAB map and the 408 MHz Haslam map, the complex gains (amplitudes and phases) for PAON-4 feeds are determined, and calibrated data streams are produced. We have then applied the m -mode map making algorithm in spherical harmonic domain to reconstruct sky maps from cleaned calibrated PAON-4 data.

Résumé

Quelques aspects de l'extraction du signal cosmologique de la raie 21-cm à partir d'observations radio, ainsi que le traitement des données interférométriques pour l'observation terrestre et les missions spatiales ont été étudiés et discutés dans cette thèse. Nous avons construit un modèle d'avant-plan radio cohérent à haute résolution et nous avons étudié une méthode d'extraction du signal à 21-cm, par filtrage en fréquence et en angle. Nous avons également développé et testé un algorithme d'imagerie pour un interféromètre en orbite lunaire, avec une réponse d'antenne couvrant une large fraction du ciel et variant dans le temps. Enfin, nous avons effectué une première analyse des observations en mode transit de l'interféromètre PAON-4.

Il est difficile d'extraire le signal cosmologique à 21-cm de l'hydrogène atomique neutre des observations large bande en radio, tout d'abord parce que les avant-plans astrophysiques du récepteur sont 4–5 ordres de grandeur plus intense que le signal. De plus, il n'existe pas de modèles d'avant-plan ayant une résolution suffisamment élevée pour correspondre aux performances des interféromètres modernes. Dans cette thèse, nous présentons un modèle d'avant-plan à haute résolution aux fréquences moyennes et basses, qui comprend un modèle de sources ponctuelles et un modèle d'émission diffuse. Notre modèle peut générer les avant-plans radio dans la bande de fréquence de 10 MHz à 2,3 GHz et avec une résolution de 1 minute d'arc. Ce modèle peut fournir une carte du ciel en entrée pour la simulation d'observation avec de grands réseaux interférométriques modernes.

Nous avons effectué une première évaluation d'un algorithme d'extraction de signal à 21-cm basé sur un filtrage à deux niveaux, en fréquence et ensuite, dans le plan transverse ou angulaire. En fréquence, le long d'une ligne de visée, les émissions d'avant-plan varient lentement avec la fréquence, tandis que le signal à 21-cm et le bruit varient rapidement. L'avant plan peut donc être soustrait des observations par filtrage dans le domaine fréquentiel. Dans le domaine angulaire, le bruit du récepteur devrait être quasi non corrélé entre les différentes directions, tandis que le signal cosmologique à 21-cm suit la structure à grande échelle de l'Univers et présente donc des corrélations à différentes échelles angulaires. La

différence entre les propriétés de corrélation angulaire du bruit et le signal à 21-cm est utilisée pour filtrer le bruit. Deux filtres de Wiener ont été étudiées.

Les ondes radio de grande longueur d'onde, de fréquence inférieure à 30 MHz, sont fortement réfléchies et réfractées par l'ionosphère terrestre et sont également largement contaminées par les interférences électromagnétiques (RFI). Les observations depuis le sol restent donc difficiles à ces fréquences, tandis qu'un interféromètre en orbite autour de la lune pourrait être un instrument idéal. Les observations ne seraient en effet pas affectées par l'atmosphère terrestre et la lune protégerait les antennes des perturbations électromagnétiques provenant de la Terre. Toutefois, l'imagerie interférométrique à partir d'antennes sur une orbite fixe produira une image avec une symétrie miroir par rapport au plan orbital. En outre, l'ombre de la lune sur le ciel variant dans le temps, les algorithmes d'imagerie à grand champ largement utilisés tels que la projection en W et l'empilement en W ne sont pas applicables. Dans la méthode que nous avons développée, la précession du plan orbital du satellite est utilisée pour résoudre la symétrie miroir, et un algorithme d'imagerie basé sur la relation linéaire entre les pixels de la carte du ciel et les visibilitées est utilisé pour résoudre le problème d'imagerie, appliqué dans l'espace angulaire ou dans l'espace des harmoniques sphériques. De plus, les impacts de la distribution des lignes de base sur la performance de l'imagerie sont également discutés.

Enfin, nous avons fait une première analyse des données de l'interféromètre prototype PAON-4, avec des observations en mode transit. En partant des données brutes, nous avons identifié les RFIs, effectué l'étalonnage du système et reconstruit une carte du ciel. Nous avons évalué la performance globale de l'instrument, en termes de température de bruit et de la réponse des antennes. En utilisant des calibrateurs standard ainsi que les données publiques, telles que les cartes LAB à 21-cm du ciel et la carte Haslam à 408 MHz, les gains complexes (amplitude, phase) des signaux PAON-4 ont été déterminés et un ensemble de données calibrées a été produit. Nous avons ensuite appliqué l'algorithme de reconstruction de carte exploitant la décomposition en mode m des harmoniques sphériques pour produire des cartes du ciel à partir de données PAON-4 calibrées et nettoyées.

Acknowledgements

First of all, I would like to express my sincere gratitude to my two supervisors: Prof. Réza Ansari and Prof. Xuelei Chen, this dissertation is finished under their strict demands, thoughtful guidance and continuous encouragement over the years. Their profound knowledge, rigorous academic attitude, keen academic vision, profound insight and kind attitude towards others have set a model for me as an excellent scientific researcher, give me a lifetime of inexhaustible precious spiritual wealth!

Prof. Réza Ansari invited me to study in Université Paris-Sud, France, patiently and kindly helped me not only on study but also on life. I clearly remember the first day I just arrived in France, Prof. Réza Ansari led me walking around the campus, handled all stuffs of my basic life in school, including accommodation, office and computer, meal card, laboratory entry permission, mailbox, etc., it touched my heart very much.

Prof. Xuelei Chen led me into the vast universe of the astronomy, continuously supported and encouraged through the study, gave me a freely platform to improve my ability, especially gave me the chance to participate the space mission of DSL concept of China, it broadened my field of vision very much.

I would like to thank also the two referees, Dr. Yannick Giraud-Héraud and Dr. Yi Mao who have reviewed the manuscript, as well as Dr. Fabien Cavalier and Dr. Jean-Michel Martin who have accepted to be jury members.

Besides my two supervisors, I would like to thank the faculty and staff members in both France and China. In France, Dr. Jean-Eric Campagne helped me a lot, he introduced the PAON-2 and PAON-4 experiments to me, explained what should be focused on, taught me how to analyze the data, I learned a lot from him. Dr. Christophe Magneville also helped me a lot on my research, not only the data analysis but also the electronic system. I also thank PAON-4 team members, Daniel Charlet, Claude Pailler and Monique Taurigna for guiding me to operate the PAON-4 for testing when I visited Nançay, as this was my first time to operate the antenna array manually. I thank also other Dark Energy team members, Olivier Perdereau, Marc Moniez, Stéphane Plaszczyński, Guillaume Blanc and Jérémy Neveu.

I would like to thank the teachers and classmates in China. Xiuqiong Hou stood by my side over the years, took care of me, encouraged me to keep going. Associate Prof. Fengquan Wu helped me a lot on many aspects, especially when I encountered problems on the manuscript writing, he gave me significant support and help, thanks again. I would also like to thank Associate Prof. Yougang Wang for teaching and helping me to solve many problems on my research, Prof. Youjun Lu for discussing through the whole astronomy, providing me many new ideas. Thank Prof. Bin Yue, Associate Prof. Yidong Xu, Prof. Changjun Gao and Prof. Yan Gong, we often discussed and I learned a lot from them. I thank also Zhigang Li, Haijun Tian, Wei Liu, Jie Zhou, Xiaoyuan Huang, Yichao Li, Fupeng Zhang, Dongyao Zhao, Xiaoxia Zhang, Shumei Wu, Xiaoxian Duan, Shijie Sun, Jixia Li, Chao Yang, Shifan Zuo, Qiuyuan Tian, Hongming Zhu, Chenhui Liu, Qunxiong Wang, Yan Fu, Xiang Ji, Ju Chen, Wenkai Hu, Ye Cao, Gong Cheng, Tao Liu, Tiantian Li, Jingyu Zhang for useful discussions and support.

I would also like to thank the China Scholarship Council, which supported my study in Université Paris-Sud.

Finally, I am sincerely grateful to my family, Decheng Huang, Yanping Ye and Xingwei Huang, they gave me all their love, unconditionally supported my study and life, provided me limitless motivation to move forward.

Contents

Abstract	iii
Résumé	v
Acknowledgements	vii
List of figures	xiii
List of tables	xxiii
1 Introduction	1
2 Basis of Cosmology and Radio astronomy	5
2.1 Standard cosmological model	5
2.1.1 Friedmann-Lemaître model	5
2.1.2 Λ CMD model	7
2.2 Early Universe	8
2.2.1 Cosmic inflation	8
2.2.2 Big Bang Nucleosynthesis	9
2.3 Evolution of the Universe	14
2.3.1 Cosmic Recombination and CMB	14
2.3.2 Cosmic Dark Ages	15
2.3.3 Cosmic Reionization	16
2.3.4 Large-scale structure	17
2.4 Cosmological 21-cm signal	21
2.5 Development of radio astronomy	24
2.6 Radio interferometer and imaging	28
2.6.1 Radio interferometer	28
2.6.2 Imaging algorithm	34

3	A high-resolution self-consistent whole sky foreground model	39
3.1	Basis	41
3.1.1	Resolution	41
3.1.2	Confusion limit	42
3.2	The datasets	43
3.3	Point source model	43
3.3.1	Bright sources	45
3.3.2	Faint radio sources	47
3.3.3	Confusion limit of a telescope	50
3.3.4	Radio source maps in different resolutions	52
3.4	Diffuse emission	53
3.4.1	Galactic free-free emission	53
3.4.2	Galactic synchrotron emission	55
3.5	Total foreground	58
3.6	Brief summary	63
4	Cosmological signal extraction by frequency and angular filtering	65
4.1	The simulated data	66
4.2	Wiener filter	69
4.3	Signal extraction by Wiener filter	73
4.3.1	Filtering in frequency domain	73
4.3.2	Filtering in angular domain	74
4.3.3	The effect of inaccurate beam model	79
4.4	Brief summary	80
5	Imaging algorithm for lunar orbit interferometer array	81
5.1	Research background	81
5.2	Imaging algorithm	85
5.2.1	Mirror symmetry	86
5.2.2	Imaging algorithm in pixel	88
5.2.3	Imaging algorithm in spherical harmonic space	90
5.3	Simulation	92
5.3.1	Input maps	92
5.3.2	Orbit and baselines	92
5.3.3	Imaging from 3D baselines	96
5.4	Effects on imaging	97
5.4.1	The effect of blockage by the Moon	97

5.4.2	Pixel method v.s. spherical harmonic method	101
5.4.3	The effect of baseline distribution	103
5.5	Brief summary	106
6	Data analysis for transit interferometer of PAON-4	109
6.1	PAON-4	109
6.2	Raw visibility data	110
6.3	RFI mitigation	113
6.3.1	Surface fitting	113
6.3.2	Mitigation method	114
6.4	System gain	117
6.5	Beam and pointing	123
6.5.1	Antenna pointing	125
6.5.2	Effective diameter	127
6.6	Phase calibration	128
6.7	Flux calibration	134
6.7.1	Standard calibrator	134
6.7.2	Data noise	136
6.7.3	Flux calibration on cross-correlation	137
6.7.4	Flux calibration on auto-correlation	139
6.8	System temperature	143
6.9	Map-making	143
6.9.1	PAON-4 scan	143
6.9.2	Algorithm	144
6.9.3	PAON-4 reconstructed map	149
6.10	Brief summary	149
7	Summary and Outlooks	153
	References	157
	Appendix A Radio source count	179
A.1	Radio luminosity function	179
A.2	radio normalized differential count	180
	Appendix B The relationship between auto- and cross-correlation of noise	183
	Appendix C My publications	185

List of figures

2.1	The most important reactions in BBN (cited from [73]).	10
2.2	1σ bounds on the effective number of neutrinos [107].	11
2.3	Theoretical predictions of the light element abundances of ^4He (mass fraction), D, ^3He and ^7Li (number ratio to H) as functions of the baryon-to-photon ratio η (lower axis) as well as the density parameter of baryon $\Omega_B h^2$ (upper axis) [72, 144]. The vertical band is the 2σ band of baryon-to-photon of the CMB baryonic density from the Planck observation [195], and the horizontal hatched area represent the primordial abundances [73].	12
2.4	Time and temperature evolution of primordial light-element abundances during the BBN era. The solid and dotted lines indicate the results for the classical MB distribution ($q = 1$) and the non-extensive distribution ($q = 1.0755$), respectively.	13
2.5	History of the Universe (image is from ¹).	14
2.6	The 2018 Planck map of the temperature anisotropies of the CMB at $80'$ resolution, extracted using the SMICA method. The gray outline shows the extent of the confidence mask [197].	15
2.7	The power spectra of radiation and matter respectively [258]. The oscillation peaks in the radiation power spectrum are obvious, while those in the matter power spectrum are less obvious. Although they are caused by the same oscillation, the position of the peaks are different [100, 258].	19
2.8	The measured power spectra for the LRG (luminous red galaxies) sample of SDSS (Sloan Digital Sky Survey) data using the FKP method [104] and for the WMAP-3yr [228] (cited from [239]).	20
2.9	The measured large-scale correlation function of 6dFGS, the BAO signal at $105 h^{-1}$ Mpc is detected [36].	21

2.10	Top panel: Evolution of the CMB temperature T_{CMB} (dotted curve), the gas kinetic temperature T_{K} (dashed curve), and the spin temperature T_{s} (solid curve). Middle panel: Evolution of the gas fraction in ionized regions x_{i} (solid curve) and the ionized fraction outside these regions (due to diffuse X-rays) x_{e} (dotted curve). Bottom panel: Evolution of mean 21-cm brightness temperature T_{b} (cited from [201]).	23
2.11	The cosmological 21-cm signal [202]. Top: emission and absorption of 21-cm signal. Bottom: evolution of 21-cm signal with redshift.	23
2.12	The atmosphere window of the Earth. For the astronomical observation on the ground there are three main windows: optical, infrared and radio (cited from ²).	26
2.13	Some 21-cm experiments.	29
2.14	Configuration of two units interferometer.	29
2.15	The synthetic beams of two units interferometer. The diameters of each units are both 5 m, and the frequency is 1420 MHz. Left column is the 2D beam, and right column is the E-plane (cross-section at $\varphi = 0^\circ$) of the corresponding beam. From top to bottom are for single antenna, 15 m, 20 m and 25 m baselines, respectively.	32
2.16	Top: (u, v, w) coordinate system, $+w$ is perpendicular to the uv plane, $+v$ points to the local north, $+u$ points to the local east. $(u, v, w) = (x, y, z)/\lambda$ is the baseline coordinate in the unit of wavelength. Bottom: (l, m, n) coordinate system.	33
3.1	The beams of Tianlai interferometric array [64], left is the primary beam, right is the synthetic beam of the whole array, at 750 MHz. Interferometric method can provide higher resolution, but higher sidelobe level at the same time.	42
3.2	The survey data of radio sources: left is NVSS, right is SUMSS.	44
3.3	The spectral index of flux density. Red columns are the probability densities of the indices computed from the 7515 overlay sources, blue curve is the best fit Gaussian function of $N(\mu = 0.8157, \sigma^2 = 0.1509)$	45
3.4	Source count below 1 Jy. The curves of NVSS and SUMSS drop quickly below $S_{\text{NVSS}} = 2.7$ mJy and $S_{\text{SUMSS}} = 12$ mJy respectively, because the surveys become incomplete.	46
3.5	Top left: NVSS data at 1.4 GHz. Top right: SUMSS data at 843 MHz. Bottom: the combination of NVSS and SUMSS at 1.4 GHz, it covers almost the whole sky, and the flux limit is 15 mJy.	48

3.6	The distribution of the bright sources which is modelled by the combination of NVSS and SUMSS. The missing data is fill by the Rayleigh-Lévy random walk.	48
3.7	Radio normalized differential count. $n(S)$ is the number of radio source per steradian per flux density. Blue points are computed by the complete sample of NVSS+SUMSS, red curve is from Eq. (3.9).	49
3.8	The number distribution of radio sources all over the sky from 0.5 mJy to 15 mJy, based on the differential count.	50
3.9	Using the Rayleigh-Lévy random walk to simulate the faint radio sources in the flux density range of 0.5 mJy to 15 mJy at frequency 1.4 GHz. The flux densities and the corresponding counts of sources are obtained from the normalized differential count.	51
3.10	Radio source maps simulated by our model. From top to bottom are maps at 800 MHz in 1° , at 800 MHz in 0.4° and at 100 MHz in 0.7° , respectively.	54
3.11	A simulation map of the Galactic free-free emission at 1.4 GHz in 1° resolution.	55
3.12	The fitted curve of the spectral index of the Galactic synchrotron emission.	59
3.13	The simulated Galactic synchrotron emission at 1.4 GHz in 1°	59
3.14	The total foreground maps at 750 MHz in different observational resolutions of 1° , 0.4° and 0.1° . As the observational resolution becomes higher and higher, more and more sources are detected.	61
3.15	The zoom-in maps in different observational resolutions of 1° , 0.4° and 0.1° in the region of Dec from 10° to 50° . As the observational resolution becomes higher and higher, more and more sources are detected.	62
3.16	Relative Differences of the GSM2008 (a), GSM2016 (b), and our model (c) to the 2014 version of Haslam map.	62
3.17	The angular power spectra of the diffuse and total power maps at 1° and 0.1° resolutions. For comparison, we also plot the angular power spectrum from a map generated by the CORA code.	63
4.1	The power spectrum of dark matter after the nonlinear correction at redshift $z = 0.7755$ (computed from CAMB [155]).	67
4.2	The simulated 21-cm signal (left column) and foreground (right column) at 600 MHz (top panel) and 800 MHz (middle panel). The bottom panel is the signal convolved with a telescope beam, with an aperture size of $D = 100$ m. The pixel sizes of the maps are 200×200 , over an angular area of $4.6^\circ \times 4.6^\circ$	70

- 4.3 The frequency spectrum of simulated observational data along a line of sight, from 600 MHz to 1000 MHz, with a frequency resolution of 0.1 MHz. Top panel is the input 21-cm signal. Middle panel is the convolution of input 21-cm signal with a frequency-dependent telescope beam, as the aperture size of the telescope is fixed, at lower frequency, the resolution of the beam is lower, thus the convolved 21-cm signal is lower. Bottom panel is the total brightness temperature including 21-cm signal, foreground and noise. . . . 71
- 4.4 Left: extracted foreground $\mathbf{W}_v^f \mathbf{y}$. Right: extracted 21-cm signal + noise $\mathbf{W}_v \mathbf{y}$. From top to bottom, they are the models of single index and frequency running index, respectively. 74
- 4.5 Top: the 21-cm angular power spectrum C_l at redshift $z \sim 0.8$. Bottom: the corresponding angular correlation function $C(\theta) = \mathbf{S}_{\vec{\theta}, \vec{\theta}'}$. The correlation of 21-cm signal decrease rapidly beyond $l \sim 10^2$ (corresponding to an order of 1°). 76
- 4.6 The extracted 21-cm signal after a Wiener filter. Top: 21-cm signal + noise, the 21-cm signal is submerged in the strong noise. Middle: the extracted 21-cm signal. Bottom: the residual between the input and extracted 21-cm signal. Left: the case of noise temperature is 200 mK, 1000 times of the 21-cm signal. Right: the case of noise temperature is 2000 mK, 10000 times of the 21-cm signal. 78
- 4.7 Effect of inaccurate beam on map reconstruction. We assume here the real beam size (FWHM) is 0.25° . Top Left: input 21-cm map; Top Right: reconstructed 21-cm map from noise of 200 mK, with the correct beam size of 0.25° ; Bottom: reconstructed maps with the incorrect beam width of 0.23° (bottom left) and 0.20° (bottom right), respectively. 79
- 5.1 China's Chang'e-4 mission with a communications relay satellite named Queqiao in a halo orbit around the Earth-Moon L2 point to maintain communication between the lander on the far-side of the Moon and Earth ground control (the image is cited from ³). 83
- 5.2 Left: a linear array of flying satellites around the Moon. Right: the baselines between satellite pairs in the array swipe a number of concentric rings on the (u, v) plane. 84
- 5.3 Mirror symmetry about the orbital plane. 86

- 5.4 The threshold which is set to stabilize the solution of SVD. It is the threshold that the cumulation ratio $\sum_{i=1}^{N_{thr}} \lambda_i / \sum_{i=1}^{N_{all}} \lambda_i$ is upto 0.99. It can not only maintain most of information but also avoid the impact of small singular values during the pseudo-inverse solution. Top: singular values. Bottom: the cumulation ratio. 91
- 5.5 Sky map with a few bright sources only, in the ecliptic coordinate system, at 10 MHz. In order to avoid the superposition or blandin of sources, only 9 brightest sources are selected, which correspond to Cas A, Cyg A, Cyg X, Tau A, Ori A, For A, Cen A, Rosette nebula and Vir A. Note that the map has been convolved with a PSF manually, so that sources can be seen clearly by eyes. 93
- 5.6 Sky map contains not only bright point sources but also diffuse emission, in the ecliptic coordinate system, at 10 MHz, in 1° resolution. 93
- 5.7 Top: 3D baseline distribution, the view angles to the orbital plane are 15° (top-left) and 45° (top-right). Bottom-left: the cross-section of 3D baseline distribution through the center, upper and lower pyramids are dug. Bottom-right: all baselines are on the orbital plane. 95
- 5.8 Point source imaging with baselines distributed on a single plane. The orbital plane is represented by a white dashed curve, with a pitch angle of 30° with respect to the eliptic plane. 96
- 5.9 Synthetic imaging of point sources. Top: 90% of baselines are on a single plane and 10% of baselines are out of the plane. Middle: 70% and 30% of baselines are on and out of the plane respectively. Bottom: complete or full 3D baseline distribution. 98
- 5.10 Synthetic imaging of diffuse emission. Top: 90% of baselines are on a single plane and 10% of baselines are out of the plane. Middle: 70% and 30% of baselines are on and out of the plane respectively. Bottom: complete or full 3D baseline distribution. 99
- 5.11 The effect of blockage by the Moon. Top: the blockage ratio of each part of the sky. Middle: reconstructed maps of point source. Bottom: reconstructed maps of diffuse emission. Left: fixed blockage (similar to the ground-based antenna array). Right: blockage varying with time, following the relative position of satellites with respect to the Moon. 100

5.12	Reconstructed maps and their relative errors. Left: pixel method. Right: spherical harmonic method. The relative error map is restricted in the range of -5% to +5%, so that the slight error can be seen clearly. The maximum value, minimum value, average value and medium value of the relative error of pixel method are $\sim 45\%$, $\sim 0.02\%$, $\sim 2.3\%$ and $\sim 1.7\%$, while they are $\sim 20\%$, $\sim 0.006\%$, $\sim 1.6\%$ and $\sim 1.2\%$ for the spherical harmonics method. Obviously, no matter from the view of map quality or the error, spherical harmonics method performs better.	102
5.13	Influence of l_{\max} on PSF. Top: $l_{\max} = 100$. Bottom: $l_{\max} = 200$	104
5.14	Top: imaging only using long baselines of 6–10 km. Bottom: imaging only using short baselines of 100–500 m.	105
5.15	Synthetic imaging of asymmetric baseline distribution. Baselines are concentrated in a 1/4 of the sphere, from longitude 0° to 90° . Top: the zoom-in of a point source, its shape is distorted, the side lobes appear asymmetric change. Bottom: a reconstructed map of diffuse emission plus point sources. Actually all structures in the map are distorted, but such slight distortion is not clear compared to the diffuse structure, however, the distortion of the point source is clear.	107
6.1	Left: PAON-4 radio interferometric array. Right: its location.	110
6.2	Left: the configuration of PAON-4. Three dishes are on the three vertices of an equilateral triangle with edge length of 12 m, where two vertices are along the North-South direction (North-South edge), while the third vertex is on the West of the North-South edge (West vertex). The fourth dish is on the perpendicular line of North-South edge going through the West vertex, 6 m away from the West vertex on the East. Top right: the primary beam of a single dish of PAON-4, 5 m physical diameter with $\sim 2.9^\circ$ angular resolution at 1375 MHz. Bottom right: the synthetic beam of PAON-4 array, the FWHM resolution is $\sim 1.3^\circ$ at the center frequency of 1375 MHz for the full array.	111

- 6.3 The raw dataset of CygA17nov16, at the observational declination of $+40.733^\circ$. Top left: 21-cm signal from the HI inside the Milky Way at the frequency of 1420.4 MHz. Top right: Cygnus A plus the Galactic synchrotron emission at the frequency of 1.4 GHz. The second panel is the auto-correlations of channel 2V and 4V. For the third and fourth panels, left is the real and imaginary parts of cross-correlation of 1H2H, the real parts shift along $+y$ axis due to the correlator noise; right is the real and imaginary parts of 2V4V, a resistor of 50Ω is put at the front end of the first level of low noise amplifier (LNA) of channel 4V. 112
- 6.4 Top panel: a duration of the auto-correlation data of 1H at 1400 MHz. Second, third, fourth and fifth panels are for the uniform filter, Gaussian filter, median filter and minimum filter, respectively. Each column is for the region 1, 2, 3 in the top panel, respectively. 115
- 6.5 Top panel: frequency-time plane of auto-correlation data of 1H viewed at different angles. Bottom panel: the same as the top panel but for that after minimum filtering. The frequency is from 1250 MHz to 1500 MHz, the duration is one sidereal day. 116
- 6.6 The false-positives of the SumThreshold method when mitigating the RFI on the simulated data with a Rayleigh distribution. χ is the average threshold relative to the distribution mode (figure is cited from [178]). 118
- 6.7 (a) the result of the RFI mitigation using the SumThreshold method for PAON-4 data. (b) the same as (a) but plotted in 2D. 118
- 6.8 The comparison of PAON-4 data before and after the RFI mitigation. (a) is the auto-correlation. (b) and (c) are the real part (blue) and the imaginary part (green) of the cross-correlation. Only one frequency of 1420.4 MHz is shown in the figure. 119
- 6.9 The variation of the system gain of PAON-4 with time (thus with air temperature). The gain increases as the air temperature decreases at night, while the gain decreases as the air temperature increases during the day. . . . 120
- 6.10 (a) The bandpass gain $g(\nu)$ for channel 4V and its stability over time. The total period of time is split into 131 intervals, it can be seen that $g(\nu)$ varies little with time, its time-stability is fairly high. Colorful curves are for the 131 intervals, while the black curve is for the whole period of time. (b) $g(\nu)$ for the eight PAON-4 channels, their differences due to the analog electronic hardware, amplifiers and filters for the eight channels are clearly visible. . . 122

- 6.11 (a) The time-varying gain of PAON-4 $g(t)$ for the blind channel 4V. The entire bandwidth is divided into 29 segments (colorful curve), $g(t)$ varies little with frequency, showing the stability of $g(t)$ with frequency. (b) The auto-correlation data (channel 1H at 1400 MHz) of the observed sky, the distortion of the observed auto-correlation data is mainly due to the time-variation of the system gain. 122
- 6.12 PAON-4 1H auto-correlation data from CygA17nov16, before (top) and after (bottom) gain calibration. Left: signal at 1400 MHz, including mainly the Galactic synchrotron and radio sources (Cygnus A). Right: signal at 1420.4 MHz, due to the Milky Way neutral hydrogen 21-cm emission. The two crossings of the Galactic plane are clearly visible. 124
- 6.13 Top: Auto-correlation visibilities as a function of time for the four H-polarisation feeds. The source transit times, corresponding to Cygnus A going through the beam center, determined from auto-correlations is also shown on the graph. Bottom: source (Cygnus A) transit time, as a function of frequency, determined by solving the linear system of equations from H-polarization cross-correlation visibilities. 126
- 6.14 Left: auto-correlation data of channel 1H at 1400 MHz, the peak at around 16 o'clock is produced by Cygnus A, while the one around 16:30 is produced by the star-forming region the Cygnus X, they are close and affect each other. Right: norm of 1H-2H cross-correlation data, the cross-correlation of the diffuse emission as well as the Cygnus X is much smaller than that of the Cygnus A, the peak of Cygnus A is clear and nearly unaffected by Cygnus X and diffuse emissions. 127
- 6.15 Gaussian fit to cross-correlation visibilities $|V_{ij}(t)|$ at $\nu = 1400$ MHz for the six PAON-4 baselines, for the H-polarisation feeds. 128
- 6.16 Effective dish diameters for the four PAON4 H-polarisation feeds, obtained by solving the system of linear equations Eq. (6.12), after determination of $D_{ij}(\nu)$ from a Gaussian fit to cross-correlation visibilities $|V_{ij}(t)|$, as a function of frequency. The sine like oscillation in the effective dish diameter as a function of frequency might be due to standing waves between the feed and reflector. 129
- 6.17 Fitting the complex phase by the trigonometric function of $\cos(\Phi_{ij}) + i \sin(\Phi_{ij})$ 131

6.18	Fitting directly the real (top) and imaginary (bottom) part of the time dependent visibility $V_{ij}(t)$, at 1400 MHz. Baseline 1H-2H (left) and 2H-3H (right) are shown as an example.	131
6.19	The fitted lengths of East-West baselines, as a function of frequency, for 1H-2H (left) and 2H-3H (right) baselines.	132
6.20	The fitted extra phase as a function of frequency.	132
6.21	Phase closure checking.	133
6.22	Linear variation of the instrumental phase $\Delta\Phi_{ij}$ with frequency, for 1H-2H (left) and 2H-3H (right) baselines.	133
6.23	The phase before (top) and after (bottom) the calibration. Two sources in the image have strong cross-correlation, one is Cygnus A, the other is Cygnus X which is a active star-forming region near Cygnus A.	133
6.24	Flux densities of Cassiopeia A (red), Cygnus A (green) and Taurus A (blue) as a function of frequency, adapted from reference [22], with fading for Cas A and Tau A.	135
6.25	The solid angle of Gaussian beam as a function of FWHM resolution. . .	136
6.26	The ratio of $\frac{\sigma_{Ax}\sigma_{Ay}}{2\sigma_{c_{XY}}^2}$ of PAON-4 data, which is close to 1.	137
6.27	Cross-correlation data of channel 1H-2H at 1400 MHz after amplitude calibration, Horizontal axis correspond to time converted into right ascension, and vertical axis in the brightness temperature in Kelvin. Top and bottom panels are for real part and imaginary part, respectively.	138
6.28	Left and right columns are the maps of SSM and LAB, up and down panels are at 1400 MHz and 1420.4 MHz, respectively. The angular resolutions of the maps are $\sim 3^\circ$	140
6.29	The scans of SSM+LAB which are used to calibrate the PAON-4 auto-correlation data, at the declination $\delta = +40.733^\circ$, with a frequency resolution of 0.488 MHz and an angular resolution of $\sim 4.3^\circ$. Up and down panels are the scans at 1400 MHz and 1420.4 MHz respectively. From left to right columns are SSM, LAB, SSM+LAB (total temperature). Horizontal axis is RA from 0° to 360° , vertical axis is brightness temperature, 0 to 12 K for the left panels, and 0 to 60 K for the center and right panels.	140
6.30	The calibrated PAON-4 auto-correlation data for the scan at declination $\delta = +40.733^\circ$. Left and right figures are at 1400 MHz and 1420.4 MHz, respectively.	141

-
- 6.31 System temperatures T_{sys} as a function of frequency, estimated from auto-correlation signals, calibrated using sky maps (SSM + LAB). From left to right, top to bottom, 1H, 2H, 3H, 4H. 144
- 6.32 System temperatures T_{sys} as a function of frequency, estimated from cross-correlation signals. calibrated using the Cygnus A source transit. From left to right, top to bottom, the six plots show the system temperature for the six baselines, 1H-2H, 1H-3H, 1H-4H, 2H-3H, 2H-4H, 3H-4H. 145
- 6.33 PAON-4 reconstructed sky maps using the m -mode decomposition in spherical harmonics algorithm [223, 264]. Top panel shows the reconstructed sky map from the calibrated PAON-4 November 2016 data at 1.4 GHz, Cygnus A and the Galactic plane can be seen clearly. For comparison, the middle panel shows the reconstructed sky map from simulated visibility data in the same sky region and at the same frequency. Bottom panel: the zoom-in around Cygnus A, RA from 290° to 325° and Dec from $+32^\circ$ to $+50^\circ$, the reconstructed map from PAON-4 observations is shown on the left, while the right hand side shows the map reconstructed from simulated visibilities. . . . 150
- A.1 The local radio luminosity function at 1.4 GHz. Blue, green and yellow points are the late-type galaxies, radio loud active galactic nucleus and their sum respectively. Red, purple and blank curves are the fitting curves of late-type galaxies, radio loud active galactic nucleus and their sum respectively. 181

List of tables

2.1	The predicted abundances for the BBN primordial light elements, the observational data are listed for comparison (cited from [128]).	13
3.1	Sky maps which are used to model the diffuse foreground.	44
3.2	The fitted β_i parameters.	58
5.1	The relative errors of reconstructed maps from pixel method and spherical harmonics method.	103
6.1	Effective diameters of each channels.	128
6.2	The flux densities of Cygnus A, Cassiopeia A and Taurus A at some frequencies predicted by the polynomial fitting.	134
6.3	The brightness temperature of Cygnus A at two frequencies of 1.4 GHz and 1420.4 MHz. Due to the different effective diameters of each channels, the brightness temperatures of Cygnus A in each channels are different in the unit of Kelvin.	138
6.4	The standard deviation of noise in cross-correlation data in Kelvin, with frequency resolution of 0.488 MHz and integration time of 0.4s, at frequencies of 1.4 GHz and 1420.4 MHz as an example.	142
6.5	The standard deviation of noise in auto-correlation data in Kelvin, with frequency resolution of 0.488 MHz and integration time of 0.4s, at frequencies of 1.4 GHz and 1420.4 MHz as an example.	143
6.6	PAON-4 November 2016 dataset used in this section, which covers the declination range $\delta = +35.7^\circ$ to $+45.7^\circ$, around Cygnus A at $\delta = +40.7^\circ$	146

Chapter 1

Introduction

The redshifted 21-cm line from neutral hydrogen is becoming a more and more potential tool to study our Universe. The tomographic observation of redshifted 21-cm line can help us to study the Epoch of Reionization (EOR) [69, 161], to trace the evolution of the large-scale structure of the Universe, to constraint the cosmological parameters including the equation of state of dark energy [59, 163]. In principle, it can even probe the cosmic Dark Ages [158, 159]. The Cosmic Microwave Background (CMB) gives 2D information from the last scattering surface at Recombination, while the neutral hydrogen 21-cm line evolves with redshift thus it can provide 3D information of the Universe. Therefore, compared with CMB, the redshifted 21-cm line can provide more information, and insight about the evolution of the Universe.

In recent years, a number of experiments have tried to detect the cosmological 21-cm line. For the purpose of detecting the EOR, there are LOFAR (the LOw-Frequency Array) [250], MWA (the Murchison Widefield Array) [244], PAPER (the Precision Array for Probing the Epoch of Re-ionization) [185], 21CMA [272], HEAR (the Hydrogen Epoch of Reionization Array) [91], etc., with observational frequency ranges of roughly 100–300 MHz. For the 21-cm intensity mapping probing the large-scale structure of the Universe, there are CHIME (the Canadian Hydrogen Intensity Mapping Experiment) [25], Tianlai[64], the proposed BINGO (BAO from Integrated Neutral Gas Observations) [31], etc., which focus on the HI in the galaxies. General-purpose telescopes such as GBT (the Green Bank Telescope) [58, 164, 236] and GMRT (the Giant Metrewave Radio Telescope) [184], FAST [173] also set the 21-cm observation as one of their principle scientific goals.

However, detecting the cosmological 21-cm line is still a big challenge. One of the main reasons is that the astrophysical foregrounds are several orders of magnitude stronger than the 21-cm signal. At low frequencies, the astrophysical foregrounds mainly include three components: the Galactic synchrotron emission which arises from the relativistic electrons

moving in the Galactic magnetic field, the Galactic free-free emission which is produced by the scattering of free electrons with diffuse warm ionized gases, bright radio sources such as supernova remnants (SNRs) and extragalactic radio sources such as radio-loud galaxies, quasars and BL Lac objects [138, 222]. In order to study the foreground removal methods and evaluate its impact on the 21-cm experiments by numerical simulation, a good sky foreground model is needed.

Various studies on the foregrounds have been carried out for the 21-cm experiments [93, 89, 156, 270, 223, 224]. To investigate how the different foreground subtraction techniques work, or to make forecast of the experiments, simulations with foreground models are needed. The Global Sky Model (GSM) [89] is widely used for this purpose, with a recent updated version [270], the foreground map of the GSM constructed from sky maps at different frequencies combined using the Principal Component Analysis (PCA). However, owing to the limitation of the available whole sky surveys, the angular resolution of GSM is limited to $\gtrsim 1^\circ$ at low frequency. A high-resolution whole sky model is provided in the 21-cm simulation software package CORA [223, 224]. It uses the Haslam map as well as the GSM to simulate the diffuse emission. To include structures on the small scales, CORA adds bright point sources drawn from the matched ones in the VLA Low-Frequency Sky Survey (VLSS) [74] and the NRAO VLA Sky Survey (NVSS) [79]. There are also other high-resolution models, e.g. the Tiered Radio Extragalactic Continuum Simulation (T-RECS) [40], but only a limited patches of sky are covered.

It is difficult to extract the neutral hydrogen (HI) 21-cm signal from the observational data, because not only the 21-cm signal is very weak (~ 1 mK at the redshift of $z \sim 1$ [58, 164]), but also it is significantly contaminated by the foreground which is 5–6 orders of magnitude stronger than the 21-cm signal [89, 156].

Meanwhile, there is no enough accurate foreground model which can assist removing the foreground. A number of 21-cm extraction methods have been proposed, such as the polynomial fitting in frequency domain [255, 113], the cross-correlation among different frequencies [215]. Other blind and semi-blind methods such as the Singular Value Decomposition (SVD) [184, 164], the Robust Principle Component Analysis (RPCA) [273], the Independent Component Analysis (ICA) [61, 261] have been recently proposed. Their basic ideas are applying the different properties between the foreground and 21-cm signal. Along a line of sight (LOS), the cosmological 21-cm signal varies randomly along the redshift (so that the frequency), as the distribution of the neutral hydrogen is considered to be randomly in the Universe, while the foreground which dominated by synchrotron emission varies smoothly, so in principle, the 21-cm signal and the foreground can be separated in frequency domain. However, the receiver noise, which is considered to be white Gaussian noise, is difficult

to be separated from the 21-cm signal in frequency domain. Fortunately, they can still be distinguished in angular domain, as the receiver noise is uncorrelated in angular direction, while the 21-cm signals are correlated at different scales because it traces the large-scale structure of the Universe.

Radio astronomy originated from the observation at 20.5 MHz by Karl Jansky [136]. In January 1931, using a highly directional antenna, Jansky received a maximum radio interference signal every one sidereal day (23 hours 56 minutes and 4 seconds) at the wavelength of 14.6 meters. After more than one year of measurement and analysis, in 1932, Jansky published an article claiming that this interference signal was radio radiation from the center of the Milky Way. As a result, radio waves from space were captured for the first time, and the radio astronomy was born.

In recent years, low-frequency radio astronomy is renewed, especially the redshifted 21-cm observations for the Epoch of Reionization (EOR), the cosmic dawn and the Dark Ages [202]. However, it is not suitable to carry out very low-frequency observation on the ground, due to the strong refraction and absorption by the ionosphere below 30 MHz. In addition, because of the reflection by the ionosphere, low-frequency radio frequency interference (RFI) is omnipresent. On the ground, except for a few strong radio phenomena from the solar system, such as the solar radio bursts and the planetary radio activities, there is no other radio observation below 30 MHz. Although some ground-based experiments, such as LOFAR [210] and LWA (the Long Wavelength Array) [143], have the frequency band coverage below 30 MHz, they mostly make observations at higher frequency, at lower frequency the observations mainly focus on the Sun and planets. Until now, the radio sky below 30 MHz is still poorly known [48, 55, 53]. Therefore, it is worthwhile to observe the very low frequency band from the space.

My dissertation focuses on some problems of cosmological 21-cm signal extraction and interferometric data processing, both theoretically and experimentally for ground observation and space mission. The structure of this dissertation is as follows.

In chapter 2, some basic concepts of standard cosmology model, neutral hydrogen 21-cm signal and radio interferometric observation are briefly reviewed, including the Λ CDM model and the evolution of the Universe, the evolution of HI 21-cm signal and its observation, the principle of interferometer and imaging algorithms.

In chapter 3, a high-resolution self-consistent foreground model is introduced. The foreground can be roughly divided into radio sources and diffuse emission. According to the confusion limit, radio sources can be divided into resolved radio sources and unresolved radio sources. According to the flux density, the resolved radio source can be further divided into bright radio sources and faint radio sources. The diffuse emission includes synchrotron

emission, free-free emission, dust emission, etc., whose generation mechanisms are different. To model the bright sources, the complete sample of NVSS+SUMSS is used. For the faint sources, they are generated randomly by the Rayleigh-Lévy random walk. Meanwhile, to calculate the confusion limit, the radio differential count of sources should be calculated first. To obtain higher resolution diffuse map, a deconvolution algorithm in spherical harmonic domain is applied.

In chapter 4, a 21-cm signal extraction algorithm based on frequency and angular filtering is introduced. To perform the simulation for the algorithm, 21-cm signal is generated, multiple foreground models are tested, with noise of various levels. In both frequency and angular domains, it is verified that using Wiener filter and Gaussian filter to extract 21-cm signal is applicable and has good results.

In chapter 5, an imaging algorithm for lunar orbital interferometer is introduced. For the all-sky field of view, the interferometric imaging of satellite array in a fixed orbit may produce a mirror image about the orbital plane. Such mirror symmetry problem can be eliminated by the procession of satellite orbital plane. For time-varying non-coplanar baselines and time-varying all-sky response, two imaging algorithms in spherical harmonic domain and angular domain are compared. It is found that the algorithm in spherical harmonic costs less time and has better quality of reconstructed map. In addition, the blockage of the Moon and various asymmetric baseline distributions are also discussed.

In chapter 6, the observational data of the ground radio interferometer—PAON-4 is calibrated, and a sky map is reconstructed based on the PAON-4 calibrated data. For the analysis and calibration process, radio frequency interferences (RFIs) are removed, the gain of the system as well as the antenna pointings are calibrated, and the receiving efficiency of the antenna is evaluated. Using the standard calibrators as well as the previous observation sky map, the phase and the amplitude of PAON-4 data are calibrated, and the system temperature is evaluated and analyzed. Applying the m-mode algorithm in spherical harmonic domain, the sky map of PAON-4 calibrated data is reconstructed.

Chapter 2

Basis of Cosmology and Radio astronomy

2.1 Standard cosmological model

2.1.1 Friedmann-Lemaître model

The distribution of objects in the Universe seems to be homogeneous and isotropic from the observations of the large-scale homogeneous distribution of galaxies and the isotropy of the cosmic microwave background radiation. This is the cosmological principle which is proposed by Einstein: The Universe is globally homogeneous and isotropic in large-scale.

According to the cosmological principle, the Robertson-Walker metric, which is the metric on a constant-time 3-dimensions surface with uniform spatial curvature, can be obtained

$$ds^2 = c^2 dt^2 - a^2(t) \left[\frac{dr^2}{1 - kr^2} + r^2 (d\theta^2 + \sin^2 \theta d\phi^2) \right] \quad (2.1)$$

where r is a comoving radial coordinate, $a(t)$ is the cosmic scale factor at cosmic time t , so the physical coordinate is $a(t)r$. $k = +1, 0, -1$ is the sign of the spatial curvature: $k = +1$ corresponds an open universe of an infinite and hyperbolic space; $k = 0$ corresponds to the critical universe of an infinite and flat space; $k = -1$ corresponds to a closed universe of a finite and spherical space.

Eq. (2.1) can be written in metric formalism

$$ds^2 = -g_{\mu\nu} dx^\mu dx^\nu \quad (2.2)$$

where $x^0 = t$, $x^1 = r$, $x^2 = \theta$, $x^3 = \varphi$. The metric tensor $g_{\mu\nu}$ is called the Friedmann-Lemaître-Robertson-Walker (FLRW) metric.

The dynamics in the General Relativity (GR) is described by the Einstein's gravitational field equations

$$G_{\mu\nu} \equiv R_{\mu\nu} - \frac{1}{2}g_{\mu\nu}R + \Lambda g_{\mu\nu} = \frac{8\pi G}{c^4}T_{\mu\nu} \quad (2.3)$$

where $G_{\mu\nu}$ is the Einstein tensor, G is the Newton's gravitational constant, $T_{\mu\nu}$ is the energy-momentum tensor, Λ is the cosmological constant, $R_{\mu\nu} \equiv \Gamma_{\mu\nu,\rho}^{\rho} - \Gamma_{\mu\rho,\nu}^{\rho} + \Gamma_{\mu\nu}^{\rho}\Gamma_{\rho\sigma}^{\sigma} - \Gamma_{\mu\sigma}^{\rho}\Gamma_{\nu\rho}^{\sigma}$ is the Ricci tensor, and $R \equiv R^{\mu\nu}R_{\nu\mu}$ is the curvature scalar which is the contraction of the Ricci tensor.

Substituting the Robertson-Walker metric into Einstein's gravitational field equations, the Friedmann equations are obtained

$$H^2 \equiv \left(\frac{\dot{a}}{a}\right)^2 = \frac{8\pi G}{3}\rho + \frac{\Lambda}{3} - \frac{k}{a^2} \quad (2.4)$$

$$\ddot{a} = -\frac{4\pi G}{3}(\rho + 3P)a + \frac{\Lambda}{3}a \quad (2.5)$$

where H is the Hubble parameter, $\dot{a} \equiv \partial a / \partial t$.

For the current Universe (the lower index "0" refers to present time t_0), Eq. (2.5) becomes

$$H_0^2 = \frac{8\pi G}{3}\rho_0 + \frac{\Lambda}{3} - \frac{k}{a_0^2} \quad (2.6)$$

The density is the sum of the matter and the radiation, $\rho_0 = \rho_{m0} + \rho_{r0}$. The critical density of the Universe as well as the density parameters of the ratio of matter, radiation and vacuum energy to the critical density are

$$\rho_c = \frac{3H_0^2}{8\pi G} \quad (\text{critical density}) \quad (2.7)$$

$$\Omega_m = \frac{\rho_{m0}}{\rho_c} = \frac{8\pi G\rho_{m0}}{3H_0^2} \quad (\text{density parameter of matter}) \quad (2.8)$$

$$\Omega_r = \frac{\rho_{r0}}{\rho_c} = \frac{8\pi G\rho_{r0}}{3H_0^2} \quad (\text{density parameter of radiation}) \quad (2.9)$$

$$\Omega_\Lambda = \frac{\rho_\Lambda}{\rho_c} = \frac{\Lambda}{3H_0^2} \quad (\text{density parameter of vacuum energy}) \quad (2.10)$$

$$\Omega_k = -\frac{k}{H_0^2 a_0^2} \quad (2.11)$$

and they might be constrained to be

$$\Omega_m + \Omega_r + \Omega_\Lambda + \Omega_k = 1 \quad (2.12)$$

The cosmological model which is satisfied with the Friedmann equations is generally called the Friedmann model. For $k = 0$ and $\Lambda \neq 0$, it is called the Friedmann-Lemaître model, which is the most important model for current Universe.

2.1.2 Λ CMD model

The Λ CMD (Λ Cold Dark Matter) model is the simplest model of the Universe which is compatible with the observational evidences, such as the existence and anisotropy of CMB; the Baryon Acoustic Oscillation (BAO) feature of large-scale galaxy distribution; the abundances of hydrogen, helium and lithium; the accelerating expansion of the Universe observed by distant supernovae, etc.

For the Λ CMD, Λ refers to the cosmological constant, matter is consist of cold dark matter and bayron, radiation includes photons and neutrinos, and the spatial curvature also contributes to the total density. For the Friedmann-Lemaître model, the evolution of the Hubble parameter is

$$H(z) = H_0 \sqrt{\Omega_m(1+z)^3 + \Omega_r(1+z)^4 + \Omega_k(1+z)^2 + \Omega_\Lambda} \quad (2.13)$$

If replace the cosmological constant by a Dark Energy fluid, $\Omega_\Lambda \rightarrow \Omega_{\text{DE}}(1+z)^{3(1+w)}$, Eq. (2.13) becomes

$$H(z) = H_0 \sqrt{\Omega_m(1+z)^3 + \Omega_r(1+z)^4 + \Omega_k(1+z)^2 + \Omega_{\text{DE}} e^{3 \int_0^z \frac{1+w(z')}{1+z'} dz'}} \quad (2.14)$$

where w is the equation of state of dark energy.

For the standard spatially-flat 6-parameter Λ CMD model, the curvature $k = 0$ and the equation of state $w = -1$, the evolution of the Hubble parameter becomes

$$H(z) = H_0 \sqrt{(\Omega_b + \Omega_c)(1+z)^3 + \Omega_r(1+z)^4 + \Omega_\Lambda} \quad (2.15)$$

and the constraint of the geometry of the Universe becomes $\Omega_b + \Omega_c + \Omega_r + \Omega_\Lambda = 1$.

Cosmological parameter results from Planck 2018 were presented detailly in [196]. Combining temperature (TT power spectrum) and polarization (TE and EE polarization spectra) information and CMB lensing, [196] found that cold dark matter density $\Omega_c h^2 =$

0.1200 ± 0.0012 , baryon density $\Omega_b = 0.02237 \pm 0.00015$, Hubble constant $H_0 = 67.36 \pm 0.54 \text{ km s}^{-1} \text{ Mpc}^{-1}$ (thus matter density $\Omega_m = 0.3153 \pm 0.0073$) and matter fluctuation amplitude $\sigma_8 = 0.8111 \pm 0.006$. Combining with Type Ia supernovae (SNe), the measured equation of state parameter of dark energy is $w_0 = -1.03 \pm 0.03$, closing to the cosmological constant with density $\Omega_\Lambda = 0.6847 \pm 0.0073$. Combining with BAO measurements, the spatial curvature density $\Omega_k = 0.001 \pm 0.002$, meaning an almost flat universe. Combining with the large-scale polarization measurements from the Planck HFI, the reionization optical depth which describes the scattering of free electrons to the CMB anisotropy is well constrained to be $\tau = 0.0544 \pm 0.0073$. The scalar spectral index which is parameterized as a power-law index of the scale-dependent CMB power spectrum to the primordial scalar power spectrum is found to be $n_s = 0.9649 \pm 0.0042$ (cosmological parameters listed above are in 68% confidence region).

2.2 Early Universe

2.2.1 Cosmic inflation

To solve the horizon problem, the flatness problem and the monopole problem of the standard hot big bang model, inflation, which is an idea claiming that the early Universe expanded very rapidly in an exponential law, is proposed. Inflation explains why our observable universe is so large, flat, and homogenous on large-scale. The quantum fluctuations during inflation can provide the seeds for structure formation of the Universe.

The Lagrangian density of the scalar field driving inflation is

$$L_\phi = \frac{1}{2} \partial_\mu \phi \partial_\mu \phi - V(\phi) \quad (2.16)$$

where V is a potential energy. The corresponding energy-momentum tensor of scale field is

$$T_{\mu\nu} = \partial_\nu \phi \partial_\mu \phi - g_{\mu\nu} L_\phi \quad (2.17)$$

For a homogeneous and isotropic field $\nabla \phi / a = 0$, the energy density and the isotropic pressure of vacuum field are

$$\rho_\phi = \frac{1}{2} \dot{\phi}^2 + V(\phi) \quad (2.18)$$

$$P_\phi = \frac{1}{2} \dot{\phi}^2 - V(\phi) \quad (2.19)$$

Substituting Eq. (2.18) and Eq. (2.19) into the Friedmann equation and fluid continuity equation then get

$$H^2 = \frac{8\pi G}{3} \left[\frac{1}{2} \dot{\phi}^2 + V(\phi) \right] \quad (2.20)$$

$$\ddot{\phi} + 3H\dot{\phi} + V'(\phi) = 0 \quad (2.21)$$

where $\dot{\phi} = \partial\phi/\partial t$ and $V'(\phi) = \partial V(\phi)/\partial\phi$.

For the slow roll inflation with approximate conditions of $\dot{\phi}^2 \ll V(\phi)$ and $\ddot{\phi} \ll \dot{\phi}$, or the slow roll parameters are satisfied with

$$\varepsilon(\phi) \equiv \frac{1}{16\pi G} \left(\frac{V'(\phi)}{V(\phi)} \right)^2 \ll 1; \quad \eta(\phi) \equiv \frac{1}{8\pi G} \frac{V''(\phi)}{V(\phi)} \ll 1 \quad (2.22)$$

Eq. (2.20) and Eq. (2.20) become

$$H^2 \approx \frac{8\pi G}{3} V(\phi) \quad (2.23)$$

$$3H\dot{\phi} + V'(\phi) \approx 0 \quad (2.24)$$

For the formalism of potential V , a large amount of novel models have been devised, such as the polynomial chaotic inflation [172], power-law inflation [160, 142], Natural inflation [108, 4, 88, 109], Hybrid inflation [97, 147]. In recent years, model with multi-field (more than one scale field) becomes popular, e.g. [151, 46, 70, 86, 112, 114, 1, 183].

During the inflationary phase, the temperature of the Universe was relatively low and the number density of matter was extremely low, small quantum fluctuations were stretched to large scales, forming the primordial seeds for all structures created in the later Universe. After the inflation, the energy density stored in the inflation field was converted back into conventional matter and filled the Universe, the temperature of the Universe returned to the pre-inflationary temperature, this is called reheating. Due to the reheating, the Universe was filled with a dense and hot quark–gluon plasma, which occurred at $\sim 10^{-12}$ s after the Big Bang, and baryon-antibaryon asymmetry may have taken place during this quark epoch.

2.2.2 Big Bang Nucleosynthesis

The Big Bang Nucleosynthesis (BBN) happened within the first 3 minutes after the Big Bang [253], The primordial light elements were generated, mainly ${}^4\text{He}$, and a few of $\text{D}({}^2\text{H})$, ${}^3\text{He}$, ${}^3\text{H}$, ${}^7\text{Li}$, ${}^7\text{Be}$.

The baryon-to-photon ratio η is a very important value for BBN, which enables us to constrain the baryon density (see Fig. 2.3). It can also be used to constrain the effective number of neutrinos N_{eff} [107] (see Fig. 2.2).

$$\eta \equiv \frac{n_b}{n_\gamma} \approx 2.75 \times 10^{-8} \Omega_b h^2 \quad (2.28)$$

where n_b and n_γ are the number densities of baryon and photon respectively.

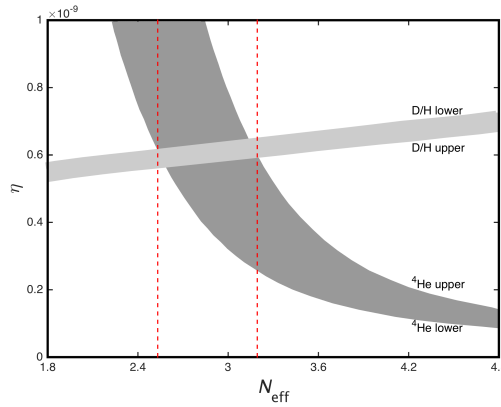


Fig. 2.2 1σ bounds on the effective number of neutrinos [107].

To determine the primordial ${}^4\text{He}$ abundance Y_p , E. Aver et al. included the effect of He I 10830 to observations of helium and hydrogen emission lines from metal-poor extragalactic HII regions then got $Y_p = 0.2449 \pm 0.0040$ [20]. This value is well fitted with the theoretical one of $\sim 25\%$ from BBN [20]. The ${}^4\text{He}$ abundance is one of the most powerful evidences for the Big Bang model ([134, 73] for a detailed review).

The primordial abundance of Deuterium can be well measured in the very metal-poor Ly α absorption systems in the foreground of high redshift QSOs. Through the measurement at redshift $z = 3.06726$ toward the QSO SDSS J1358+6522, R. Cooke et al. obtained a precise measure of the primordial abundance of deuterium $D/H = 2.53 \pm 0.04 \times 10^{-5}$ [80].

Besides the BBN, ${}^3\text{He}$ is also produced by stars. So, the abundance of ${}^3\text{He}$ is important not only for cosmology, but also for understanding stellar evolution and the chemical evolution of the Galaxy. By combining the observations in Galactic star-forming (HII) regions with recent theoretical developments of light-element synthesis and destruction in stars, T. M. Bania et al. determined an upper limit for the primordial abundance of ${}^3\text{He}$ relative to hydrogen ${}^3\text{He}/\text{H} \leq (1.1 \pm 0.2) \times 10^{-5}$ [26].

The warm metal-poor dwarfs in the halo of the Galaxy or GGC (Galactic Globular Clusters) are the ideal targets for probing the primordial abundance of lithium [231]. Recent observations from such dwarfs yield ${}^7\text{Li}/\text{H} = 1.58 \pm 0.31 \times 10^{-10}$ [219] while the standard

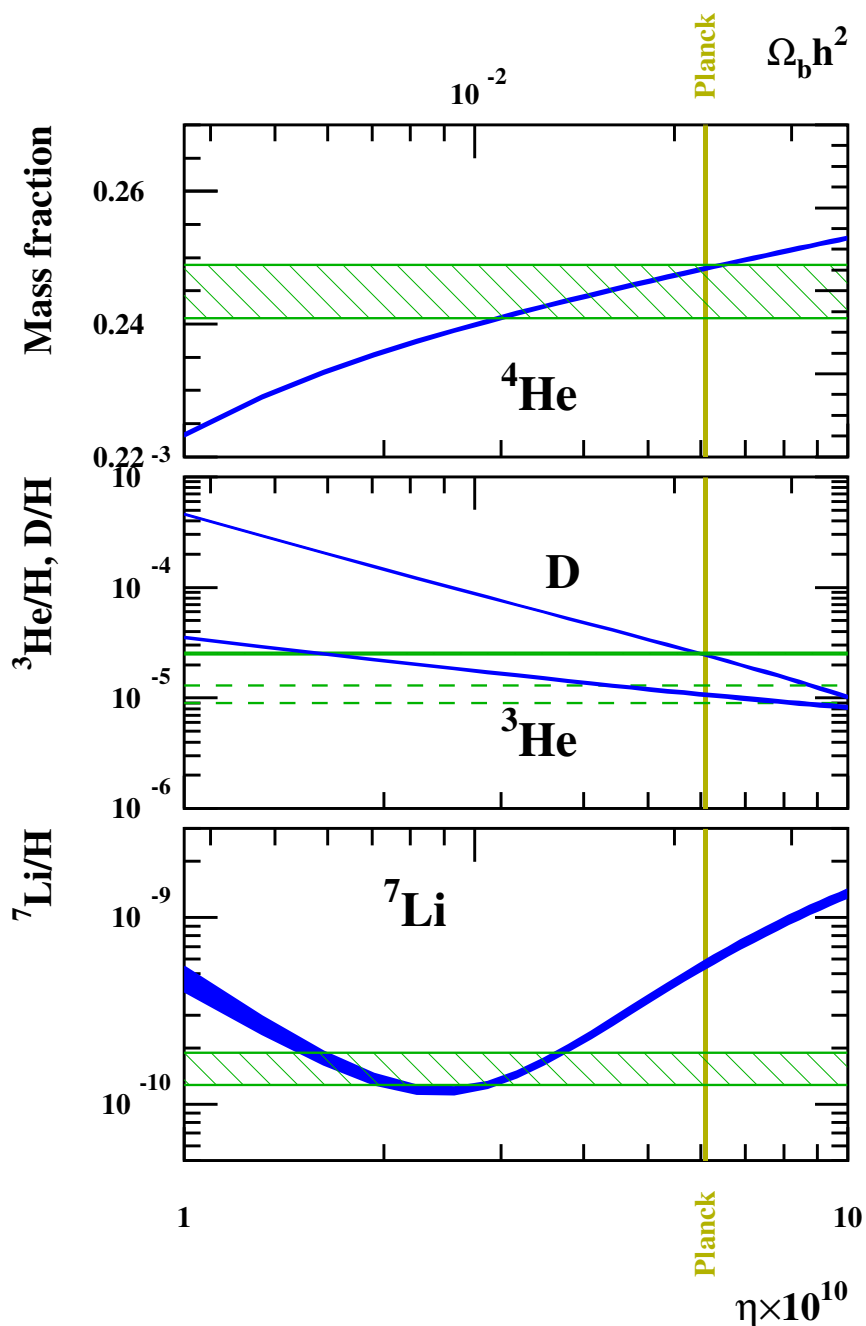


Fig. 2.3 Theoretical predictions of the light element abundances of ${}^4\text{He}$ (mass fraction), D , ${}^3\text{He}$ and ${}^7\text{Li}$ (number ratio to H) as functions of the baryon-to-photon ratio η (lower axis) as well as the density parameter of baryon $\Omega_b h^2$ (upper axis) [72, 144]. The vertical band is the 2σ band of baryon-to-photon of the CMB baryonic density from the Planck observation [195], and the horizontal hatched area represent the primordial abundances [73].

Nuclide	Coc et al. [71]	Cybur et al. [85]	Bertulani et al. [35]	S. Q. Hou et al. [128]		Observation
	($q = 1$)	($q = 1$)	($q = 1$)	$q = 1$	$q = 1.069 \sim 1.082$	
^4He	0.2476	0.2470	0.249	0.247	0.2469	0.2449 ± 0.004 [20]
D/H ($\times 10^{-5}$)	2.59	2.58	2.62	2.57	3.14~3.25	2.53 ± 0.04 [80]
$^3\text{He}/\text{H}$ ($\times 10^{-5}$)	1.04	1.00	0.98	1.04	1.46~1.50	1.1 ± 0.2 [26]
$^7\text{Li}/\text{H}$ ($\times 10^{-10}$)	5.24	4.65	4.39	5.23	1.62~1.90	1.58 ± 0.31 [219]

Table 2.1 The predicted abundances for the BBN primordial light elements, the observational data are listed for comparison (cited from [128]).

BBN model predicts $^7\text{Li}/\text{H} = 4.648 \times 10^{-10}$ [85]. The primordial abundance of ^7Li from observations is only $\sim 1/3$ of the BBN prediction, this is the so-called Cosmological Lithium Problem. Recently, S. Q. Hou et al. adopted a generalized distribution to describe the velocities of nucleons in the framework of Tsallis non-extensive statistics to solve this problem [128]. The velocity distribution of classical particles is the Maxwell–Boltzmann (MB) distribution which is verified under a temperature $\lesssim 1000$ K. S. Q. Hou et al. considered that during the BBN, the temperature ($\sim 10^9$ K) was so high that the velocity distribution of nucleons was no longer the MB distribution. The generalized Tsallis non-extensive distribution they adopted is characterized by a parameter “ q ”, and reduces to the usually Maxwell–Boltzmann distribution for $q = 1$. They found that the Cosmological Lithium Problem can be successfully solved when the value of the non-extensive parameter is $1.069 \leq q \leq 1.082$, as seen in Tab. 2.1 and Fig. 2.4.

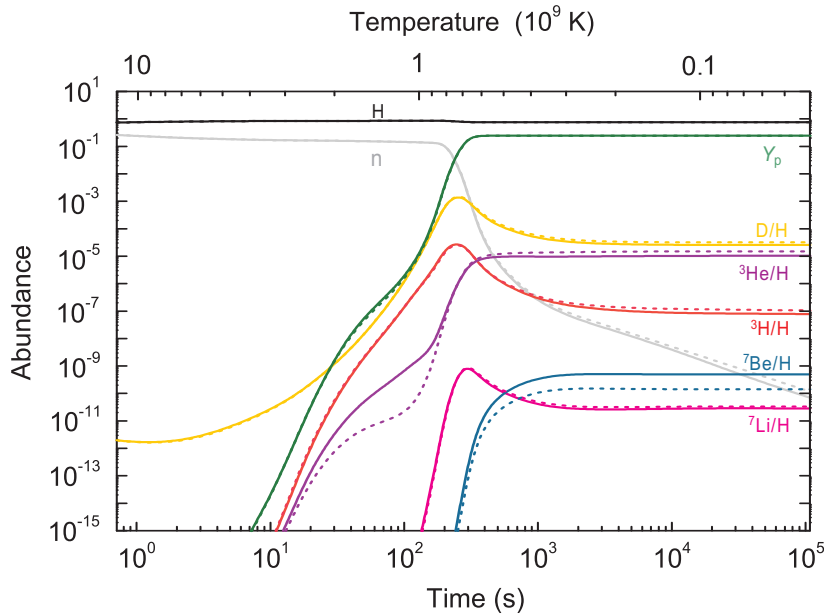


Fig. 2.4 Time and temperature evolution of primordial light-element abundances during the BBN era. The solid and dotted lines indicate the results for the classical MB distribution ($q = 1$) and the non-extensive distribution ($q = 1.0755$), respectively.

2.3 Evolution of the Universe

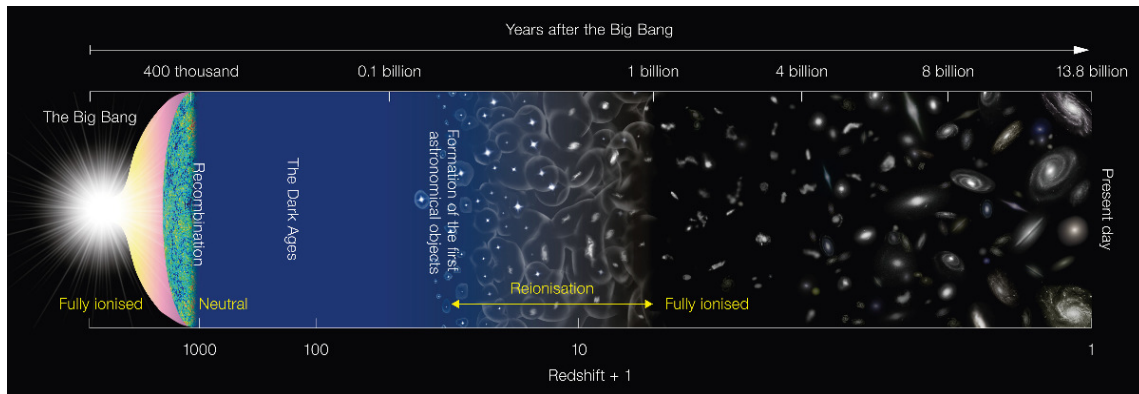


Fig. 2.5 History of the Universe (image is from ¹).

2.3.1 Cosmic Recombination and CMB

In the early stage of the Universe, the density and temperature of the Universe were very high, photons collided and ionized the matter into plasma of protons and electrons. At the same time, photons could not propagate further because of such colliding and scattering, the Universe was “opaque” due to the short photon mean free path. At this time, the matter was ionized, it was the plasma of free electron, proton, nucleus as well as photon. All particles distribute highly homogeneously over the Universe. Because of the strong coupling between radiation and matter, their temperature is comparable, and the radiation spectrum is a blackbody spectrum.

As the Universe expanded, the temperature of photons decreased. About 38 million years after the Big Bang, photons were redshifted to the infrared band, their energy were not enough to ionize matter, the matter became non-relativistic, mainly includes H and He, the Universe was matter dominated. When the temperature reduced to ~ 4000 K, almost all free electrons were bound into the nuclei, formed mainly neutral hydrogen atoms and a small amount of neutral helium atoms, this is the cosmic recombination.

As the free electrons reduced, photons could propagate freely without scattering, radiation and matter were decoupled, the Universe became transparent. There was a last time scattering between cosmic photon and free electron, it is called the last scattering surface. Since then, those photons were only affected by cosmological redshifts and have no impact on other matters, they propagated freely as a background, it is the cosmic microwave background radiation (CMB) that we had observed.

¹<https://www.eso.org/public/images/eso1620a>

The probability of photon being scattered in redshift interval dz at redshift z is

$$P(z) = e^{-\tau} \frac{d\tau}{dz}, \quad \tau = \int_0^z \sigma_T n_e c \frac{dt}{dz} dz \quad (2.29)$$

where τ is the optical depth of a photon from redshift z to the observer, $\sigma_T = 6.65 \times 10^{-25} \text{ cm}^2$ is the cross section of Thomson scattering. The maximum of Eq. (2.29) is at $z \approx 1100$, which is called the last scattering surface, and the full width at half maximum (FWHM) of $P(z)$ is $\delta z \approx 200$, which is called the last scattering shell.

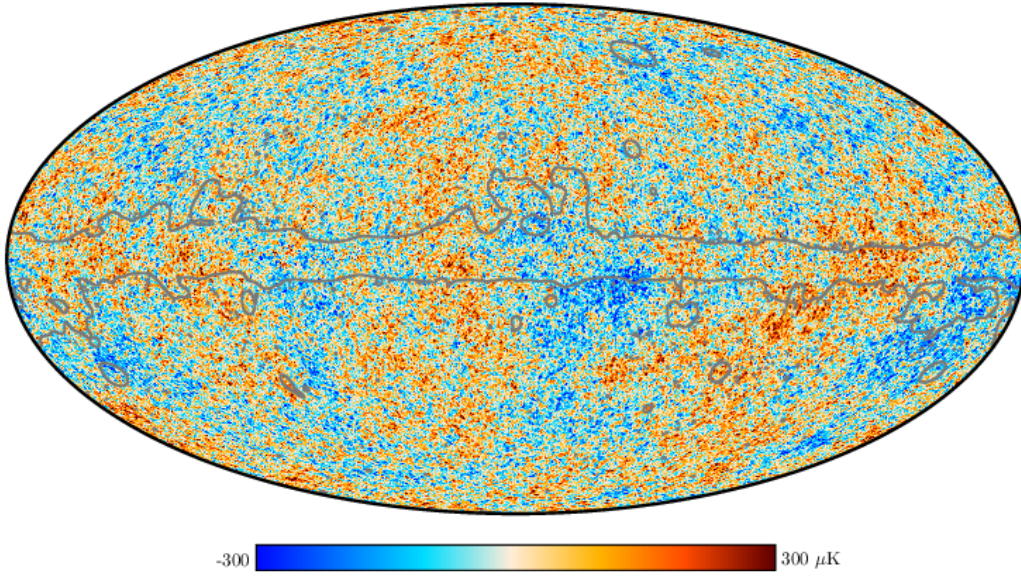


Fig. 2.6 The 2018 Planck map of the temperature anisotropies of the CMB at $80'$ resolution, extracted using the SMICA method. The gray outline shows the extent of the confidence mask [197].

2.3.2 Cosmic Dark Ages

The Cosmic Dark Ages refers to the period from the end of recombination to the forming of first generation of stars [220, 67]. As the Universe expanded, the CMB was redshifted to infrared (no longer visible light), and there was not luminous stars in this period, the Universe looked like “dark”.

Our existing astronomical observations can see the Universe before the Dark Ages (through the CMB) or after the Dark Ages (through high-redshift stars, galaxies and quasars) [84], but have not yet been able to observe the Dark Ages. Because in this period, the

Universe was highly homogeneous and isotropic, and was not illuminated, no lighting stars except neutral hydrogen and helium. The principle way to probe the Dark Ages is using the 21-cm absorption against the CMB in the intergalactic medium [133]. However, on the other hand, also because there is no effect of stars, the Dark Ages is more clear to model.

Probing the Dark Ages is a enormous challenge, mainly because the 21-cm line from this period is redshifted to $\nu \lesssim 45$ MHz, refraction and absorption on such low-frequency radio waves are significant by Earth's ionosphere. Meanwhile, the terrestrial broadcasts at low radio frequencies also produce strong interference on the Dark Ages observations. It is difficult to probe the Dark Ages on the ground. However, a satellite array on the lunar far side can overcome the above two interferences, due to the Moon lacks an ionosphere and blocks the radio frequency interferences (RFI) from the Earth [129].

2.3.3 Cosmic Reionization

As the Universe continuously expanded, the density and temperature decreased further, the primary density perturbation increased slowly by the gravity, thus the dark matter gradually gathered into dark matter halos. As the dark matter halos became larger, they had strong enough gravity to overcome the pressure of baryon gas then absorbed the gases. When the gas temperature was below 10^3 K, it was cooled mainly by hydrogen molecules, thus the pressure decreased, the gas shrank and the density increased. As the gas was continuously accumulated, when the temperature rised above 10^4 K, it cooled mainly through the Ly α emitting from hydrogen atoms [119, 96]. As halos increased to 10^6 – 10^8 solar mass, they began to form the first generation of stars, which emitted UV photons ionizing the surrounding gas through photoionizing neutral hydrogen and possibly helium [2, 50, 51].

Cosmic reionization began when the first generation of stars formed and emitted the first lights in the Universe, the high-energy photons emitted by stars and galaxies ionized the thin gases around them. As galaxies continually formed, the ionization zones expanded and connected with each other. The cosmic reionization finished when the ionization zone covered the whole intergalactic medium throughout the Universe [27, 157, 68, 169]. The Epoch of Reionization (EOR) is the key stage of the formation and evolution of galaxies, and became a very active research field in cosmology and astrophysics in recent years.

Due to free electrons scattering the photons of CMB during the epoch of reionization, the temperature anisotropy of CMB could be converted into polarization. According to the polarization measurements of CMB, reionization occurred at an average redshift of ~ 11 [99]. On the other hand, in the spectra of the high-shift quasars, complete absorption was observed at a frequency higher than the Ly α (Gunn-Peterson trough), thus it could be estimated that the reionization finished at a redshift of ~ 6 [103]. In addition to hydrogen's reionization,

helium was also reionized. The ionization energy of one electron in helium atom is 24.6 eV, which is close to that of hydrogen atom of 13.6 eV, so they might finish at the same time. Ionizing two electrons from helium needs 54.4 eV, the photon energy produced by ordinary stars was not enough, so such ionization might be carried out by the high-energy photon from quasars in a later period (redshift ~ 3).

As the cosmic reionization is a direct consequence of the formation of first luminous sources and affects subsequent structure formation, it is importance in the study of Universe's history. However, detecting the cosmic reionization is difficult, since the redshift of the reionization is very high. In addition, due to the large optical depth of the absorption of Ly α photons by neutral hydrogen, it is difficult to make any restrictions on the region whose neutral ratio is higher than 10^{-2} . Although galaxies at high-redshift of 7–8 were found, those galaxies are all high-brightness galaxies that can't represent the most of galaxies in the epoch of reionization, their limits on cosmic reionization are also weak. The cosmological 21-cm line, which is redshifted to a frequency range of 30–70 MHz at a wavelength range of 4.5–10 m, is still a promising tool to detect the EOR. There are a number of experiments underway hoping to make progress in EOR detection in the near future, such as LOFAR (LOW-Frequency Array) [250], MWA (Murchison Widefield Array) [244], PAPER (Precision Array for Probing the Epoch of Re-ionization) [185], 21CMA [191], and even the next generation radio interferometer SKA (Square Kilometre Array) [132].

2.3.4 Large-scale structure

The observation result of Planck 2018 showed that the dark energy, which accelerates the expansion of the Universe rather than to slow it down due to gravity, accounts for 68.5% of the total density of the Universe [196].

It is significantly difficult to observe the dark energy directly. Although there are some experimental studies of dark energy, they are mainly based on the observation of visible objects, the properties of dark energy are determined indirectly [6]. The most fundamental of the dark energy properties is its equation of state parameter w , different dark energy models give different w , e.g. the simplest dark energy model—the cosmological constant gives $w = -1$. In some dynamic dark energy models, w is not equal to -1 , and it changes with verseredshift. The equation of state parameter w affects the history of cosmic expansion. Therefore, by observing the cosmic expansion rate $H(z)$ at different redshift z can measure the equation of state of dark energy (see Eq. (2.14)).

The main question is to measure the Hubble parameter $H(z)$, i.e. to measure the cosmological distance—luminosity distance $D_L(z)$ or angular diameter distance $D_A(z)$. The luminosity distance is defined from the relation between the intrinsic luminosity L of a

source and the measured flux F

$$D_L(z) \equiv \sqrt{\frac{L}{4\pi F}} = a_0(1+z)\chi \quad (2.30)$$

where a_0 is today's cosmic scale factor, χ is the comoving distance

$$\chi = \begin{cases} \sin f(z), & k = -1 \\ f(z), & k = 0 \\ \sinh f(z), & k = +1 \end{cases}, \quad f(z) = \frac{c}{a_0} \int_0^z \frac{dz'}{H(z')} \quad (2.31)$$

The angular diameter distance is defined as the ratio of an object's physical size s to its angular size θ viewed from the Earth

$$D_A(z) = \frac{s}{\theta} = \frac{D_L(z)}{(1+z)^2} \quad (2.32)$$

The Baryon Acoustic Oscillation (BAO) method, which is used to accurately measure the cosmic expansion rate and distance scale of the Universe, is considered as one of the main methods to detect dark energy [6]. In the early stage of the Universe, the primordial fluctuations would cause the acoustic oscillation in the photon-baryon flow, i.e. the BAO. As the Universe expanded and the temperature dropped, when the plasma in the Universe was combined, the photon was decoupled from the baryon, such oscillation stopped. This oscillation produced some BAO characteristics such as peaks and valleys in the mass density correlation function and power spectrum (Fig. 2.7), their scale were determined by the horizon of the acoustic wave (i.e. the maximum distance of the propagation of acoustic waves) at the time of recombination, and its comoving scale is

$$k_n = \left(n + \frac{1}{2}\right) \frac{\pi}{s} \quad (2.33)$$

where $s = 105 h^{-1}$ Mpc is the horizon of the acoustic wave, which is given by

$$s = \int_0^{t_{\text{rec}}} C_a(1+z) dt = \int_{z_{\text{rec}}}^{\infty} \frac{C_a dz'}{H(z')} \quad (2.34)$$

Given cosmological parameters and dark energy models, the scale k_n can be calculated, so it can be used as standard scale. The observation of similar peaks in the cosmic microwave background (CMB) greatly improves the measurement accuracy of cosmological parameters. Similarly, the BAO in the mass density power spectrum or correlation function can be used to determine the Hubble expansion ratio and angular diameter distance at different redshifts

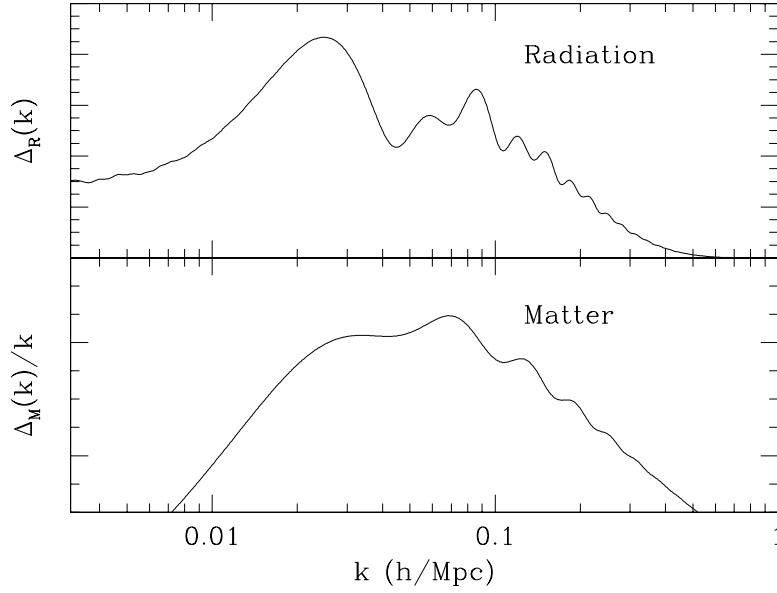


Fig. 2.7 The power spectra of radiation and matter respectively [258]. The oscillation peaks in the radiation power spectrum are obvious, while those in the matter power spectrum are less obvious. Although they are caused by the same oscillation, the position of the peaks are different [100, 258].

in the Universe, thereby determining the equation of state of dark energy [100]. Specifically, at redshift z , the distances corresponding to a scale, which are parallel and perpendicular to the line of sight, are

$$r_{\perp} = (1+z)D_A(z)\Delta\theta \quad (2.35)$$

$$r_{\parallel} = \frac{c\Delta z}{H(z)} \quad (2.36)$$

Therefore, by measuring the angle θ subtending the BAO scale, the corresponding angular diameter distance $D_A(z)$ can be obtained.

When the corresponding radial redshift difference is measured, the corresponding Hubble parameter $H(z)$ can be obtained (note that the redshift distortion caused by the peculiar velocity of galaxies should be corrected for the radial observation). In order to realize the above observations, it is necessary to observe the matter distribution of large volume in the Universe, and obtain the three-dimensional power spectrum of its density fluctuation.

Compared with the methods of constraining the expansion history by redshift–luminosity distance relationship such as supernova, the physical basis of BAO relies mainly on linear physics or quasi-linear physics which can be calculated fairly accurately and do not need phenomenological supernovae absolute luminosity standardisation procedure. so it is possible

to achieve a smaller systematic error [258]. Compared with another important dark energy probe—weak gravitational lens observation, BAO observation requires less observational conditions and does not require very high angular resolution. Because of these advantages, BAO provides a powerful method for dark energy detection [36, 239, 59, 221, 19, 30].

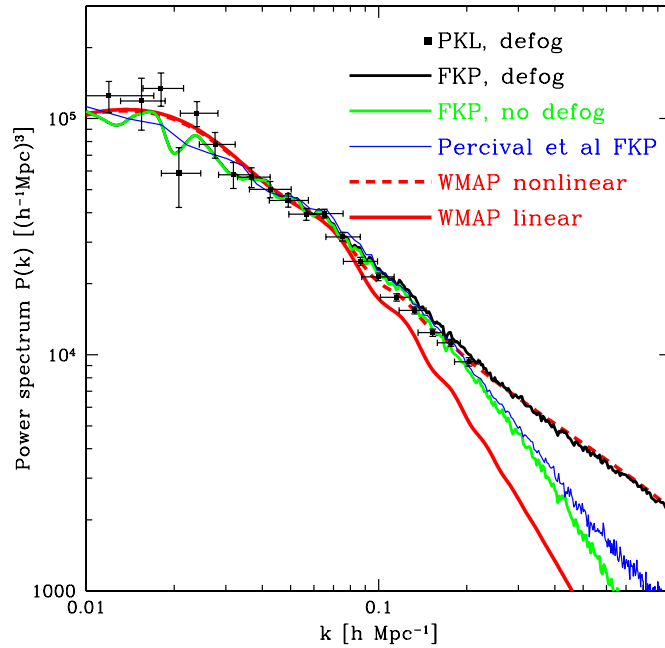


Fig. 2.8 The measured power spectra for the LRG (luminous red galaxies) sample of SDSS (Sloan Digital Sky Survey) data using the FKP method [104] and for the WMAP-3yr [228] (cited from [239]).

After the reionization (redshift below 6), hydrogen in intergalactic medium has been ionized and neutral hydrogen exists mainly in galaxies. However, due to the low angular resolution of radio observation, it is difficult to observe galaxies one by one, as that for optical survey.

However, what we are primarily interested is the large-scale structure, it is not necessary to observe individual galaxies one by one, but directly measure the three-dimensional distribution of neutral hydrogen on a larger-scale (there can be hundreds of galaxies in each resolution volume element), it is the so-called Intensity Mapping method [59, 190]. This method is especially suitable for the radio frequency band with relatively low angular resolution, and for the low-frequency 21-cm signal, RFIs are less, so it is most convenient to use this method for observation [115].

By observing the redshifted 21-cm signal, the three-dimensional large-scale structure distribution of matter can be determined. For this dark energy detection principle, GBT (Green Bank Telescope), the largest movable radio telescope in the world, was used to

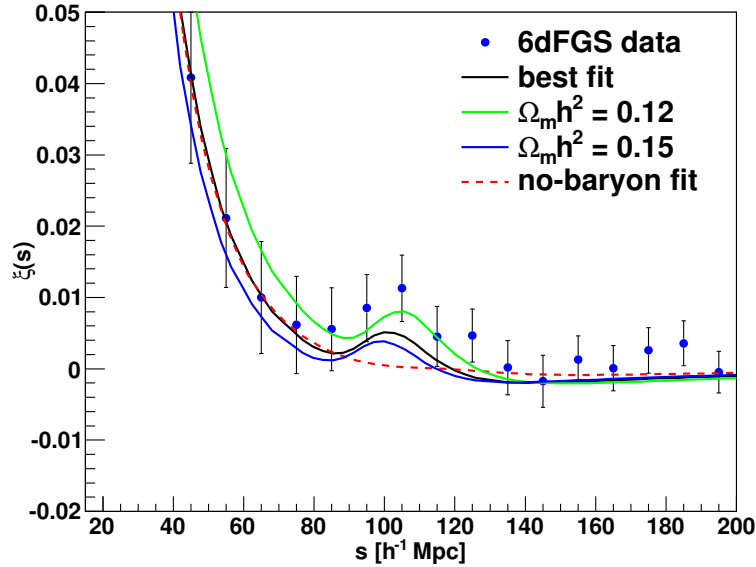


Fig. 2.9 The measured large-scale correlation function of 6dFGS, the BAO signal at $105 h^{-1}$ Mpc is detected [36].

observe the redshifted 21-cm signal, and it is cross-correlated with the optical observation of the Deep2 survey [58]. It is proved that the distribution of neutral hydrogen is consistent with the distribution of galaxies, they both can reflect the large-scale structure distribution of matter.

2.4 Cosmological 21-cm signal

The cosmological 21-cm line arises from the transition between two hyperfine levels of neutral hydrogen atom [117], this hyperfine splitting is because of the interaction of the magnetic moments of the proton and the electron. The hydrogen atom has higher energy when the spin directions of the proton and the electron are the same than opposite, the energy difference is $\Delta E = 5.9 \times 10^{-6}$ eV. The electron has a certain probability to transit from high-energy state to low-energy state, the spontaneous transition coefficient is $A_0 = 2.85 \times 10^{-15} \text{ s}^{-1}$. The transition releases a signal at a frequency of $\nu_0 = 1420.40575$ MHz (wavelength of $\lambda_0 = 21.106$ cm), this is the 21-cm signal. For an HI cloud at cosmological distance with redshift z , the 21-cm line will be redshifted to a lower frequency ($\nu_{\text{obs}} = \nu_0 / (1 + z)$) as the expansion of the Universe, so the cosmological 21-cm line is needed to be observed in radio band, 300–1400 MHz. Meanwhile, radio telescopes with large receiving area and high sensitivity are necessary because the 21-cm signal is very weak and radio contaminated.

Follow the references [110, 202], the relative number density ratio of the high energy state to the low energy state of the hyperfine structure of the hydrogen atom is

$$\frac{n_1}{n_0} = 3 e^{-T_*/T_s} \quad (2.37)$$

where $T_* = \Delta E/k_B = 0.068$ K is the equivalent temperature of the energy difference, $k_B = 1.3807 \times 10^{-23}$ J/K is the Boltzmann constant, T_s is the spin temperature.

In astrophysics, usually $T_s \gg T_*$ so $n_1 \approx 3n_0$, it means that about 3/4 of hydrogen atoms are in the high-energy state of hyperfine structure. Specifically, this ratio is related to three effects, one is the absorption of CMB photons by hydrogen atom; the other is the collision between hydrogen atom and free electron as well as proton, due to the scattering section of electron is larger, it is mainly the collision between hydrogen atom and free electron; the third is the scattering between hydrogen atom and Lyman α photon. The spin temperature can be expressed as [105]

$$T_s = \frac{T_{\text{CMB}}^{-1} + x_c T_K^{-1} + x_\alpha T_c^{-1}}{1 + x_c + x_\alpha} \quad (2.38)$$

Where T_{CMB} is the temperature of CMB, T_K is the dynamic temperature of gas, T_c is the color temperature of Lyman α , x_c and x_α are the coupling coefficients of the collision and Lyman α scattering, respectively.

The optical depth of the 21-cm signal in the diffuse intergalactic medium is [27]

$$\tau(z) \approx 9.2 \times 10^{-3} (1 + \delta) x_{\text{HI}} \left(\frac{T_{\text{CMB}}(z)}{T_s} \right) \left(\frac{\Omega_b h}{0.03} \right) \left(\frac{\Omega_m}{0.3} \right)^{-1/2} \left(\frac{1+z}{10} \right)^{3/2} \quad (2.39)$$

Where $T_{\text{CMB}}(z) \approx 2.7255(1+z)$ K is the average temperature of CMB at redshift of z [195], $(1 + \delta)$ is the relative density of matter, x_{HI} is the neutral fraction.

Because the CMB from the last scattering surface is ubiquitous, the usual measurement is the relative temperature of the 21-cm signal to the CMB [27]

$$\delta T_b(z) = 25 \text{ mK} \cdot (1 + \delta) x_{\text{HI}} \left(\frac{\Omega_b h}{0.03} \right) \left(\frac{\Omega_m}{0.3} \right)^{-1/2} \left(\frac{1+z}{10} \right)^{1/2} \left(1 - \frac{T_{\text{CMB}}(z)}{T_s} \right) \quad (2.40)$$

With T_s is larger than, smaller than or equal to T_{CMB} , the 21-cm signal appears as emission line, appears as absorption line or doesn't exist, respectively. When $T_s \gg T_{\text{CMB}}$, the brightness temperature of 21-cm signal is independent of the spin temperature.

Neutral hydrogen 21-cm signal evolves as the Universe evolves, as shown in Fig. 2.11. At the redshift of $1100 \geq z \geq 150$, the Compton scattering of the remaining free electrons after

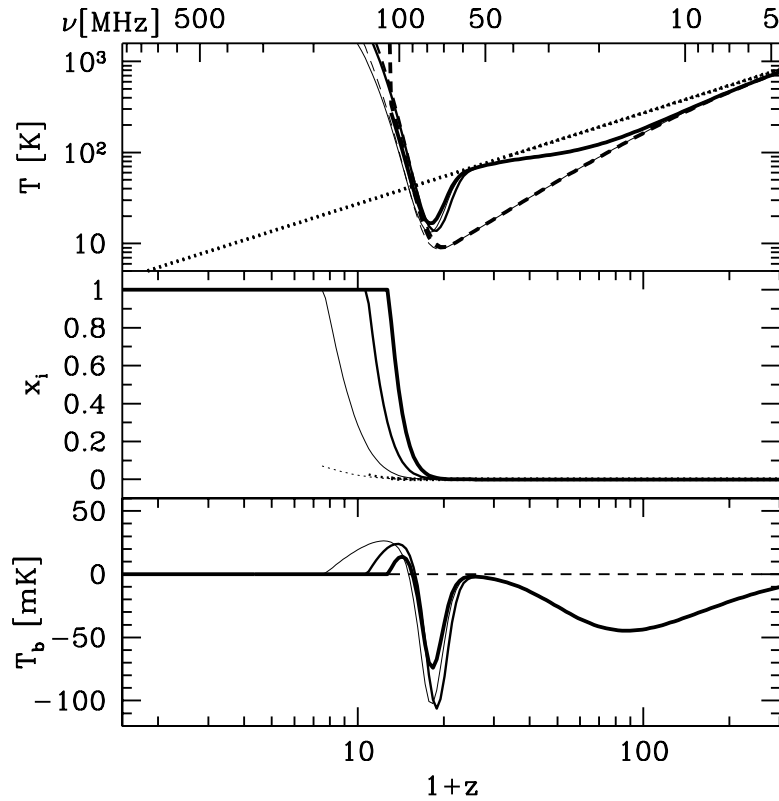


Fig. 2.10 Top panel: Evolution of the CMB temperature T_{CMB} (dotted curve), the gas kinetic temperature T_K (dashed curve), and the spin temperature T_s (solid curve). Middle panel: Evolution of the gas fraction in ionized regions x_i (solid curve) and the ionized fraction outside these regions (due to diffuse X-rays) x_e (dotted curve). Bottom panel: Evolution of mean 21-cm brightness temperature T_b (cited from [201]).

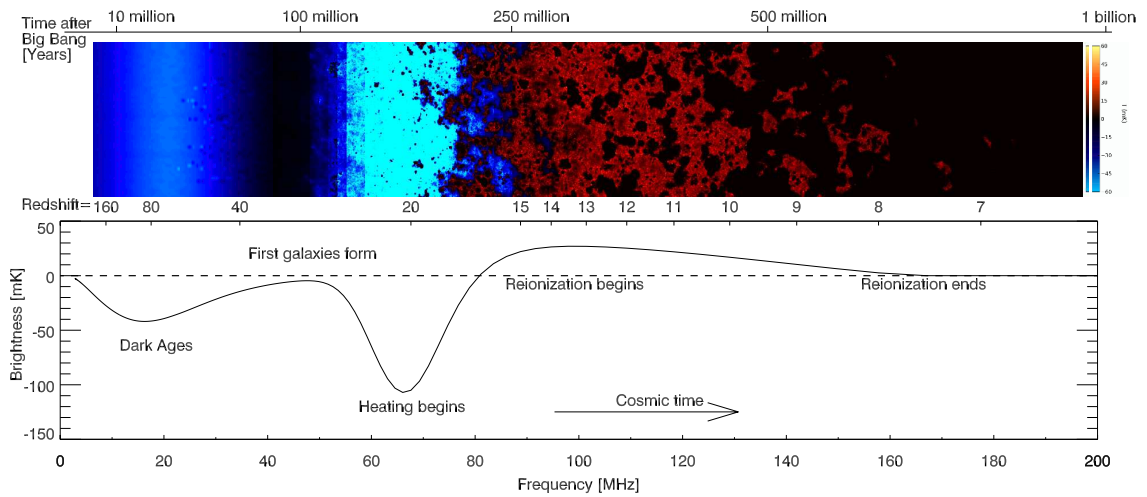


Fig. 2.11 The cosmological 21-cm signal [202]. Top: emission and absorption of 21-cm signal. Bottom: evolution of 21-cm signal with redshift.

the recombination maintains the thermal coupling of the gas with CMB $T_K = T_{\text{CMB}}$, and the effective collision coupling of the high-density gas makes the spin temperature $T_s = T_{\text{CMB}}$. Therefore, at this time $\delta T_b = 0$, there is no neutral hydrogen 21-cm signal.

At the redshift of $150 \geq z \geq 30$, because the gas temperature changes with redshift $T_K \propto (1+z)^2$ and the CMB temperature $T_{\text{CMB}} \propto (1+z)$, as the Universe expands, the gas cools faster than CMB. Meanwhile it is in the Dark Ages, stars have not yet formed and the gas is not heated, thus $T_K < T_{\text{CMB}}$. Because the density of the Universe is still relatively high, the collision coupling is strong enough, the spin temperature deviates from the CMB temperature and tends to the gas temperature, thus $T_s < T_{\text{CMB}}$ and $\delta T < 0$, the 21-cm signal appears to be a weak absorption signal.

At the redshift of $30 \geq z \geq 20$, as the Universe expands, the density decreases further, the collision is not strong enough to maintain the coupling between spin temperature and gas temperature, they deviate from each other gradually. At this time, due to stars have just formed, the gas has not been heated, and Lyman α is relatively weak, there is no effective mechanism to separate the spin temperature from the CMB temperature. Thus $T_s = T_{\text{CMB}}$, $\delta T_b = 0$, and there is no 21-cm signal.

At the redshift of $20 \geq z \geq 15$, the gas is still unheated, and the gas temperature cools much faster with the expansion of the Universe than CMB, thus $T_K < T_{\text{CMB}}$. But at this time Lyman α has become strong enough to couple spin temperature to gas temperature, thus $T_s < T_{\text{CMB}}$, the 21-cm signal appears to be a strong absorption signal.

At the redshift of $15 \geq z \geq 11$, as more and more stars and galaxies form, gas is heated to its temperatures well above CMB temperatures, and spin temperature is coupled by gas temperatures due to Lyman α , thus $T_s = T_K > T_{\text{CMB}}$, $\delta T_b > 0$, the 21-cm signal is a strong emission signal.

At the redshift of $11 \geq z \geq 6$, during the epoch of reionization, although the gas temperature is heated higher and higher, as the reionization proceeds, the neutral hydrogen in the intergalactic medium becomes less and less, the cosmological 21-cm emission signal becomes weaker and weaker, and it basically disappears by the end of reionization.

At the redshift of $z \leq 6$, neutral hydrogen in the intergalactic medium is fully ionized and the rest neutral hydrogen is concentrated in galaxies. The 21-cm distribution observed at this time follows the distribution of the galaxy (see Sec. 2.3.4).

2.5 Development of radio astronomy

Radio astronomy is a very important branch of modern astronomy. Through radio observations, pulsars, quasars, cosmic microwave background (CMB) and interstellar molecules have

been discovered. Radio observation is one of the most important means of understanding the origin, evolution and future of the Universe.

The development of radio astronomy depends on the research and development of radio receiver and antenna technology, as well on electromagnetic wave propagation. On the basis of a comprehensive examination of Coulomb's law, Biot-Savart Law and Faraday's law, Maxwell unified the electricity and the magnetism by mathematical analysis (Maxwell's equations), and put forward the concept of "electromagnetic wave". Hertz proved the existence of electromagnetic wave through experiments, and pointed out the direction for the development of radio and radar. Planck had made a breakthrough in quantizing the energy of electromagnetic wave, along with Einstein's photoelectric effect, de Broglie's matter wave and Schrodinger's wave function, laid a foundation for the study of electromagnetic theory.

Based on the research and development of electromagnetic theory, scientists can apply it to engineering. Began from that Marconi succeeded to transmit messages in the form of electromagnetic wave across the Atlantic, radiotelephone services became commercialised and promoted further development of radio communication, and finally it allowed scientists to detect weak radio wave from the center of the Milky way. Karl Jansky succeeded to detect radio signals from the center of the Milky way in 1932 [136], it is the first important contribution of radio observation to astronomy. Grote Reber successfully developed a radio telescope and drew the first radio astronomical map based on the observation in 1943 [203], since then radio astronomy borned. In 1946, Martin Ryle interfered the signals received by two radio telescopes separated from each other and obtained a resolution equivalent to that of a radio telescope with aperture size as the distance between the two places [211], thus the synthetic aperture radio telescope was invented, and Martin Ryle won the Nobel Prize for Physics due to this huge contribution in 1974².

Modern computer can combine signals from multiple antennas, thus effectively forming large aperture for higher resolution, such as VLA (Very Large Array)³, VLBA (Very Long Baseline Array)⁴. At present, radio interference technology has developed to VLBI (Very Long Baseline Interferometry) [44] and even SVLBI (Space Very Long Baseline Interferometry)⁵, which provides a powerful tool for the development of radio astronomy.

In different frequency bands, due to the different mechanisms of radiation generation, the pictures shown by the Universe are significantly different. For example, through optical observation, we can study stars, clusters and galaxies, as well as hot gas ionized by stars, visible objects such as planets and the Moon which reflect visible light. Through infrared ob-

²<https://www.nobelprize.org/prizes/physics/1974/ryle/facts>

³<http://www.vla.nrao.edu/>

⁴<https://public.nrao.edu/telescopes/vlba>

⁵<https://www.jpl.nasa.gov/missions/space-very-long-baseline-interferometry-space-vlbi>

ervation, we can see star formation inside the nebula. Through X-ray and γ ray observations, we can study the high-energy objects and high-energy phenomena of the Universe, such as the accretion of dense objects (e.g. neutron stars, black holes), supernova remnants and so on. Through radio observation, we have discovered pulsars, quasars, cosmic microwave background and interstellar molecules (the four major discoveries in astronomy in the 1960s). Through cosmological 21-cm line, we can study the large-scale three-dimensional structure of the Universe and unveil the mystery of dark energy.

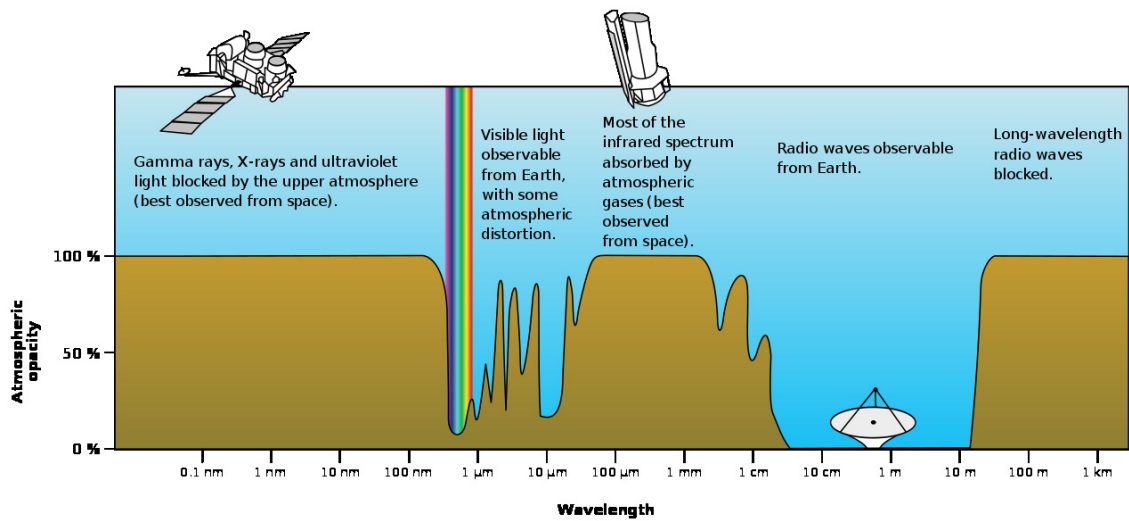


Fig. 2.12 The atmosphere window of the Earth. For the astronomical observation on the ground there are three main windows: optical, infrared and radio (cited from ⁶).

Optical observation can be carried out on the ground. The wavelength of the optical window is about 300–700 nm, but the radiation with a wavelength shorter than 300 nm can hardly reach the ground. The observations of these frequency bands should be carried out outside the atmosphere. Near-ultraviolet radiation at 200–300 nm is absorbed by the ozone layer in the atmosphere, far-ultraviolet radiation at 100–200 nm is absorbed by oxygen molecules, X-ray and γ ray with wavelengths shorter than 100 nm are absorbed by oxygen atoms, oxygen molecules, nitrogen atoms, nitrogen molecules and so on in the atmosphere. The atmosphere absorbs little of the visible band of 300–700 nm, its weakening is mainly due to Rayleigh scattering by the atmosphere. Therefore, early astronomical observations were limited to visible objects, mainly stars, clusters and galaxies, and also hot gas ionized by stars (e.g. the Orion Nebula), visible objects such as planets and the moon. A number of large telescopes and associated cameras and spectrographs observe in the optical window, such

⁶<http://www.sun.org/encyclopedia/electromagnetic-spectrum>

as the 10.4-meter Gran Telescopio Canarias⁷ located on La Palma in the Canary Islands of Spain; the 10-meter Keck I & II telescopes⁸ located near the summit of Mauna Kea in the U.S. state of Hawaii; the 10-meter Hobby–Eberly Telescope (HET)⁹ located on Mount Fowlkes near Fort Davis, Texas, USA; the 10-meter Southern African Large Telescope (SALT)¹⁰ located at the South African Astronomical Observatory near Sutherland, South Africa; the 8.2-meter Subaru Telescope¹¹ located at the Mauna Kea Observatory on Hawaii; the Canada France Hawaii Telescope (CFHT)¹² located near the summit of Mauna Kea mountain on Hawaii’s Big Island; the Very Large Telescope (VLT) of European Southern Observatory (ESO)¹³ located in the world’s driest desert—the Atacama Desert of northern Chile; etc. Optical telescopes are greatly influenced by the “seeing”, so the optical telescopes outside the atmosphere can obtain much clearer images than ground-based optical telescopes, such as the Hubble Space Telescope which is 580 km far from the ground.

Due to the ultraviolet, X-ray and γ ray are absorbed by ozone molecules, oxygen atoms, oxygen molecules, nitrogen atoms, nitrogen molecules and so on in the atmosphere, they are necessary to be observed outside the atmosphere, such as the IUE satellite, the CHANDRA satellite, etc.

In the infrared band, there are three observation windows on the ground, they are 2–2.4 μm (near-infrared), 3.3–4.8 μm (mid-infrared) and 8–13.5 μm (far-infrared). Other wavelengths need to be observed outside the atmosphere in particular due to absorption by water molecules and carbon dioxide molecules. Ground infrared telescopes such as the United Kingdom Infrared Telescope (UKIRT), the NASA Infrared Telescope Facility (NASA IRTF)¹⁴; space observations such as the Wide-field Infrared Survey Explorer (WISE)¹⁵; the Herschel Space Observatory¹⁶; the Spitzer Space Telescope (SST)¹⁷; etc.

For radio observation, the wavelength of the window on the ground is about 2 cm–20 m, depending on the density of the ionosphere, the geographical position of the observation point and the solar activity. When the frequency of the electromagnetic wave is lower than the critical frequency of the ionosphere (wavelength $\gtrsim 20$ m), the electromagnetic wave will be reflected by the ionosphere, this is the low frequency limit of the radio window, about

⁷<http://www.gtc.iac.es>

⁸<http://www.keckobservatory.org/>

⁹<http://mcdonaldobservatory.org/research/telescopes/HET>

¹⁰<https://www.salt.ac.za>

¹¹<https://subarutelescope.org>

¹²<http://www.cfht.hawaii.edu>

¹³<https://www.atlasobscura.com/places/very-large-telescope>

¹⁴<http://irtfweb.ifa.hawaii.edu>

¹⁵<http://www.nasa.gov/wise>

¹⁶<http://www.esa.int/herschel>

¹⁷<http://www.spitzer.caltech.edu>

20 MHz. For higher frequencies (wavelength $\lesssim 2$ cm), the scattering effect of water in the atmosphere is strong, this is the high frequency truncation of radio window, about 20 GHz. Even if radio observations are carried out in space, due to the absorption of interplanetary plasma, signals outside the solar system at $\lesssim 1$ MHz is hardly able to be received, this is the lowest limit of astronomical electromagnetic spectrum observations.

One of the advantages of radio observation over optical observation is the low requirement for atmospheric conditions, another advantage is that radio observation can be carried out both during the day and at night. The Rayleigh scattering of atmosphere makes the optical sky so bright during the daytime that optical observation can only take place at night. Because radio wavelengths are much longer than atmospheric dust so that they are not scattered, the radio very bright objects such as the Sun can't always illuminate the entire radio sky, artificial radio broadcasts don't cover the entire radio band, radio observations can be made at any time in principle. For med- and low-frequency radio telescopes, the location is mainly limited by radio frequency interference (RFI). For high-frequency radio telescope, atmospheric humidity should be also considered, dry areas should be chosen.

There are a number of telescopes working at radio bands. For the purpose of detecting the EOR, there are LOFAR (the LOW-Frequency Array) [250], MWA (the Murchison Widefield Array) [244], PAPER (the Precision Array for Probing the Epoch of Re-ionization) [185], 21CMA [272], HEAR (the Hydrogen Epoch of Reionization Array) [91], etc., with observable frequency ranges are roughly 100–300 MHz. For the 21-cm intensity mapping to probe the large-scale structure of the Universe, there are CHIME (the Canadian Hydrogen Intensity Mapping Experiment) [25], Tianlai[64], the proposed BINGO (BAO from Integrated Neutral Gas Observations) [31], etc., which focus on the HI in the galaxies. General-purpose telescopes such as GBT (the Green Bank Telescope) [58, 164, 236], GMRT (the Giant Metrewave Radio Telescope) [184] and FAST [173] also set the 21-cm observation as one of their principle scientific goals.

2.6 Radio interferometer and imaging

2.6.1 Radio interferometer

As shown in Fig. 2.14, two antennas i and j , which are separated a distance of D , receive radio waves from the same direction θ , the wave received by antenna i propagates an extra optical path of $D \cos \theta = c \tau$ (τ is the time delay generated by the baseline) compared with that received by antenna j . Because the object is so far away from the Earth, the received radio wave can be regarded as plane wave $\vec{E} = E_0 e^{i(\vec{k}\vec{x} - 2\pi\nu t)}$. The radio signals (voltages) U_i

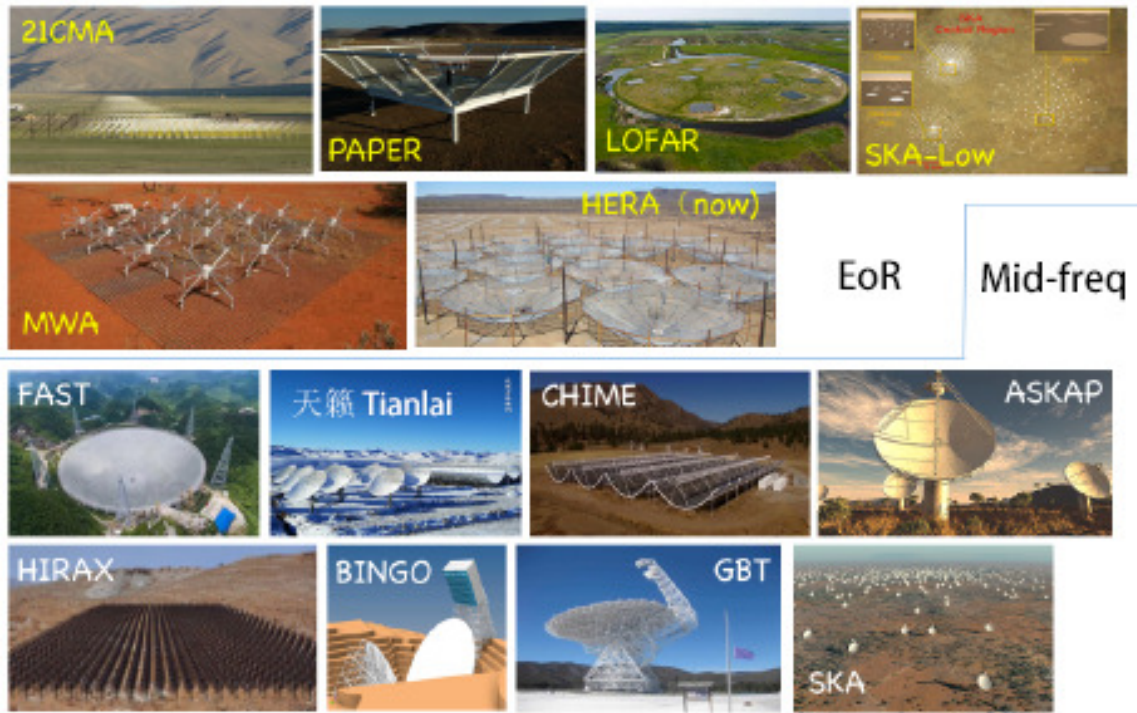


Fig. 2.13 Some 21-cm experiments.

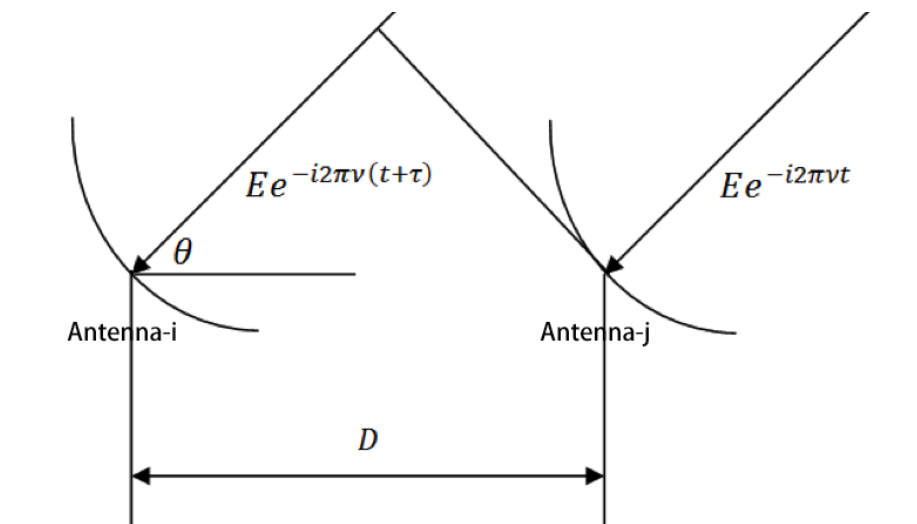


Fig. 2.14 Configuration of two units interferometer.

and U_j received by antenna i and j are

$$U_i = \int_{\Omega} B_i(\vec{n}) E_0(\vec{n}) e^{i\vec{k}\vec{x} - i2\pi\nu(t+\tau)} d^2\vec{n}, \quad U_j = \int_{\Omega} B_j(\vec{n}) E_0(\vec{n}) e^{i\vec{k}\vec{x} - i2\pi\nu t} d^2\vec{n} \quad (2.41)$$

where ν is the observation frequency, \vec{n} is the direction vector of incident wave, B_i is the primary beam of antenna i .

The visibility, which is obtained by radio interferometer, is the correlation of two signals from antennas

$$V_{ij} = \langle U_i U_j^* \rangle = e^{-i2\pi\nu\tau} \left\langle \int_{\Omega} B_i(\vec{n}) E_0(\vec{n}) e^{-i2\pi\nu t} d^2\vec{n} \cdot \int_{\Omega} B_j^*(\vec{n}') E_0^*(\vec{n}') e^{i2\pi\nu t} d^2\vec{n}' \right\rangle \quad (2.42)$$

where $\langle \bullet \rangle = \frac{1}{T} \int_{-\frac{T}{2}}^{\frac{T}{2}} \bullet dt$ denotes time average.

In general, astronomical signals from different directions are considered uncorrelated (i.e., Coherence condition of astronomical radiation)

$$\langle E_0(\vec{n}) E_0^*(\vec{n}') \rangle = |E_0(\vec{n})|^2 \delta(\vec{n} - \vec{n}') \quad (2.43)$$

then Eq. (2.42) becomes

$$V_{ij} = \int_{\Omega} A_{ij}(\vec{n}) T(\vec{n}) e^{-i\vec{k} \cdot \vec{r}_{ij}} d^2\vec{n} \quad (2.44)$$

where $A_{ij}(\vec{n}) = B_i(\vec{n}) B_j^*(\vec{n})$ is the synthetic beam of antenna pair (i, j) , $T(\vec{n}) = |E_0(\vec{n})|^2$ is the brightness on direction \vec{n} , $\vec{k} = \frac{2\pi}{\lambda} \vec{n}$ is the incident wave vector, \vec{r}_i and \vec{r}_j are the position vectors of antenna i and h , $\vec{r}_{ij} = \vec{r}_i - \vec{r}_j$ is the baseline vector.

For an antenna array with N units, the total signal U_a received by the whole array is

$$U_a = \sum_{i=1}^N U_i \quad (2.45)$$

Assuming signals from each feeds have the same polarizations, the intensity of the total signal received by the whole antenna array I_a is the auto-correlation of U_a , which can be considered as the convolution between the real Intensity with synthetic beam of the interferometer:

$$\begin{aligned} I_a &= \langle U_a U_a^* \rangle = \int_{\Omega} \left[\sum_{i=1}^N \sum_{j=1}^N A_{ij}(\vec{n}) e^{-i\vec{k} \cdot \vec{r}_{ij}} \right] I(\vec{n}) d^2\vec{n} \\ &= \int_{\Omega} A_{\text{syn}}(\vec{n}) I(\vec{n}) d^2\vec{n} = A_{\text{syn}}(\vec{n}) \otimes I(\vec{n}) \end{aligned} \quad (2.46)$$

and the synthetic beam of the interferometer is defined as

$$\begin{aligned}
 A_{\text{syn}}(\vec{n}) &= \sum_{i=1}^N \sum_{j=1}^N B_i(\vec{n}) B_j^*(\vec{n}) e^{-i\vec{k}\vec{r}_{ij}} = \sum_{i=1}^N \sum_{j=1}^N \left[B_i(\vec{n}) e^{-i\vec{k}\vec{r}_i} \right] \left[B_j(\vec{n}) e^{-i\vec{k}\vec{r}_j} \right]^* \\
 &= \left[\sum_{i=1}^N B_i(\vec{n}) e^{-i\vec{k}\vec{r}_i} \right] \left[\sum_{i=1}^N B_i(\vec{n}) e^{-i\vec{k}\vec{r}_i} \right]^* = \left| \sum_{i=1}^N B_i(\vec{n}) e^{-i\vec{k}\vec{r}_i} \right|^2
 \end{aligned} \tag{2.47}$$

Fig. 2.15 shows the synthetic beam of two units interferometer. If the distance between two antennas is larger than the size of single one, the resolution of the synthetic beam is obviously improved than that of the latter, but the sidelobe of the synthetic beam is larger due to incomplete uv coverage.

The visibility in (u, v, w) and the map in direction cosine (l, m, n) is a two-dimensional Fourier pair in the case of a small field of view. In this case, the visibility can be transformed into two-dimensional inverse Fourier transform to obtain the sky (dirty) map.

For the direction cosine (l, m, n) coordinates which are shown in Fig. 2.16

$$l = \cos(\alpha), \quad m = \cos(\beta), \quad n = \cos(\gamma) = \sqrt{1 - l^2 - m^2} \tag{2.48}$$

and a spherical coordinate (θ, φ) whose $+\vec{z} \parallel +\vec{w}$, thus $\gamma = \theta$, then

$$\cos(\theta) = \sqrt{1 - l^2 - m^2} \tag{2.49}$$

$$\sin(\theta) = \sqrt{l^2 + m^2} \tag{2.50}$$

$$\cos(\varphi) = \sqrt{\frac{l^2}{l^2 + m^2}} \tag{2.51}$$

and their derivatives

$$d[\sin(\theta)] = \sqrt{1 - l^2 - m^2} d\theta = \frac{l dl + m dm}{\sqrt{l^2 + m^2}} \tag{2.52}$$

$$d[\tan(\varphi)] = \frac{d\varphi}{\cos^2(\varphi)} = \frac{l dm - m dl}{l^2} \tag{2.53}$$

Using such a Jacobian determinant

$$\mathbf{J} = \begin{vmatrix} \frac{\partial \theta}{\partial l} & \frac{\partial \theta}{\partial m} \\ \frac{\partial \varphi}{\partial l} & \frac{\partial \varphi}{\partial m} \end{vmatrix} = \frac{1}{\sqrt{l^2 + m^2} \sqrt{1 - l^2 - m^2}} \tag{2.54}$$

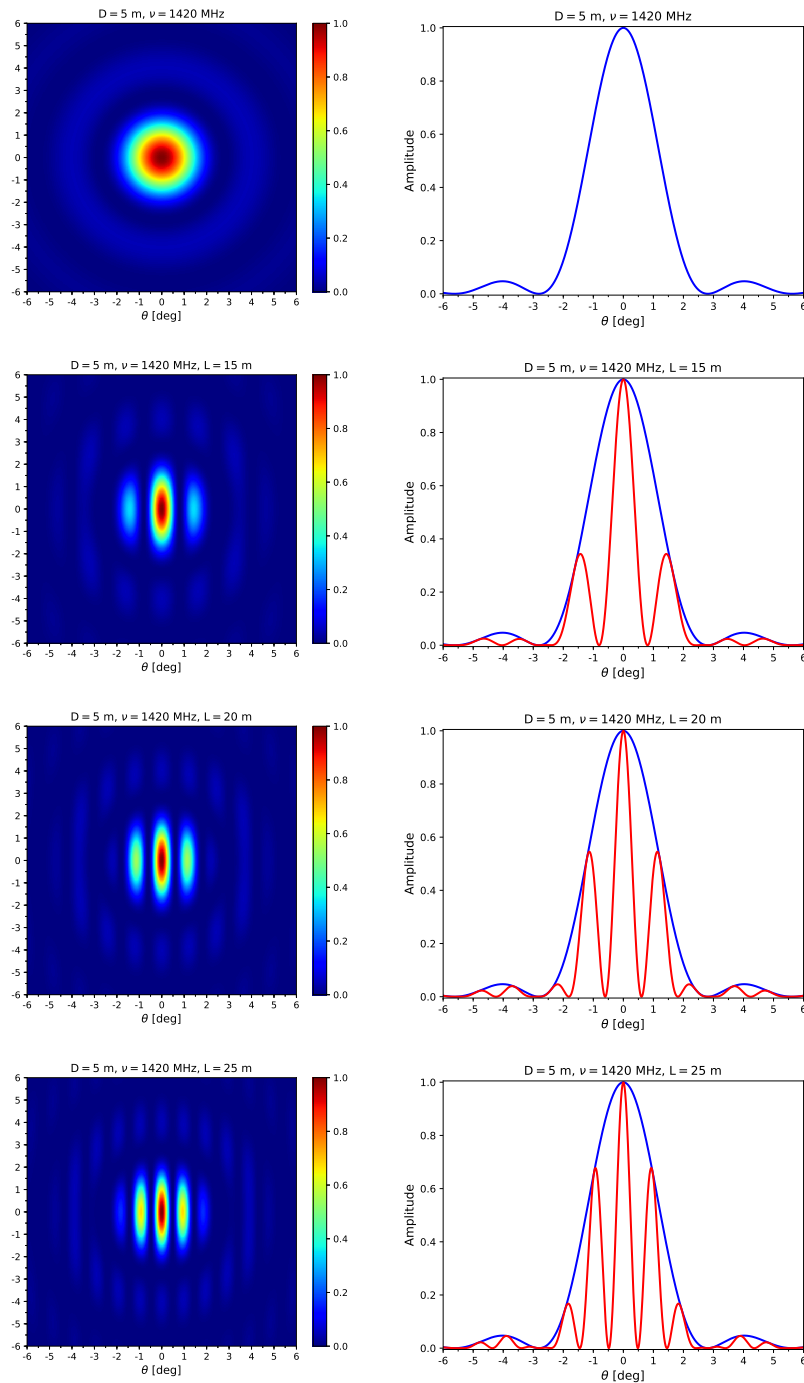


Fig. 2.15 The synthetic beams of two units interferometer. The diameters of each units are both 5 m, and the frequency is 1420 MHz. Left column is the 2D beam, and right column is the E-plane (cross-section at $\phi = 0^\circ$) of the corresponding beam. From top to bottom are for single antenna, 15 m, 20 m and 25 m baselines, respectively.

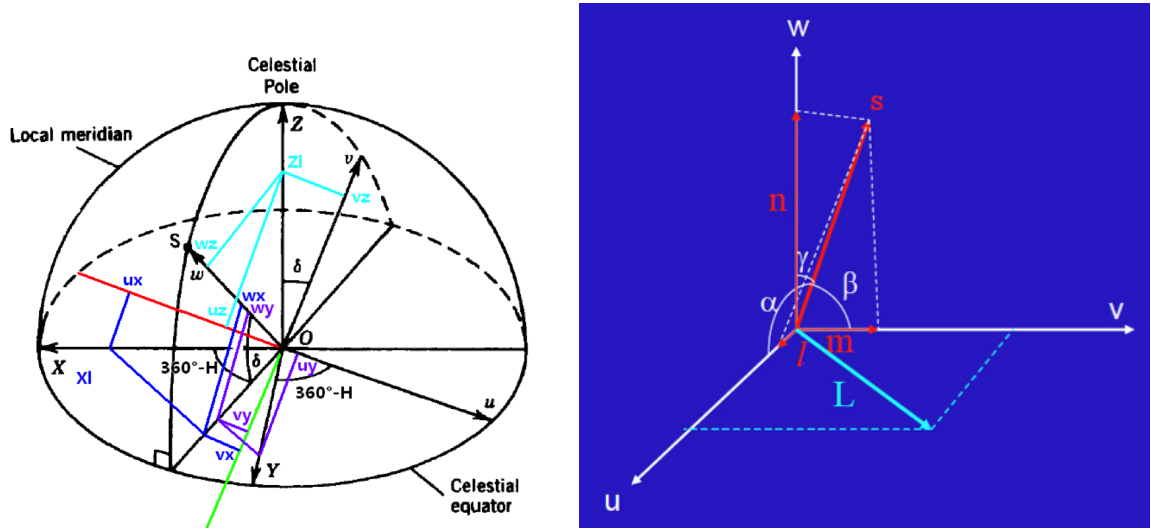


Fig. 2.16 Top: (u, v, w) coordinate system, $+w$ is perpendicular to the uv plane, $+v$ points to the local north, $+u$ points to the local east. $(u, v, w) = (x, y, z)/\lambda$ is the baseline coordinate in the unit of wavelength. Bottom: (l, m, n) coordinate system.

the cell $d\Omega$ can be written in (l, m, n) as

$$d\Omega = \sin(\theta)d\theta d\varphi = \mathbf{J} \cdot \sqrt{l^2 + m^2} dl dm \quad (2.55)$$

$$= \frac{dl dm}{\sqrt{1 - l^2 - m^2}} \quad (2.56)$$

Finally, Eq. (2.44) becomes

$$V_{ij}(u, v, w) = \int A_{ij}(l, m, n) I(l, m, n) e^{-i2\pi[ul+vm+w(n-1)]} \frac{dl dm}{\sqrt{1 - l^2 - m^2}} \quad (2.57)$$

For narrow field of view, i.e., $l \sim 0$, $m \sim 0$ thus $w \sim 1$, Eq. (2.57) is approximately Fourier transform

$$V_{ij}(u, v) = \int A_{ij}(l, m) I(l, m) e^{-i2\pi(ul+vm)} dl dm \quad (2.58)$$

where $I'(l, m) = A_{ij}(l, m)I(l, m)$ for simplicity.

For a realistic antenna array, the number of baselines (i.e., (u, v, w) points) is limited, but the sky (l, m, n) is continuous. Therefore, the limited observational visibility points are samples of the continuous visibility

$$V_{ij}(u, v) = S(u, v) \cdot \mathcal{F}[I'(l, m)] = \mathcal{F}[W(l, m) \otimes I'(l, m)] \quad (2.59)$$

where $S(u, v)$ is the sampling function, the dirty beam $W(l, m) = \mathcal{F}^{-1}[S(u, v)]$ is the inverse Fourier transform of sampling function.

In addition, iterative deconvolution algorithms such as ‘‘CLEAN’’ [127] can reduce the influence of dirty beam and improve the imaging quality.

2.6.2 Imaging algorithm

Eq. (2.59) gives an imaging algorithm for a narrow field of view. In the narrow field of view, the visibility and the sky map are two-dimensional Fourier pairs. However, for wide field of view, the w -term of $2\pi w \left(\sqrt{1 - l^2 - m^2} - 1 \right)$, which is present for non-coplanar baseline, no longer tends to zero, the effect of the w -term can't be ignored. Also, because of the spherical geometry, the 2D Fourier transform is not the correct mathematical formalism for wide field of view. In order to solve the non-coplanar imaging problem of radio interferometer with wide field of view, a number of algorithms were introduced, such as the 3D Fourier transform [230, 83, 187], Faceting, W-Projection [81, 82], W-Stacking[180], etc.

The three-dimensional Fourier transform method, by compensating a phase, makes (u, v, w) and (l, m, n) become a pair of three-dimensional Fourier transform bases. From Eq. (2.57), two sides compensate a phase of $e^{i2\pi w}$, then obtain

$$V(u, v, w)e^{-i2\pi w} = \int \frac{I(l, m) \delta \left(\sqrt{1 - l^2 - m^2} - n \right)}{\sqrt{1 - l^2 - m^2}} e^{-i2\pi (ul + vm + wn)} dl dm dn \quad (2.60)$$

Considering the incomplete uvw coverage, introducing a sampling function $S(u, v, w)$ and its Fourier transform $W(l, m, n)$ (dirty beam), it is obtained

$$V(u, v, w)e^{-i2\pi w} = \mathcal{F}^{-1} \left[W(l, m, n) \otimes \frac{I(l, m) \delta \sqrt{1 - l^2 - m^2} - n}{\sqrt{1 - l^2 - m^2}} \right] \quad (2.61)$$

Note that a requirement for performing an (inverse) Fourier transform is that all primary beams of feeds are the same. The three-dimensional Fourier transform method is intuitionistic, but the disadvantage is that the memory usage is large and the calculation is slow.

Cornwell et al. developed a multi-domain based method, which decomposes visibility into several sub-domains, so that each sub-domain can continue to use two-dimensional Fourier transform, thus imaging, this is the so-called Faceting method. They then developed the W-Projection method [81, 82], which projects the visibility of $w \neq 0$ onto the $w = 0$ plane, so that the 2D Fourier transform can continue to be used. The performance of W-Projection

is much better than that of Faceting. Let

$$K(l, m, w) = e^{-i2\pi w(\sqrt{1-l^2-m^2}-1)} \quad (2.62)$$

According to convolution theorem, Eq. (2.57) can be rewritten to

$$\begin{aligned} V(u, v, w) &= \int \frac{I(l, m)}{\sqrt{1-l^2-m^2}} K(l, m, w) e^{-i2\pi(ul+vm)} dl dm \\ &= V(u, v, 0) \otimes \mathcal{K}(u, v, w) \end{aligned} \quad (2.63)$$

where $\mathcal{K}(u, v, w)$ is the kernel, which is the 2D Fourier transform of $K(l, m, w)$ on lm

$$\mathcal{K}(u, v, w) = \int K(l, m, w) e^{-i2\pi(ul+vm)} dl dm \quad (2.64)$$

$V(u, v, 0)$ is the 2D Fourier transform of $\frac{I(l, m)}{\sqrt{1-l^2-m^2}}$ on lm

$$V(u, v, 0) = \int \frac{I(l, m)}{\sqrt{1-l^2-m^2}} e^{-i2\pi(ul+vm)} dl dm \quad (2.65)$$

Eq. (2.63) represents the visibility of $w \neq 0$, which can be obtained by convolving the visibility of $w = 0$ with the kernel function $\mathcal{K}(u, v, w)$. However, in a realistic radio observation, what we got is $V(u, v, w)$ but not $V(u, v, 0)$. In order to image the data, it is needed to project the visibility of $w \neq 0$ onto the $w = 0$ plane to get $V(u, v, 0)$. As it can be seen from Eq. (2.63), the kernel function $\mathcal{K}(u, v, w)$ is needed to be deconvolved. Direct deconvolution operation is quite difficult, however, using the property of $\mathcal{K}(u, v, w)$, so that the deconvolution operation can be achieved by convolving its conjugate $\mathcal{K}^*(u, v, w)$, this is because

$$\begin{aligned} \mathcal{K}(u, v, w) \otimes \mathcal{K}^*(u, v, w) &= \mathcal{F}^{lm} \{ \mathcal{F}^{-uv} [\mathcal{K}(u, v, w)] \cdot \mathcal{F}^{-uv} [\mathcal{K}^*(u, v, w)] \} \\ &= \mathcal{F}^{lm} \{ K(l, m, w) \cdot K^*(l, m, w) \} = \mathcal{F}^{lm}(1) \\ &= \delta(u, v) \end{aligned} \quad (2.66)$$

Therefore, by convolving $V(u, v, w)$ with $\mathcal{K}^*(u, v, w)$, the projection on $w = 0$ can be obtained

$$\begin{aligned} V(u, v, w) \otimes \mathcal{K}^*(u, v, w) &= V(u, v, 0) \otimes \mathcal{K}(u, v, w) \otimes \mathcal{K}^*(u, v, w) \\ &= V(u, v, 0) \otimes \delta(u, v) = V(u, v, 0) \end{aligned} \quad (2.67)$$

The key is computing $\mathcal{K}(u, v, w)$, which is generally difficult to obtain the analytic solution, in most cases, it is obtained by numerical calculation. In addition, if angles are small, $l^2 + m^2 \ll 1$, expand $K(l, m, w)$ as Taylor expansion and keep the first order term, a Gaussian function can be obtained. The Fourier transform of a Gaussian function is another Gaussian function

$$K(l, m, w) \approx e^{i\pi w(l^2 + m^2)} \quad (2.68)$$

$$\mathcal{K}(u, v, w) = \mathcal{F}^{lm}[K(l, m, w)] \approx \frac{i}{w} e^{-i\pi \left(\frac{u^2 + v^2}{w}\right)} \quad (2.69)$$

After got $V(u, v, 0)$, perform a two-dimensional Fourier transform on uv to get the image

$$\frac{I(l, m)}{\sqrt{1 - l^2 - m^2}} = \mathcal{F}^{-uv}[V(u, v, 0)] \quad (2.70)$$

W-Stacking handles the w -term differently from W-Projection. W-Projection projects the visibility data $V(u, v, w)$ onto the $w = 0$ plane by convolving a kernel function, and then performs a two-dimensional Fourier transform to get the image. W-Stacking divides the value of w into several layers (called the w -layer), each layer corresponds to a certain range of w values. Then each layer is transformed by two-dimensional Fourier transform. Finally, summing all results of layers to get the image.

$V(u, v, w)$ in Eq. (2.63) can be viewed as the 2D Fourier transform of $\frac{I(l, m)}{\sqrt{1 - l^2 - m^2}} e^{-i2\pi w(\sqrt{1 - l^2 - m^2} - 1)}$ on lm

$$\frac{I(l, m)}{\sqrt{1 - l^2 - m^2}} = e^{i2\pi w(\sqrt{1 - l^2 - m^2} - 1)} \int V(u, v, w) e^{i2\pi(uv + vm)} du dv \quad (2.71)$$

Then the two sides integrate w to get the image

$$\frac{I(l, m)}{\sqrt{1 - l^2 - m^2}} (w_{\max} - w_{\min}) = \int_{w_{\min}}^{w_{\max}} e^{i2\pi w(\sqrt{1 - l^2 - m^2} - 1)} \mathcal{F}^{-uv}[V(u, v, w)] dw \quad (2.72)$$

For a realistic radio array, w points are finite discrete points, then the integral of Eq. (2.72) on w becomes summation

$$\frac{I(l, m)}{\sqrt{1 - l^2 - m^2}} (w_{\max} - w_{\min}) = \sum_{w_k = w_{\min}}^{w_{\max}} \Delta w_k e^{i2\pi w_k(\sqrt{1 - l^2 - m^2} - 1)} M(l, m, w_k) \quad (2.73)$$

where $M(l, m, w_k)$ is the 2D Fourier transform of k -th w -layer data of $V(u, v, w_k)$.

Above classical wide field of view imaging algorithms are widely used in the imaging of radio interferometric data. However, those algorithms have an implicit prerequisite: the

antenna response is invariable during the imaging process. For the time-varying antenna response case, such as lunar orbit interferometer, above algorithms are not applicable. In this case, it is necessary to develop a new imaging algorithm based on the basic principle of interferometric observation, as detailed in [Chapter 5](#).

Chapter 3

A high-resolution self-consistent whole sky foreground model

Various studies on the foregrounds have been carried out for the 21-cm experiments [93, 89, 156, 270, 223, 224]. To investigate how the different foreground subtraction techniques work, or to make forecast of the experiments, simulations with foreground sky models are needed. The Global Sky Model (GSM) [89] is widely used for this purpose, with a recent updated version [270]. We denote the original and updated GSM models as GSM2008 and GSM2016 respectively. GSM is based on the method of Principal Component Analysis (PCA), it uses several whole sky or large area sky maps, especially the Haslam map [124] at 408 MHz as input data, to extract the principal components in the pixel-frequency space, to generate maps at other frequencies. GSM2008 applies the PCA once on the whole pixel-frequency data set, while GSM2016 applies the PCA iteratively on the outputs of each iterations. However, owing to the limitation of the available whole sky surveys (e.g. the Haslam map has an angular resolution of 0.85°), the angular resolutions of these models are limited at low frequencies.

A high resolution whole sky model is provided in the 21-cm simulation software package CORA [223, 224]. It uses the 2003 version of the Haslam map¹ as the base map, with the spectral index given by GSM, plus a randomly generated variation in the spectral index. To include structures on the small scales, CORA added bright radio sources drawn from the matched ones in the VLSS [74] and NVSS [79] surveys, plus a mock sample of randomly generated radio sources according to the distribution given in Matteo's paper [94], and finally, based on Santos's paper [215], very faint radio sources are taken into account as a whole in the small scale angular power spectrum. There are also other high resolution models, e.g. the

¹https://lambda.gsfc.nasa.gov/product/foreground/haslam_408.cfm

Tiered Radio Extragalactic Continuum Simulation (T-RECS) [40], but only a limited patches of the sky are covered.

In this chapter, we present the method of constructing a high-resolution self-consistent sky model at low frequencies, which incorporates both diffuse foreground and radio sources [130]. My diffuse map is constructed by generating physical foreground components including the Galactic synchrotron emission and Galactic free-free emission. The radio source samples are generated using the actual data from the NRAO VLA Sky Survey (NVSS) and the Sydney University Molonglo Sky Survey (SUMSS) where they are available and complete in flux limit, and mock radio sources according to statistical distributions. The entire model is made self-consistent by removing the integrated flux of the radio sources from the diffuse map so that this part of radiation is not double counted. We show that with the radio sources added, a significant angular power is introduced in the mock sky map, which may be important for foreground subtraction simulations.

For the diffuse component, our model differs from the GSM in that instead of using the purely mathematical approach of PCA in GSM (2008 and 2016), we fit the spectral index, varying both with frequency and angular direction using the multi-wavelength data. Such model is less general than the PCA model, but may have some advantages in certain applications, e.g. employing data from other wave bands to improve the foreground model, or to make more extreme extrapolation. We also use the updated Haslam map which is source-subtracted and destriped² [208] as our basis. We achieve a higher angular resolution by adding radio sources to the low resolution maps. This procedure is possible because radio sources, i.e. sources unresolved up to the angular resolution of the survey, have been detected in surveys with higher angular resolutions, further, their statistical distribution is known or can be inferred. However, these radio sources are not detected individually in surveys with low angular resolutions, but are merged into the diffuse foreground. Our procedure differs from that of CORA in detail, for example in the choice of statistical model, and the placement of the points: CORA assumed a uniformly random distribution of points, whereas we consider angular clustering of the radio sources and use Rayleigh-Lévy random walk to place the mock radio sources.

²http://www.jb.man.ac.uk/research/cosmos/haslam_map

3.1 Basis

3.1.1 Resolution

Based on the diffraction theory, the beam pattern of power response of a single telescope is given by the Airy disk:

$$A(\theta) = \left[\frac{2\mathbf{J}_1\left(\frac{\pi D}{\lambda} \sin \theta\right)}{\frac{\pi D}{\lambda} \sin \theta} \right]^2 \quad (3.1)$$

where $\mathbf{J}_1(\bullet)$ is the Bessel function of first order, D is the aperture of the telescope, λ is the observational wavelength.

For a telescope with circular or elliptic beam, such as dish or cylinder telescope, its beam pattern can be modelled as a circular- (Eq. 3.2) or an elliptic- (Eq. 3.3) Gaussian function

$$B(\theta) = \exp\left\{-4 \ln 2 \frac{\theta^2}{\theta_0^2}\right\}, \quad \sigma_{\text{fwhm}} = \frac{\theta_{\text{fwhm}}}{\sqrt{8 \ln 2}} \quad (3.2)$$

$$B(\theta, \varphi) = \exp\left\{-4 \ln 2 \theta^2 \left[\left(\frac{\cos \varphi}{\theta_{0x}}\right)^2 + \left(\frac{\sin \varphi}{\theta_{0y}}\right)^2 \right]\right\} \quad (3.3)$$

The full width at half maximum (FWHM) resolution of a telescope is $\theta_{\text{fwhm}} \approx k \frac{\lambda}{D}$ (for circular beam, D is the diameter; for elliptic beam, D is the length of major axis or minor axis), where θ is the minimum angular distance between two sources which are just distinguished, this is the resolution limit of the telescope. k is a factor of order ~ 1 , depending on the material and structure of the telescope, for an ideal dish telescope, $k = 1.029$ (thus $\sigma_{\text{fwhm}} = \frac{\lambda}{2.288D}$ for Gaussian beam). As we can see, when the observational wavelength (or frequency) is fixed, the larger aperture the telescope has, the higher the resolution is.

The interferometric method can improve the observational resolution. For an N -elements interferometric array, its beam pattern is as shown in Fig. 3.1. The resolution of an interferometer is much higher compared with a single telescope, sources which can not be distinguished by a small aperture telescope, may be distinguished by an interferometer.

However, the obvious disadvantage of the interferometer is that its sidelobes are much higher than the primary beam. With a fixed number of telescopes, sparse distribution of elements can achieve longer baseline leading to higher resolution, but with higher sidelobe. Dense distribution can lower the sidelobe, but provides lower resolution at the same time. Therefore, it is very important how the configuration of the interferometer is, it will affect the sidelobe level significantly, so that the quality of imaging.

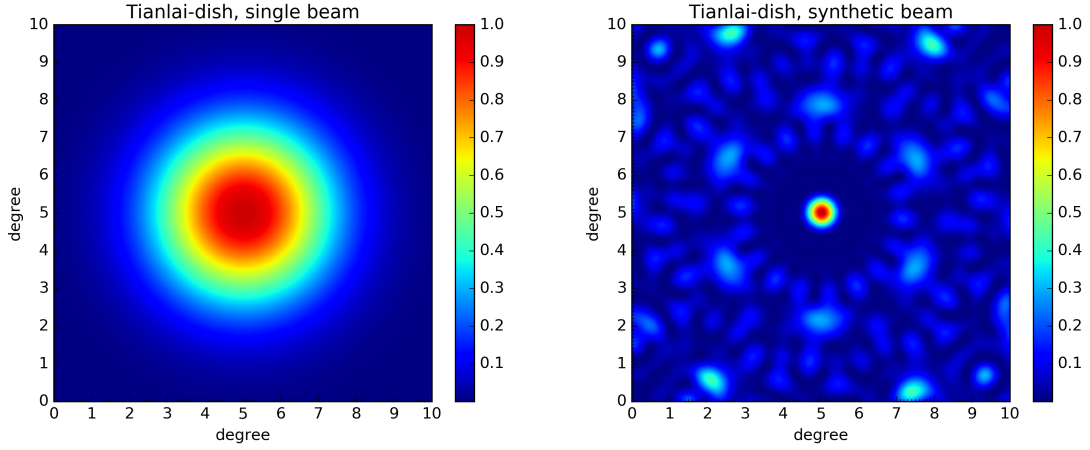


Fig. 3.1 The beams of Tianlai interferometric array [64], left is the primary beam, right is the synthetic beam of the whole array, at 750 MHz. Interferometric method can provide higher resolution, but higher sidelobe level at the same time.

3.1.2 Confusion limit

Most radio sources are outside the Milky Way, and very far away, their distribution can be considered random. For a telescope with limited resolution, there are many radio sources inside one beam, they are confused and can not be distinguished. For this telescope, the confusion of these radio sources can be considered as a nonuniform radio background, and limits the sensitivity of the telescope. The magnitude of this confusion background is the so-called confusion limit, radio sources with flux densities below the confusion limit S_c are undetected.

Below we briefly introduce the calculation of the confusion limit, for detail, please see [171, 247, 252, 78]. The confusion limit can be determined by integrating the differential count $n(S)$ to an upper limit. First, assuming the positions of sources on the sky are random, and their differential count is a power-law

$$n(S) = kS^{-\gamma} \quad (3.4)$$

For a radio source with flux density S , the response of this source by a telescope inside one beam $B(\theta, \varphi)$ is $S_B = S \cdot B(\theta, \varphi)$. In a solid angle of $d\Omega$, the average count of sources in a range from S_B to $S_B + dS_B$ is

$$N(S_B) = \int_{\Omega_B} \frac{n\left(\frac{S_B}{B(\theta, \varphi)}\right)}{B(\theta, \varphi)} d\Omega = kS_B^{-\gamma} \frac{\pi \theta_0^2}{(\gamma - 1) 4 \ln 2} \quad (3.5)$$

Let $S_c = Q\sigma_c$, where Q is a factor of 3–5 [171], the RMS confusion σ_c is [247, 252, 78]

$$\sigma_c^2 = \int_0^{S_c} S_B^2 N(S_B) dS_B \quad (3.6)$$

If the differential count $n(S)$ is a single power-law, then from Eq. (3.6), it is obtained

$$S_c = \left[\frac{Q^2 k \pi \theta_0^2}{(3 - \gamma)(\gamma - 1) 4 \ln 2} \right]^{\frac{1}{\gamma - 1}} \quad (3.7)$$

However, actually $n(S)$ is not a single power-law, we can split $n(S)$ in to several parts, each part can be considered as a single power-law.

3.2 The datasets

In order to model the bright sources, two radio surveys are used: the NVSS (NRAO VLA Sky Survey) [79] and the SUMSS (Sydney University Molonglo Sky Survey) [39, 165], because the sky coverage of NVSS+SUMSS is almost the whole sky, and their resolutions and sensitivities are similar. NVSS covers the latitudes $> -40^\circ$, about 82% of the celestial sphere, its observational frequency is 1.4 GHz, FWHM resolution is $\theta = 45''$, flux density limit is 2.5 mJy, and produces a catalogue containing about 2×10^6 radio sources. SUMSS covers the latitudes $< -30^\circ$, its observational frequency is 843 MHz, FWHM resolution is $\theta = 45'' \times 45'' \text{cosec}|\delta|$ (varying with latitude), flux density limit is 6 mJy, and produces a catalogue containing about 2×10^5 radio sources. Source distributions of NVSS and SUMSS are shown in Fig. 3.2

In order to model the diffuse emission, both the observation and simulation data are used, which are listed in Tab. 3.1. Maps at 10, 22, 45, 85, 150, 408, 1420 MHz are the total brightness temperature maps, which contain the Galactic synchrotron emission, the Galactic free-free emission, the extragalactic radio source, CMB, etc. Note that the 1420 MHz map has been removed the Cassiopeia A and Cygnus A. The 2.3 GHz map has been removed the CMB. The 23, 33, 41, 61 94 GHz maps are the simulated Galactic synchrotron maps produced by WMAP-9yr data [33].

3.3 Point source model

Above mJy there are mainly the bright radio galaxies, quasars and BL Lacertae objects, while below mJy, the late-type galaxies (most are spiral galaxies) becomes dominated [76, 135].

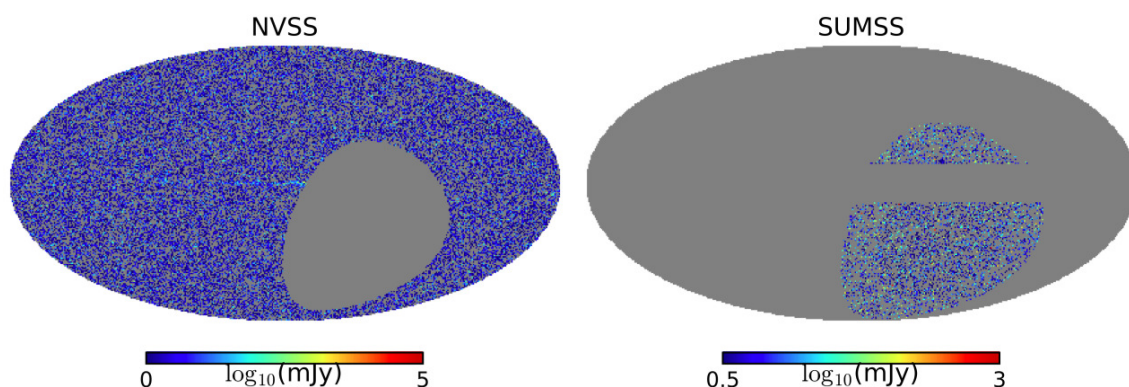


Fig. 3.2 The survey data of radio sources: left is NVSS, right is SUMSS.

Table 3.1 Sky maps which are used to model the diffuse foreground.

Frequency	FWHM	Reference
10 MHz	$2.6^\circ \times 1.9^\circ$	[56]
22 MHz	$1.1^\circ \times 1.7^\circ$	[209]
45 MHz	5°	[118]
85 MHz	$3.8^\circ \times 3.5^\circ$	[150]
150 MHz	2.2°	[150]
408 MHz	0.85°	[124]
1420 MHz	0.6°	[206]
2300 MHz	$2.3^\circ \times 1.9^\circ$	[240]
23, 33, 41, 61, 94 GHz (WMAP)	$\sim 0.5^\circ$	[33]

Maps from (a) to (i) are at frequencies of 10 MHz, 22 MHz, 45 MHz, 85 MHz, 150 MHz, 408 MHz, 1420 MHz, 2300 MHz and 23 GHz, in the Equatorial coordinate system, in the unit of $\log_{10}(K)$.

When observe the radio sources, the angular resolution of the telescope is a significant parameter. A source can be observed as resolved or unresolved depending on the confusion limit of the telescope. Generally, a source with flux density above $3-5S_c$ is resolved. Therefore, our radio source model includes three components: bright source, resolved faint source and the unresolved source which is determined by the confusion limit.

3.3.1 Bright sources

To model the bright sources, NVSS and SUMSS surveys are used. There is an about 10° overlap region between two surveys, latitude from -40° to -30° , and about 7515 sources are identified both in the two surveys. The overlap sources mainly include two types: late-type galaxies and radio loud active galactic nucleus (radio loud AGN) [212]. In our model, types of the sources are not taken into account, only their flux densities are concerned. Therefore, using two types of radio sources together, the spectral index of flux density can be computed and is fitted by a Gaussian function of $N(\mu = 0.8157, \sigma^2 = 0.1509)$, which is shown in Fig. 3.3.

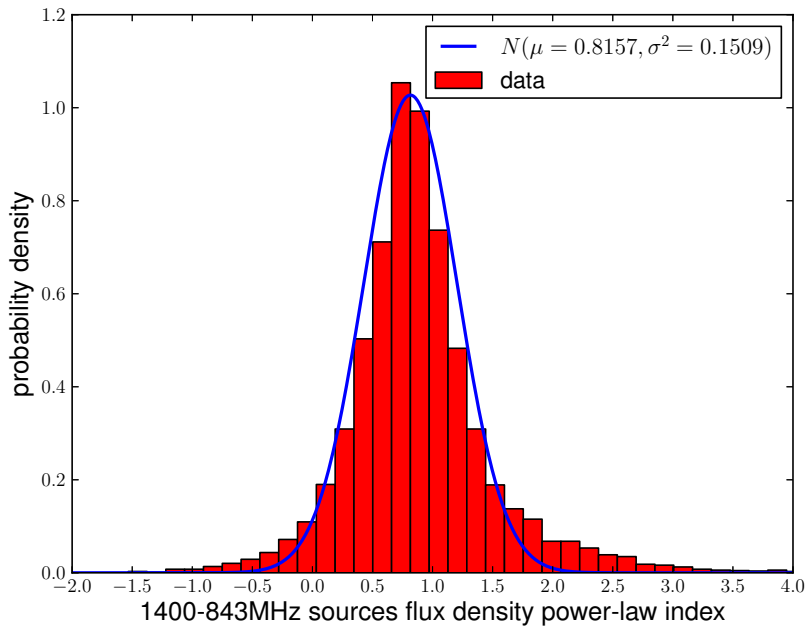


Fig. 3.3 The spectral index of flux density. Red columns are the probability densities of the indices computed from the 7515 overlay sources, blue curve is the best fit Gaussian function of $N(\mu = 0.8157, \sigma^2 = 0.1509)$.

Because of the detection limit, the sample of the sources becomes incomplete while the flux density lower than one threshold. It is important to make sure that the sample of the sources is complete when it is used. Fig. 3.4 shows the source counts of two surveys, the curves drop quickly below thresholds because the samples become incomplete. For the NVSS and SUMSS, the thresholds are $S_{\text{NVSS}} = 2.7$ mJy and $S_{\text{SUMSS}} = 12$ mJy respectively.

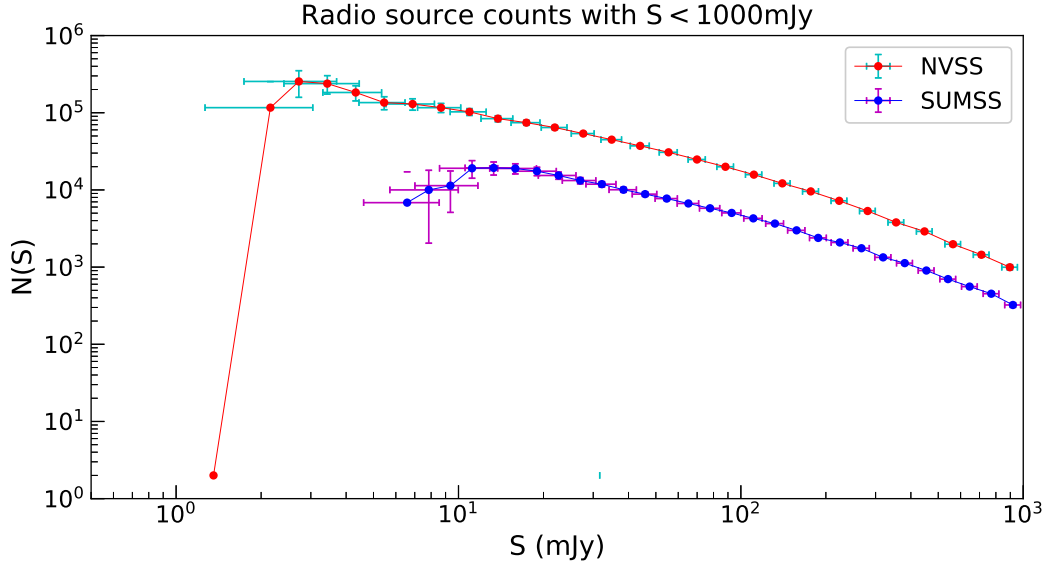


Fig. 3.4 Source count below 1 Jy. The curves of NVSS and SUMSS drop quickly below $S_{\text{NVSS}} = 2.7$ mJy and $S_{\text{SUMSS}} = 12$ mJy respectively, because the surveys become incomplete.

In order to combine the NVSS and SUMSS data, three conditions should be satisfied in advance. First is two samples must be complete, second is the surface densities of two samples should be the same, third is two samples must be at the same frequency. Based on the spectral index (Fig. 3.3), the flux density of SUMSS at 1.4 GHz can be scaled according to $S_{1.4\text{GHz}}^{\text{SUMSS}} = S_{843\text{MHz}}^{\text{SUMSS}} \left(\frac{1.4\text{GHz}}{843\text{MHz}}\right)^\alpha$. The specific indices of each radio sources α can be generated randomly by a Gaussian distribution of $N(\mu = 0.8157, \sigma^2 = 0.1509)$. Then, to obtain complete samples, sources above 15 mJy in NVSS and above 22 mJy in SUMSS are selected. The combined catalogue which covers almost the whole sky is shown in Fig. 3.5.

To fill the missing data in Fig. 3.5, the simplest methodology is to place mock sources with a uniform random distribution on the celestial sphere. However, angular clustering among radio sources has been observed, as would be expected for the general matter distribution [182, 93]. To generate radio sources with such angular clustering, we used the Rayleigh-Lévy random walk [162, 122, 121, 75, 111, 138, 9], in which the probability distribution of a

source distancing from the previous source with an angular distance Θ is given by

$$P(\Theta > \theta) = \begin{cases} \left(\frac{\theta}{\theta_0}\right)^{-\gamma}, & \theta \geq \theta_0 \\ 1, & \theta < \theta_0 \end{cases} \quad (3.8)$$

The θ_0 and γ parameters can be obtained from the two-point correlation function from radio source survey [111, 75]. Here, we follow the result obtained from [182] to use $\theta_0 = 6'$ and $\gamma = 0.8$.

We executed the following steps to generate the radio sources with the Rayleigh-Lévy random walk:

1. Beginning from an arbitrary position, place the first source;
2. Choose a random direction \vec{n} , a random angular distance θ from the current source, and a uniform random number u . If $u > P$, place the subsequent source at the coordinate (\vec{n}, θ) ;
3. Repeat step 2 until all the sources are placed;
4. Specify the flux density of each source at 1.4 GHz. For each flux density bin centering at S_0 with width ΔS_0 , the number of sources over the whole sky is $N_0 = 4\pi \int_{S_0 - \Delta S_0/2}^{S_0 + \Delta S_0/2} n(S) dS$. So we randomly select N_0 sources from the mock map and provide flux densities as uniform random values from $S_0 - \Delta S_0/2$ to $S_0 + \Delta S_0/2$, with the spectral index given by a Gaussian random number with $N(\mu = 0.8157, \sigma^2 = 0.1509)$.

The final distribution of bright sources (including mock sources) is shown in Fig. 3.6.

3.3.2 Faint radio sources

The faint radio sources in our model are indicated the sources with flux densities below the lower limit of the bright sources described in Sec. 3.3.1 of 15 mJy but above the confusion limit of 0.5 mJy which will be explained in Sec. 3.3.3, i.e. the faint radio sources are still resolved, but fainter than the complete sample of NVSS+SUMSS.

To model the faint radio sources, Rayleigh-Lévy random walk is applied, as introduced in Sec. 3.3.1. Obviously, the differential count of radio source $n(S)$, which is the number of radio sources per steradian per flux density, is needed to determinate how many sources in the range of flux density which is needed to be simulated. In order to obtain $n(S)$, the radio luminosity function is required.

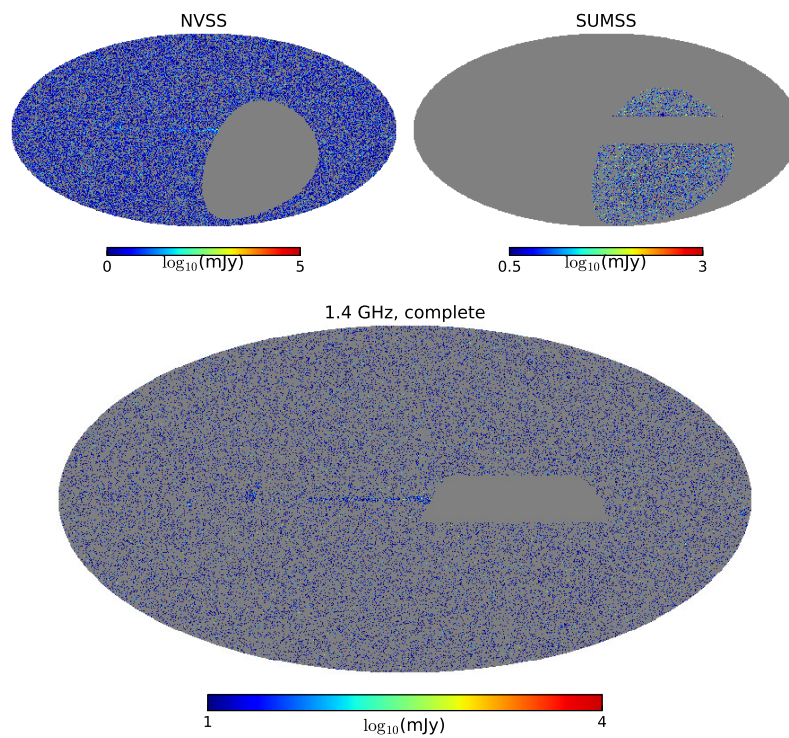


Fig. 3.5 Top left: NVSS data at 1.4 GHz. Top right: SUMSS data at 843 MHz. Bottom: the combination of NVSS and SUMSS at 1.4 GHz, it covers almost the whole sky, and the flux limit is 15 mJy.

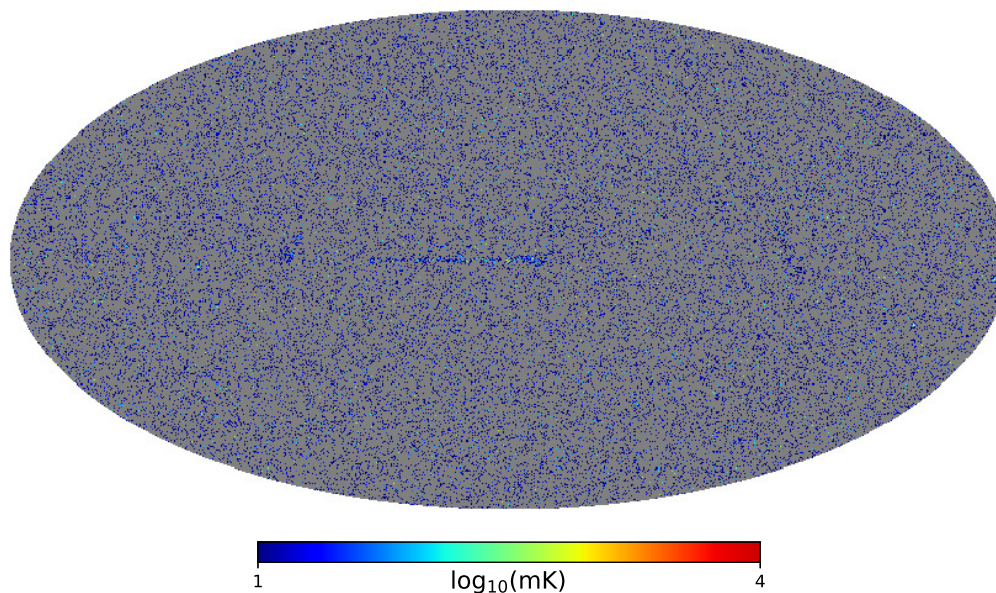


Fig. 3.6 The distribution of the bright sources which is modelled by the combination of NVSS and SUMSS. The missing data is fill by the Rayleigh-Lévy random walk.

The normalized differential count $n(S)$ is defined as [76]

$$S^{5/2}n(S) \equiv \frac{1}{4\pi} \int_0^\infty S^{5/2}\eta(S,z)dz \quad (3.9)$$

where $\eta(S,z)$ is the number of radio sources per unit flux density per unit redshift, the weight $S^{5/2}$ is for the traditional “static Euclidean” normalization [79].

Using the complete sample of NVSS+SUMSS (Sec. 3.3.1), $n(S)$ is computed and shown in Fig. 3.7. For the detail of the computation, please see Appendix A.

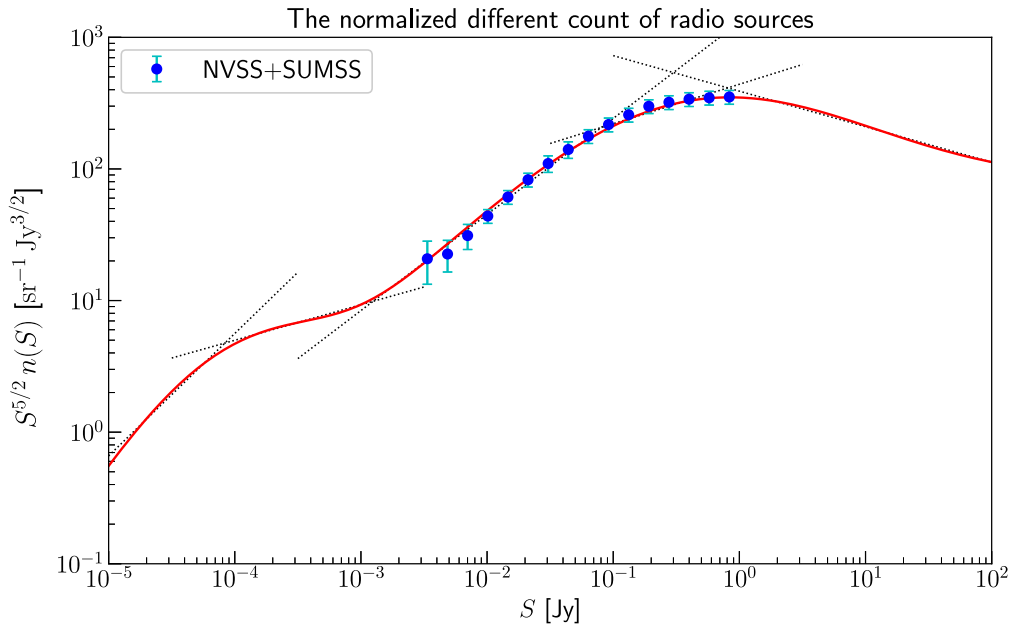


Fig. 3.7 Radio normalized differential count. $n(S)$ is the number of radio source per steradian per flux density. Blue points are computed by the complete sample of NVSS+SUMSS, red curve is from Eq. (3.9).

The sky map of bright radio source obtained in Sec. 3.3.1 is at frequency 1.4 GHz at a FWHM resolution of $45''$ with flux density above 15 mJy. Because of the confusion, sources with flux densities below 0.5 mJy are unresolved (Sec. 3.3.3). Therefore, in the flux density range of 0.5 mJy to 15 mJy, the radio sources are needed to simulate.

The normalized differential count (Fig. 3.7) can indicate how many radio sources in the range of 0.5 mJy to 15 mJy, there are about 2.5×10^8 all over the sky, their number distribution is shown in Fig. 3.8. For a flux density interval of S to $S + dS$, the number of sources is $N_s = \int_S^{S+dS} N(S)dS$.

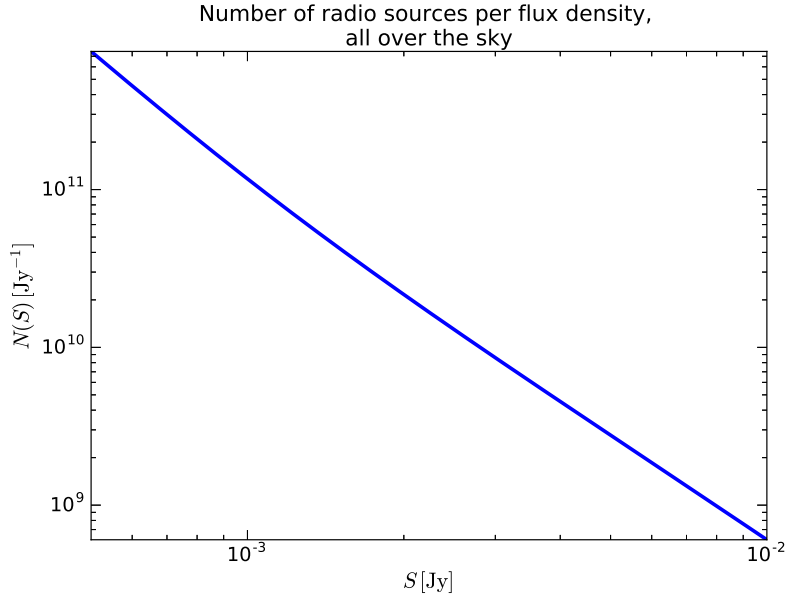


Fig. 3.8 The number distribution of radio sources all over the sky from 0.5 mJy to 15 mJy, based on the differential count.

To model the faint radio source, Rayleigh-Lévy random walk is adopted. The detail steps to generate the radio source maps are as that described in Sec. 3.3.1, The simulated map in the flux density range of 0.5 mJy to 15 mJy at frequency 1.4 GHz is shown in 3.9.

3.3.3 Confusion limit of a telescope

If the differential count $n(S)$ is a single power-law, the confusion limit can be computed by Eq. (3.7). However, Fig. 3.7 shows that $n(S)$ is actually not a single power-law. Relatively nearby radio sources (thus maybe brighter) have differential counts with a power-law index of $\gamma \sim 2.5$ in a Euclidean universe, while the power-law indices of differential counts of further sources drop to $\gamma \sim 1.8$ because of the space time structure of the expanding Universe and source evolution [234]. In this section, we split the distribution of $n(S)$ into five power-laws instead of two, which can describe the $n(S)$ more accurate in wide flux density range:

$$S^{5/2}n(S) = k_n S^{5/2-\gamma_n}, \quad n = 1, 2, 3, 4, 5 \quad (3.10)$$

where k_n and γ_n are the amplitudes and power-law indices of $n(S)$ in different flux density ranges.

It means that the confusion limit can be obtained by integrating the five power-law functions instead of a complicated function as the red curve shown in Fig. 3.7. The values of

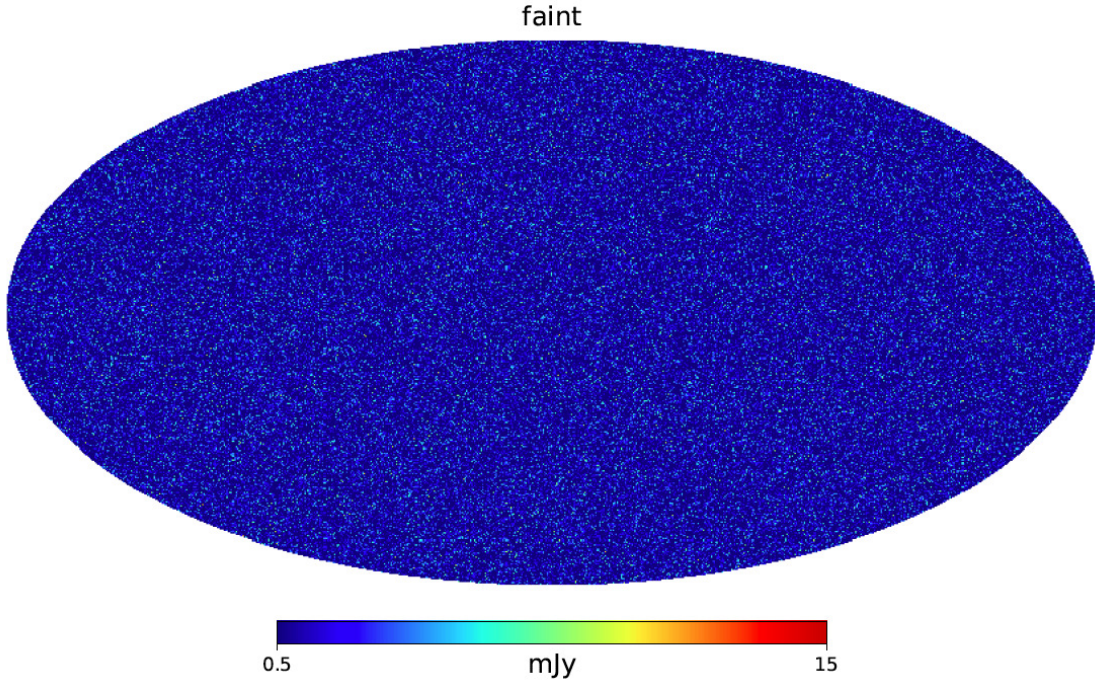


Fig. 3.9 Using the Rayleigh-Lévy random walk to simulate the faint radio sources in the flux density range of 0.5 mJy to 15 mJy at frequency 1.4 GHz. The flux densities and the corresponding counts of sources are obtained from the normalized differential count.

k_n and γ_n of five power-laws are

$$\left\{ \begin{array}{ll} \gamma_1 = 1.57, \quad k_1 = 29500 & \text{if } S \leq 10^{-4} \text{ Jy} \\ \gamma_2 = 2.23, \quad k_2 = 60 & \text{if } 10^{-4} < S \leq 10^{-3} \text{ Jy} \\ \gamma_3 = 1.77, \quad k_3 = 1300 & \text{if } 10^{-3} < S \leq 10^{-1} \text{ Jy} \\ \gamma_4 = 2.20, \quad k_3 = 440 & \text{if } 10^{-1} < S \leq 1 \text{ Jy} \\ \gamma_5 = 2.77, \quad k_3 = 390 & \text{if } S > 1 \text{ Jy} \end{array} \right. \quad (3.11)$$

Combine Eq. (3.11) with Eq. (3.6), the confusion limits for different resolutions can be obtained as

$$S_c = \left\{ \begin{array}{ll} 0.05 \text{ mJy} \cdot Q^{3.51} \left(\frac{\theta_0}{\text{arcmin}} \right)^{3.51} \left(\frac{\nu}{1.4\text{GHz}} \right)^{-2\alpha}, & \theta_0 \leq 0.25 \text{ arcmin} \\ 0.07 \text{ mJy} \cdot Q^{1.53} \left(\frac{\theta_0}{\text{arcmin}} \right)^{1.53} \left(\frac{\nu}{1.4\text{GHz}} \right)^{-2\alpha}, & 0.25 < \theta_0 \leq 1.13 \text{ arcmin} \\ 0.01 \text{ mJy} \cdot Q^{2.56} \left(\frac{\theta_0}{\text{arcmin}} \right)^{2.56} \left(\frac{\nu}{1.4\text{GHz}} \right)^{-2\alpha}, & 1.13 < \theta_0 \leq 7.18 \text{ arcmin} \\ 0.3 \text{ mJy} \cdot Q^{1.63} \left(\frac{\theta_0}{\text{arcmin}} \right)^{1.63} \left(\frac{\nu}{1.4\text{GHz}} \right)^{-2\alpha}, & 7.18 < \theta_0 \leq 30 \text{ arcmin} \\ 3 \text{ mJy} \cdot Q^{1.18} \left(\frac{\theta_0}{\text{arcmin}} \right)^{1.18} \left(\frac{\nu}{1.4\text{GHz}} \right)^{-2\alpha}, & \theta_0 > 30 \text{ arcmin} \end{array} \right. \quad (3.12)$$

where ν is the observational frequency, α is the spectral index of flux density of sources and the typical values are 0.7–0.9 (Fig. 3.3).

Thus for the NVSS survey with angular resolution of $45''$ at 1.4 GHz, the confusion limit with $Q = 5$ is about 0.5 mJy.

The result estimated by Eq. (3.12) is consistent with other surveys by using various telescope or array, e.g.

- Condon et al. [78] estimated the confusion limit of ASKAP EMU (Extragalactic Map of the Universe) survey which covers most of the sky at 1.3 GHz with 10 arcsec FWHM resolution [175], they obtained $S_c = 5 \mu\text{Jy}$, while our estimation of the same case by Eq. 3.12 is $4.95 \mu\text{Jy}$, which is very close to [78].
- Vedantham et al. [252] estimated the confusion limit of MWA with 512 antenna tiles at 300 MHz, the longest baseline is 5 km, they obtained $S_c = 2.3 \text{ mJy}$, while our estimation is 2.6 mJy.
- Subrahmanyam et al. [234] estimated the confusion limit of SKA with 1 arcmin FWHM resolution at 10 GHz with only the relatively short baselines, they obtained $S_c = 8 \mu\text{Jy}$, while our estimation is $15 \mu\text{Jy}$.

3.3.4 Radio source maps in different resolutions

In this chapter, the models of bright and faint radio sources are constructed and the confusion limit is computed, then the radio source maps at different frequencies in different resolutions can be generated as follow.

Firstly, we generate a map of radio sources based on the description of radio source distribution developed in the previous sections (Sec. 3.3.1, 3.3.2 and 3.3.3), including bright sources, faint sources and the confusion background, at the frequency of 1.4 GHz. The angular size of sources is $50''$. In order to make sure there is only one source in one pixel, the map is pixelized in HEALPix scheme [116] with $n_{\text{side}} = 4096$.

Secondly, apply spectral indices to each pixels to scale the flux density of the radio source map generated in the first step to other frequencies. The spectral indices can be generated by Gaussian random numbers of $N(\mu = 0.8157, \sigma^2 = 0.1509)$ (Sec. 3.3.1), or by a running index of $\alpha = 0.8157 - \Delta\alpha \ln\left(\frac{\nu}{1.4\text{GHz}}\right) \pm 0.3873$ where $\Delta\alpha = -0.05$ [255].

Thirdly, convolve the radio source map with a beam. The beam can be modelled as a circular Gaussian function or an elliptic Gaussian function if the beam of telescope is circular or elliptic, such as dish antenna or cylinder antenna, respectively. For a circular

Gaussian beam with FWHM resolution of θ_0 , the resolution of achieved map becomes $\theta' = \sqrt{(50'')^2 + \theta_0^2}$

Fig. 3.10 shows the generated radio source maps at 800 MHz in 1° angular resolution, at 800 MHz in 0.4° and at 100 MHz in 0.7° , respectively.

3.4 Diffuse emission

At mid- and low- frequencies, the diffuse foreground mainly includes the Galactic free-free emission and the Galactic synchrotron emission.

3.4.1 Galactic free-free emission

The Galactic free-free emission is produced by the scattering of free electrons on diffuse warm ionized gas. Although it only accounts for about 1% of the total foreground [222], its magnitude and fluctuation are still several orders of that of the cosmological 21-cm signal, and it plays a non-ignorable role in the 21-cm detection. At high Galactic latitudes, the diffuse warm ionized gas is optical thin and local thermodynamic equilibrium, then the $H\alpha$ is proportional to the emission measure (EM), therefore, we can use the Galactic $H\alpha$ to trace the Galactic free-free emission. As the Galactic $H\alpha$ is measured more and more accurate, and the gas is optical thin at higher frequency, the spectral index of the Galactic free-free emission is measured well, from -2.13 to -2.17 at higher frequencies [32]. The spectral index of the Galactic free-free emission can be predicted by [32]

$$\beta_{\text{ff}} = -2 - \left[10.48 + 1.5 \ln \left(\frac{T_e}{8000\text{K}} \right) - \ln \left(\frac{\nu}{\text{GHz}} \right) \right]^{-1} \quad (3.13)$$

where T_e is the temperature of the free electron, which has a typical range of 7500–8500 K. Our model takes the medium value $T_e = 8000$ K [181, 32].

The Galactic free-free emission maps at some frequencies can be extracted from WMAP data and Planck data. Bennett et al. [33] applied the maximum entropy method and MCMC chain method to the WMAP data to obtain the Galactic free-free maps at 22, 33, 41, 61 and 94 GHz. Ade et al. [194] combined the Planck 2015 data with the WMAP-9yr data to obtain the Galactic free-free map at Planck frequencies.

For other frequencies, we can scale the achieved Galactic free-free map [33, 194] by a power-law. The spectral index of the free-free emission at 1.4 GHz can be predicted to be $\beta_{\text{ff}}^{1.4\text{GHz}} = -2.10$ by Eq. (3.13). As an example, a map of the Galactic free-free emission at 1.4 GHz in 1° resolution is simulated and shown in Fig. 3.11.

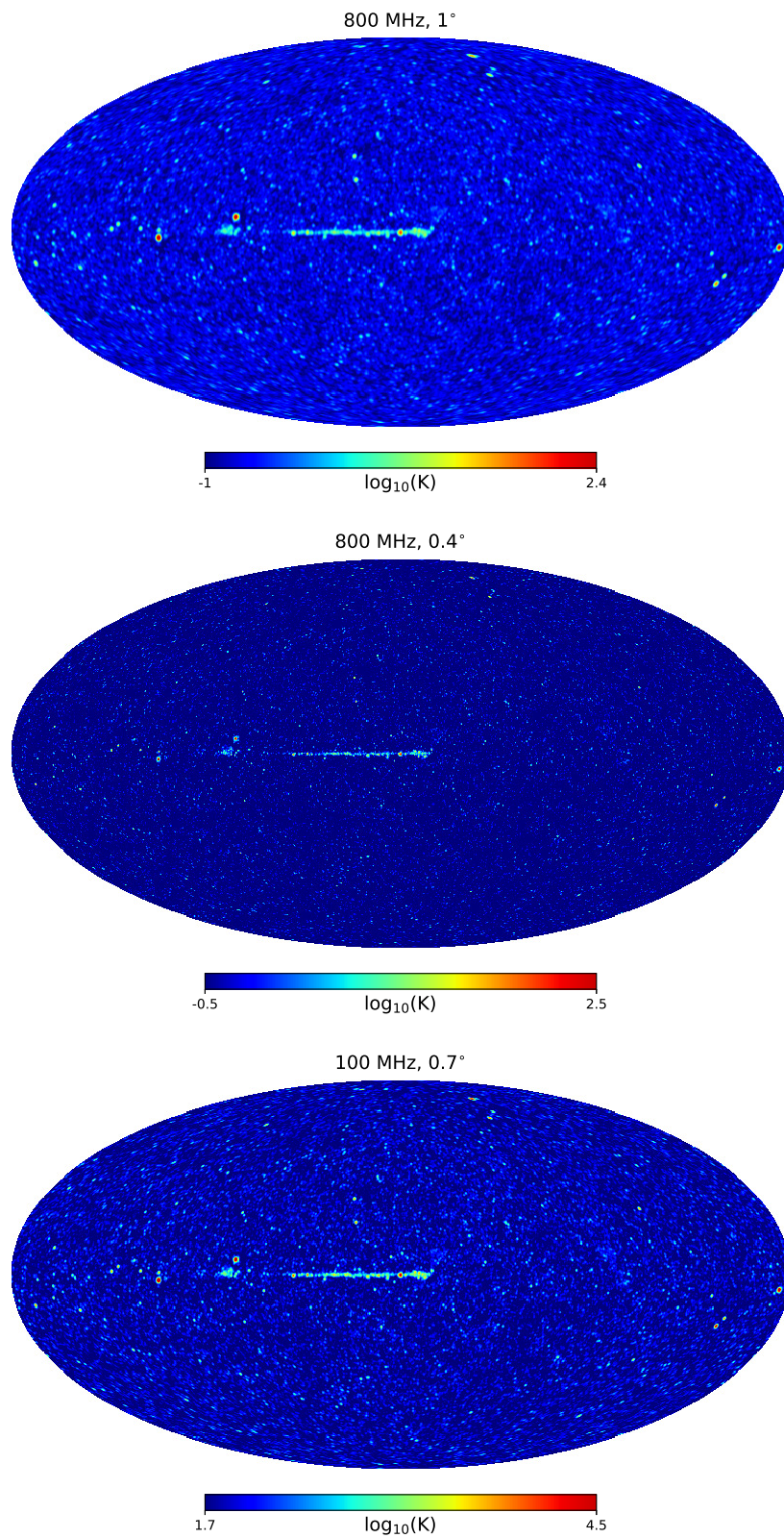


Fig. 3.10 Radio source maps simulated by our model. From top to bottom are maps at 800 MHz in 1° , at 800 MHz in 0.4° and at 100 MHz in 0.7° , respectively.

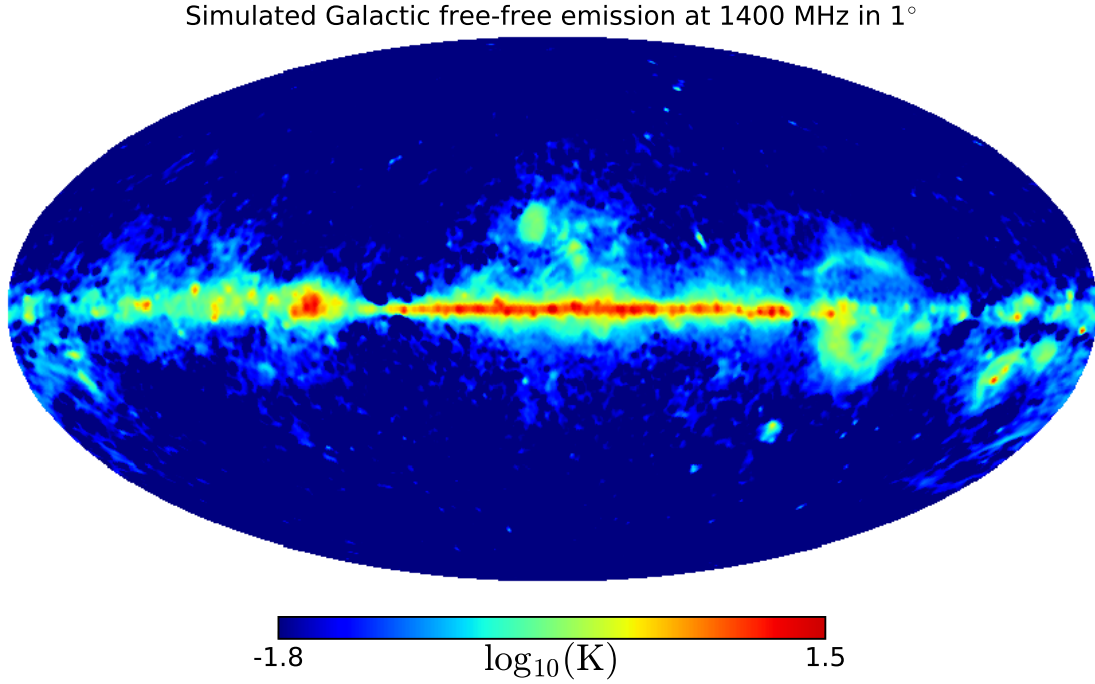


Fig. 3.11 A simulation map of the Galactic free-free emission at 1.4 GHz in 1° resolution.

3.4.2 Galactic synchrotron emission

The Galactic synchrotron emission arises from the relativistic electrons moving in the Galactic magnetic field. It is the principal component of the diffuse foreground, which accounts for about 70% of total temperature of the sky at low frequency [222].

The observed energy distribution of cosmic-ray electrons is roughly a power-law [148, 232, 3]

$$n(E)dE \propto E^{-p}dE \quad (3.14)$$

where $n(E)dE$ is the number of cosmic-ray electrons per unit volume in an energy range of E to $E + dE$. The power-law of cosmic-ray electrons energy distribution leads the Galactic synchrotron emission also a power-law [233, 255]

$$T_{\text{syn}}(\nu) = T_{\text{syn}}(\nu_0) \left(\frac{\nu}{\nu_0} \right)^{-\beta} \quad (3.15)$$

where $\beta = (p + 3)/2$.

For the spectral index of brightness temperature of the synchrotron emission, at high latitude, Platania et al. [198] gave $\beta = 2.81 \pm 0.16$ at the frequency range 1–10 GHz, and

$\beta = 2.76 \pm 0.11$ at 0.4–7.5 GHz combining with the Haslam 408 MHz map [125] and Reich & Reich 1420 MHz map [205, 241]. At lower frequencies, such as 100 MHz, $\beta \approx 2.55$. The spectral index of synchrotron emission varies with frequency, at \sim GHz, $\beta \approx 2.8$ –3 [47, 225, 257, 54, 152, 205, 24, 198].

Actually, the spectral index of synchrotron emission β varies not only with frequency, but also with different line of sight. $\beta(\mathbf{v}, \vec{r})$ is proportional to the spectral index of the cosmic electron $p(\mathbf{v}, \vec{r})$, which is difficult to be determined directly. Fortunately, a number of observations were taken at different frequencies from 10 MHz to 2.3 GHz. One method to obtain β is to fit the polynomial function [89]

$$\beta(\mathbf{v}, \vec{r}) = \beta_0(\vec{r}) + \beta_1(\vec{r}) \left[\ln \frac{\mathbf{v}}{\mathbf{v}_0} \right] + \beta_2(\vec{r}) \left[\ln \frac{\mathbf{v}}{\mathbf{v}_0} \right]^2 + \dots \quad (3.16)$$

where \vec{r} is the unit vector of a line of sight. The reference frequency is taken $\mathbf{v}_0 = 408$ MHz in our calculation.

Take logarithm of Eq. (3.15)

$$\ln \left[\frac{T_{\text{syn}}(\vec{r}, \mathbf{v})}{T_{\text{syn}}(\vec{r}, \mathbf{v}_0)} \right] = \beta_0(\vec{r}) \left[\ln \frac{\mathbf{v}}{\mathbf{v}_0} \right] + \beta_1(\vec{r}) \left[\ln \frac{\mathbf{v}}{\mathbf{v}_0} \right]^2 + \beta_2(\vec{r}) \left[\ln \frac{\mathbf{v}}{\mathbf{v}_0} \right]^3 + \dots \quad (3.17)$$

and re-write Eq. (3.17) to a matrix form

$$\mathbf{y} = \mathbf{A} \mathbf{x} + \mathbf{n} \quad (3.18)$$

Then for any line of sight, the observation data \mathbf{y} is a $N_{\mathbf{v}} \times 1$ vector

$$\mathbf{y} = \left[\ln \left[\frac{T_{\text{syn}}(\vec{r}, \mathbf{v}_1)}{T_{\text{syn}}(\vec{r}, \mathbf{v}_0)} \right], \ln \left[\frac{T_{\text{syn}}(\vec{r}, \mathbf{v}_2)}{T_{\text{syn}}(\vec{r}, \mathbf{v}_0)} \right], \ln \left[\frac{T_{\text{syn}}(\vec{r}, \mathbf{v}_3)}{T_{\text{syn}}(\vec{r}, \mathbf{v}_0)} \right], \dots \right]^t \quad (3.19)$$

and \mathbf{x} is a $N_{\beta} \times 1$ vector

$$\mathbf{x} = [\beta_0(\vec{r}), \beta_1(\vec{r}), \beta_2(\vec{r}), \dots]^t \quad (3.20)$$

and \mathbf{A} is a $N_\nu \times N_\beta$ matrix

$$\mathbf{A} = \begin{bmatrix} \ln \frac{\nu_1}{\nu_0} & \left[\ln \frac{\nu_1}{\nu_0} \right]^2 & \cdots & \left[\ln \frac{\nu_1}{\nu_0} \right]^{N_\beta} \\ \ln \frac{\nu_2}{\nu_0} & \left[\ln \frac{\nu_2}{\nu_0} \right]^2 & \cdots & \left[\ln \frac{\nu_2}{\nu_0} \right]^{N_\beta} \\ \vdots & \vdots & \ddots & \vdots \\ \ln \frac{\nu_{N_\nu}}{\nu_0} & \left[\ln \frac{\nu_{N_\nu}}{\nu_0} \right]^2 & \cdots & \left[\ln \frac{\nu_{N_\nu}}{\nu_0} \right]^{N_\beta} \end{bmatrix} \quad (3.21)$$

where N_ν and N_β are the number of frequency bins and the expansion order of the spectral index of synchrotron emission, respectively. The extra term n is the measured noise with mean value of $\langle n \rangle = 0$ and covariance matrix of $\mathbf{N} = \langle n n^t \rangle$.

The estimator \hat{x} can be obtained by the least square fitting

$$\hat{x} = [\mathbf{A}^t \mathbf{N}^{-1} \mathbf{A}]^{-1} \mathbf{A}^t \mathbf{N}^{-1} \mathbf{y} \quad (3.22)$$

Before using the observation data listed in Tab. 3.1, the synchrotron component should be separated from the data. The 23, 33, 41, 61, 94 GHz are already the synchrotron component from the WMAP-9yr data [33]. For the other maps, the processing steps are as follow:

1. Subtract the Cosmic Microwave Background (CMB). The 2300 MHz map has already been subtracted out the CMB temperature. For the other observational maps, the average CMB temperature 2.7255 K and its anisotropy fluctuation [193] are subtracted.
2. Subtract the contribution of radio sources. Note that in the 1420 MHz map some of the strongest sources such as Cassiopeia A and Cygnus A have already been removed. For the other maps, we subtract the simulated radio source maps which is modelled in Sec. 3.3. I.e. firstly, we generate a radio source map at the same frequency as the observational sky map, in the resolution of $50''$; secondly, if the observational sky map has a circular beam θ_0 or an elliptic beam $\theta_{0x} \times \theta_{0y}$, a circular Gaussian function (Eq. 3.2) or an elliptic Gaussian function (Eq. 3.2) is used to convolve the radio source map, then a radio source map in the same resolution as the observational sky map is obtained; finally, the simulated radio source map is subtracted from the observational sky map.
3. Subtract the Galactic free-free emission. The Galactic free-free emission at different frequencies in different resolution is simulated and subtracted from the observational sky map based on the model described in Sec. 3.4.1.

4. The maps obtained after above three processing steps can be considered to be the Galactic synchrotron emission. Note that these maps are in different resolution. In order to perform a self-consistent calculation, all maps need to be converted to the same resolution before being used. Decreasing the resolution can be done by convolving a beam, while increasing the resolution needs the deconvolution which is difficult to perform. Therefore, all maps are decreased but not increased into the same resolutions, they are converted to 5° FWHM resolution which is the lowest resolution among maps—the resolution of the 45 MHz map.

With the maps preprocessed after above four steps, the spectral index of the synchrotron foreground is computed and fitted. As there are only 13 frequency channels of maps, i.e. for each line of sight, there are only 13 values being used to be fitted, the random error of the result might be large. In order to lower the random error, we fit an average spectral index using all directions of pixels together instead of pixel by pixel. After obtain the average spectral index, the direction-varying spectral indices of each pixels are generated by Gaussian random numbers of $N(\mu = \bar{\beta}(v), \sigma^2 = 0.024 (\frac{v}{408\text{MHz}})^2)$ [126, 199]. The best-fit of β_i of the average spectral index are shown in Tab. 3.2, and the best-fit curve is shown in Fig. 3.12.

Table 3.2 The fitted β_i parameters.

parameter	value and error
β_0	2.55 ± 0.035
β_1	0.06 ± 0.002
β_2	$(3.33 \pm 0.069) \times 10^{-2}$
β_3	$(2.57 \pm 0.093) \times 10^{-3}$
β_4	$(-1.7 \pm 0.028) \times 10^{-3}$
β_5	$(-9.14 \pm 0.162) \times 10^{-5}$
β_6	$(2.86 \pm 0.038) \times 10^{-5}$

With the spectral index of Galactic synchrotron emission fitted above, the Galactic synchrotron emission map can be simulated by scaling the preprocessed 408 MHz map obtained in the item (4). As an example, Fig. 3.13 is the simulated Galactic synchrotron map at 1.4 GHz in 1° resolution.

3.5 Total foreground

Now, the total sky foreground map can be obtained by summing up the diffuse foreground map (which is itself the sum of the Galactic synchrotron and Galactic free-free emission maps) and the radio sources. In the sky regions covered by the NVSS and SUMSS surveys,

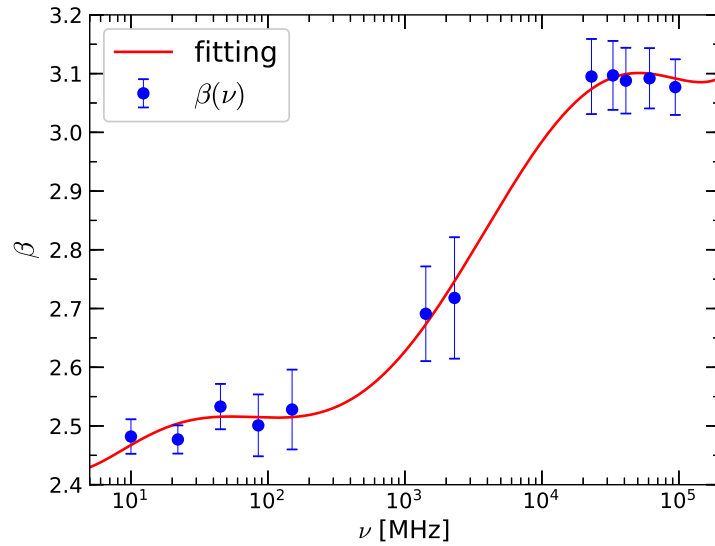


Fig. 3.12 The fitted curve of the spectral index of the Galactic synchrotron emission.

Simulated Galactic synchrotron emission at 1.4 GHz in 1°

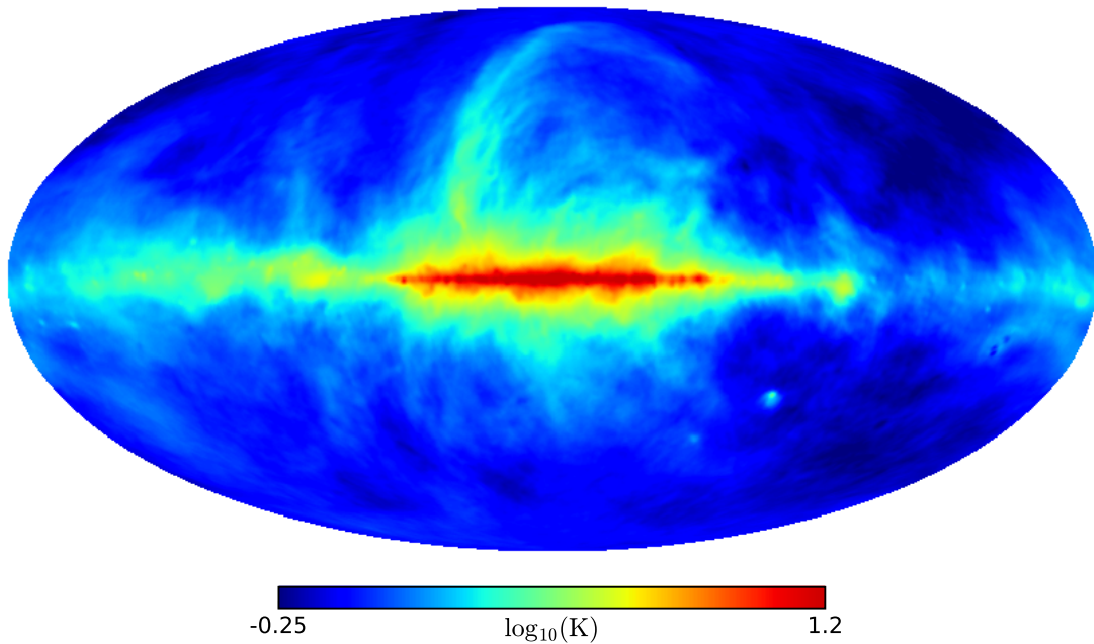


Fig. 3.13 The simulated Galactic synchrotron emission at 1.4 GHz in 1° .

the brighter sources are from the actual catalogues. For sky regions not covered by the surveys, or for the fainter sources, radio sources are generated by the Rayleigh-Lévy random walk according to the statistical distribution. Using the spectral indices for the Galactic synchrotron, the Galactic free-free and the radio sources respectively, the flux at the desirable frequencies are computed, and then convolved with a beam of assumed resolution.

Fig. 3.14 and Fig. 3.15 shows the all-sky and zoom-in maps at the mid-declination in different observational resolutions of 1° , 0.4° and 0.1° . As the observational resolution improved, more radio sources can be seen clearly in the map, some sources which are merged in the low observational resolution appear distinct at higher observational resolutions, while the overall temperature/power of the map remains the same.

We also compare our model and the GSM (2008 and 2016) with the observational sky map of the 2014 version of Haslam map at 408 MHz in a resolution of $\sim 1^\circ$, the relative differences are shown in Fig. 3.16. Compared with the original 1982 version, in the 2014 version of Haslam map [208], the strong baseline stripings are removed, however the stronger radio sources are also removed. So it can be seen that the GSM2008 which is based on the original 1982 version of Haslam map shows difference of stripes and points. The GSM2016 is itself based on the 2014 version of Haslam map, so there is very small difference. Our own model also has relatively small differences with respect to the 2014 version of Haslam map, but as we added back the radio sources, the difference of sources appears. Only for the diffuse component, our model is more consistent with the observational map.

With the addition of the radio sources, significant changes are expected in the angular power spectrum. Fig. 3.17 shows the angular power spectrum for both our diffuse map and total map, in 1° and 0.1° observational resolutions. For comparison, the CORA code is also used to generate mock maps in such observational resolutions and the corresponding angular power spectrum is also plotted in this figure. For the diffuse map, the angular power is basically flat until it begins to drop at the scale corresponding to the map observational resolution. With the addition of the radio sources, there are significant powers on the small scales. The angular power spectrum actually raises before reaching the map observational resolution. The general shape of our angular power spectrum is similar to that of the CORA map, though there are slight differences in the amplitude. As the two maps are both generated with random distribution, and there are differences in the details of both the assumed distribution and the method of generation, such difference is not unexpected. Compared with the low observational resolution GSM map, such angular power will have important impacts on the foreground removal results.

Our model has some limitations and potential to be improved. In terms of applicable frequency range, our model is only available from 10 MHz to 2.3 GHz. At this mid-to-low

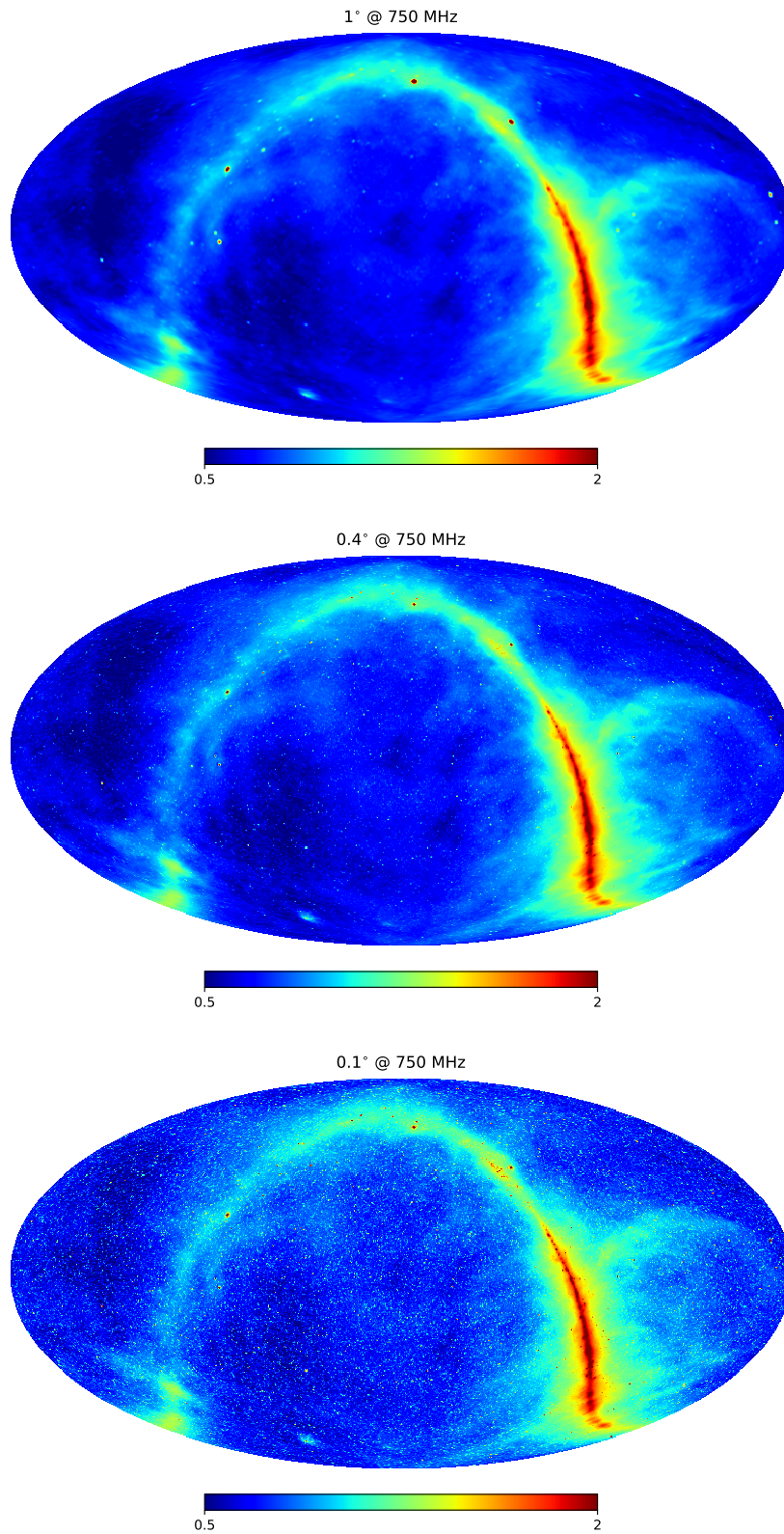


Fig. 3.14 The total foreground maps at 750 MHz in different observational resolutions of 1° , 0.4° and 0.1° . As the observational resolution becomes higher and higher, more and more sources are detected.

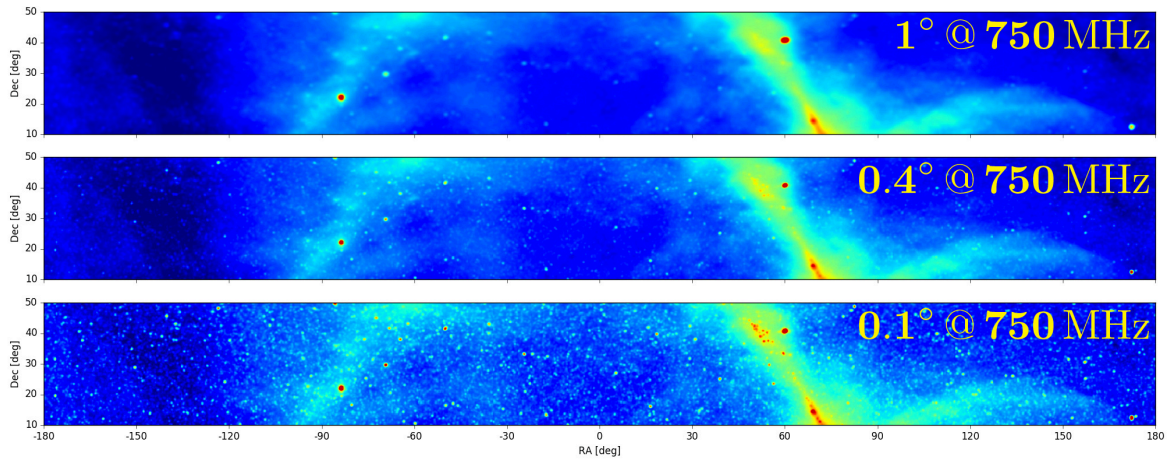


Fig. 3.15 The zoom-in maps in different observational resolutions of 1° , 0.4° and 0.1° in the region of Dec from 10° to 50° . As the observational resolution becomes higher and higher, more and more sources are detected.

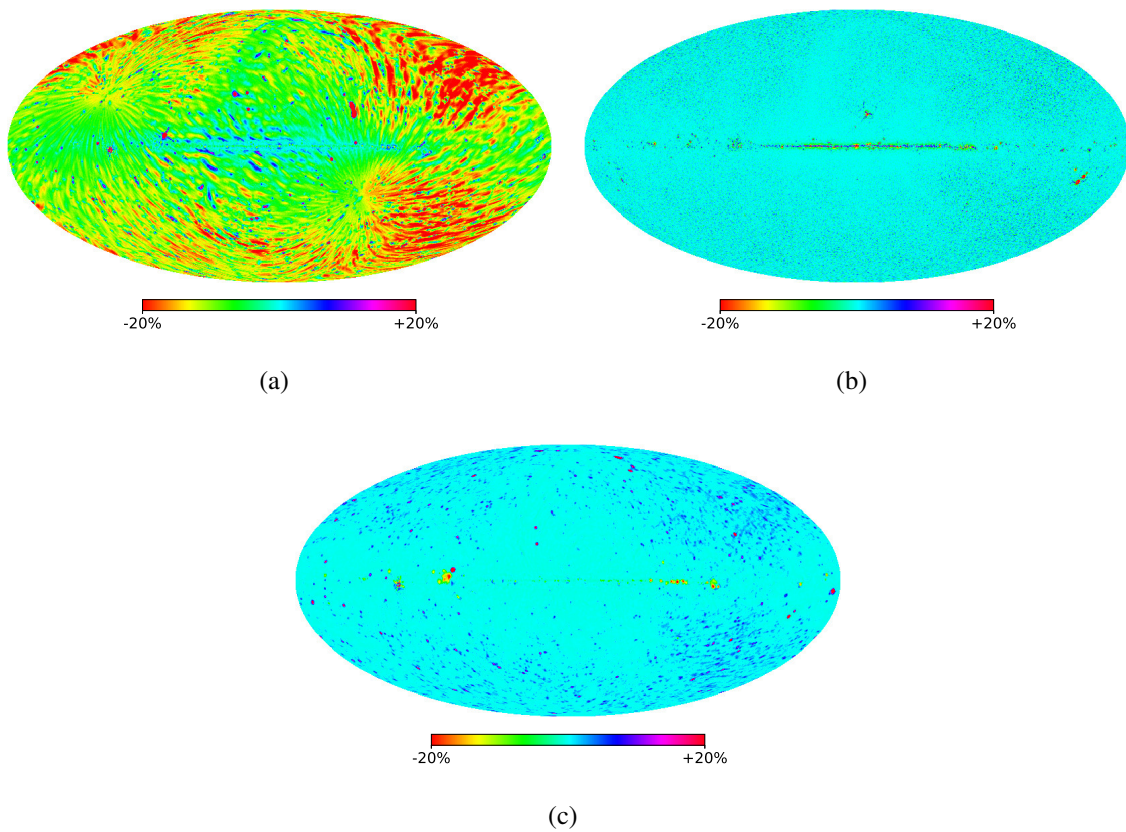


Fig. 3.16 Relative Differences of the GSM2008 (a), GSM2016 (b), and our model (c) to the 2014 version of Haslam map.

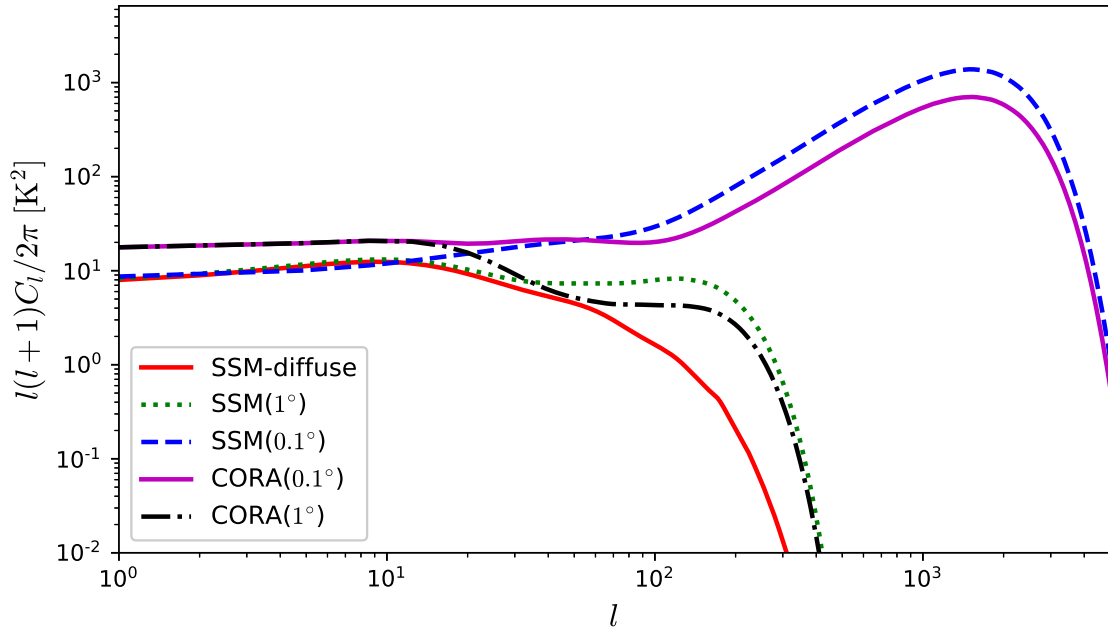


Fig. 3.17 The angular power spectra of the diffuse and total power maps at 1° and 0.1° resolutions. For comparison, we also plot the angular power spectrum from a map generated by the CORA code.

frequency range, the main components of the foreground radiation can be modeled with the Galactic synchrotron emission, Galactic free-free emission and the extragalactic sources which are also primarily radiating by these mechanism. In addition, the propagation effects such as absorption, refraction and scattering are not considered in our model. At the very low frequencies, these effects may have significant impact. For example, the radio waves at a few MHz may suffer significant absorption by the interstellar medium electrons. What's more, our model only considered unpolarized emission. In fact, the Galactic synchrotron emission is highly polarized, and some radio sources are also polarized [248]. The polarized emission is also very important in the foreground subtraction analysis, because the Faraday rotation induce an oscillation along the frequency which is similar to the 21-cm signal [137, 17, 16, 249, 15, 229].

3.6 Brief summary

The cosmological 21-cm line is becoming a more and more important tool to study our universe. Internationally, a number of telescopes or arrays with variable configurations at variable frequencies are participating in the 21-cm observation. The relevant simulations, especially the 21-cm signal extraction, are indispensable. However, until now, there is not a

foreground model which is suitable to the modern large telescope array whose resolution is very high, especially the full sky radio source model. Because of such requirement, in this chapter, a high resolution self-consistent foreground model is constructed, which separately deals with the bright radio sources, the faint radio sources, the unresolved radio sources (the confusion), the Galactic free-free emission and the Galactic synchrotron emission. Our model can generate the foreground map in the observational resolutions $\gtrsim 1$ arcmin, at frequencies from 10 MHz to 2.3 GHz.

Chapter 4

Cosmological signal extraction by frequency and angular filtering

A number of 21-cm signal extraction methods have been proposed, which exploit the differences in statistical properties between the foreground and 21-cm signal. Along a line of sight, the cosmological 21-cm signal can be considered as a random signal (although it is slightly correlated in ~ 1 degree scale) along the redshift (so that the frequency), as the distribution of the neutral hydrogen is closely linked to the underlying random matter density field, while the foreground varies smoothly. Therefore, in principle, the 21-cm signal and the foreground can be separated in frequency domain, and a number of methods have been proposed, such as the polynomial fitting in frequency domain [13, 255, 113], or using the cross-correlation among different frequencies [215]. Recently, blind and semi-blind methods such as the Singular Value Decomposition (SVD) [164, 236, 37, 235], the Robust Principle Component Analysis (RPCA) [273], the Independent Component Analysis (ICA) [61, 261, 10], the Generalized Morphological Component Analysis (GMCA) [60] have also been proposed.

However, the noise, which arises from the electronic receiver, is approximately a white Gaussian noise, it is difficult to be separated from the 21-cm signal in frequency domain. Fortunately, they can still be distinguished in angular domain, as the receiver noise is uncorrelated in angular direction, while the 21-cm signals are correlated because it traces the large scale structure of the Universe.

In this chapter, we study an variant of cosmological 21-cm signal extraction method, using a cascade of two filters [131]: firstly, for the original data, applying a 1D filter to each line of sight in frequency domain, removing the frequency-smooth foreground from the data; secondly, for the output data from the first filter, it is assumed to only contain 21-cm signal and noise, applying a 2D filter in angular domain to remove the noise, then the 21-cm signal is achieved. Because the extraction method uses the priori knowledge about the 21-cm signal,

the foreground and the noise, and the optimal filter depends on their statistical properties, if the signal, the foreground or the noise change, the optimal filters also change.

4.1 The simulated data

In our simulation, the simulated data which will be treated as the input of the filter is generated as follow:

1. Generate a cube box of 21-cm signal, where the redshift, thus the frequency for 21-cm signal, along one dimension, and the angular directions along the other two dimensions.
2. Generate a cube box of foreground as the same shape of the 21-cm signal box.
3. The sum of the 21-cm signal and foreground is considered to be the total sky signal, then we convolve the sky signal with a frequency-dependent Gaussian beam, to model the observational signal received by a telescope.
4. Add a white Gaussian noise to the convolved sky signal, the noise level is set to be ≥ 1000 times of the 21-cm signal.

The detail of each steps is described as follow.

The frequency range of the simulation is from 600 MHz ($z \sim 1.4$) to 1000 MHz ($z \sim 0.4$), with a frequency resolution of 0.1 MHz. This redshift range corresponds to the mid-frequency Baryon Acoustic Oscillation of the large scale structure. Some experiments such as the ongoing survey projects with GBT [164, 236], and dedicated experiments such as Tianlai [64, 262, 265, 266], CHIME [25] BINGO [95] and HIRAX [174]. Such instruments have an equivalent or synthetic aperture size around ~ 100 m, corresponding to an FWHM resolution of $\sim 0.25^\circ$ at ~ 800 MHz.

The simulated cosmological 21-cm signal is generated as follow. The cosmological parameters are adopted from Planck 2018 [196]. The center frequency is 800 MHz, corresponding a redshift of $z = 0.7755$ and a comoving angular diameter distance $D_A = 1068.95 \text{ Mpc } h^{-1}$. Considering to a frequency resolution of 0.1 MHz, the corresponding comoving distance interval is $\Delta D_c = 0.43 \text{ Mpc } h^{-1}$. In order to achieve a uniform cube box to simulate the 21-cm signal, the angular interval should be $\Delta \theta = \Delta D_c / D_A = 0.023^\circ$. Considering the performance of the computer, we generate a cube box with 200^3 voxels, covers an angular volume of $(4.6^\circ)^3$ at $z = 0.7755$. The comoving volume of the cube box in real space is $V = L^3 = (86 \text{ Mpc } h^{-1})^3$, and the corresponding minimum interval in k -space is $\Delta k = 2\pi/L = 0.073 \text{ hMpc}^{-1}$. Note that, the frequency interval of this cube box is only 20

MHz, in order to obtain a frequency range from 600 MHz to 1000 MHz, we generate 20 such cube boxes center at different redshifts (thus different frequencies), then append them along redshift direction.

Then, we generate a random density field of dark matter inside these cube boxes, based on the dark matter power spectrum $P(k)$ from CAMB¹ [155]. The power spectrum of dark matter after the nonlinear correction at redshift $z = 0.7755$ is shown in Fig. 4.1.

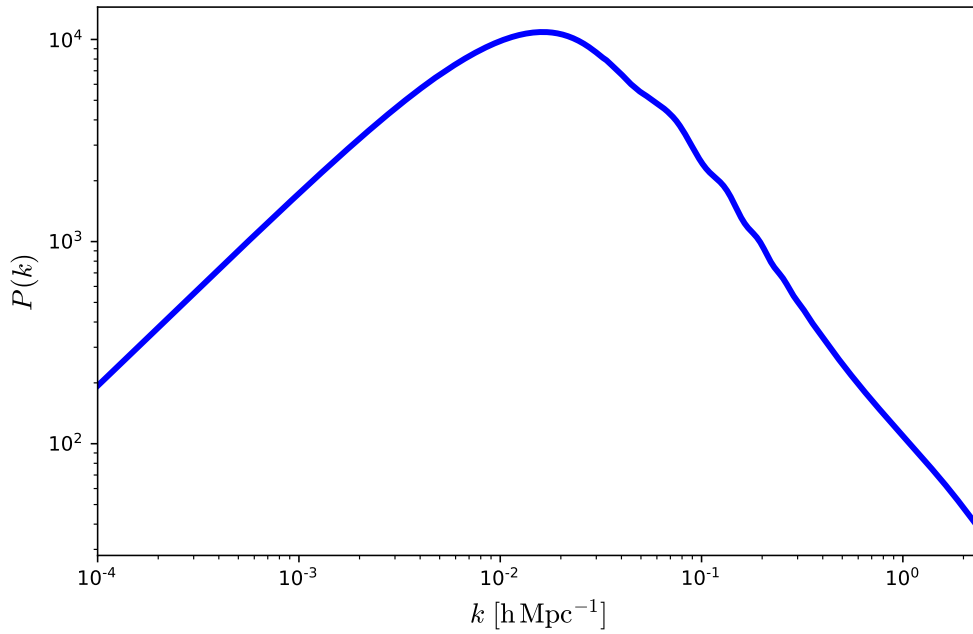


Fig. 4.1 The power spectrum of dark matter after the nonlinear correction at redshift $z = 0.7755$ (computed from CAMB [155]).

Assume the dark matter fluctuation $\delta(\vec{x}) = \rho(\vec{x})/\bar{\rho} - 1$ and its Fourier transformation $\delta(\vec{k})$ can be described by Gaussian random fields

$$\delta(\vec{k}) = \sqrt{\frac{V}{2}P(k)} (a_k + ib_k) \quad (4.1)$$

$$\delta(\vec{x}) = \frac{1}{V} \sum \delta(\vec{k}) e^{i\vec{k}\cdot\vec{x}} \quad (4.2)$$

where $P(k)$ is the dark matter power spectrum after the nonlinear correction, V is the comoving volume of the cube box, a_k and b_k are mutually independent Gaussian random numbers with zero mean and unity variance.

¹<https://camb.info/>

The cosmological 21-cm fluctuation field can be computed from the dark matter density fluctuations through the linear trace of $\delta T_{21}(\vec{x}) = b_{\text{HI}} \bar{T}_{21} \delta(\vec{x})$, where \bar{T}_{21} is the average brightness temperature of 21-cm signal, b_{HI} is the HI bias parameter.

From the cross-correlation between the GBT data of 21-cm observation at $z = 0.6\text{--}1$ and the WiggleZ Dark Energy Survey [98], Masui et al. [164] gave the neutral hydrogen fraction of $\Omega_{\text{HI}} = 6.6 \times 10^{-4}$, and the HI bias $b_{\text{HI}} = 0.70$. The average brightness temperature of 21-cm signal at $z \sim 0.8$ can be given by [58, 164]

$$\bar{T}_{21} \approx 0.284 \text{ mK} \cdot \left(\frac{\Omega_{\text{HI}}}{10^{-3}} \right) \left(\frac{h}{0.73} \right) \left(\frac{1+z}{1.8} \right)^{1/2} \left(\frac{\Omega_{\text{m}} + \Omega_{\Lambda}(1+z)^{-3}}{0.37} \right)^{-1/2} \quad (4.3)$$

For the foreground, two different models are studied. The first model has a single spectral index, which assume that the Galactic diffuse emission dominates the mid- and low-frequency sky. The second model has a spectral index running with frequency, which is a more realistic model, as the Galactic synchrotron emission, the Galactic free-free emission and the extragalactic radio sources all have spectral indices varying with frequency.

For the model with a single spectral index, the foreground brightness temperature $T_{\text{f}}(\nu, \vec{r})$ can be written as (here we use $f(\nu, \vec{r})$ instead of $T_{\text{f}}(\nu, \vec{r})$ for simpler notation) [270]

$$f(\nu, \vec{r}) = A_*(\vec{r}) \left(\frac{\nu}{\nu_*} \right)^{\beta_*} \quad (4.4)$$

where \vec{r} indicates different line of sight on the sky, the spectral index $\beta_* = -2.76$ [205, 241]. $A_*(\vec{r})$ is brightness temperature map of foreground at the reference frequency of $\nu_* = 800$ MHz, which can be generated by our foreground model described in chapter 3.

For the model with running spectral index, $f(\nu, \vec{r})$ can be written as [255]

$$f(\nu, \vec{r}) = A_*(\vec{r}) \left(\frac{\nu}{\nu_*} \right)^{\beta_* - 0.1 \ln(\nu/\nu_*)} \quad (4.5)$$

To convolve the sky signal (21cm signal + foreground), we use a frequency-dependent Gaussian beam, and perform the convolution frequency by frequency. The frequency-dependent Gaussian beam is modelled as

$$B(\theta) = \exp \left\{ -4 \ln 2 \frac{\theta^2}{\theta_0^2} \right\} = \exp \left\{ -4 \ln 2 \frac{\theta^2}{\left(1.029 \frac{\lambda}{D} \right)^2} \right\} \quad (4.6)$$

where λ is the observational wavelength, D is the aperture size of the telescope. In our simulation, $D = 100$ m.

The simulated sky signal, which is the sum of 21-cm signal and foreground, is shown in Fig. 4.2. Note that there are total 200 frequency bins in our simulation, Fig. 4.2 only shows the maps at 600 MHz and 800 MHz as an example.

For the receiver noise added to the observational data, we model it as a white Gaussian noise, its standard deviation can be computed by

$$\sigma_n = \frac{T_{\text{sys}}}{\eta \sqrt{\Delta t \Delta \nu}} \quad (4.7)$$

where $\eta < 1$ is the efficiency of the system, T_{sys} , Δt and $\Delta \nu$ are the system temperature, integration time and frequency resolution, respectively. For the telescope (or array) focusing on the mid-frequency BAO of the large scale structure, such as PAON-4² [12, 264] and Tianlai³ [63–65], the typical system temperature is ~ 100 K, and the integration time of each observational data point is ~ 1 s, e.g. for PAON-4, $T_{\text{sys}} = 110$ K and $\Delta t = 1$ s (see Sec. 6); for Tianlai-dish, $T_{\text{sys}} = 75$ K and $\Delta t = 1$ s; and for Tianlai-cylinder, $T_{\text{sys}} = 90$ K and $\Delta t = 4$ s. In our simulation, $\Delta \nu = 0.1$ MHz, so the standard deviation of noise is in an order of $100 \text{ K} / (\eta \sqrt{2 \text{ s} \times 0.1 \text{ MHz}}) \gtrsim 200$ mK. However, in the realistic telescopes there might be a noise floor of non-thermal origin preventing the noise reaching the low thermal value, no matter how long the integration time is, so the actual noise might be higher.

Fig. 4.3 shows an example of the frequency spectrum of simulated observational data, which is a sum of sky signal convolved with a telescope beam and noise, along a line of sight, from 600 MHz to 1000 MHz, with a frequency resolution of 0.1 MHz. Because the foreground is the most principle component of the data, and it is smooth thus change slightly after the beam convolution, the global shape of the spectrum is determined by foreground. As the 21-cm signal is fairly random, after the beam convolution, its amplitude becomes much lower, which depends on the size of the beam. The noise is added to the data after the telescope beam, its level is much larger than the 21-cm signal, so the oscillation of the spectrum is mainly due to the noise.

4.2 Wiener filter

In a realistic data analysis process, preprocessing roughly includes the bad data removal (due to the equipment malfunction or the RFI contamination), data calibration, frequency and

²<https://groups.lal.in2p3.fr/bao21cm>

³<http://tianlai.bao.ac.cn/>

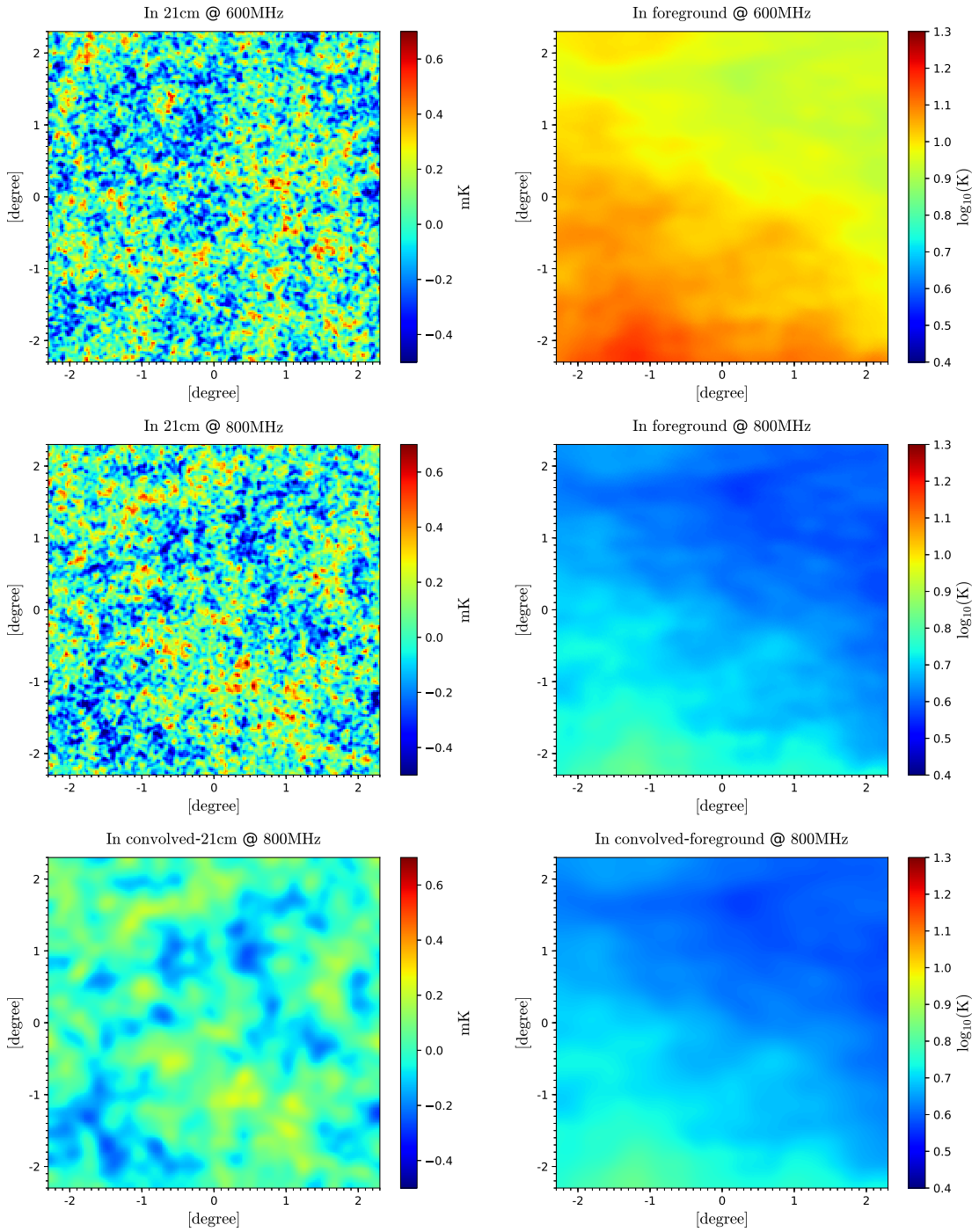


Fig. 4.2 The simulated 21-cm signal (left column) and foreground (right column) at 600 MHz (top panel) and 800 MHz (middle panel). The bottom panel is the signal convolved with a telescope beam, with an aperture size of $D = 100$ m. The pixel sizes of the maps are 200×200 , over an angular area of $4.6^\circ \times 4.6^\circ$.

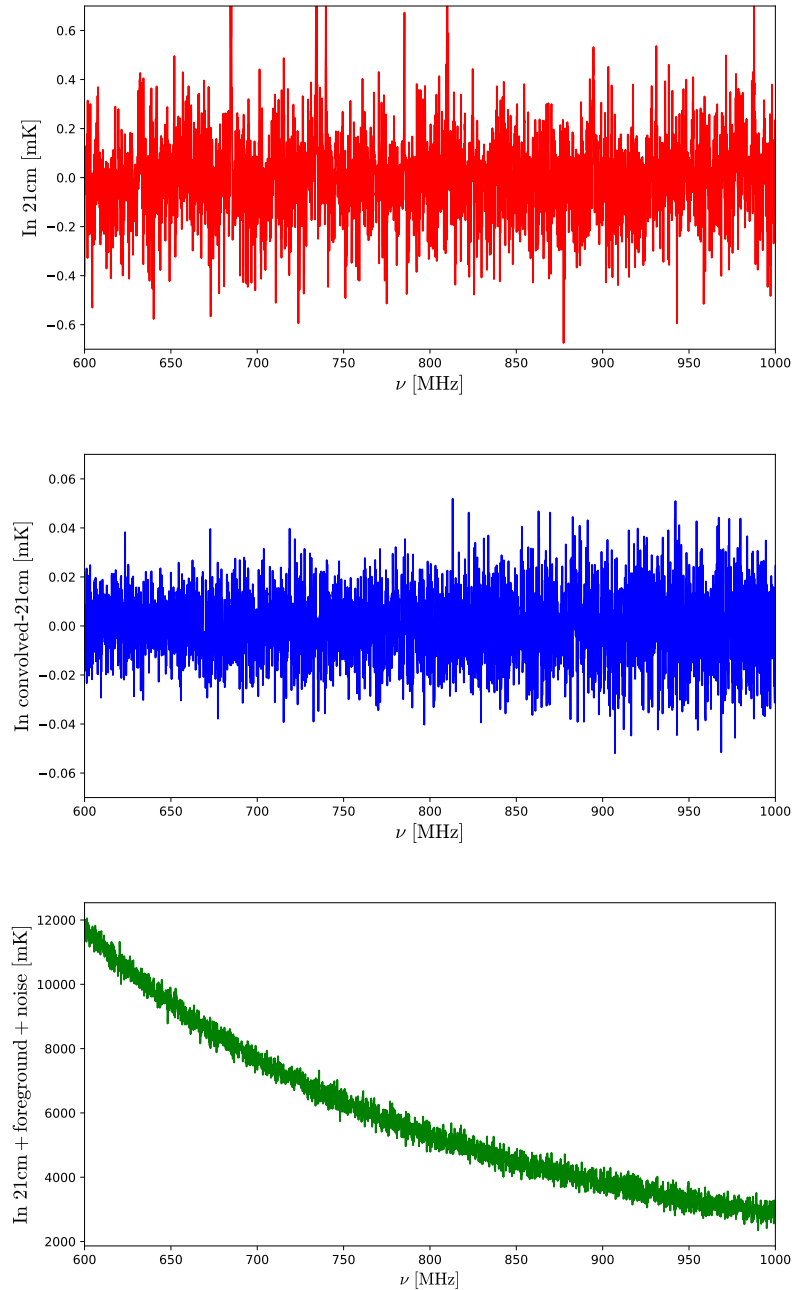


Fig. 4.3 The frequency spectrum of simulated observational data along a line of sight, from 600 MHz to 1000 MHz, with a frequency resolution of 0.1 MHz. Top panel is the input 21-cm signal. Middle panel is the convolution of input 21-cm signal with a frequency-dependent telescope beam, as the aperture size of the telescope is fixed, at lower frequency, the resolution of the beam is lower, thus the convolved 21-cm signal is lower. Bottom panel is the total brightness temperature including 21-cm signal, foreground and noise.

time re-binning. These steps may be variable for different telescope system, for example, the preprocessings of dish telescope and cylinder telescope are different. Here, we assume that the data have been preprocessed for RFI removal, calibration and map-making. The input data would then be 3D radio maps, with angular directions along the first two dimensions, and frequency along the third dimension.

Two steps are used to extract the 21-cm signal. First step, along each line of sights (frequency domain), extract the random 21-cm signal + noise from the foreground. Second step, the output data from the first step is considered to only contain 21-cm signal and noise, then extract the 21-cm signal from the noise in angular domain, as their angular correlations are different.

Wiener filter is an optimal filtering system proposed by Norbert Wiener [259], which minimizes the mean square error between the estimated random process and the desired process. By using the correlation properties and spectral properties of stationary stochastic processes, Wiener filter can be used to extract signal from the mixed noise.

For a general radio observation, there is a linear mapping between the observational data y from a telescope and the sky signal x :

$$y = \mathbf{A}x + n \quad (4.8)$$

where \mathbf{A} is the response matrix of the system, n is the random noise.

The covariance matrices of the sky signal and the noise are $\mathbf{S} = \langle xx^T \rangle$ and $\mathbf{N} = \langle nn^T \rangle$. An unbiased estimator can be obtained by applying the Wiener filter [238]

$$\hat{x} = \mathbf{W}y \equiv \mathbf{S}\mathbf{A}^T [\mathbf{A}\mathbf{S}\mathbf{A}^T + \mathbf{N}]^{-1} y \quad (4.9)$$

which is from the least square estimation of

$$V = \langle (x - \hat{x})(x^T - \hat{x}^T) \rangle \quad (4.10)$$

where \hat{x} is the desired signal.

4.3 Signal extraction by Wiener filter

4.3.1 Filtering in frequency domain

In frequency domain, if ignore the side bands of different frequency bins, take $\mathbf{A} = \mathbf{I}$ an identity matrix, then Eq. (4.8) becomes

$$y(\mathbf{v}) = f(\mathbf{v}) + s(\mathbf{v}) + n(\mathbf{v}) \quad (4.11)$$

where $f(\mathbf{v})$ is the foreground, $s(\mathbf{v})$ is the 21-cm signal, $n(\mathbf{v})$ is the noise with zero mean. And assuming they are uncorrelated mutually, i.e.

$$\langle (f + s + n)(f + s + n)^T \rangle = \mathbf{F} + \mathbf{S} + \mathbf{N} \quad (4.12)$$

where $\mathbf{S} = \langle s s^T \rangle$, $\mathbf{F} = \langle f f^T \rangle$ and $\mathbf{N} = \langle n n^T \rangle$ are their covariance matrices, respectively.

In frequency domain, foreground has strong frequency-frequency correlation, while pure white noise has only auto-correlation (zero cross-correlation between different frequencies), and 21-cm signal has limited frequency-frequency correlation. If performing a Fourier transform along frequency ($\mathbf{v} \rightarrow k$), the foreground spectrum would be concentrated at low frequencies, the noise spectrum would be flat, and the 21-cm spectrum, although not flat, would extend to higher k modes with much lower amplitude compared to the foreground. Thus, the foreground can be removed by applying such property difference. Ignoring the slight difference among frequency bins, the Wiener filter which is designed to remove the foreground is

$$\mathbf{W}_v^f = \mathbf{F} [\mathbf{F} + \mathbf{S} + \mathbf{N}]^{-1} \quad (4.13)$$

the top right label “ f ” denotes the foreground. Then the Wiener filter which is designed to extract 21-cm signal + noise is

$$\mathbf{W}_v = \mathbf{I} - \mathbf{W}_v^f \quad (4.14)$$

We note that in the real world, the foreground is unknown, so strictly speaking the Wiener filter method cannot be applied. Nevertheless, the foreground is believed to be smooth in frequency space, so that even though the Wiener filter constructed this way is not very precise, it could still serve as a low-pass filter to extract the smooth component of the data. In fact, we also tried applying a simple low-pass filter and found the result is practically the same.

Along one line of sight, Fig. 4.4 shows the separated foreground $\mathbf{W}_v^f \mathbf{y}$, and 21-cm signal + noise $\mathbf{W}_v \mathbf{y}$. The two panels, from top to bottom, corresponding to two foreground models, single index model and running index model, respectively. It is showing that the smooth part and the oscillatory part are separated, but the 21-cm signal is still submerged in the noise.

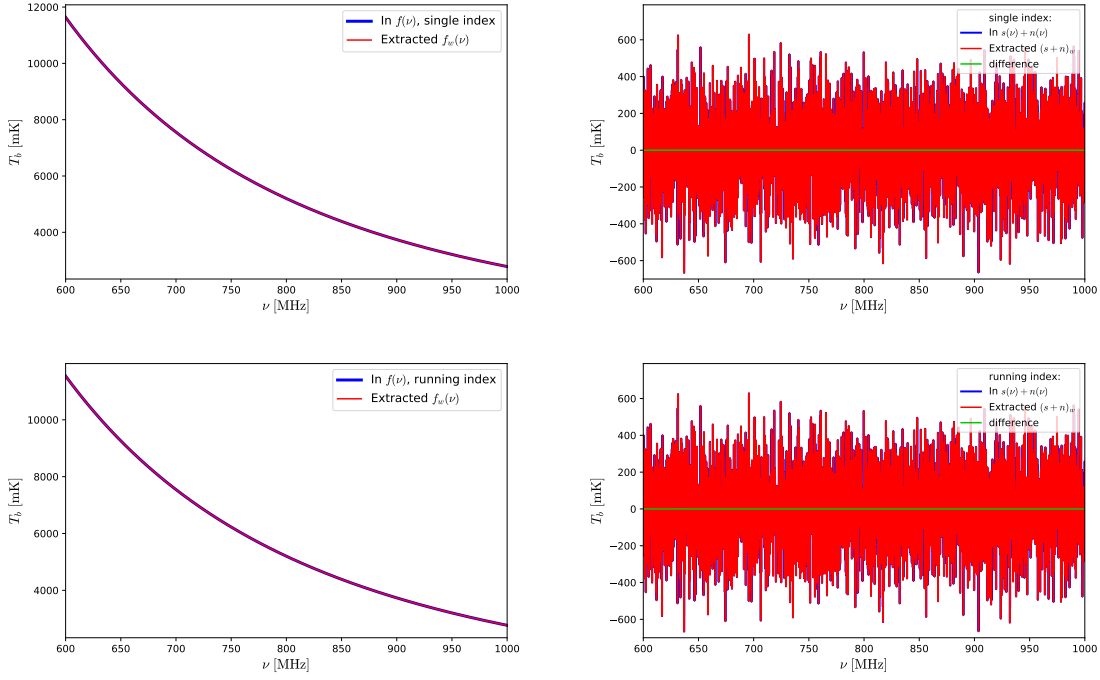


Fig. 4.4 Left: extracted foreground $\mathbf{W}_v^f \mathbf{y}$. Right: extracted 21-cm signal + noise $\mathbf{W}_v \mathbf{y}$. From top to bottom, they are the models of single index and frequency running index, respectively.

4.3.2 Filtering in angular domain

After filtering in frequency domain, the 3D temperature map is separated into two components, one corresponds to the estimated foreground, and the other one contains the sum of 21-cm signal and noise. Then a 2D filter is applied in angular domain to separate the noise and 21-cm signal. Below, for brevity, the lower label “ ν ” is omitted, but note that, all observational quantities and telescope response are frequency dependent.

Assuming the 21-cm signal is statistical uniform and isotropy, the covariance matrix of the signal \mathbf{S} can be obtained from the angular correlation coefficients

$$\mathbf{S}_{\vec{\theta}, \vec{\theta}'} = \langle T_{21}(\vec{\theta}) T_{21}(\vec{\theta}') \rangle = C(|\vec{\theta} - \vec{\theta}'|) \quad (4.15)$$

it means that the statistical property of 21-cm signal is independent from the position of $(\vec{\theta} - \vec{\theta}')$ on the sky.

Performing the spherical harmonic expansion to the 21-cm brightness temperature map

$$T(\vec{\theta}) = \sum_{lm} a_{lm} Y_{lm}(\vec{\theta}) \quad (4.16)$$

and from the isotropy and uniformity of 21-cm temperature field, we have

$$\langle a_{lm} a_{l'm'}^* \rangle = C_l \delta_{ll'} \delta_{mm'} \quad (4.17)$$

where $\delta_{xx'}$ is a Dirac function. Then it is obtained

$$C(|\vec{\theta} - \vec{\theta}'|) = \sum_{lm} C_l Y_{lm}(\vec{\theta}) Y_{lm}^*(\vec{\theta}') \quad (4.18)$$

The normalized spherical harmonic is

$$\sum_{m=-l}^l Y_{lm}(\vec{\theta}) Y_{lm}^*(\vec{\theta}') = \frac{2l+1}{4\pi} P_l(\vec{\theta} \cdot \vec{\theta}') \quad (4.19)$$

where P_l is the Legendre polynomial of order l , θ is the angle between the reference direction $\vec{\theta}$ and $\vec{\theta}'$. Let $\vec{\theta} = \vec{\theta}'$, the correlation function can be written as

$$\mathbf{S}_{\vec{\theta}, \vec{\theta}'} = C(\vec{\theta}, \vec{\theta}') = \sum_l \frac{2l+1}{4\pi} C_l P_l(\cos \theta) \quad (4.20)$$

The angular power spectrum C_l can be obtained by projecting the 3D power spectrum to a shell in a bandwidth $\Delta\nu$ [215]

$$C_l(\nu) = \frac{2(\Delta\nu)^2}{\pi} \int k^2 dk P_{2l}(k, \nu) j_l^2[kr(\nu)] \quad (4.21)$$

Fig. 4.5 shows the 21-cm angular power spectrum C_l at redshift $z \sim 0.8$ (top) and the corresponding angular correlation function $\mathbf{S}_{\vec{\theta}, \vec{\theta}'}$ (bottom). The correlation of 21-cm signal decrease rapidly beyond $l \sim 10^2$ (corresponding to an order of 1°) in our frequency range of simulation.

The noise covariance matrix reduces then to a diagonal matrix proportional to the identity matrix, as noise is assumed to be completely white

$$\mathbf{N}_{\vec{\theta}, \vec{\theta}'} = N_0 \delta_{\vec{\theta}, \vec{\theta}'} \quad (4.22)$$

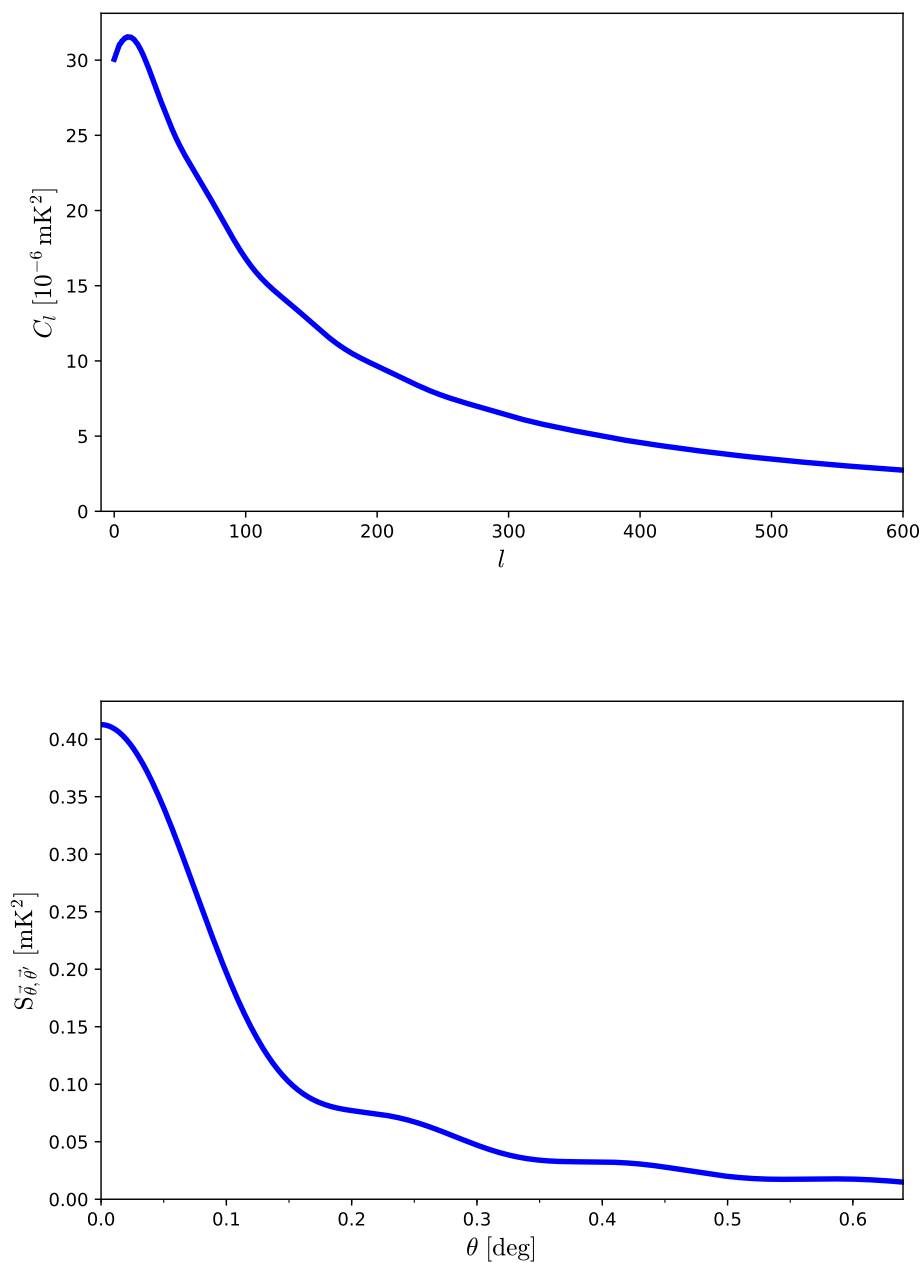


Fig. 4.5 Top: the 21-cm angular power spectrum C_l at redshift $z \sim 0.8$. Bottom: the corresponding angular correlation function $C(\theta) = S_{\vec{\theta}, \vec{\theta}'}$. The correlation of 21-cm signal decrease rapidly beyond $l \sim 10^2$ (corresponding to an order of 1°).

Indeed, as we assume that the noises affecting different pixels are completely independent from each other, the cross-correlation is 0, $N_0 = \sigma_n^2$ in Eq. (4.22) is the variance of the noise. Note that, in Eq. (4.8), if vector \mathbf{x} represents the sky and \mathbf{y} represents the time series signal, then elements of \mathbf{n} are from different time, therefore, noises can be considered random and independent, and the noise matrix \mathbf{N} is a diagonal matrix.

The map-making process is however likely to introduce noise correlations between different map pixels. The measured noise itself might not be stationary and white. For example, the noise level might be direction dependent, or the noise power varies with the sky temperature, or the noise is affected by the observational environment, etc. In addition, although the noises are collected at different time, they might be still correlated because of the $1/f$ effect. However, the above effects can all be dealt with by the Wiener filter, as long as the covariance matrix of the noise \mathbf{N} is known. In this chapter, considering a simplified case, we assume that the noise is uncorrelated.

Fig. 4.6 shows the extracted 21-cm signal after the second Wiener filter in angular domain, after filtering out the foreground in frequency domain. Top panel shows the 21-cm signal + noise, the 21-cm signal is submerged in the strong noise. Middle panel shows the extracted 21-cm signal, and bottom panel is the residual. Left column is the case of a noise temperature of 200 mK, 1000 times of the 21-cm signal, the same order as described in Sec. 4.1. Further, in order to test the ability of Wiener filter in 21-cm signal extraction, we take a worse noise level of 2000 mK, 10000 times of the 21-cm signal (right column). It is shown that, although the 21-cm signal is much fainter than the noise, the Wiener filter still succeeds to extract the 21-cm signal, and the residual is relatively small, about $\pm 5\%$, as long as all the prior knowledge, the telescope beam, the covariance matrices of foreground, 21-cm signal and noise, is known accurately.

However, note that, the angular correlation function which is used by the Wiener filter is an ensemble mean computed from the cosmological model, there might be difference between the computed value and the real one, the signal might not be reconstructed well.

When applying a 2D Wiener filter in angular domain, the output map is automatically deconvolved (see Eq. (4.9)). In the above simulation, the beam is assumed to be perfectly known, so the recovery is accurate even when noise is present. However, in the real world the beam is only known either by electromagnetic field simulation, or by calibration measurements, and both approaches have errors. Here we make a demonstration of the effect of inaccurately known beam as follow.

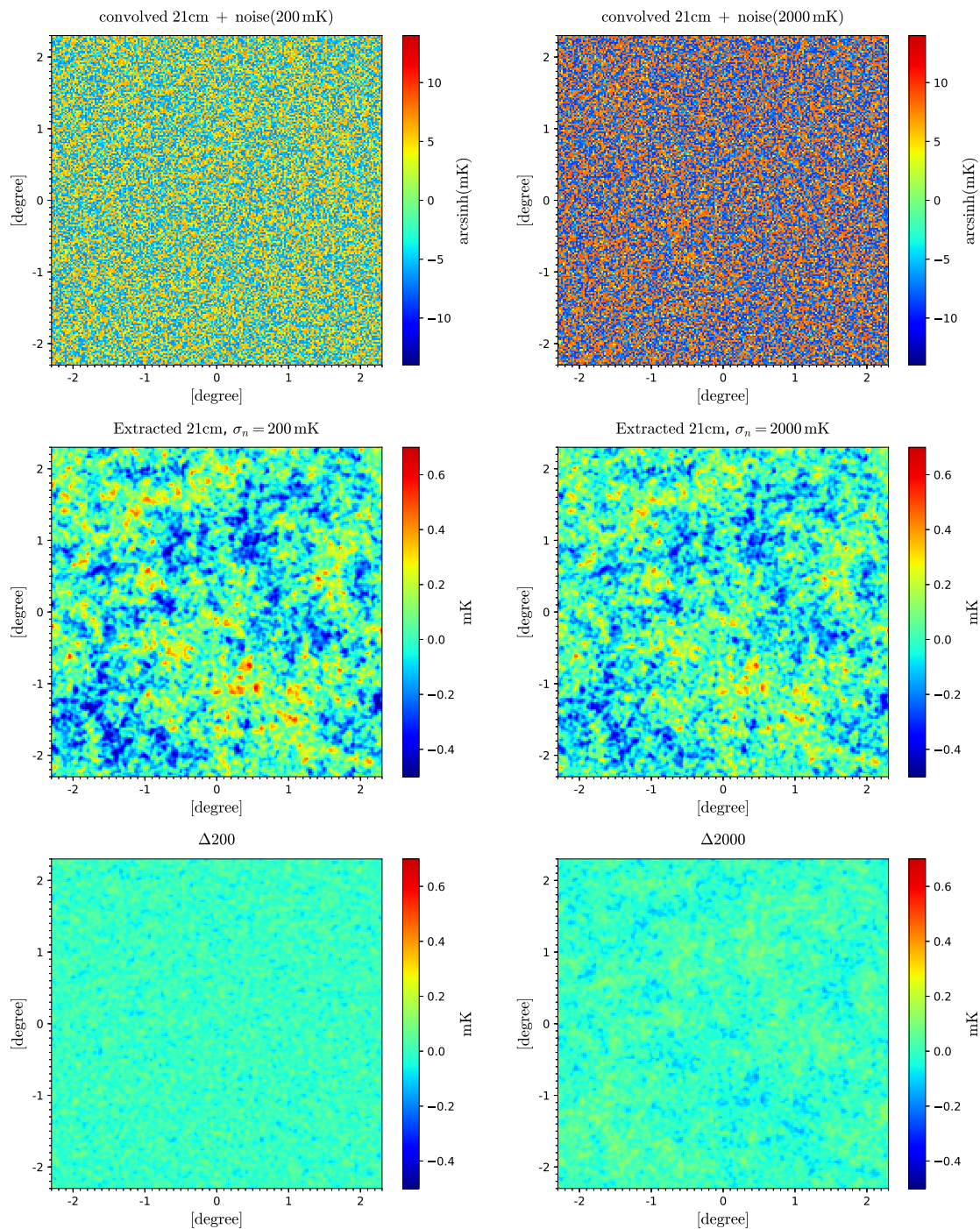


Fig. 4.6 The extracted 21-cm signal after a Wiener filter. Top: 21-cm signal + noise, the 21-cm signal is submerged in the strong noise. Middle: the extracted 21-cm signal. Bottom: the residual between the input and extracted 21-cm signal. Left: the case of noise temperature is 200 mK, 1000 times of the 21-cm signal. Right: the case of noise temperature is 2000 mK, 10000 times of the 21-cm signal.

4.3.3 The effect of inaccurate beam model

In the above simulation, the FWHM resolution of the Gaussian beam at 800 MHz we used is 0.25° , thus in the reconstruction, we use Gaussian beams with slightly different FWHM resolutions, 0.23° and 0.20° . The reconstructed maps are shown in Fig. 4.7. The top panels show the original 21-cm signal (top left) and the reconstructed map with the correct beam size (top right, same as the middle left panel of Fig. 4.6). The bottom panels show the reconstructed maps with Gaussian beams of incorrect FWHM resolution of 0.23° (bottom left) and 0.20° (bottom right). It can be seen that when the incorrect beam widths are used, the whole reconstructed map become fuzzier, the finer details of the original maps are lost, though the overall large scale structure are still similar. In the real world, of course, the deviation from the beam might be more irregular and complicated.

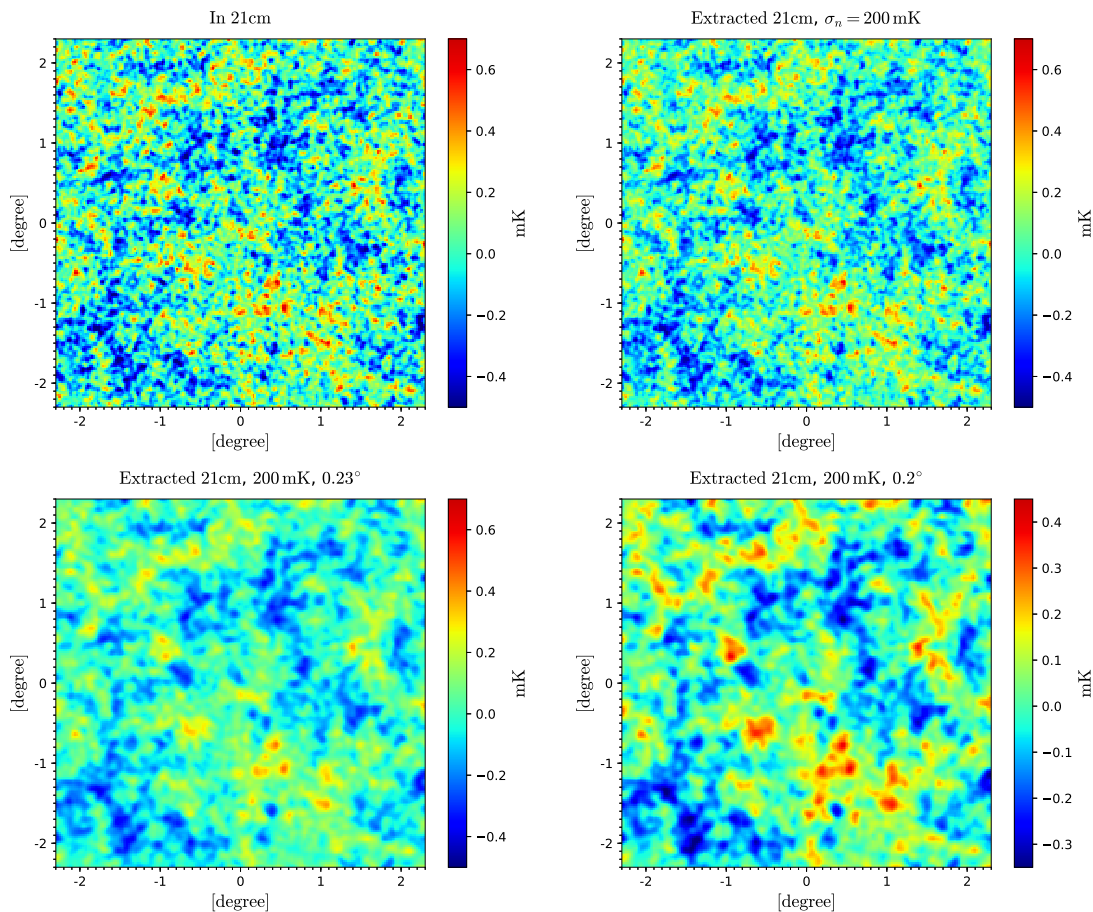


Fig. 4.7 Effect of inaccurate beam on map reconstruction. We assume here the real beam size (FWHM) is 0.25° . Top Left: input 21-cm map; Top Right: reconstructed 21-cm map from noise of 200 mK, with the correct beam size of 0.25° ; Bottom: reconstructed maps with the incorrect beam width of 0.23° (bottom left) and 0.20° (bottom right), respectively.

4.4 Brief summary

Large scale 3D cosmological HI survey is one of the most efficient paths to study the universe. A number of experiments have been built and is going into relevant observations. However, it is a big challenge to extract 21-cm signal from the observational data, because the foreground and the noise are several orders than the signal, both on magnitude and on fluctuation. In order to extract the 21-cm signal well, an effective extraction method is needed. In this chapter, we have explored the possibility of extracting the 21-cm cosmological signal from radio observations, applying a cascade of two filters, the first along the frequency axis, separating the foregrounds due to Galactic and radio sources, assumed to be smooth, i.e. slowly varying with frequency. The second filter is applied in angular domain, to the component dominated by noise and 21-cm signal, resulting the first filter output. The second stage filter is based on the absence of noise correlation among map pixels in a given frequency shell. In the framework of a very simplified and optimistic data model used here, we have shown that this two stage filtering seems quite promising for extracting the 21-cm signal. However, in the present study we have made a number of simplifying assumptions. In an actual experiment, the beam shape is more complicated, frequency-dependent and only known to a limited precision, the calibration procedure may introduce additional errors, and the noise may be non-thermal and have more complicated statistical properties. All of these factors may affect the extraction of the 21-cm signal.

Chapter 5

Imaging algorithm for lunar orbit interferometer array

5.1 Research background

Radio astronomy originated from the observation at 20.5 MHz by Karl Jansky in 1932 [136], benefiting from the technological developments for radio communication and radar, such as the successful messages transmission across the Atlantic Ocean in the form of an electromagnetic wave by Guglielmo Marconi in 1901 [41]. Grote Reber also made lots of observations at low-frequency (hundred meters wavelength) [204]. However, due to the strong refraction and absorption by the ionosphere below 30 MHz, it is not suitable to carry out very low-frequency observation on the ground. Further more, because of the reflection by the ionosphere, low-frequency radio frequency interference (RFI) is omnipresent. From the ground, except for a few strong radio phenomena from the solar system, such as the solar radio bursts and the planetary radio activities, there are nearly no other radio observation below 30 MHz. The sky beyond the solar system is thus poorly known at low frequencies [48, 55, 53].

In recent years, low-frequency radio astronomy is renewed, especially the redshifted 21-cm observations of the epoch of reionization (EoR), the cosmic dawn and the dark edge [202]. Some ground-based experiments, such as LOFAR (the Low Frequency Array) [210] and LWA (the Long Wavelength Array) [143], have the frequency band coverage below 30 MHz. However, these instruments mostly make observations at higher frequency (≥ 20 MHz), at lower frequency, the observations mainly focus on the Sun and planets. Therefore, it is worthwhile to observe from the space.

In 1970s, some space missions of low-frequency observations continuously carried out, such as IMP-6 [52], RAE-1 (Radio Astronomy Explore-1) [8] and RAE-2 [7]. These missions proved that the Moon can shield the strong RFI from the Earth. Therefore, the far-side of the Moon provides an ideal environment for low-frequency observation. Nevertheless, limited by the technology at that time, the resolution of the reconstructed maps at a frequency range of 1.31–9.18 MHz by the RAE mission is rather poor (dozens of degrees) [176]. Additionally, the frequency bands of these missions are different from each other, they were not coincident [146].

Since 1980s, several space missions which focused on low-frequency observation were proposed, although none of them were realized. Some proposals which target observing from the earth orbit, such as SunRISE [153], are relatively inexpensive and technically mature. However, strong RFI from the Earth significantly affects the radio sky observation, including instruments probing the dark ages. Other proposals have considered satellite arrays at the Sun-Earth L2 point, such as ALFA [140], FIRST [34] and SURO-LC [38], allowing all-time observation. However, they are still exposed to the strong RFI from the Earth, although the RFI becomes weaker due to longer distance, it still has significant influence on the observation. In addition, launching and maintaining the configuration of the satellite array on the unstable L2 point, calculating their relative positions and sending back the data to the Earth increase the technological complexity and requirements, and consume substantial resources.

Observing on the far-side of the Moon is a feasible choice (see [149, 139, 167, 263] for review). The first realized experiment is the lunar orbit microsatellite Longjiang-2 (although Longjiang-1 failed to enter lunar orbit, but Longjiang-2 succeeded and operated in lunar orbit until 31 July 2019), which is a part of China's Chang'e-4 mission [254].

Chang'e-4 mission¹ is a Chinese National Space Administration (CNSA) lander to the far-side of the Moon, part of the second phase of the Chinese Lunar Exploration Program². It achieved the first soft landing on the far-side of the Moon on 3 January 2019. However, direct communication with Earth is impossible on the far-side of the Moon, since transmissions are blocked by the Moon. To solve the communication problem, before the launching of the main mission of Chang'e-4, an additional tracking and data relay satellite system (TDRSS), named as Queqiao, was first launched to a halo orbit around the Earth-Moon L2 point in May 2018, as shown in Fig. 5.1. There are two microsatellites named Longjiang-1 and Longjiang-2 were launched along with Queqiao. For the original objective, these two microsatellites, also known as Discovering the Sky at Longest Wavelengths Pathfinder (DSLWP), would form a

¹<http://www.cnsa.gov.cn/n6758823/n6758844/n6760026/index.html>

²<http://moon.bao.ac.cn>

two-element interferometer array to observe the radio sky at frequencies lower than 30 MHz. The work described in this chapter is motivated by such orbital interferometer array.

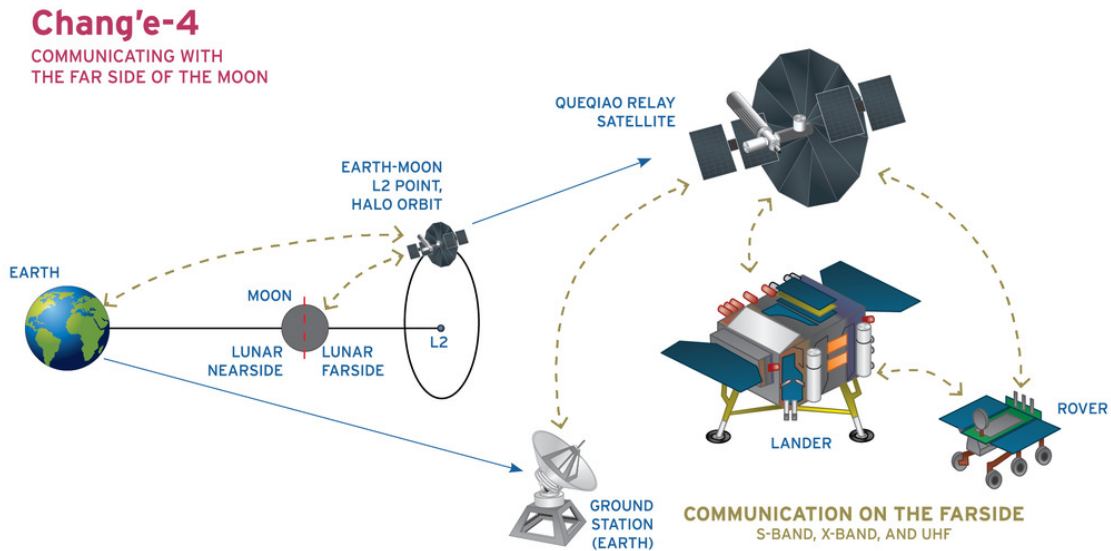


Fig. 5.1 China's Chang'e-4 mission with a communications relay satellite named Queqiao in a halo orbit around the Earth-Moon L2 point to maintain communication between the lander on the far-side of the Moon and Earth ground control (the image is cited from ³).

However, for a telescope array on the lunar surface, techniques and tools developed on the ground can be used directly. In addition, during the night of the Moon which lasts half month, supplying power to the equipments is a major difficulty, special energy sources, such as nuclear power or radio thermal generator (RTG) would be needed.

Observing from the lunar orbit has several advantages comparing to other approaches. In the side of technique, it is easier to realize. The Moon shields the strong RFI from the Earth, provides an ideal environment for low-frequency observation. Different from the equipments on the lunar surface, for that on lunar orbit, the orbital period is only several hours, making the use of solar power a good option. Meanwhile, the observational data can be sent back to the Earth when satellites are on the near-side, no additional and complicated deployment is needed, e.g. the TDRSS. Single lunar orbital satellite, such as the DARE [200] which has been on the agenda, can measure the average spectrum of the whole sky, detect strong radio sources, and even obtain a low resolution image of the sky using the moving shadow of the Moon. Higher resolution can be obtained by the orbit interferometric arrays [29, 62]. Some relevant conceptual research is on-going, including DARIS [43] and DSL (the Discovering the Sky at Longest wavelength) [42, 66].

³<https://earthsky.org/space/china-change-4-spacecraft-landing-moon-far-side>

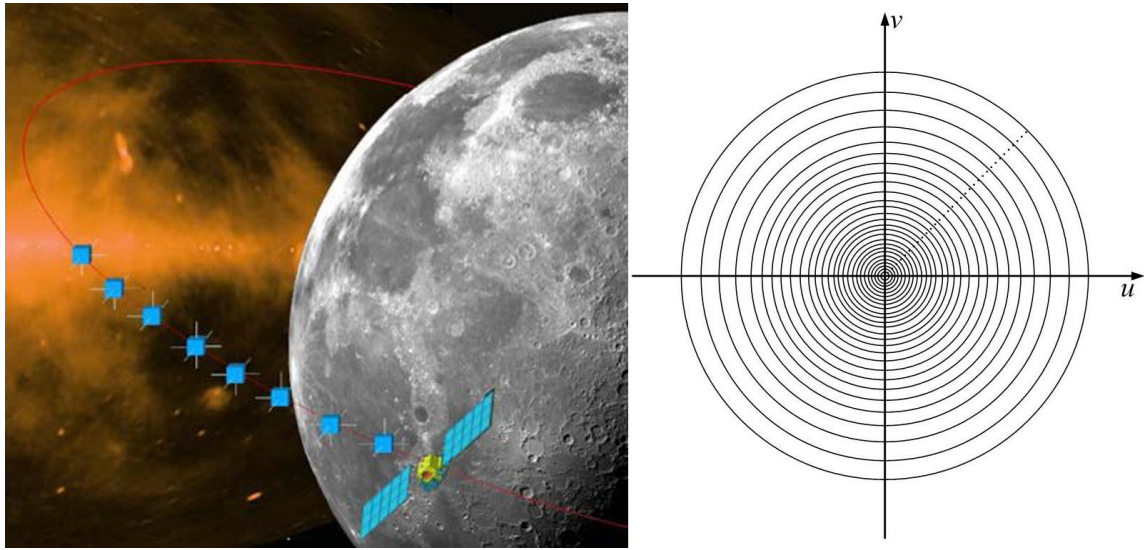


Fig. 5.2 Left: a linear array of flying satellites around the Moon. Right: the baselines between satellite pairs in the array swipe a number of concentric rings on the (u, v) plane.

DSL concept is based on a mother satellite leading several child satellites in an orbit around the Moon, baseline vectors between different satellite pairs generates a series of concentric rings on the (u, v) plane as shown in Fig. 5.2. The mother satellite continuously detects the relative positions and distances of the child satellites by optical or microwave equipments, and determine to know the configuration of the array at any time. When the satellite array is on the far-side of the lunar orbit, all child satellites will make radio interferometric observations on the sky by the electric short antennas equipped on them, all data from the child satellites will be sent to the mother satellite which will perform the real-time calculation of all antenna pair correlations. The calculated visibilities are stored and sent back to the Earth when the array is on the near-side of the lunar orbit. After flying several periods, lots of different visibilities are cumulated. If the rapid variable sources can be removed, combining the visibilities, a sky image can be made, in a way similar to the ground case. The first lunar orbital satellite array was launched in 2018 by China's Chang'e-4 mission [268].

Although lunar orbit satellite array can make a good quality observation to the low-frequency sky below ~ 30 MHz, reconstructing the sky image from the observations remains a challenge. Classical ground-based imaging algorithms are not suitable, mostly due to two reasons: the first one is that the field of view is very large, almost the whole sky; the second is that if baselines are distributed on a single plane, symmetric images on the two sides of the plane will appear, it is hard to distinguish which one is real and which one is fake. An additional complication arises from the fact that as satellites move around the Moon, the

shadow of the Moon blocks a fraction of the sky, creating a changing beam pattern for each satellite, in addition to the change of baselines with time.

For the telescope array on the lunar surface, algorithms or methods developed for interferometric arrays on Earth are applicable. However, for the lunar orbit satellite array whose field of view is the whole sky and the baselines as well as the beam pattern is time-variable, there is no applicable imaging algorithm until now. Fortunately, the sky intensity is linearly mapped to the observed visibility. In this chapter, an imaging algorithm for the lunar orbit satellite array is presented [129]. We show that the imaging ambiguity arising from the symmetry with respect to the orbital plane can be solved thanks to the 3D baseline distribution obtained by the orbit precession. We also show that our method handle well the complexity due to time-variable baselines and beam patterns. We discuss also the impact of nonuniform baseline distribution on the imaging quality.

5.2 Imaging algorithm

Note that only the unpolarized sky is discussed in this chapter. An visibility corresponding to the correlation of a pair of antenna signal can be written as (see Sec. 2.6.1 for detail):

$$V_{ij} = \int A_{ij}(\vec{n}) T(\vec{n}) e^{-i\vec{k}\cdot\vec{r}_{ij}} d^2\vec{n} \quad (5.1)$$

where $A_{ij}(\vec{n})$ is the combined beam of two antennas, $T(\vec{n})$ is the sky temperature on direction \vec{n} . $\vec{k} = \frac{\omega}{c}\vec{n}$ is the wave vector, $\vec{r}_{ij} = \vec{r}_i - \vec{r}_j$ is the baseline vector between i -th and j -th antennas.

The visibility can be also written in the (u, v, w) coordinate system in the unit of wavelength, where w points to the phase reference on the celestial sphere

$$V(u, v, w) = \int A_{ij}(l, m) T(l, m) e^{-i2\pi[ul+vm+w(n-1)]} \frac{dl dm}{\sqrt{1-l^2-m^2}} \quad (5.2)$$

where (l, m, n) is the direction cosine, and $n = \sqrt{1-l^2-m^2}$.

Since the invention of interferometers, a number of imaging algorithms, for reconstructing sky from visibilities have been developed, The most basic is the 2D Fourier transform method, applicable in particular to the case of narrow field of view ($l \sim 0, m \sim 0 \Rightarrow n \sim 1$) and coplanarity, Eq. (5.2) can be cast into a 2D Fourier transform formalism

$$V(u, v) = \int A_{ij}(l, m) T(l, m) e^{-i2\pi(ul+vm)} dl dm \quad (5.3)$$

The sky temperature can be obtained by performing a 2D inverse Fourier transform. But notice that a visibility for a given baseline corresponds to a point in the Fourier (u, v) plane, the incomplete coverage of the (u, v) plane makes good quality imaging difficult, even for this simplified case. However, for the case of wide field of view, the w -term in Eq. (5.2) can not be ignored. A number of wide field of view imaging algorithms have been developed, such as the faceting [83], 3D Fourier transform [230, 83, 187], W-Projection [81, 82], A-Projection [237], W-Stacking [180]. To improve imaging quality and remove artefacts in the dirty map, which corresponds to the sky image obtained after the 2D Fourier transform step, iterative deconvolution methods such as CLEAN [127] are used [217]. To deal with the direction dependent effect during the calibration and the wide field of view problem in low-frequency observation, more precise methods such as “software holography” [168] have been developed. However, Most of these algorithms are adapted to the ground instrument configurations but are not suited to interferometric arrays in lunar orbit.

5.2.1 Mirror symmetry

For a set of satellites following a given orbit, baselines would be distributed over a single plane which is the orbital plane. For an array on the ground, the ground shields half of the sky, while for the array on the lunar orbit, the blockage of the sky by the Moon is small and the direction is always in the orbital plane. Therefore, for the direction perpendicular to the orbital plane, there is no blockage, due to the Moon shadow. Hence, a pair of mirror images would appear on the two sides of the orbital plane, as shown in Fig. 5.3. This is because for any baseline on the orbital plane, two directions which are symmetric with respect to the orbital plane have the same pitch angles, then their phase delays will be identical. Due to this mirror symmetry, it would be hard to solve the degeneracy between these two symmetric directions.

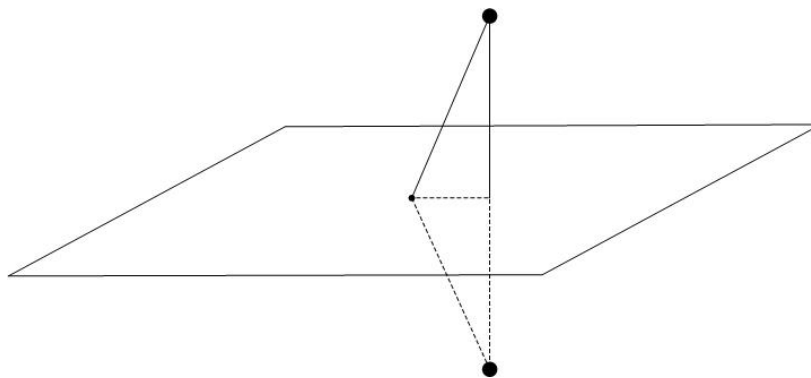


Fig. 5.3 Mirror symmetry about the orbital plane.

Such degenerated state can be broken by asymmetric antenna beam. In practice, for the common type of antenna made of a reflector and a feed, because the response of back lobe is dozens of dB lower than the main lobe, the mirror symmetry is broken by the asymmetric antenna beam pattern. However, for the long wavelength ($\gtrsim 10$ m) observation, using such reflector type antenna is unrealistic, an electric short antenna such as dipole antenna is used generally. RAE-2 satellite was equipped for example several long antennas, the longest is a V shaped antenna of 229 m, however, it is hard to equip smaller satellites with such long antenna. And for an electric short antenna, its primary beam is too wide to distinguish the signal from the two sides of the orbital plane. Another to break the mirror symmetry is the rotation of the antenna during observation, but it increases the difficulties of satellite design and data analysis.

There is another simple and effective method to break the mirror symmetry, thanks to the three-dimensional (3D) baseline distribution. 3D baseline distribution can be obtained by precession of the orbital plane, which is a natural phenomenon for most of objects. The orbital plane can precesse a full 360° in 1.29 years [66]. Practically, it is only after several months of observation that the distribution of visibilities become 3D. By combining observations scattered over a long duration, about a year, the mirror symmetry can be eliminated. However, an effective 3D imaging algorithm is needed, which is also a challenge.

Some algorithms are applicable to deal with the noncoplanar synthetic imaging. Based on Eq. (5.2), the sky intensity can be obtained from a direct 3D inverse Fourier transform in principle [230, 83, 187]

$$A(l, m) T(l, m) \frac{\delta(n - n')}{n} = \int V(u, v, w) e^{i2\pi(ul + vm + wn')} du dv dw \quad (5.4)$$

where $\delta(n - n')$ is a Dirac function. However, similar to other methods, this method is not applicable for the lunar orbit array, because as satellites fly around the Moon, the shadowed or blocked part of the sky by the Moon changes. In other words, the response function $A(l, m)$ is time-variable, $A(l, m) \rightarrow A(l, m, t)$.

Assume the Moon is an opaque ball without reflection, and ignore the slight difference among distances of satellites to the Moon

$$V_{ij}(\vec{r}) = \int A_{ij}(\vec{n}) S(\vec{n}, \vec{R}) T(\vec{n}) e^{-i\vec{k} \cdot \vec{r}_{ij}} d^2\vec{n} \quad (5.5)$$

where $S(\vec{n}, \vec{R})$ denotes the blockage of the sky by the Moon at direction \vec{n} , \vec{R} denotes the relative position of the satellite to the center of the Moon. $S(\vec{n}, \vec{R}) = 0$ denotes complete blockage while $S(\vec{n}, \vec{R}) = 1$ denotes no blockage. However, for a satellite array on a circular

orbit, baseline vectors are almost tangent to the circular orbit, it means $\vec{r}_{ij} \propto \vec{R} \times \vec{N}$ where \vec{N} is the unit vector perpendicular to the orbital plane, $S(\vec{n}, \vec{R})$ is thus a function of \vec{r}_{ij} , therefore, the direct 3D inverse Fourier transform is not applicable. The imaging algorithm must have the ability to deal with the time-variable blockage.

Fortunately, the visibility data and the sky brightness are related through a linear mapping. The imaging problem can be written as a linear system, relating the complete set of visibilities, organised as a vector, to the sky brightness, organised also as a vector. In this chapter, we discuss the explicit expression of this linear system and its solution.

5.2.2 Imaging algorithm in pixel

As visibility is linearly related to the sky brightness, solving this linear mapping can reconstruct sky map. The ground-based antenna array MITEoR had been detailly discussed and applied this method [271]. In our imaging algorithm, such idea is adopted and improved for the lunar orbit satellite array.

The integration of the sky temperature can be approximately equivalent to the sum of all pixels of the sky

$$V_{ij}(t) = \sum_n^{N_{\text{pix}}} H(n, t) T(n) \Delta\Omega \quad (5.6)$$

here using the index of pixel n instead of the direction vector \vec{n} , and all quantities except the sky temperature are time-dependent, as we assume the sky temperature is stable. $T(n)$ is the pixelized sky map, $H(n, t) = A_{ij}(n, t) S(n, t) e^{-i\vec{k} \cdot \vec{r}_{ij}(t)}$ is the pixelized antenna complex response, $A_{ij}(n, t)$ is the combined beam, $S(n, t)$ is the blockage of the sky by the Moon, $\Delta\Omega$ is the pixel size.

Considering the noise, Eq. (5.6) can be written in a matrix formalism

$$\mathbf{V} = \mathbf{HT} + \mathbf{n} \quad (5.7)$$

where \mathbf{H} is a $(N_{\text{bl}} \cdot N_t) \times N_{\text{pix}}$ matrix. N_{bl} is the number of baselines, N_t is the number of visibility measurements in time, N_{pix} is the number of the full sky map pixels. The $N_{\text{pix}} \times 1$ vector \mathbf{T} is the flatten pixelized sky map. \mathbf{V} is the visibility vector with shape of $(N_{\text{bl}} \cdot N_t) \times 1$. Vector \mathbf{n} is random noise with zero mean, whose covariance matrix is $\langle \mathbf{n} \mathbf{n}^\dagger \rangle = \mathbf{N}$.

The sky map is pixelized to HEALPix [116], $N_{\text{col}} = N_{\text{pix}} = 12n_{\text{side}}^2$ is determined by the value of $n_{\text{side}} \equiv 2^m$, where m is a nonnegative integer. For example, if need the pixel size of 1° , $n_{\text{side}} = 64$ is taken.

The least square estimator of \mathbf{T} is

$$\hat{\mathbf{T}} = (\mathbf{H}^\dagger \mathbf{N}^{-1} \mathbf{H})^{-1} \mathbf{H}^\dagger \mathbf{N}^{-1} \mathbf{V} \equiv \mathbf{B}^{-1} \mathbf{V} \quad (5.8)$$

where we simplify the whole inverse-like matrix $(\mathbf{H}^\dagger \mathbf{N}^{-1} \mathbf{H})^{-1} \mathbf{H}^\dagger \mathbf{N}^{-1}$ to a single notation \mathbf{B}^{-1} . Assuming the noise is uncorrelated, i.e. $\mathbf{N} \propto \mathbf{I}$, the covariance matrix of noise is proportional to the identify matrix. As \mathbf{B} is a nonsquare matrix, the pseudo-inverse instead of the inverse is used, which can be solved by the Singular Value Decomposition (SVD)

$$\mathbf{B} = \mathbf{U} \mathbf{\Sigma} \mathbf{W}^\dagger \quad (5.9)$$

where $\mathbf{\Sigma}$ is a diagonal matrix, whose diagonal elements are the singular values.

Only select the singular values larger than a threshold, i.e. $\bar{\mathbf{\Sigma}} = \mathbf{\Pi} \mathbf{\Sigma}$ where $\mathbf{\Pi}$ is a projection matrix, the pseudo-inverse becomes

$$\bar{\mathbf{B}}^{-1} = \left(\mathbf{U} \bar{\mathbf{\Sigma}}^{-1} \mathbf{W}^\dagger \right)^\dagger \quad (5.10)$$

where $\bar{\mathbf{\Sigma}}^{-1}$ is also a diagonal matrix whose diagonal elements are the reciprocal values of that of $\bar{\mathbf{\Sigma}}$.

A point spread function (PSF) can be used to reconstruct the sky map

$$\hat{\mathbf{T}} = \mathbf{P} \mathbf{T} \quad (5.11)$$

the point spread function \mathbf{P} is

$$\mathbf{P} \equiv \bar{\mathbf{B}}^{-1} \mathbf{B} = \left(\mathbf{U} \bar{\mathbf{\Sigma}}^{-1} \mathbf{W}^\dagger \right)^\dagger \mathbf{U} \mathbf{\Sigma} \mathbf{W}^\dagger \quad (5.12)$$

Very small singular values may cause numerical instability and increases the noise while solving the pseudo-inverse. In order to stabilize the solution of SVD, two kinds of thresholds can be set: an absolute threshold and a relative threshold to the maximum singular value [264, 267]. Singular values smaller than these two thresholds will be set to be 0, either their reciprocal values. However, the values of two thresholds depend on the specific singular matrix, different singular matrix has different thresholds. What's more, setting the values of thresholds significantly relies on the experience, manual setting has a sense of arbitrariness. Therefore, an automatic and stable method for threshold setting is required: finding a singular value that the cumulation ratio of singular value to the sum is upto 0.99. The ratio of singular value to the sum $\lambda_i / \sum_{i=1}^N \lambda_i$ can be considered as the ratio of information this singular

value contains. The cumulation ratio $\sum_{i=1}^{N_{\text{thr}}} \lambda_i / \sum_{N_{\text{all}}} \lambda_i = 0.99$ means that the first N_{thr} singular values contains 99% of the total information, setting the threshold to be λ_{thr} can not only maintain most of information but also avoid the impact of small singular values during the pseudo-inverse solution. Fig. 5.4 shows the threshold of the simulation in this chapter.

Solving the pseudo-inverse consumes most of time and memory during the solution of linear equation system. Therefore, as far as the quality of reconstructed map is not affected, reducing the size of matrix \mathbf{B} as much as possible has a positive significance.

5.2.3 Imaging algorithm in spherical harmonic space

Instead of pixelizing the sky map and antenna beam as done in Sec. 5.2.2, performing the spherical harmonic expansion can not only save time and memory but also reduce the error and improve the quality of the reconstructed map.

Expanding the sky and the complex beam in spherical harmonics, we can write

$$H(\theta, \varphi, t) = \sum_{l=0}^{+\infty} \sum_{m=-l}^l \mathcal{H}_{lm}(t) Y_{lm}(\theta, \varphi) \quad (5.13)$$

$$T(\theta, \varphi) = \sum_{l=0}^{+\infty} \sum_{m=-l}^l \mathcal{T}_{lm} Y_{lm}(\theta, \varphi) \quad (5.14)$$

note that as the sky temperature is real, $\mathcal{T}_{lm} = (-1)^m \mathcal{T}_{l,-m}^*$.

In practice, the sum over l extends to a large enough value l_{max} instead of infinity $+\infty$, Eq. (5.1) becomes

$$V_{ij}(t) = \sum_{l=0}^{l_{\text{max}}} \sum_{m=-l}^l (-1)^m \mathcal{H}_{l,-m}(t) \mathcal{T}_{lm} \quad (5.15)$$

$$V_{ij}^*(t) = \sum_{l=0}^{l_{\text{max}}} \sum_{m=-l}^l \mathcal{H}_{l,m}^*(t) \mathcal{T}_{lm} \quad (5.16)$$

and in the matrix formalism

$$\mathbf{V} = \mathcal{H} \mathcal{T} + \mathbf{n} \quad (5.17)$$

The least square estimator of \mathcal{T} is

$$\hat{\mathcal{T}} = (\mathcal{H}^\dagger \mathbf{N}^{-1} \mathcal{H})^{-1} \mathcal{H}^\dagger \mathbf{N}^{-1} \mathbf{V} \equiv \mathcal{B}^{-1} \mathbf{V} \quad (5.18)$$

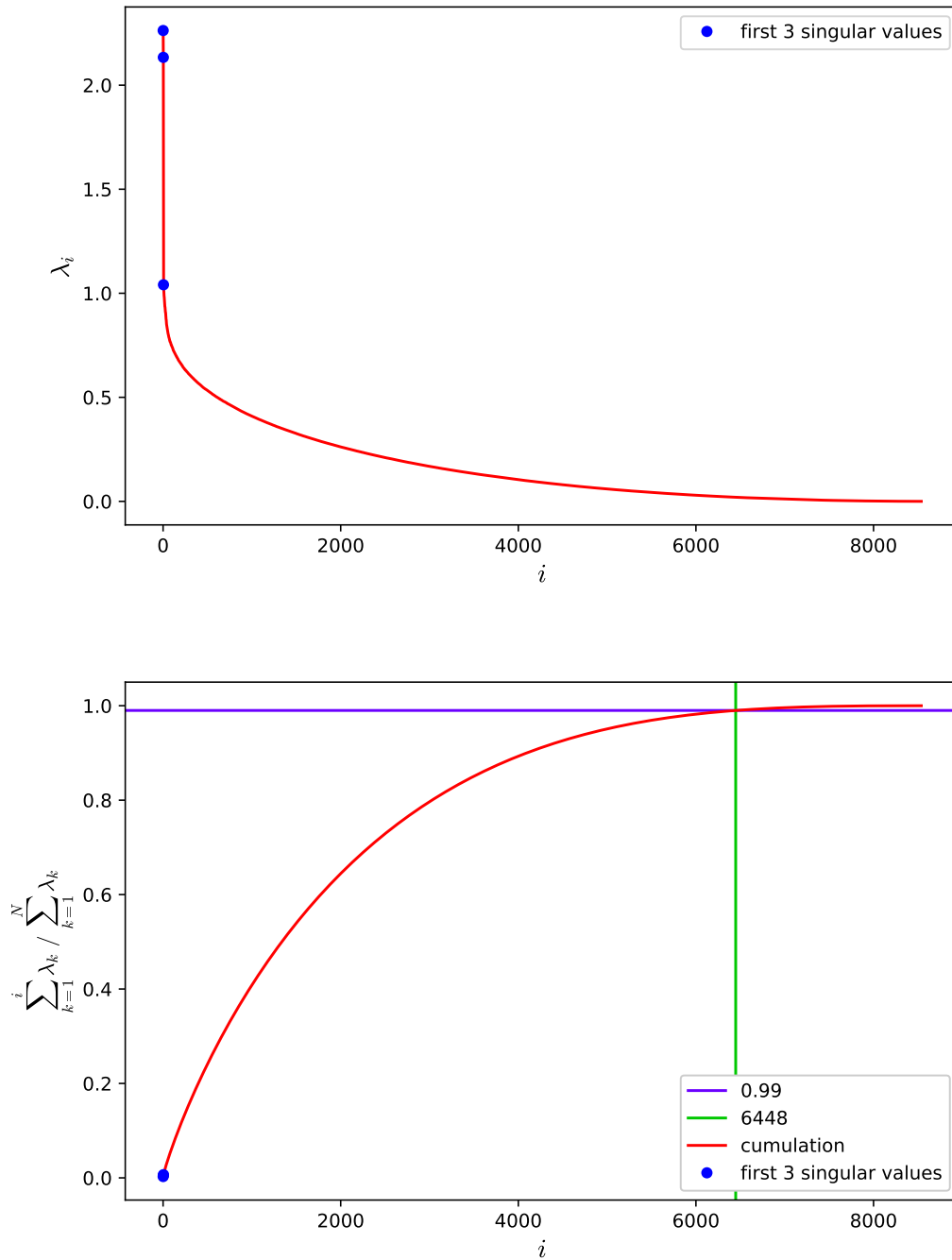


Fig. 5.4 The threshold which is set to stabilize the solution of SVD. It is the threshold that the cumulation ratio $\frac{\sum_{i=1}^{N_{\text{thr}}} \lambda_i}{\sum_{i=1}^{N_{\text{all}}} \lambda_i}$ is upto 0.99. It can not only maintain most of information but also avoid the impact of small singular values during the pseudo-inverse solution. Top: singular values. Bottom: the cumulation ratio.

For an angular resolution of θ_0 , the corresponding maximum mode is $l_{\max} \geq \pi/\theta_0$. For example, for 1° , $l_{\max} = 180$.

5.3 Simulation

In this section, we present the application of our algorithm to simulated visibilities for an interferometric array, in lunar orbit. In order to test our imaging algorithm, we shall consider a uniform isotropic beam response, over the full 4π spherical solid angle, approximating the beam of short dipole antennae widely used on artificial satellites.

5.3.1 Input maps

In order to clarify the effect of synthetic imaging, two kinds of input sky maps have been used. The first one contains only a few bright point sources, over otherwise an empty map, while the second map has diffuse emission dominated by the Galactic synchrotron and the same a few bright sources. These two input maps are shown in Fig. 5.5 and Fig. 5.6.

For the point source map, in order to avoid the superposition or blinding of sources, only 9 brightest sources which are located at distinct positions mutually on the sky are selected, which correspond to the Cassiopeia A, Cygnus A, Cygnus X, Taurus A (Crab nebula), Orion A, Fornax A, Centaurus A, Rosette nebula and Virgo A. Note that the point source map in Fig. 5.5 has been convolved with a PSF manually, so that sources can be seen clearly by eyes, but in the simulation, a point source only occupies a single pixel of angular size of ~ 6 arcmin, corresponding to $n_{\text{side}} = 512$ in HEALPix.

The diffuse component of the second sky map in Fig. 5.6 is based on the improved Global Sky Model (improved GSM) [90, 270]. The improved GSM is an iterative PCA model of diffuse emission, constructed from 29 sky maps at different frequencies. In the GSM map, the Galactic plane is the most outstanding structure, as the brightest sources have been removed out. However, in the simulation in this chapter, in order to show the changes of diffuse emission and point sources during the map imaging, the first 9 brightest sources are re-added to the GSM map, the resolutions of sources are reduced to 1° which is coincident with the GSM. Similarly, the map is pixelized to HEALPix of $n_{\text{side}} = 512$, corresponding to a pixel size of 0.115° .

5.3.2 Orbit and baselines

In the simulation, assuming the sky is static, i.e. ignoring variable sources, the sky intensity doesn't change in short time. Actually, the sky is not static, especially the radio activities of

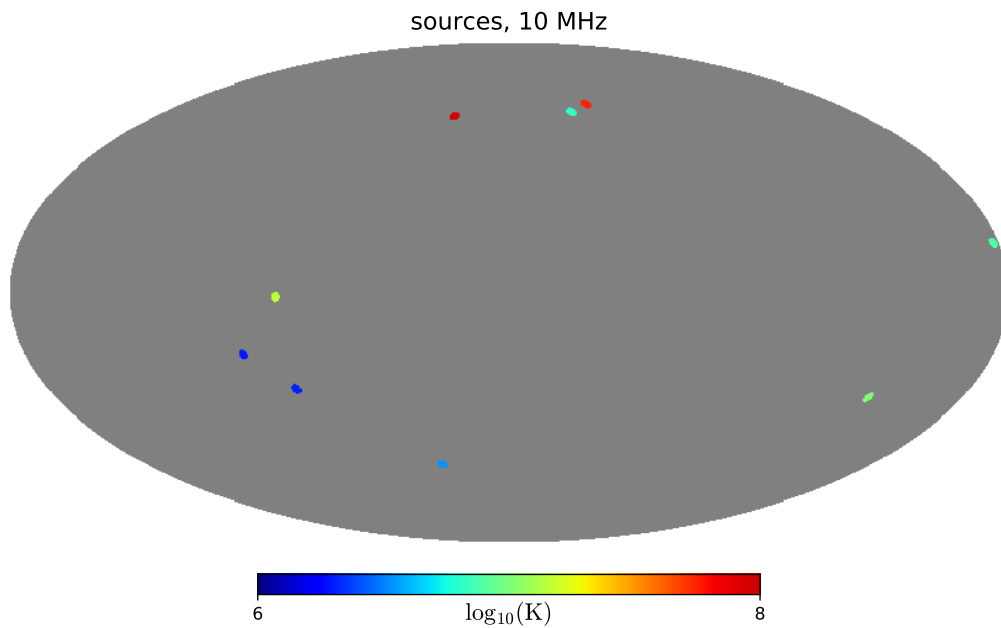


Fig. 5.5 Sky map with a few bright sources only, in the ecliptic coordinate system, at 10 MHz. In order to avoid the superposition or blinding of sources, only 9 brightest sources are selected, which correspond to Cas A, Cyg A, Cyg X, Tau A, Ori A, For A, Cen A, Rosette nebula and Vir A. Note that the map has been convolved with a PSF manually, so that sources can be seen clearly by eyes.

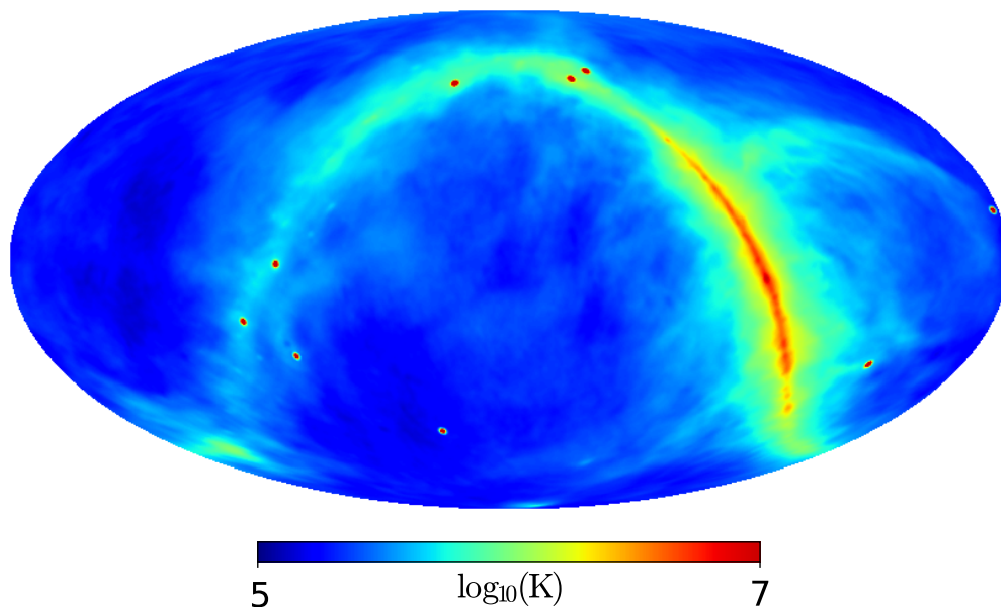


Fig. 5.6 Sky map contains not only bright point sources but also diffuse emission, in the ecliptic coordinate system, at 10 MHz, in 1° resolution.

the Sun and the gaint planets such as the Jupiter may impact significantly on the observation. However, such influence can be eliminated in principle, for example, making observation during the inactive periods of the Sun and the Jupiter, or when they are shielded by the Moon, even developing a powerful algorithm to deal with it. In the simulation in this section, variable sources are ignored, and assuming a static sky. Futhermore, visibilities obtained by lunar orbital satellite array may be not uniform, due to power supply interruption problem, data storage problem, data downlink problem, etc. But these influences vary according to different missions, so, in this chapter, only the most general case is discussed, those influences in special conditions are ignored.

The equatorial plane of the Moon as well as the orbital plane of the Moon around the Earth is very close to the ecliptic plane, the angle between them is only $\sim 5^\circ$, so, the ecliptic coordinate system is used in the simulation. As said above, in order to break the mirror symmetry effect, precession of satellite orbital plane is necessary. A 3D baseline distribution can be obtained after several months of observation. The pitch angle between satellite orbital plane and the equatorial plane of the Moon is selected to be 30° , because with this pitch angle, the precession amplitude and rate are large [42].

Assuming that all satellites are on the same orbit, but with different distances separating two consecutive satellites, the baselines will swipe a number of concentric rings on the (u, v) plane, as shown in Fig. 5.2. If the distances among satellites vary during flying, these rings will become thicker. As the orbital plane precess, baselines will distribute in a spherical shaped 3D volume whose upper and lower spherical crowns as well as pyramids are cut, as shown in Fig. 5.7. The upper and lower latitudes of the cutting planes are the positive and negative pitch angle respectively, i.e. $\pm 30^\circ$. In a realistic mission, the distances among satellites may be arranged into logarithmic interval, leading to a nonuniform baseline distribution. In this chapter, such specific and complicated cases will not be considered.

In DSL [42, 66] mission, distance between two satellite ranges from 0.1 km to 100 km. More advanced techniques are required for longer baseline, e.g. high precision measurement of angle and distance. In addition, as interference fringes of longer baseline varies much faster, it requires higher sampling rate of the correlator. Note also that the angular resolution is significantly limited by the scattering of interstellar medium (ISM) and intergalactic medium (IGM) [139], thus a 100 km baseline at 10 MHz only corresponds to ~ 1 arcmin angular resolution.

In the simulation, discussed here, we consider the range of baselines from 1 to 10 km. We have chosen a narrower range compared to the DSL mission is in order to focus on the effect of 3D baseline distribution on imaging, avoiding the complications introduced by the very long and very short baselines. Another reason is that the angular resolution of input

maps are limited [89, 270], very long baseline can not improve the precision of reconstructed map as there are no small scale structures. Furthermore, the baseline range of 1–10 km is just coincident with the requirement of Chang’e-4 lunar orbit satellite interferometric array experiment [268].

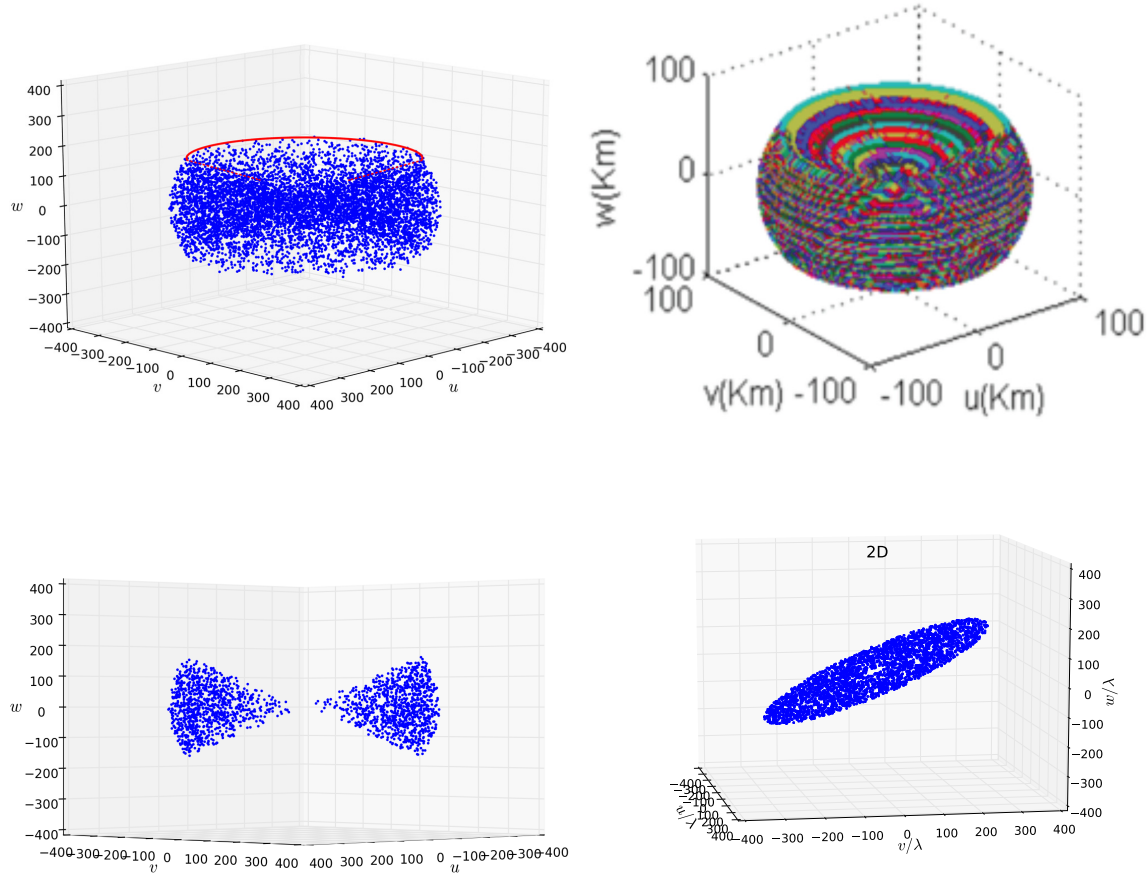


Fig. 5.7 Top: 3D baseline distribution, the view angles to the orbital plane are 15° (top-left) and 45° (top-right). Bottom-left: the cross-section of 3D baseline distribution through the center, upper and lower pyramids are dug. Bottom-right: all baselines are on the orbital plane.

Practically, the considered observational frequency in the simulation is 10 MHz, corresponding to a wavelength of 30 m, $33.3 < |\vec{u}| < 333$ for 1–10 km baseline. Roughly 8×10^3 (u, v, w) points are generated uniformly. Such number of points is enough to reconstruct a high quality sky map, and the total computation and time consumption are not too large. The generated 3D baseline distribution is shown in Fig. 5.7.

The Moon blocks a part of the sky. We assume that the Moon is a perfect opaque sphere, ignoring the deformation of the Moon and the rugged topography on the lunar surface. For the low orbit satellite, the distance between the satellite and the lunar surface is much smaller

than the radius of the Moon, the angular size of the blocked sky region is

$$\theta_m \approx 2 \arcsin \left(\frac{R_m}{R_m + h} \right) \quad (5.19)$$

where $R_m = 1737.1$ km is the average radius of the Moon, h is the height of the satellite to the lunar surface, here $h = 300$ km is selected. As satellites fly around the Moon, the blockage of the sky by the Moon also changes. If the satellite orbit is elliptical, the angular size of the blocked region also changes. Ignoring the reflection and diffraction of the radio waves by the Moon, as well as the thermal emission from the Moon. At any time, as the relative positions of satellites with respect to the moon center are different, the blockage of the sky is slightly different for each satellites, we ignored however these slight differences in the simulation that have been performed.

5.3.3 Imaging from 3D baselines

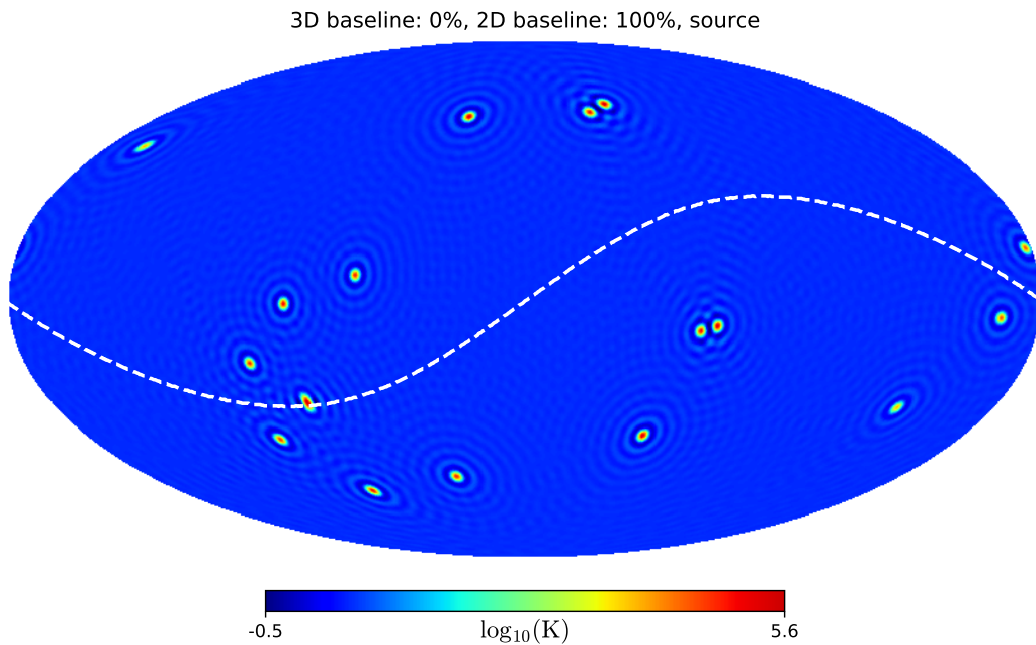


Fig. 5.8 Point source imaging with baselines distributed on a single plane. The orbital plane is represented by a white dashed curve, with a pitch angle of 30° with respect to the elliptic plane.

Fig. 5.8 shows the reconstructed image from the bright source only input sky map, from baselines distributed on a plane, corresponding to the case of nonprecessing orbital plane.

The white dashed curve shows the projection of the orbital plane. The artefact due to the mirror symmetry discussed above is clearly visible on the reconstructed map. For each source in the input map, there are two reconstructed images, one with the true position, and a second, fake image, at a position symmetric with respect to the orbital plane.

As said above, the mirror symmetry problem can be solved by increasing the noncoplanar baselines, as shown in Fig. 5.9. In order to focus on the effect of 3D baselines, we ignore the blockage effect of the Moon in this section, and assuming a uniform 4π antenna response. Fig. 5.9 shows the point source imaging for three different baseline distributions. There are the same total number of baselines in the three distributions, but the fraction of baselines out of the main orbital plane is different for each case. The top subfigure shows the imaging for the case where 90% of baselines are on the orbital plane while 10% are out of the plane. The ratio of baselines out of the orbital plane is 30% in the middle subfigure. A complete 3D baseline distribution is adopted in the bottom subfigure. It can be seen that, the top subfigure is similar with Fig. 5.8, there is a mirror image on the other side of the orbital plane, only the brightness of the mirror image is slightly lower than the real source. In the middle subfigure, the brightness of the mirror image becomes obviously lower than the real source. Finally, in the bottom subfigure, corresponding to full 3D baseline distribution, the mirror image disappears completely, the sky map is well reconstructed.

Fig. 5.10 shows the reconstructed diffuse emission map. It shows that the image is orbital plane symmetric if all baselines distribute on a single plane, it is impossible to distinguish the real one and its mirror. However, as the number of 3D baselines increasing, the mirror structure becomes weaker, the real structure and its mirror is beginning to be distinguished, although the quality of the map decreases due to the mixture of the real structure and the mirror residual. In the complete 3D baseline case, mirror image is eliminated, the reconstructed map is closed to the input map. It is shown that the 3D baseline distribution can reconstruct the map well.

5.4 Effects on imaging

5.4.1 The effect of blockage by the Moon

The Moon always blocks part of sky as satellites fly around it. The direction of blockage is position dependent: the center of the blocked sky region points to the center of the Moon, and is perpendicular to the tangent to the orbital plane. For the linear array on a circular orbit, it is perpendicular to the direction of baseline vector. The result is that, the observable sky is different for visibilities at different time, as the blocked region is different. However,

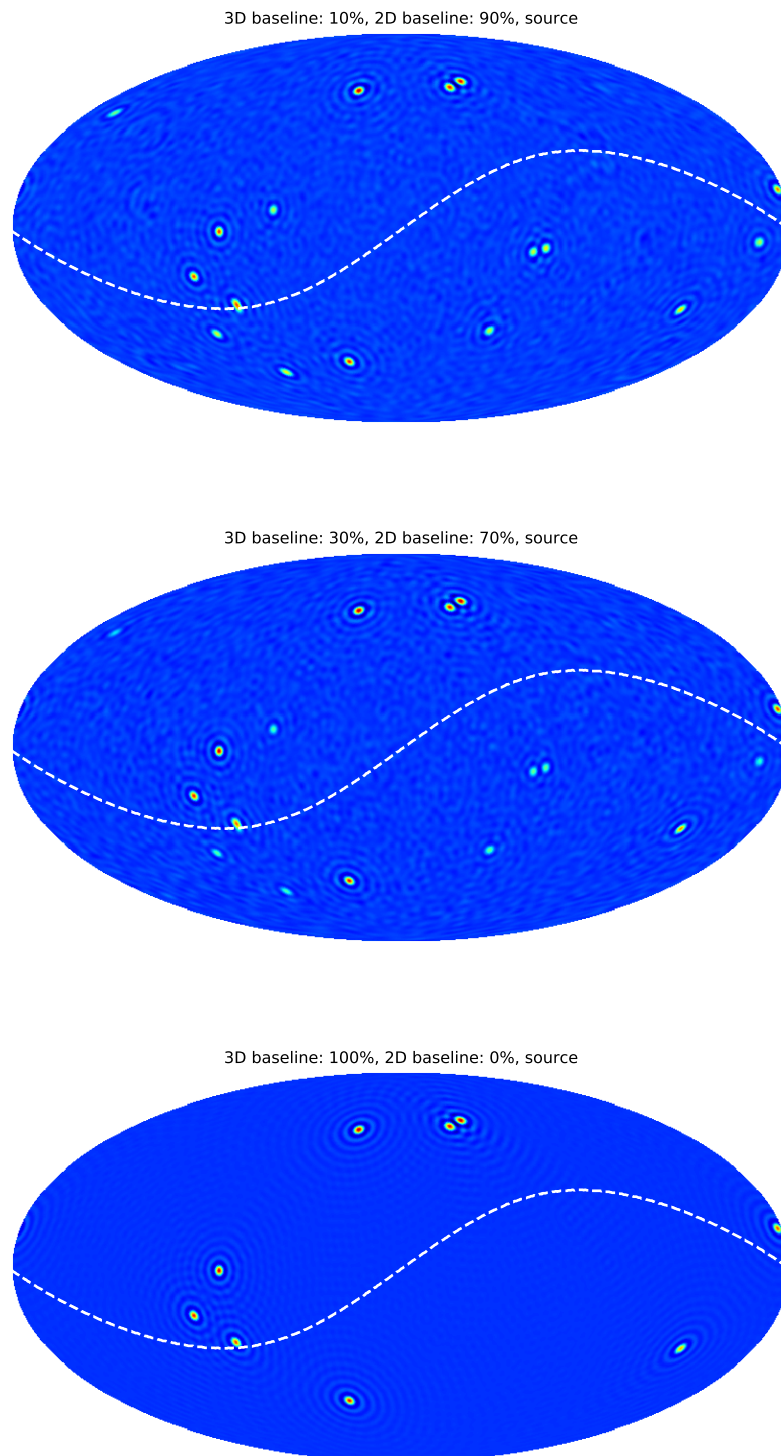


Fig. 5.9 Synthetic imaging of point sources. Top: 90% of baselines are on a single plane and 10% of baselines are out of the plane. Middle: 70% and 30% of baselines are on and out of the plane respectively. Bottom: complete or full 3D baseline distribution.

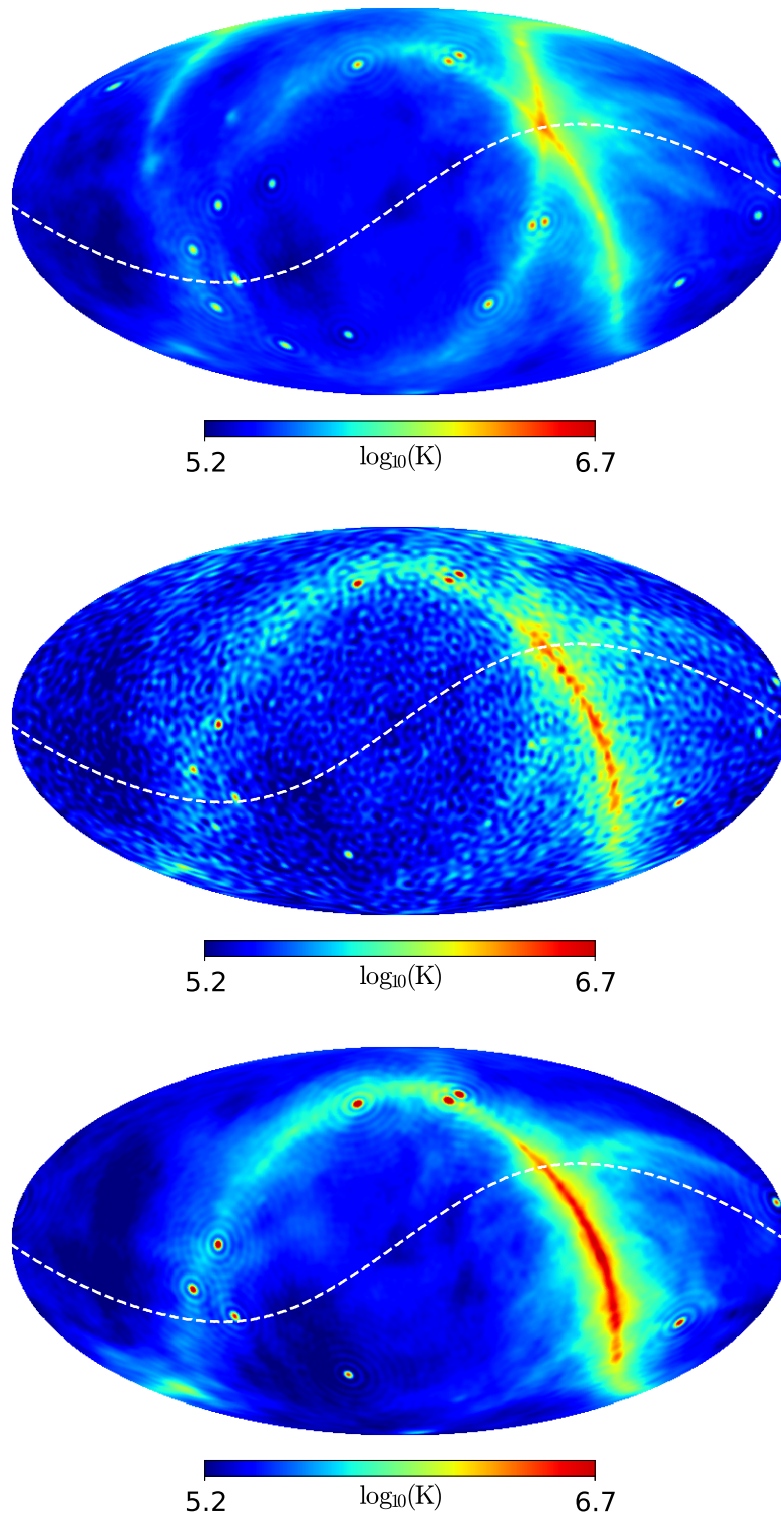


Fig. 5.10 Synthetic imaging of diffuse emission. Top: 90% of baselines are on a single plane and 10% of baselines are out of the plane. Middle: 70% and 30% of baselines are on and out of the plane respectively. Bottom: complete or full 3D baseline distribution.

because the size and position of the blocked region can be calculated, the sky map can still be reconstructed applying the imaging methods described in Sec. 5.2.2 and Sec. 5.2.3.

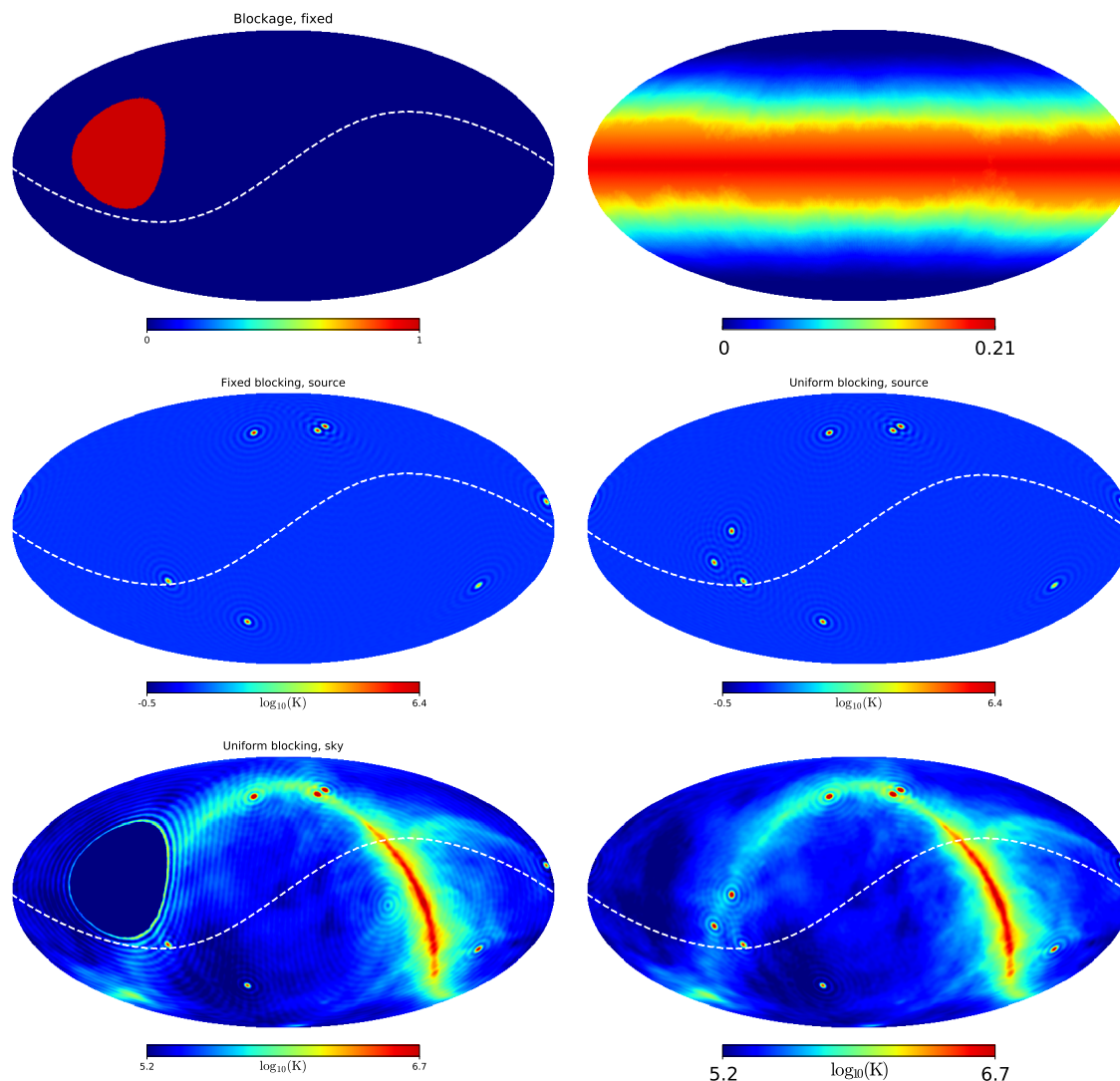


Fig. 5.11 The effect of blockage by the Moon. Top: the blockage ratio of each part of the sky. Middle: reconstructed maps of point source. Bottom: reconstructed maps of diffuse emission. Left: fixed blockage (similar to the ground-based antenna array). Right: blockage varying with time, following the relative position of satellites with respect to the Moon.

Fig. 5.11 shows the effect of the ratio of blockage on the reconstructed point source maps (middle) and diffuse maps (bottom). The blockage ratio is defined as the fraction of the observation time, when the moon blocks the view for a given sky direction. Blockage ratio equal to 0 means that the corresponding sky region is always visible, while a value of 1 means that the sky region is never visible.

As a comparison, left column is for a fixed blockage, i.e. the blocked part of the sky doesn't vary, this is similar to the ground-based telescope. Although nonrealistic, it is intended to illustrate the principle of imaging with blockage. In this case, the blocked part of the sky can not be reconstructed, as there is no information from this region, this is of course the expected result. The blocked sources disappear from the reconstructed map (middle-right), while there is a blank hole for the diffuse map (middle-left subfigure).

The right column shows a more realistic case. As the orbital plane precess continuously, the blockage moves on the celestial sphere. The blockage ratio is from 0 to 1, meaning that a given direction of sky is visible during some periods and blocked at other times. As the velocity of satellites moving around the Moon and the velocity of the precession are approximately uninfo, the blockage within positive and negative pitch angles ($\pm 30^\circ$) is roughly uniform, leading to blockage $\sim 11\%$ of times. Outside the pitch angle of 30° , the blockage is 0. emission are reconstructed well. From the right panels of Fig. 5.11, middle and bottom maps, it can be seen that the point sources as well as the diffuse emission are well reconstructed.

5.4.2 Pixel method v.s. spherical harmonic method

To solve the linear equation system in Sec. 5.2, we have used two methods: pixel method and spherical harmonic method. The pixel method is to pixelize the sky map, then directly solve the linear mapping between the sky intensity and the visibility (Sec. 5.2.2). The spherical harmonic method is to expand the sky map to spherical harmonics, then solve the linear mapping between the spherical harmonic coefficients a_{lm} and the visibilities (Sec. 5.2.3). In this subsection, the performances of these two methods are compared.

As the resolution of input map is 1° , choosing a lower resolution for the reconstructed image can quantize the error raised by different resolutions. For the pixel method, select $n_{\text{side}} = 32$ for HEALPix maps, corresponding to a pixel size of 1.83° . Comparably, we set the maximum order $l_{\text{max}} = 98$ for the spherical harmonics, corresponding to an angular resolution close to the one for HEALPix $n_{\text{side}} = 32$.

Fig. 5.12 shows the reconstructed maps (top panel) and the relative error (bottom panel). The relative error is defined as the ratio of the difference between the reconstructed map and the input map to the input map. Left column is for pixel method, while right column is for spherical harmonic method. The largest errors appear on the brightest points in both methods, because the reconstruction is not perfect, the power leaks from brighter pixel to the surrounding faint pixels, the peak of the reconstructed source is lower than the true value, while the values of surrounding pixels become larger. For this same reason, the relative error over the Galactic plane is also larger.

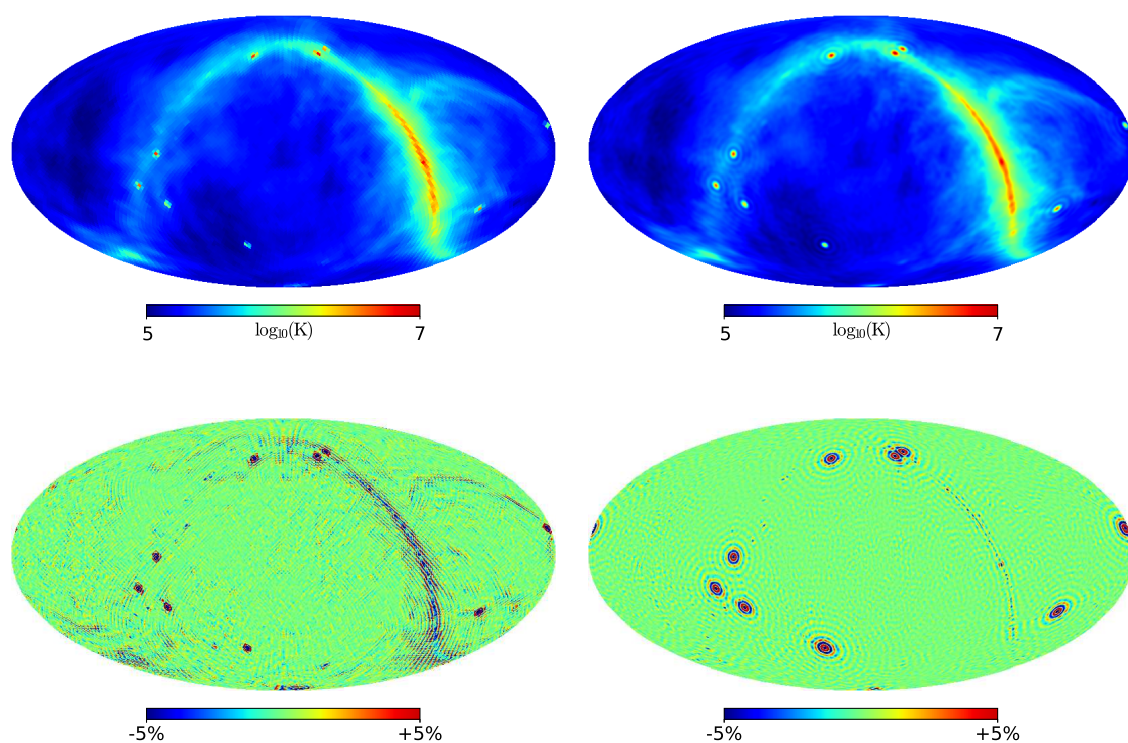


Fig. 5.12 Reconstructed maps and their relative errors. Left: pixel method. Right: spherical harmonic method. The relative error map is restricted in the range of -5% to $+5\%$, so that the slight error can be seen clearly. The maximum value, minimum value, average value and medium value of the relative error of pixel method are $\sim 45\%$, $\sim 0.02\%$, $\sim 2.3\%$ and $\sim 1.7\%$, while they are $\sim 20\%$, $\sim 0.006\%$, $\sim 1.6\%$ and $\sim 1.2\%$ for the spherical harmonics method. Obviously, no matter from the view of map quality or the error, spherical harmonics method performs better.

The difference of relative errors between the two methods is also large (see Tab. 5.1). The maximum value, minimum value, average value and median value of the relative error of pixel method are $\sim 45\%$, $\sim 0.02\%$, $\sim 2.3\%$ and $\sim 1.7\%$, while they are $\sim 20\%$, $\sim 0.006\%$, $\sim 1.6\%$ and $\sim 1.2\%$ for the spherical harmonic method. Obviously, no matter from the view of map quality or the error, the spherical harmonics method performs better.

Table 5.1 The relative errors of reconstructed maps from pixel method and spherical harmonics method.

	pixel method	spherical harmonic method
maximum	45%	20%
minimum	0.02%	0.006%
mean	2.3%	1.6%
median	1.7%	1.2%

When reconstruct sky map from spherical harmonic coefficients, actually the sum of modes can only up to a certain value l_{\max} , information from higher modes are dropped, therefore, the small scale structures in the map are lost. For a point source, the peak is lowered and ring shaped side lobes appear. The point spread functions (PSFs) for $l_{\max} = 100$ and $l_{\max} = 200$ are shown in Fig. 5.13. For larger l_{\max} , the angular size of the central peak as well as the side lobes are smaller. The side lobes could be reduced by replacing the sharp cut off in l -mode by a soft cut off, e.g. an exponential damping cut off.

5.4.3 The effect of baseline distribution

In the mission of lunar orbit array, each satellite flies along a circular or elliptic orbit. Through the variation of relative positions of satellites, different (u, v, w) points are achieved. As the number of satellites is limited, the (u, v, w) coverage must be incomplete, but the sky map can still be reconstructed by the sampling in (u, v, w) space. In the simulation above, at the reference frequency of 10 MHz, $u_{\max} \sim 300$, there are about 8×10^3 sampling points, the sampling density is about 10^{-3} , the quality of the reconstructed map is good. The top of Fig. 5.14 shows the case where only long baseline (6–10 km) have been kept, i.e. the 3D baseline distribution is hollow. Although there is no short baseline, the quality of the reconstructed map is fairly good, just the side lobes become larger. The bottom of Fig. 5.14 shows the case where only short baseline (100–500 m) have been kept, some small scale structures are lost, while large scale structures remains.

For the lunar orbit array, a number of visibility data can be collected after a period of time. In the initial period, because of limited precession of the orbital plane, the samples in

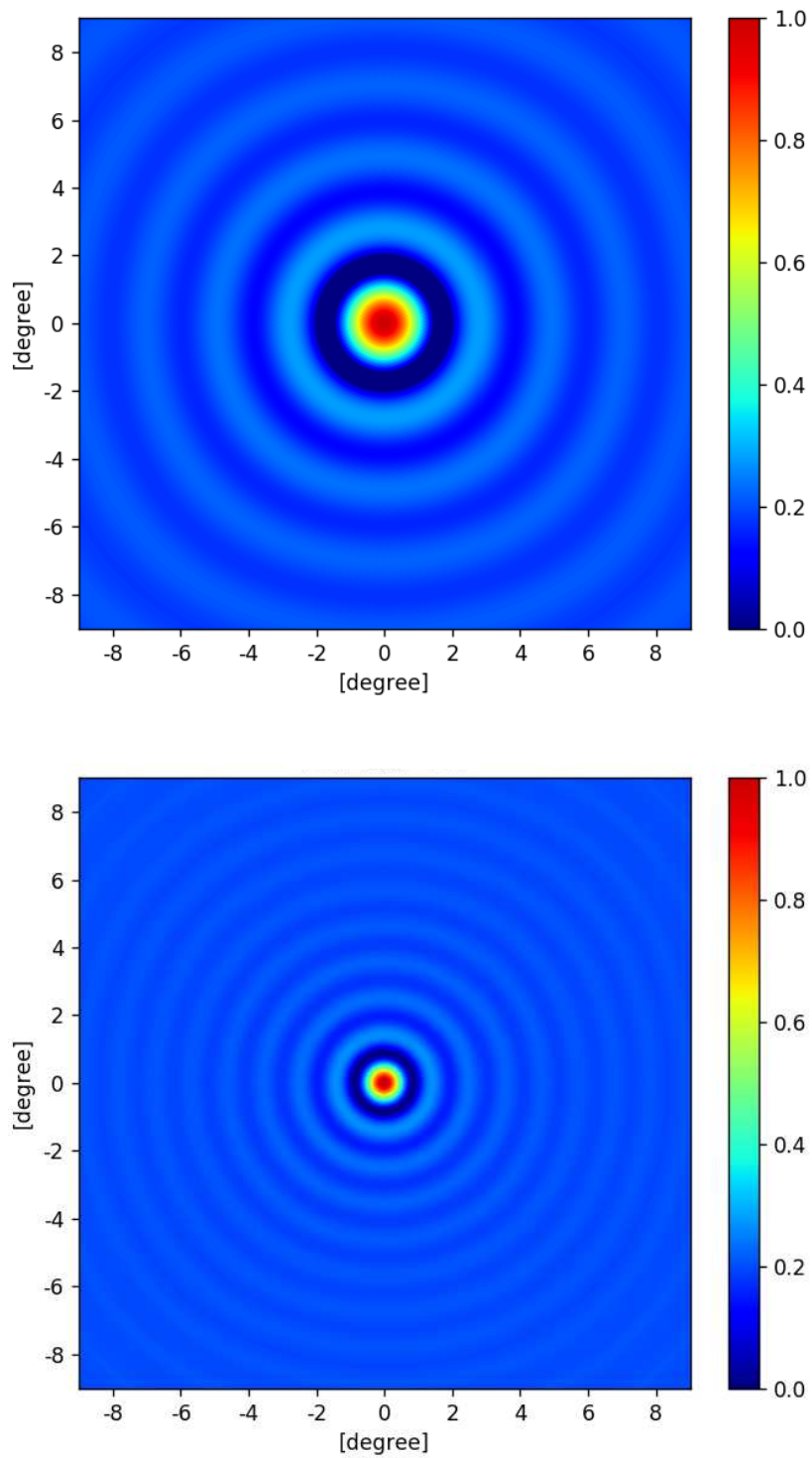


Fig. 5.13 Influence of l_{\max} on PSF. Top: $l_{\max} = 100$. Bottom: $l_{\max} = 200$.

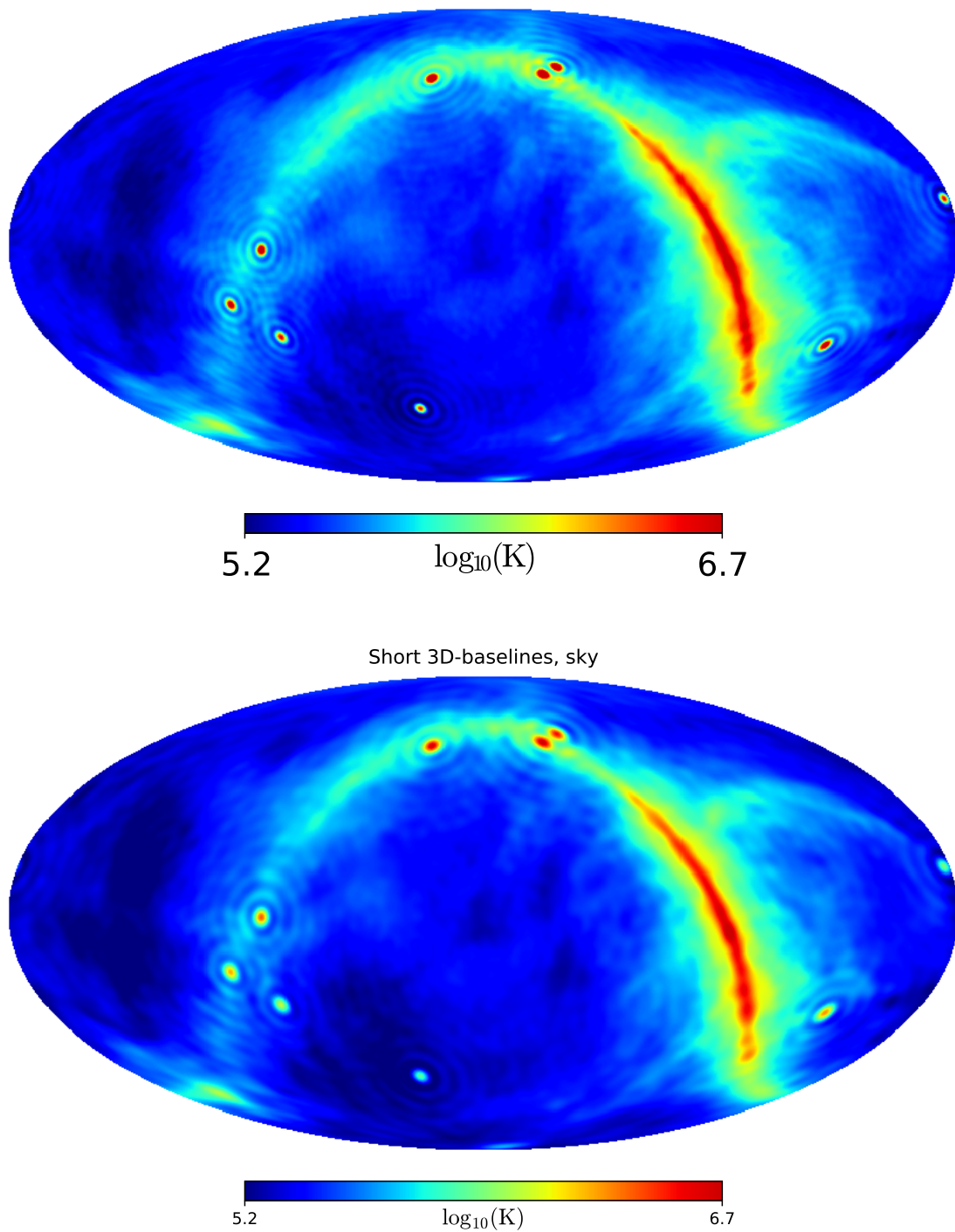


Fig. 5.14 Top: imaging only using long baselines of 6–10 km. Bottom: imaging only using short baselines of 100–500 m.

(u, v, w) space are concentrated on a thin disk, similar to the case in Sec. 5.3.3. The range of samples becomes larger over time, but the distribution is still nonuniform.

Fig. 5.15 shows one of the most extreme case of nonuniform baseline distribution: all baselines are concentrated in a 1/4 of the sphere, from longitude 0° to 90° . The top of Fig. 5.15 is the zoom-in of a point source. The point source becomes distorted, with asymmetric side lobes. The bottom of Fig. 5.15 is a reconstructed map of diffuse emission plus point sources. Actually all structures in the map are distorted, but such slight distortion is not clear compared to the diffuse structure, however, the distortion of the point source is clear. In general, although the baseline distribution is nonuniform, a fairly good sky map still can be reconstructed.

5.5 Brief summary

In this chapter, an imaging algorithm for lunar orbit interferometer array has been presented and we discussed its performance. Lunar orbit array is an ideal tool to observe the radio sky below 30 MHz, as this band is hardly observable from the ground because of the influences of the ionosphere and radio frequency interference (RFI). Comparing with the array landing on the lunar surface, the orbital array doesn't require an additional tracking and data relay satellite system (TDRSS) to transmit the observation data back to the Earth, and solar panels can be used to supply the power to the satellite.

However, the imaging algorithm for the orbital array is significantly different from that for ground based interferometers. First, from the realistic point of view, orbital satellite array can only be equipped with electric short antenna, the field of view of such an antenna is very wide (almost the whole sky), requiring a full sky imaging algorithm. Second, the Moon always blocks part of the sky, and the direction and the size of the blockage vary with time, leading to a time varying response function. Third, as the Moon can't block the direction perpendicular to the orbital plane, if the precession of the orbital plane is small or even there is no precession, mirror images will appear in symmetric positions with respect to the orbital plane. Finally, the precession of the orbital plane generates a 3D baseline distribution, requiring that the imaging deals with with noncoplanar baselines.

We have developed an imaging algorithm exploiting the linear mapping between the measured visibilities and the sky brightness and have shown that it can handle the problems listed above. We have also shown that by solving the problem in the spherical harmonic domain, we improve both the imaging performance and speed up the computation.

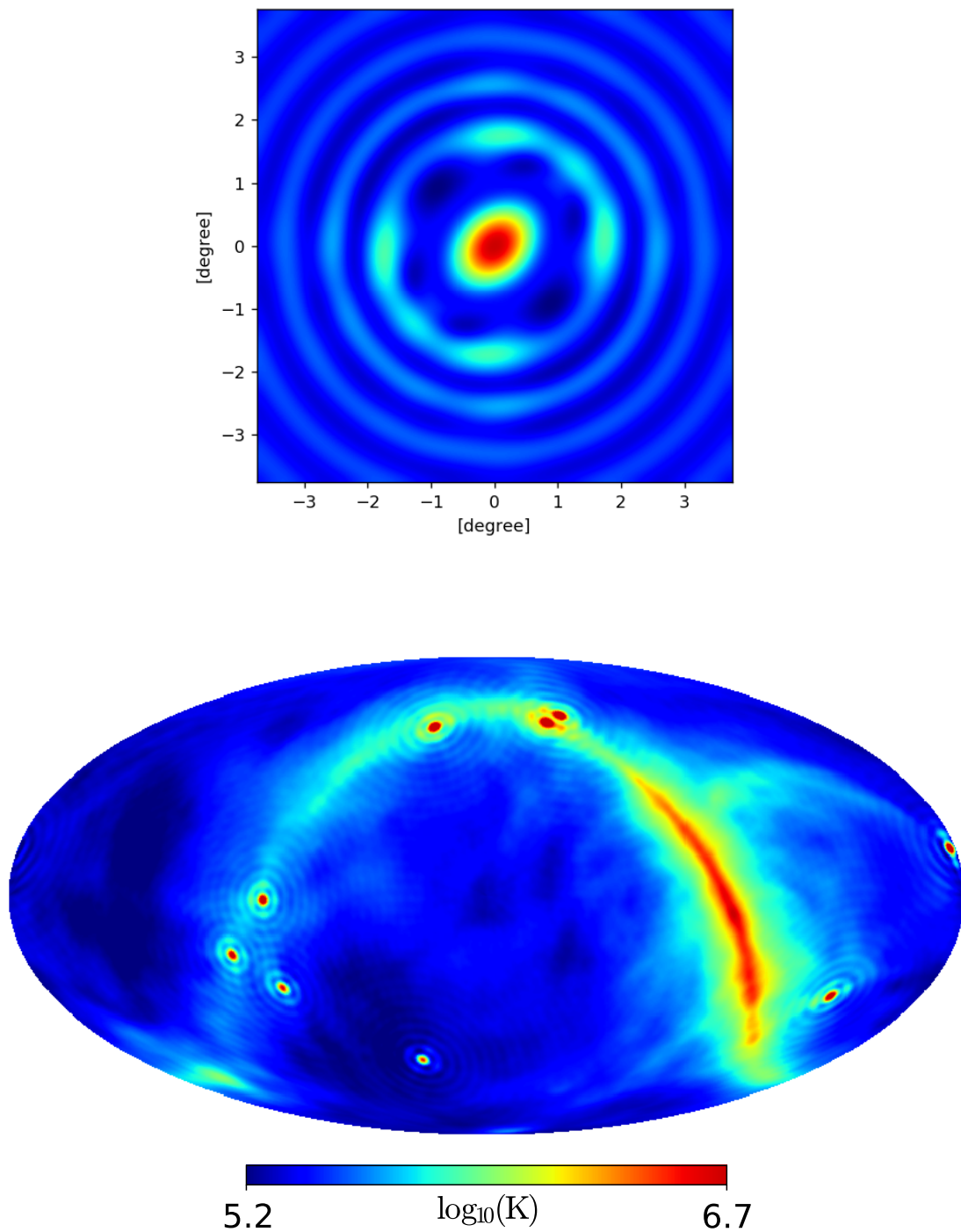


Fig. 5.15 Synthetic imaging of asymmetric baseline distribution. Baselines are concentrated in a 1/4 of the sphere, from longitude 0° to 90° . Top: the zoom-in of a point source, its shape is distorted, the side lobes appear asymmetric. Bottom: a reconstructed map of diffuse emission plus point sources. Actually all structures in the map are distorted, but such slight distortion is not clear compared to the diffuse structure, however, the distortion of the point source is clear.

Chapter 6

Data analysis for transit interferometer of PAON-4

For a realistic observation, the response, bandpass and complex gain (including amplitude and phase) are unavoidably changing. To calibrate these effects, a number of methods have been developed [243, 216, 120, 226]. In recent years, as more and more large interferometers with high precision and wide field of view are built, some new calibration methods have been proposed, such as the SAGE (Space Alternating Generalized Expectation Maximization) method [145], the ADI (alternating direction implicit) method [213], the complex optimization method based on the Wirtinger derivative [227], and the facet method [251].

In this chapter, we perform a first analysis of the observational data from PAON-4 prototype transit interferometer [11]. Starting from the raw data, we remove the RFIs using the SumThreshold method. We evaluate the overall performance of the array, in term of system temperature and antenna response. Using the standard calibrators as well as the publicly available observational sky maps such as the 21-cm LAB map and the 408 MHz Haslam map, we determine the complex gains (amplitudes and phases) for PAON-4 feeds, and calibrate the data streams. We then apply the m -mode map making algorithm [223, 267] in spherical harmonic domain to reconstruct sky maps from cleaned calibrated PAON-4 data.

6.1 PAON-4

PAON-4 (L'interféromètre PARaboles à l'Observatoire de Nançay-4)¹ is a test array aiming to evaluate the ability of small dense interferometer using small dishes with wide band (1250–1500 MHz in 4096 bins) receivers, located at the Nançay radio observatory in France

¹<https://indico.lal.in2p3.fr/category/155>

(latitude $+47^{\circ}22'55.1''$, longitude $+2^{\circ}11'58.7''$). It is designed and built for the France BAORadio project² consisting of 4 dishes of 5 m diameter, in a configuration shown in Fig. 6.1 and Fig. 6.2. Three dishes are on the three vertexes of an equilateral triangle with edge length of 12 m, where two vertexes are along the North-South direction (North-South edge), while the third vertex is on the West of the North-South edge (West vertex). The fourth dish is on the perpendicular line of North-South edge going through the West vertex, 6 m away from the West vertex on the East. The total receiving area of PAON-4 is $\sim 75 \text{ m}^2$. The array is controlled by a computer to rotate in latitude direction from $+12^{\circ}$ to $+60^{\circ}$. while it is fixed in longitude direction, the sky coverage is $\sim 5000 \text{ deg}^2$ as a result.

PAON-4 is working on an observation mode of drift scan, all antennae are pointed toward the same declination, scanning the sky as the Earth rotating for the same duration, several hours around a target (usually a bright source), or a sidereal day for the whole declination.



Fig. 6.1 Left: PAON-4 radio interferometric array. Right: its location.

6.2 Raw visibility data

With 4 dual polarization (horizontal polarization H and vertical polarization V) receivers, PAON-4 can generate 36 visibilities which is computed by the BAORadio electronic-acquisition system, 8 auto-correlations ($4 H_i H_i$ and $4 V_i V_i$) and 28 cross-correlations ($6 H_i H_j$, $6 V_i V_j$ and $16 H_i V_j$).

²<https://groups.lal.in2p3.fr/bao21cm>

The observational frequency band is 250 MHz wide from 1250 MHz to 1500 MHz, split into 4096 frequency bins with frequency resolution of ~ 61 kHz. Each digitisation frame has 8192 time samples, corresponding to $8192/500\text{MHz} = 16.384\ \mu\text{s}$. Several thousand frames are averaged into a single visibility measurements, depending on the acquisition trigger rate and visibility averaging time, leading to an on sky efficiency of $\sim 13\%$ for 6 kHz acquisition trigger rate.

Fig. 6.3 shows samples of the original dataset—CygA17nov16, which was observed at the declination of $+40.733^\circ$. It can be seen that the gain of the system varies with time, mainly due to environment temperature. To calibrate this variation, a resistor of $50\ \Omega$ is put at the front end of the first level of low noise amplifier (LNA) of the 4V channel, thus the 4V channel measures the thermal noise of this resistor. In addition, an offset along y-axis in the real part is due to an artefact of the FFT performed on the FPGA. Although correlated noise affects both the real and imaginary parts, but at a much lower level compared to this offset.

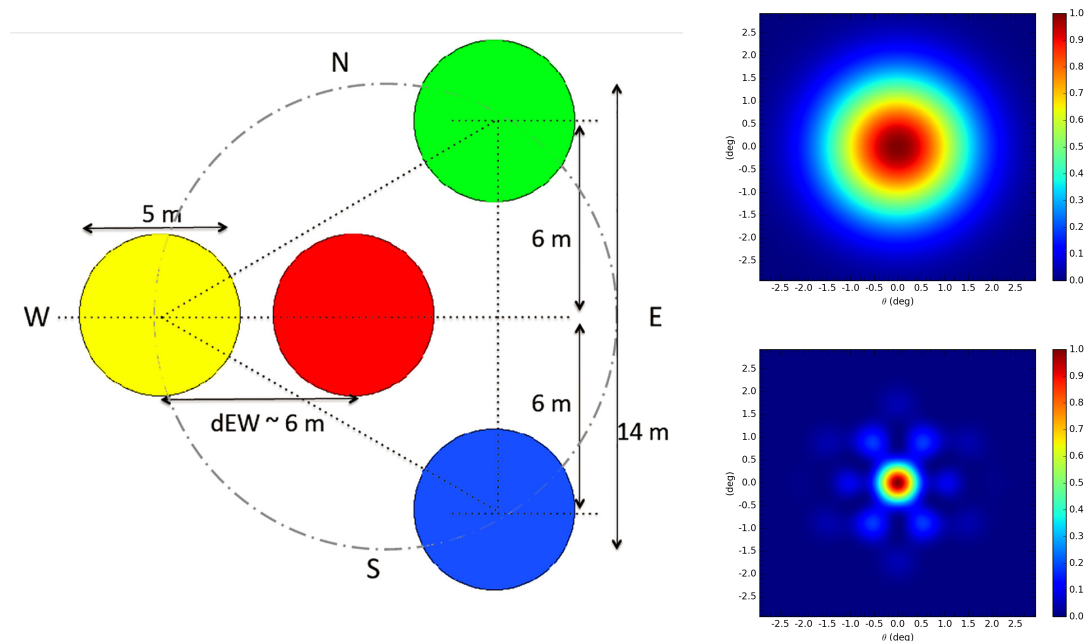


Fig. 6.2 Left: the configuration of PAON-4. Three dishes are on the three vertexes of an equilateral triangle with edge length of 12 m, where two vertexes are along the North-South direction (North-South edge), while the third vertex is on the West of the North-South edge (West vertex). The fourth dish is on the perpendicular line of North-South edge going through the West vertex, 6 m away from the West vertex on the East. Top right: the primary beam of a single dish of PAON-4, 5 m physical diameter with $\sim 2.9^\circ$ angular resolution at 1375 MHz. Bottom right: the synthetic beam of PAON-4 array, the FWHM resolution is $\sim 1.3^\circ$ at the center frequency of 1375 MHz for the full array.

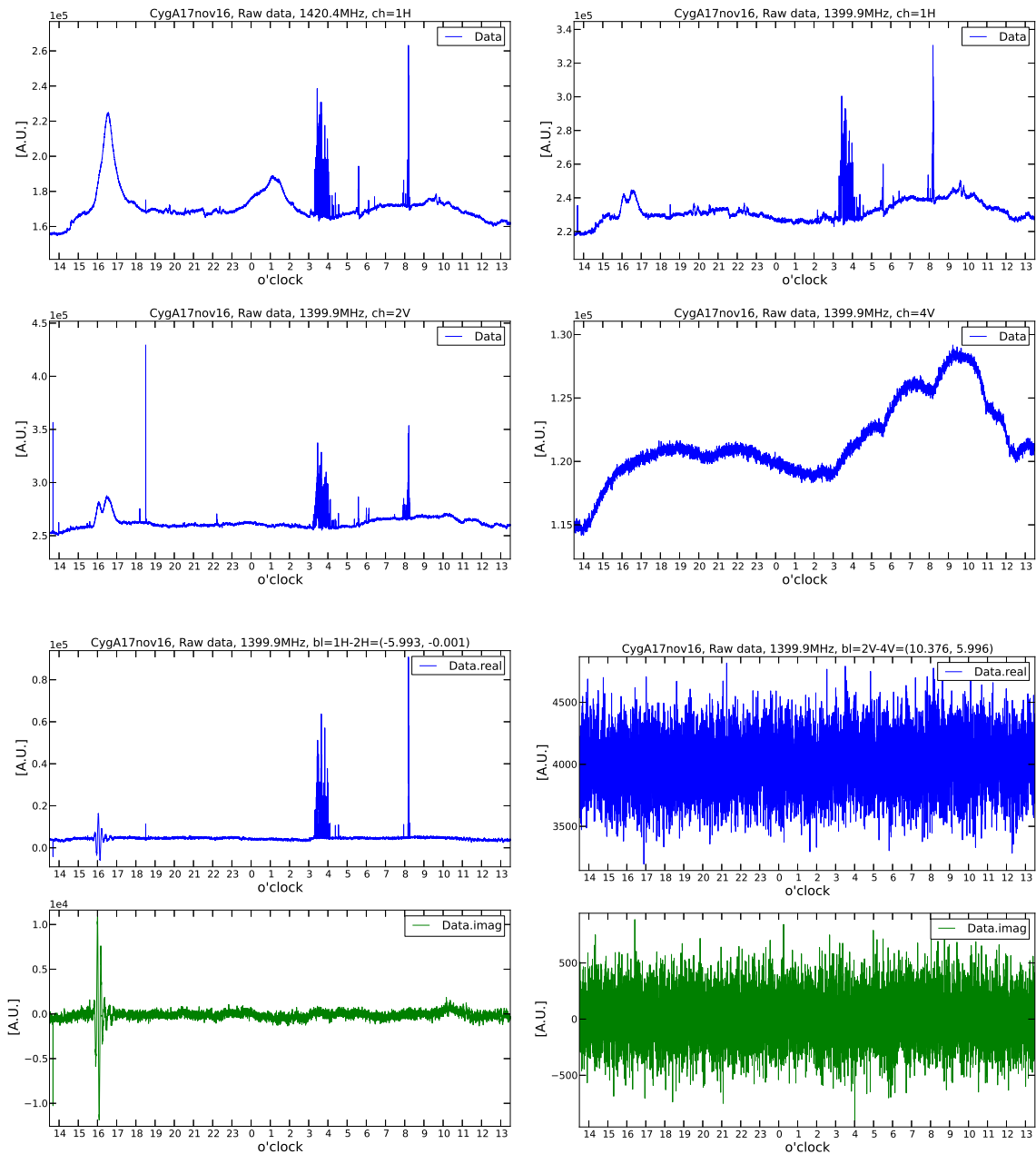


Fig. 6.3 The raw dataset of CygA17nov16, at the observational declination of $+40.733^\circ$. Top left: 21-cm signal from the HI inside the Milky Way at the frequency of 1420.4 MHz. Top right: Cygnus A plus the Galactic synchrotron emission at the frequency of 1.4 GHz. The second panel is the auto-correlations of channel 2V and 4V. For the third and fourth panels, left is the real and imaginary parts of cross-correlation of 1H2H, the real parts shift along $+y$ axis due to the correlator noise; right is the real and imaginary parts of 2V4V, a resistor of 50Ω is put at the front end of the first level of low noise amplifier (LNA) of channel 4V.

6.3 RFI mitigation

RFI (Radio Frequency Interface) is produced by narrow- and broad-band transmitters which emit radiation at frequencies overlapping with those for radio astronomical observations [101]. As the increase of the usage of the electronic devices, such as television, radio, mobile phone, wifi, radar, remote sensing, car ignitions, and many kinds of domestic appliance, RFI becomes common, causing a challenge for radio astronomical observation and data analysis [242].

To reduce the influence of the RFI, one strategy is to locate the radio telescope in a radio quiet site away from cities and other places where RFI is common³. However, even in remote places, RFI can not be completely eliminated, e.g. radiation from satellite, airplane and even lightning. In addition, because of the reflection by the ionosphere, RFI is actually omnipresent. Therefore, efficient RFI mitigation methods are essential for radio astronomical data processing, both in real-time and off-line.

Several methods have been proposed and implemented for this purpose, e.g. comparing the spectral and statistical profiles between signal and RFI based on a Generalized chi-square test theory [256]; using the adaptive-iterative canceling with a separate reference antenna designed to receive only the RFI [28]; ranking and filtering the dominant eigenvalues of the spatial correlation matrix [154]; subspace tracking and nulling the RFI by spatial projecting [102]; applying a cumulative sum (CUSUM) procedure in time-frequency plane [21]; using an independent reference signal constructed from the cross power spectrum between the signal from the telescope and the signal from an additional antenna pointing to the RFI source [49]; fitting the fringe-stop pattern of the stationary RFI in a fringe-stopped interferometer [18]; applying the VarThreshold method with a sequence of combination thresholds, which makes use of that RFI often affects multiple samples which are connected either in frequency or time, and an optimal variation of the SumThreshold method which is designed for and applied to LOFAR and WSRT data [178].

6.3.1 Surface fitting

Before applying the RFI mitigation methods, the surface of visibility data in frequency-time plane $\tilde{V}(v, t)$, which represents the astronomical signal, is assumed to be first removed. For the surface fitting, assuming a smooth surface is reasonable due to most of the astronomical signal is continuum, its amplitude doesn't change rapidly with frequency and time. Several surface fitting methods have been proposed, such as the iterative polynomial fitting to each tiles cut from the visibility matrix [260]; the 2D median filter; a blur filter with a sliding

³<https://science.nrao.edu/facilities/gbt/interference-protection/nrqz>

window (uniform filter) [179] or with a Gaussian kernel (Gaussian filter) [57]. For the RFI mitigation, in this chapter we only consider the power (amplitude) of the data. As the noise and RFI added to the astronomical signal, the power of the observational data is higher than that of the astronomical signal. Making use of this knowledge, here we use the minimum filter instead of other filters to fit the surface.

1. Select two step lengths s_v and s_t for frequency and time directions. Note that the visibility data is in an $N_v \times N_t$ matrix, where N_v and N_t are the number of frequency bins and time bins respectively, then the size of the pooled matrix is $M_v \times M_t = \lceil \frac{N_v}{s_v} \rceil \times \lceil \frac{N_t}{s_t} \rceil$, where $\lceil x \rceil$ means that taking the smallest integer which is not less than x .
2. minPooling the visibility matrix. For any visibility point $V(n_v, n_t)$, take a submatrix of $V(n_v : n_v + s_v, n_t : n_t + s_t)$, the minimum value of the submatrix is the new value of the pooled matrix with index pair $(\lceil \frac{n_v}{s_v} \rceil, \lceil \frac{n_t}{s_t} \rceil)$.
3. Interpolate the pooled matrix from the size of $M_v \times M_t$ to the original size of $N_v \times N_t$. The interpolation algorithm we select here is the cubic spline.
4. Iterate the step (2) and (3) until the sum of the power residual $V - \tilde{V}$ is convergent.

Fig 6.4 shows the comparison among the surface fitting methods. As the difference among the fitted 2D surfaces is not clear to the eyes, the comparison shown in Fig 6.4 is in 1D—time direction at 1400 MHz, but note that the fitting is in 2D. The window size for the filters except the Gaussian filter is set to be 9, which is satisfied with the most of instantaneous RFIs in our data except the RFIs covering wide frequency band and lasting for a long time. For the kernel parameters σ_g of Gaussian filter, if let 9 to be its FWHM, making the Gaussian filter has the similar total weight to the data as the other filters, then $\sigma_g = 9/\sqrt{8\ln 2} \approx 4$. We can see that the RFI is most outstanding after removing the surface fitted by minimum filter, which can perform a better RFI mitigation in the following steps. Fig 6.5 shows the surface fitting result by the minimum filter.

6.3.2 Mitigation method

For the post-correlation data, three types of methods are usually applied. The first type of methods is based on the threshold such as CUMSUM [21], VarThreshold and SumThreshold [178, 179], they mitigate the RFI through a series of thresholds on frequency-time plane, and work well to most of the RFI with various patterns [186, 5]. The second type of methods is based on the component decomposition such as Principle Component Analysis (PCA) [269] and Singular Value Decomposition (SVD) [178], they perform well if RFI is repeated over

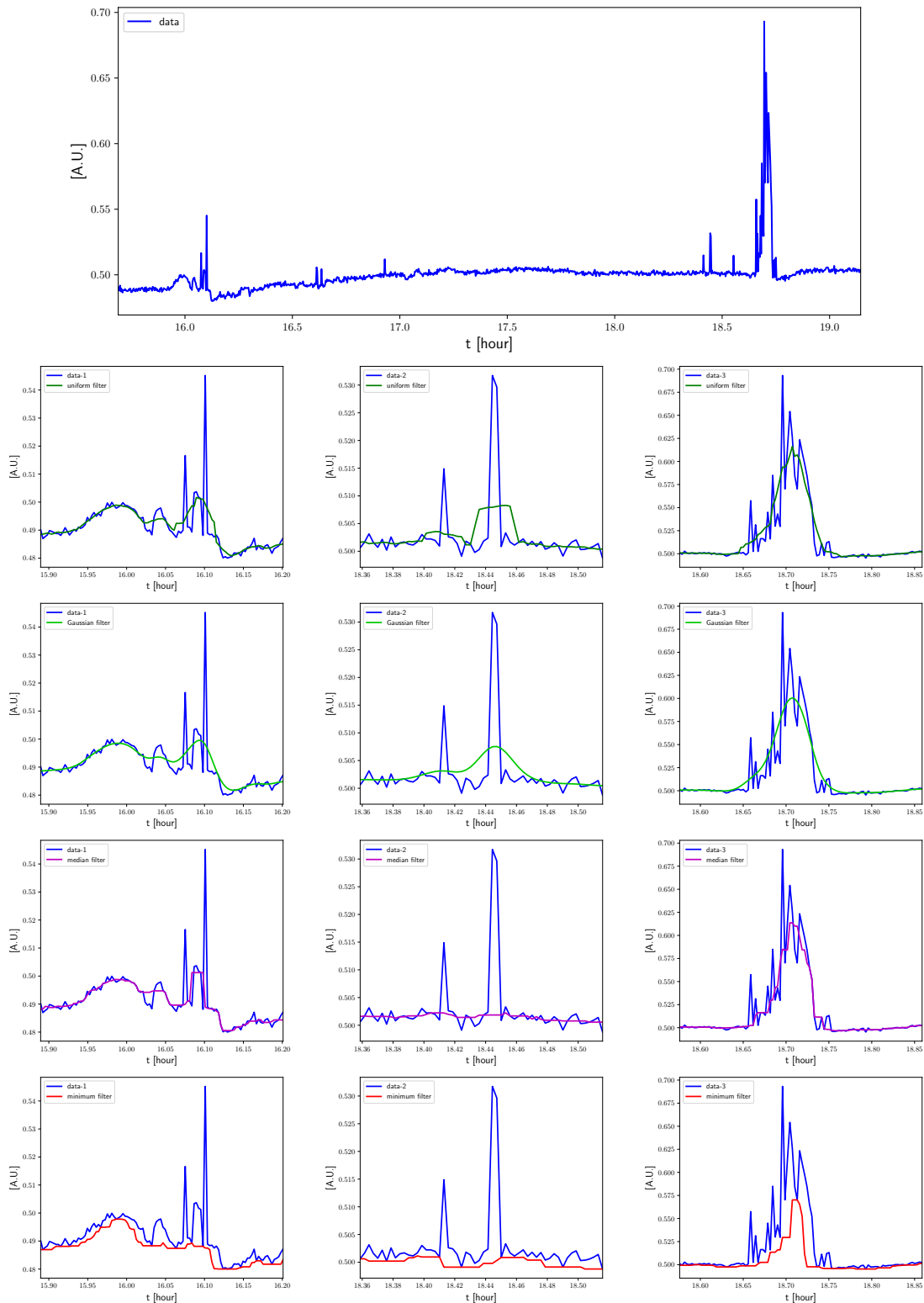


Fig. 6.4 Top panel: a duration of the auto-correlation data of 1H at 1400 MHz. Second, third, fourth and fifth panels are for the uniform filter, Gaussian filter, median filter and minimum filter, respectively. Each columns are for the region 1, 2, 3 in the top panel, respectively.

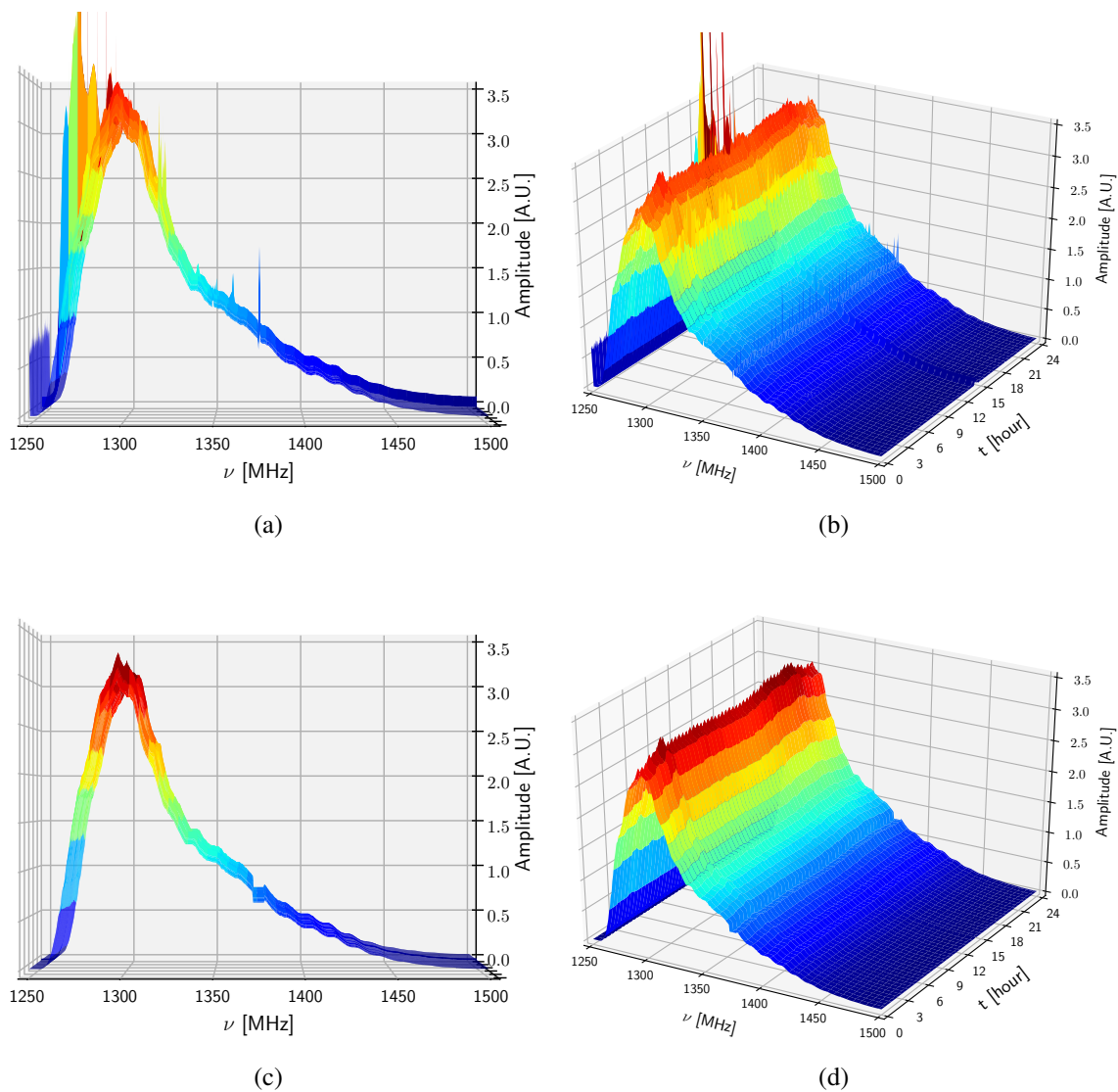


Fig. 6.5 Top panel: frequency-time plane of auto-correlation data of 1H viewed at different angles. Bottom panel: the same as the top panel but for that after minimum filtering. The frequency is from 1250 MHz to 1500 MHz, the duration is one sidereal day.

frequency and time, but can not handle with stochastic RFI. The third type of methods is using machine learning such as K-Nearest Neighbour (KNN), Random Forest and Naive Bayesian [170].

As the SumThreshold performs fairly well among the RFI mitigation methods on the radio interferometric data of LOFAR and WSRT data [178], we use this method to our PAON-4 data. Here we briefly introduce the SumThreshold method, for the detail, please see [178].

For the instantaneous and narrow-band RFI, it often affects not only the sample at one frequency and one time but also the connected samples around it, through the antenna beam. For the persistent and broad-band RFI, it directly affects a set of samples both in frequency and time. Therefore, when performing the RFI mitigation, an iterative method with incremental samples and a series of thresholds should be used. During the RFI mitigating, a sample can connect all the other samples, but empirically, the number of connected samples in each iteration can be a set of monotonically increasing number of $M = 1, 2, 4, 8, 16$, and the total false-positive ratio is shown in Fig. 6.6 [178]. χ in Fig. 6.6 is the average threshold relative to the distribution mode, a sample combination will be thresholded when their sum $\geq \chi \cdot M \cdot \sigma$, where σ is the standard deviation of the data without the fitted surface. Thus, for the combinations with samples number of $M = 1, 2, 4, 8, 16$, the corresponding $\chi = 4, 3, 2.5, 2, 1.8$. Two rules are needed to note:

1. When the lower combination of samples with RFIs is flagged by lower threshold, those samples will be replaced by the average threshold (threshold divided by the number of samples).
2. For each combination, after the replacement in step (1), the σ is recomputed.

Fig. 6.7 shows the RFI flagging using the SumThreshold method for PAON-4 data.

After removing the RFI contaminated data, mock data is estimated by cubic spline interpolation. Fig. 6.8 shows the comparison of PAON-4 data before and after the RFI mitigation, in 1D for the eyes convenient.

6.4 System gain

The gain of the system varies with time and frequency. The variation of the gain with frequency describes the frequency response of the system in the bandwidth, which is one of the performance indexes of the bandpass filter. The variation of the gain with time describes the stability of the system. For the ideal system gain, it is expected to be stable with time, but it is impossible in reality. The analog electronic gain varies with time to some extent

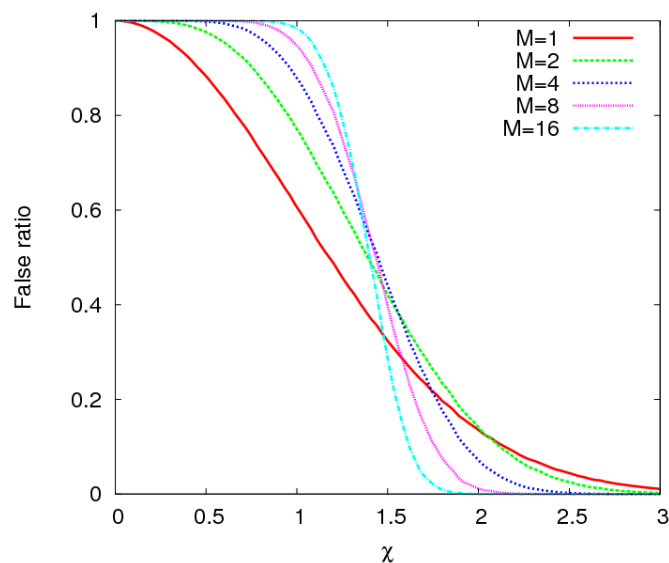


Fig. 6.6 The false-positives of the SumThreshold method when mitigating the RFI on the simulated data with a Rayleigh distribution. χ is the average threshold relative to the distribution mode (figure is cited from [178]).

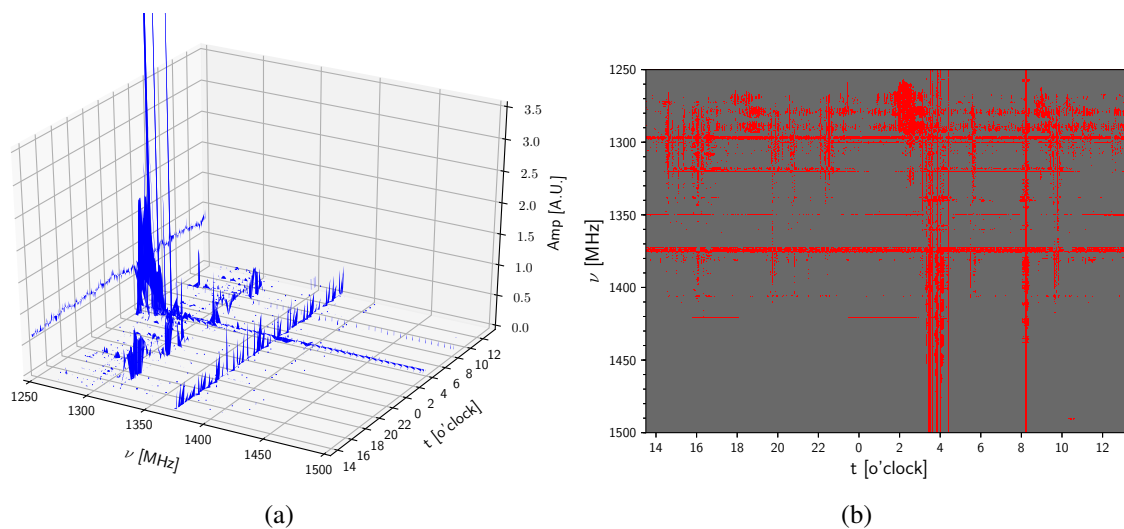


Fig. 6.7 (a) the result of the RFI mitigation using the SumThreshold method for PAON-4 data. (b) the same as (a) but plotted in 2D.

partly because of the temperature-dependent electronic hardware: the gain decreases when the temperature increases and the gain increases when the temperature decreases, as shown in Fig. 6.9.

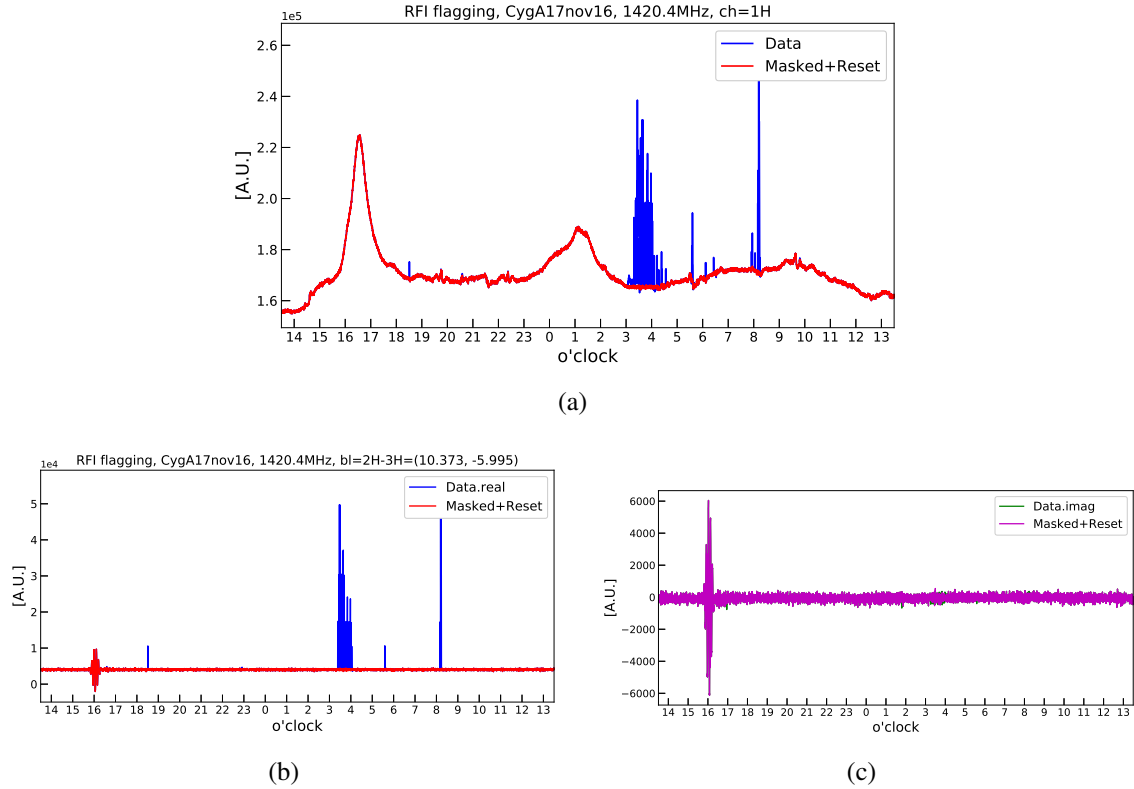


Fig. 6.8 The comparison of PAON-4 data before and after the RFI mitigation. (a) is the auto-correlation. (b) and (c) are the real part (blue) and the imaginary part (green) of the cross-correlation. Only one frequency of 1420.4 MHz is shown in the figure.

As the correlation of sky signals from different directions is relatively small, it is difficult to calibrate the system gain in the cross-correlation data beyond the fringes of bright sources. We use the auto-correlation data to calibrate the system gain. The system gain as well as the sky brightness is a function of time and frequency, if assuming that the time-varying parts and the frequency-varying parts of the system gain and the sky brightness are independent mutually, the auto-correlation visibility $V_a(t, \nu)$ where t denotes time and ν the frequency can be written as

$$V_a(t, \nu) = G(t, \nu) \cdot [I(t, \nu) + N(t, \nu)] = g(t) g(\nu) \cdot [I(t)I(\nu) + n(t)n(\nu)] \quad (6.1)$$

where $I(t, \nu)$ is sky brightness, $N(t, \nu)$ is the additive noise contribution dominated by the first LNA after the feed, $G(t, \nu)$ is the system gain.

1. For an antenna system observing the sky, $I(t, \nu)$ is the sky brightness. For a drift scanning antenna, t corresponds to different longitudes the antenna points to as the Earth rotating. However, the sky brightness is unknown, obtaining the sky brightness is instead one of the goals of the sky observation. In this case, the sky brightness resulted by previous experiments or by models is used.
2. If place a resistor on the front end of the LNA, the antenna measures the thermal noise of the resistor instead of the sky brightness, the achieved data is thus the result of gain amplification of the noise which is generally considered to be Gaussian [177, 106]. In this case, $I(t, \nu)$ is the power of white Gaussian noise which is proportional to the resistor temperature [177]

$$I(t, \nu) = P_n = k_B T_r(t) \Delta \nu \propto T_r(t) \quad (6.6)$$

where $k_B = 1.3806505 \times 10^{-23}$ J/K is the Boltzmann constant, $\Delta \nu$ is the overall bandwidth of the channel selective filtering in the receiver, $T_r(t)$ is the temperature of the resistor.

Case 1 is applicable when the sky brightness is dominated and the noise is low enough, but it is difficult to satisfy in the actual data without long integration time, and the result is sky model dependent. However, case 2 only requires a resistor on the front end of the LNA, which is easy to realize, and the characteristics of the thermal noise are known well [177]. For the actual PAON-4 data, we placed a 50 Ω resistor on front end of the LNA of channel 4V, so here we calibrate the PAON-4 gain according to the case 2.

As the spectrum of white Gaussian noise is flat in frequency, while the resistor temperature is a function of time, the $g(\nu)$ and $g(t)$ can be obtained by

$$g(\nu) \propto V_a^{\text{norm}}(\nu), \quad g(t) \propto \frac{V_a^{\text{norm}}(t)}{T_r(t)} \quad (6.7)$$

$g(t)$ is inversely correlated with the temperature, which is consistent with the result from the observation shown in Fig. 6.9.

Fig. 6.10 shows the variation of bandpass response $g(\nu)$ of PAON-4 in frequency. The whole period of time is split into 131 intervals, it can be seen that $g(\nu)$ varies little with time, its time-stability is fairly high. Fig. 6.11 shows the time-varying gain of PAON-4, the entire bandwidth is divided into 29 segments, similar to $g(\nu)$, $g(t)$ varies little with frequency. Therefore, that decomposing the system gain into two mutually independent parts of $G(t, \nu) = g(t) \cdot g(\nu)$ is reasonable.

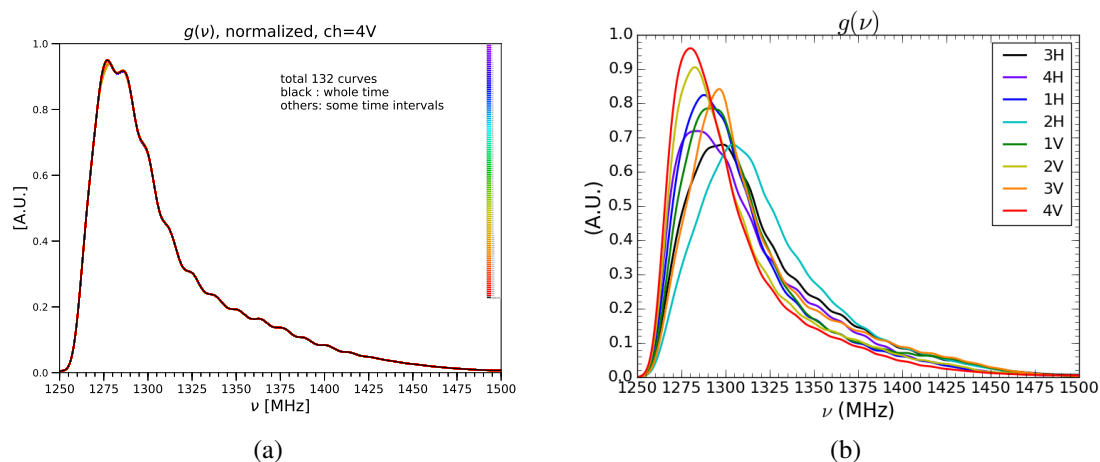


Fig. 6.10 (a) The bandpass gain $g(\nu)$ for channel 4V and its stability over time. The total period of time is split into 131 intervals, it can be seen that $g(\nu)$ varies little with time, its time-stability is fairly high. Colorful curves are for the 131 intervals, while the black curve is for the whole period of time. (b) $g(\nu)$ for the eight PAON-4 channels, their differences due to the analog electronic hardware, amplifiers and filters for the eight channels are clearly visible.

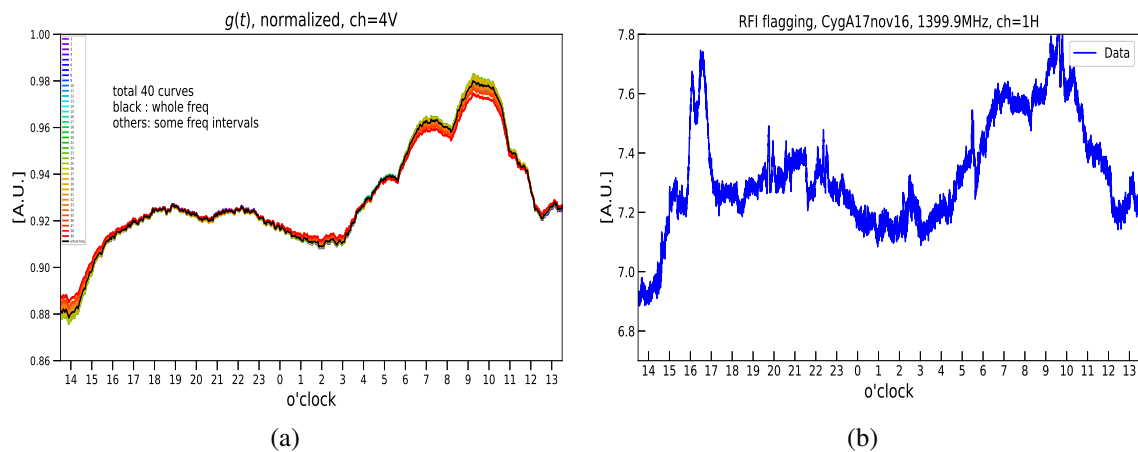


Fig. 6.11 (a) The time-varying gain of PAON-4 $g(t)$ for the blind channel 4V. The entire bandwidth is divided into 29 segments (colorful curve), $g(t)$ varies little with frequency, showing the stability of $g(t)$ with frequency. (b) The auto-correlation data (channel 1H at 1400 MHz) of the observed sky, the distortion of the observed auto-correlation data is mainly due to the time-variation of the system gain.

The data analyzed in this chapter were collected in November in Nançay, France. From the climate history of Nançay, the average variation of the air temperature in Nançay is from 277 K to 283 K in November⁴, the maximum variation ratio of the air temperature is 2.2%. However, Fig. 6.11 shows that the maximum variation of the system gain is 11.4%. If the resistor temperature follows the air temperature (local thermodynamic equilibrium), it can be concluded that the main reason for the variation of the system gain is that the gain of the LNA varies with the temperature, while the contribution of the variation of noise power of the resistor is relatively small:

- Best case: the resistor temperature is stable (e.g. placed in a thermostat), then the variation is only due to the sensitivity of LNA to temperature, the maximum variation of $g(t)$ is 11.4%.
- Worst case: the resistor temperature follows the air temperature completely (e.g. exposed to the air, in local thermodynamic equilibrium), the resistor temperature increases (or decreases) as air temperature increases (or decreases). Thus, the gain decreases (or increases) with the increasement (or decrease) of the temperature. As a result, the maximum variation ratio of $g(t)$ is 13.8%.

The data after system gain calibration can be obtained by dividing the observed data by $G(t, \nu) = g(t)g(\nu)$, which is shown in Fig. 6.12 for auto-correlation data as an example.

6.5 Beam and pointing

Based on the principle of the interferometer described in Sec. 2.6.1 and Sec. 3.1.1, the combined response of channel pair of i -th and j -th is

$$A_{ij}(\vec{s} - \vec{s}_0) = a_i(\vec{s} - \vec{s}_0) \cdot a_j^*(\vec{s} - \vec{s}_0) = \sqrt{A_i(\vec{s} - \vec{s}_0) \cdot A_j(\vec{s} - \vec{s}_0)} \quad (6.8)$$

For a Gaussian beam of Eq. 3.2, and let

$$\frac{1}{\sigma_{ij}^2} = \frac{1}{2} \left(\frac{1}{\sigma_i^2} + \frac{1}{\sigma_j^2} \right) \Rightarrow D_{ij}^2 = \frac{D_i^2 + D_j^2}{2} \quad (6.9)$$

$$\theta_{ij} = \theta_i \left(\frac{\sigma_j^2}{\sigma_i^2 + \sigma_j^2} \right) + \theta_j \left(\frac{\sigma_i^2}{\sigma_i^2 + \sigma_j^2} \right) \Rightarrow \theta_{ij} = \theta_i \left(\frac{D_i^2}{D_i^2 + D_j^2} \right) + \theta_j \left(\frac{D_j^2}{D_i^2 + D_j^2} \right) \quad (6.10)$$

⁴<http://www.meteofrance.com>

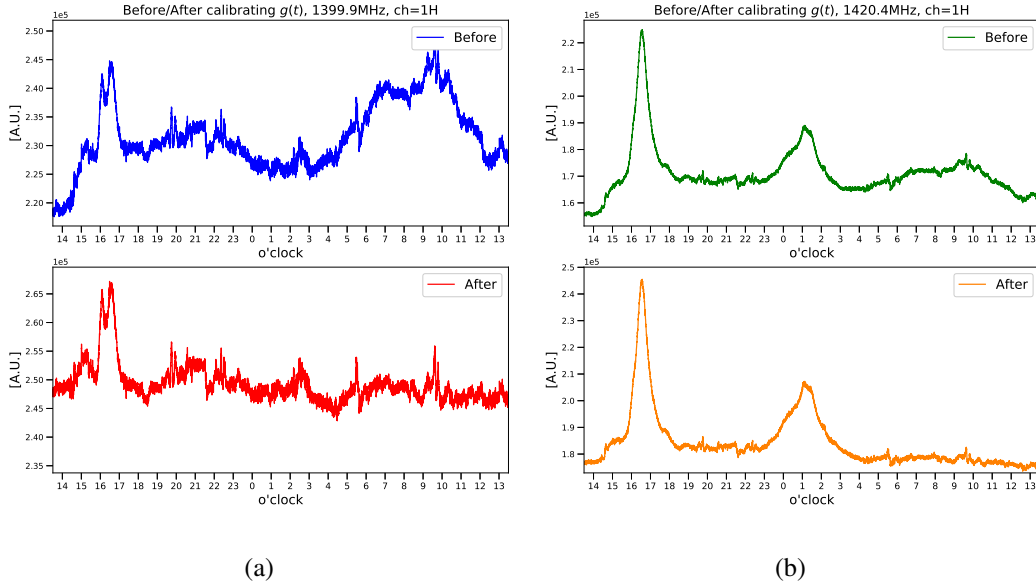


Fig. 6.12 PAON-4 1H auto-correlation data from CygA17nov16, before (top) and after (bottom) gain calibration. Left: signal at 1400 MHz, including mainly the Galactic synchrotron and radio sources (Cygnus A). Right: signal at 1420.4 MHz, due to the Milky Way neutral hydrogen 21-cm emission. The two crossings of the Galactic plane are clearly visible.

the combined response becomes

$$A_{ij}(\theta) = \sqrt{A_{i0}A_{j0} e^{-\frac{(\theta-\theta_i)^2}{2\sigma_i^2} - \frac{(\theta-\theta_j)^2}{2\sigma_j^2}}} = A_{ij0} e^{-\frac{(\theta-\theta_{ij})^2}{2\sigma_{ij}^2}} \quad (6.11)$$

The beam in cross-correlation is the combined beam of two feeds of Eq. (6.11). Solving the system of linear equations can obtain the beams of each feeds. Based on Eq. (6.9), it is obtained

$$\begin{aligned} D_1^2 + D_2^2 &= 2D_{12}^2 \\ D_1^2 + D_3^2 &= 2D_{13}^2 \\ D_2^2 + D_3^2 &= 2D_{23}^2 \\ &\dots \\ D_i^2 + D_j^2 &= 2D_{ij}^2 \end{aligned} \Rightarrow \begin{bmatrix} 1 & 1 & 0 & \dots & 0 & \dots & 0 & \dots \\ 1 & 0 & 1 & \dots & 0 & \dots & 0 & \dots \\ 0 & 1 & 1 & \dots & 0 & \dots & 0 & \dots \\ & & & \dots & & & & \\ 0 & 0 & 0 & \dots & 1 & \dots & 1 & \dots \end{bmatrix} \begin{bmatrix} D_1^2 \\ D_2^2 \\ D_3^2 \\ \dots \\ D_i^2 \\ \dots \\ D_j^2 \\ \dots \end{bmatrix} = 2 \begin{bmatrix} D_{12}^2 \\ D_{13}^2 \\ D_{23}^2 \\ \dots \\ D_{ij}^2 \end{bmatrix} \Rightarrow Ax = B \quad (6.12)$$

The least square estimator of Eq. (6.12) is

$$\hat{x} = [A^T A]^{-1} A^T B \quad (6.13)$$

To obtain the centers of each feed, i.e. the pointing directions of each antennas, let

$$d_{ij}^k = \frac{D_k^2}{D_i^2 + D_j^2} \quad (6.14)$$

then based on Eq. (6.10), it is obtained

$$\begin{aligned} d_{12}^1 \theta_1 + d_{12}^2 \theta_2 &= \theta_{12} \\ d_{13}^1 \theta_1 + d_{13}^3 \theta_3 &= \theta_{13} \\ d_{23}^2 \theta_2 + d_{23}^3 \theta_3 &= \theta_{23} \\ &\dots \\ d_{ij}^i \theta_i + d_{ij}^j \theta_j &= \theta_{ij} \end{aligned} \Rightarrow \begin{bmatrix} d_{12}^1 & d_{12}^2 & 0 & \dots & 0 & \dots & 0 & \dots \\ d_{13}^1 & 0 & d_{13}^3 & \dots & 0 & \dots & 0 & \dots \\ 0 & d_{23}^2 & d_{23}^3 & \dots & 0 & \dots & 0 & \dots \\ & & & \dots & & & & \\ 0 & 0 & 0 & \dots & d_{ij}^i & \dots & d_{ij}^j & \dots \end{bmatrix} \begin{bmatrix} \theta_1 \\ \theta_2 \\ \theta_3 \\ \dots \\ \theta_i \\ \dots \\ \theta_j \\ \dots \end{bmatrix} = \begin{bmatrix} \theta_{12} \\ \theta_{13} \\ \theta_{23} \\ \dots \\ \theta_{ij} \\ \dots \end{bmatrix} \quad (6.15)$$

Similarly, the best-fit of θ_i , i.e. the antenna pointings, can be obtained by solving Eq. (6.15).

6.5.1 Antenna pointing

Eq. (6.15) gives the direction of each channel obtained from cross-correlation data. The direction of each feed can also be obtained by fitting the peak position of bright source in the auto-correlation data. However, because of the significant effect of the system gain variation on the auto-correlation data and the diffuse emission around the bright source is nonuniform, the peak position in auto-correlation might be different from the real source position.

The top panel of Fig. 6.13 shows the estimated peak positions in auto-correlation of each of the four H-polarization feeds, and the other subfigures show the centers of each feeds obtained by solving the system of linear equations of cross-correlation data, The theoretical calculation shows that Cygnus A should reach the zenith at 962.6 minute (UTC), however from the auto-correlation or cross-correlation data the time is 963–965 minute. It means that each feed is westward by a small angle, about 0.2° – 0.6° (spherical center angle).

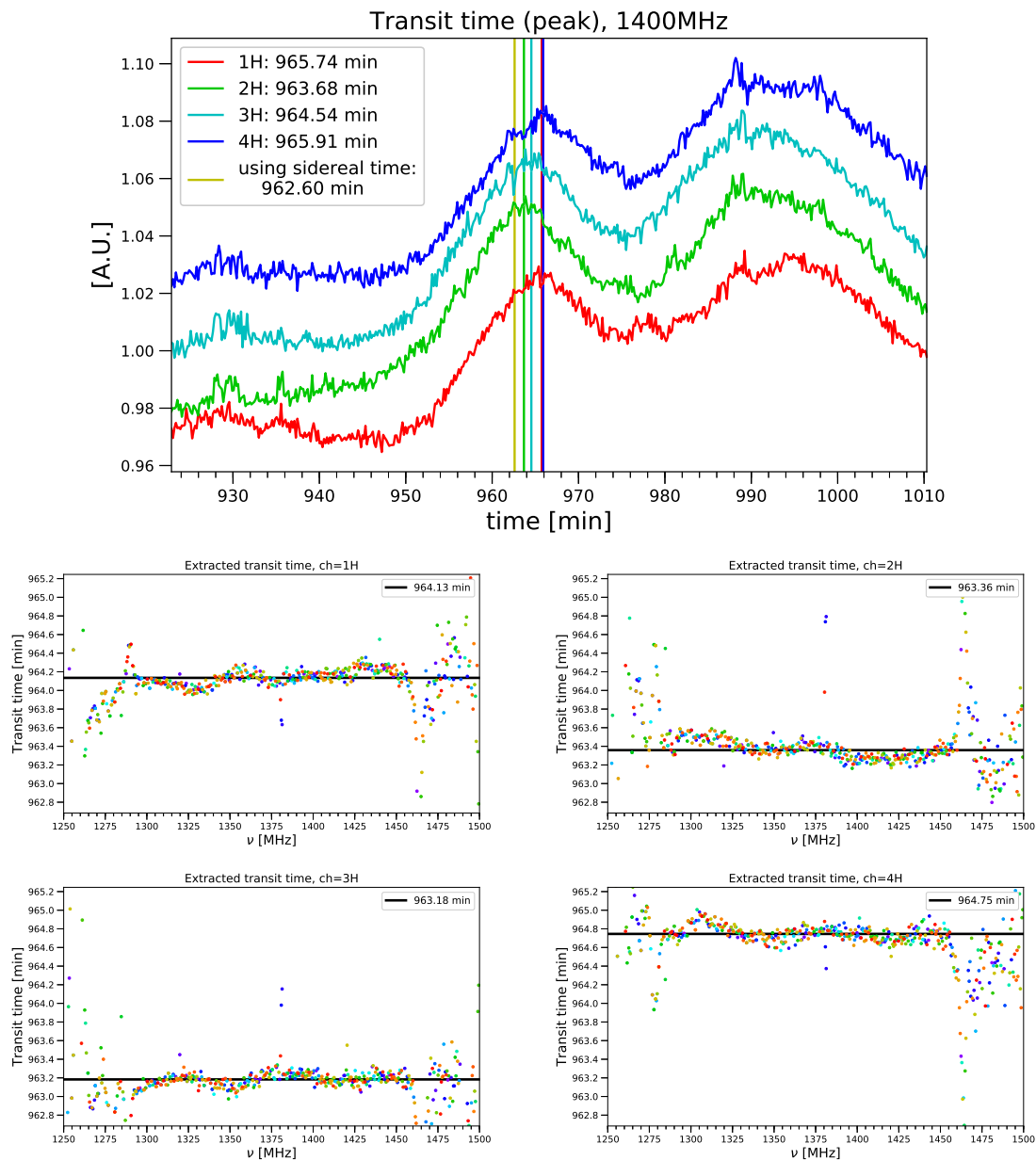


Fig. 6.13 Top: Auto-correlation visibilities as a function of time for the four H-polarisation feeds. The source transit times, corresponding to Cygnus A going through the beam center, determined from auto-correlations is also shown on the graph. Bottom: source (Cygnus A) transit time, as a function of frequency, determined by solving the linear system of equations from H-polarization cross-correlation visibilities.

6.5.2 Effective diameter

Fig. 6.14 shows the auto-correlation and the norm of cross-correlation visibilities, for 1H and 1H-2H channels respectively, at 1400 MHz. Because there is a large star-forming region the Cygnus X near and affects the peak of Cygnus A in auto-correlation, it is difficult to judge the true position of the peak of Cygnus A. In addition, due to the nonuniform distribution of the diffuse emission, it also affects the true peak position of Cygnus A in the auto-correlation data. However, in the cross-correlation data, because the cross-correlation of the diffusion emission from different line of sights is weak, and the cross-correlation of the star-forming region the Cygnus X is much weaker than that of Cygnus A, a single peak is visible, the peak position of Cygnus A can be determined easily in cross-correlation. Therefore, we use cross-correlation data to calibrate the antenna beam.

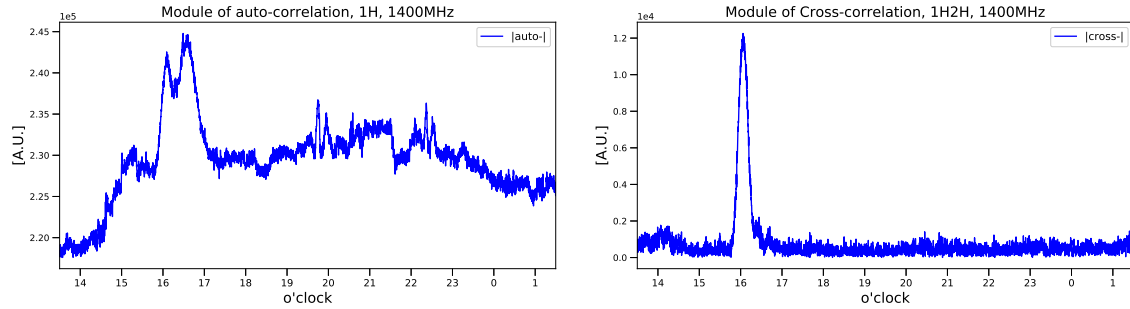


Fig. 6.14 Left: auto-correlation data of channel 1H at 1400 MHz, the peak at around 16 o'clock is produced by Cygnus A, while the one around 16:30 is produced by the star-forming region the Cygnus X, they are close and affect each other. Right: norm of 1H-2H cross-correlation data, the cross-correlation of the diffuse emission as well as the Cygnus X is much smaller than that of the Cygnus A, the peak of Cygnus A is clear and nearly unaffected by Cygnus X and diffuse emissions.

For the Cygnus A, because its angular size is much smaller than the antenna beam and its brightness is much higher than the surrounding area, it can be treated as a point source of $I(\vec{s}) = I_0 \delta(\vec{s} - \vec{s}_0)$. Thus, the norm of Eq. (6.11) can be written as

$$|V_{ij}(\theta)| = I_0 A_{ij0} e^{-\frac{\lambda^2 (\theta - \theta_{ij})^2}{2.618 D_{ij}^2}} \quad (6.16)$$

For each baseline (or feed pair), $\theta_{ij}(\nu)$ and $D_{ij}(\nu)$ for each frequency channel ν can be obtained by fitting Eq. (6.16) to the time dependent cross-correlation visibility. Fig. 6.15 shows the results from the Gaussian function fitting, and Fig. 6.16 shows the effective diameter of each feed obtained by solving the system of linear equations of Eq. (6.12). The

average effective diameter of PAON-4 is 4.2 m, corresponding to a receiving area efficiency of 70%.

Channel	1H	2H	3H	4H		
D_{eff} [m]	4.223	4.112	4.228	4.357		
Channel	1H2H	1H3H	1H4H	2H3H	2H4H	3H4H
D_{eff} [m]	4.168	4.226	4.291	4.170	4.236	4.293

Table 6.1 Effective diameters of each channels.

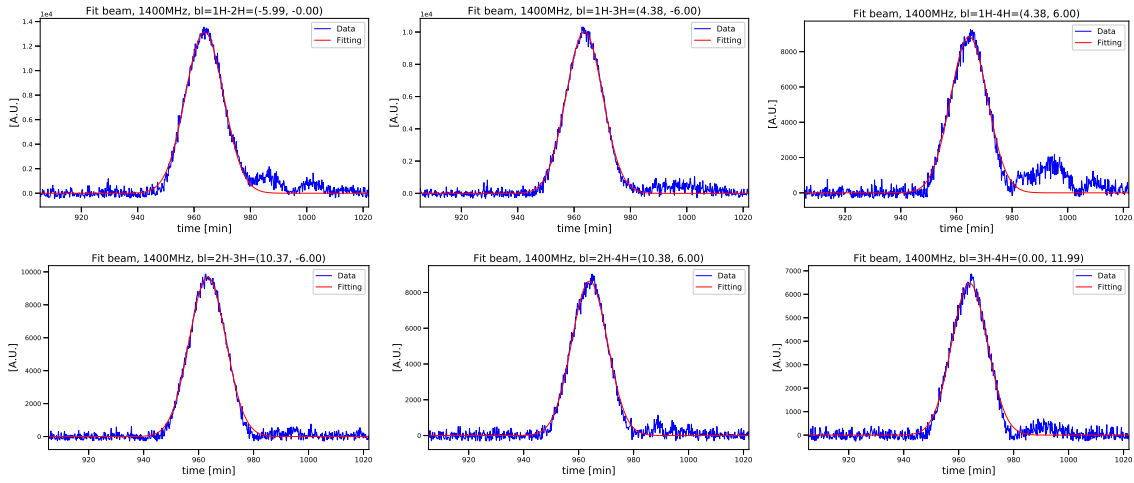


Fig. 6.15 Gaussian fit to cross-correlation visibilities $|V_{ij}(t)|$ at $\nu = 1400$ MHz for the six PAON-4 baselines, for the H-polarisation feeds.

6.6 Phase calibration

Consider two coordinate systems, the equatorial coordinate system (X, Y, Z) , and the local rectangular coordinate system (x, y, z) . For the (X, Y, Z) system, the origin point is the center of the Earth, XY plane is the Earth equator plane, $+X$ points toward RA(RightAscension) = 0, Z -axis is the rotation axis of the Earth pointing and $+Z$ points toward the celestial north pole. For the (x, y, z) system, xy plane is the horizontal plane parallel to the local ground, $+x$ points toward the local east, $+y$ points toward the local north, and $+z$ points toward the zenith. Assuming a coplanar antenna array, with all feeds at the same vertical coordinate of $z = 0$, the baseline vector $\vec{r}_{ij} = \vec{r}_j - \vec{r}_i$ and the unit direction vector \vec{s} are

$$\vec{r}_{ij} = (x_j - x_i, y_j - y_i, z_j - z_i = 0) \equiv (x, y, z = 0) \quad (6.17)$$

$$\vec{s} = (90^\circ - \delta, \alpha) = (X = \cos \delta \cos \alpha, Y = \cos \delta \sin \alpha, Z = \sin \delta) \quad (6.18)$$

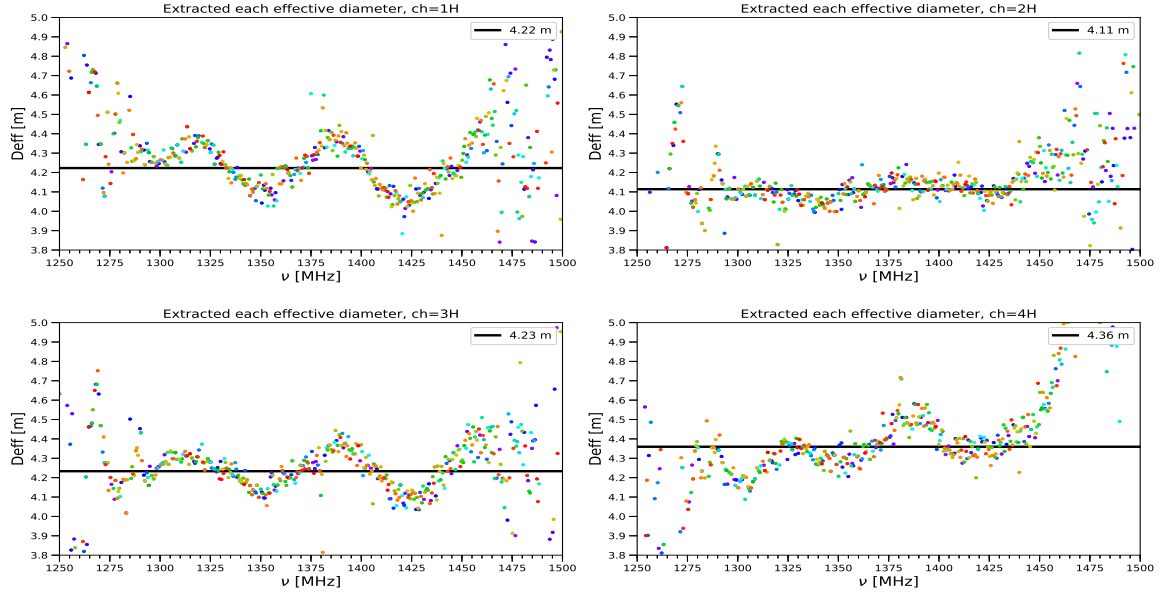


Fig. 6.16 Effective dish diameters for the four PAON4 H-polarisation feeds, obtained by solving the system of linear equations Eq. (6.12), after determination of $D_{ij}(\nu)$ from a Gaussian fit to cross-correlation visibilities $|V_{ij}(t)|$, as a function of frequency. The sine like oscillation in the effective dish diameter as a function of frequency might be due to standing waves between the feed and reflector.

where α is the longitude and δ is the latitude in the equatorial coordinate system.

The antenna array is located at a latitude of d on the Earth, and the local meridian is at a longitude of α_0 at some time, thus the coordinate of \vec{r}_{ij} on the equatorial coordinate system is

$$\begin{bmatrix} X_r \\ Y_r \\ Z_r \end{bmatrix} = \begin{bmatrix} -\sin \alpha_0 & -\cos \alpha_0 & 0 \\ \cos \alpha_0 & -\sin \alpha_0 & 0 \\ 0 & 0 & 1 \end{bmatrix} \begin{bmatrix} 1 & 0 & 0 \\ 0 & \sin d & -\cos d \\ 0 & \cos d & \sin d \end{bmatrix} \begin{bmatrix} x \\ y \\ 0 \end{bmatrix} = \begin{bmatrix} -x \sin \alpha_0 - y \sin d \\ x \cos \alpha_0 - y \sin \alpha_0 \sin d \\ y \cos d \end{bmatrix} \quad (6.19)$$

Then it is obtained

$$\begin{aligned} \vec{r}_{ij} \cdot \vec{s} &= (-x \sin \alpha_0 - y \sin d, x \cos \alpha_0 - y \sin \alpha_0 \sin d, y \cos d) \cdot (\cos \delta \cos \alpha, \cos \delta \sin \alpha, \sin \delta) \\ &= x \cos \delta \sin(\alpha - \alpha_0) - y \cos \delta \sin d \cos(\alpha - \alpha_0) + y \sin \delta \cos d \\ &= x \cos \delta \sin \alpha - y \cos \delta \sin d \cos \alpha + y \sin \delta \cos d \end{aligned} \quad (6.20)$$

For the interference fringes, due to the angle $\phi = \alpha - \alpha_0$ is small for PAON-4 (i.e. $\cos \phi \approx 1$), Eq. (6.20) becomes

$$\vec{r}_{ij} \cdot \vec{s} \approx x \cos \delta \sin \phi + y \sin(\delta - d) \quad (6.21)$$

The phase Φ_{ij} of the complex number of visibility can then be determined

$$\begin{aligned} V_{ij} = I_0 A_{ij0} e^{i \frac{2\pi}{\lambda} \vec{r}_{ij} \cdot \vec{s}} &\Rightarrow V_{ij}^{\text{real}} = I_0 A_{ij0} \cos \left(\frac{2\pi}{\lambda} \vec{r}_{ij} \cdot \vec{s} \right), \quad V_{ij}^{\text{imag}} = I_0 A_{ij0} \sin \left(\frac{2\pi}{\lambda} \vec{r}_{ij} \cdot \vec{s} \right) \\ &\Rightarrow \frac{V_{ij}^{\text{imag}}}{V_{ij}^{\text{real}}} = \tan \left(\frac{2\pi}{\lambda} \vec{r}_{ij} \cdot \vec{s} \right) \\ &\Rightarrow \Phi_{ij} = \frac{2\pi}{\lambda} \vec{r}_{ij} \cdot \vec{s} = \arctan \left(\frac{V_{ij}^{\text{imag}}}{V_{ij}^{\text{real}}} \right) \end{aligned} \quad (6.22)$$

In a realistic observation, an extra phase, the instrumental phase, $\Delta\Phi_{ij}(\lambda)$ is introduced due to differences in cable lengths, analog electronics, etc. Thus, the phase of the realistic observational data is

$$\Phi_{ij}(\lambda) = \Delta\Phi_{ij}(\lambda) + \left(\frac{2\pi}{\lambda} \right) (x \cos \delta \sin \alpha - y \cos \delta \sin d \cos \alpha + y \sin \delta \cos d) \quad (6.23)$$

Usually the extra phase $\Delta\Phi_{ij}(\lambda)$ is a linear function of frequency. As ϕ is small, $(-y \cos d \sin \delta \cos \phi + y \sin d \cos \delta)$ is closed to a constant, making the North-South coordinate y difficult to be fitted by Eq. (6.23). In fact, because the angle between antenna pointing and the zenith is small, the variation of y term affects slightly on the fringe. Therefore, we treat y term as a constant during fitting.

The phase periodicity needs to be addressed when fitting the phase Φ_{ij} , i.e. $V(\Phi = 360^\circ) = V(\Phi = 0^\circ)$. One method is to shift the phase data into a straight line, this method is applicable only when the quality of the data is good and the signal-to-noise ratio is high. If the quality of the data is not good enough, the fitting may fail due to the misidentification of the break point from 360° to 0° . Another more appropriate method is to fit the trigonometric function so that the break point from 360° to 0° can be converted to be continuous, e.g. fit the complex phase $\cos(\Phi_{ij}) + i \sin(\Phi_{ij})$ (Fig. 6.17) or directly fit the visibility data (Fig. 6.18).

Fig. 6.19 shows the fitted lengths of East-West baselines, and Fig. 6.20 shows the fitted extra phase $\Delta\Phi_{ij}$ as a function of frequency, and its linear fitting with frequency is shown in Fig. 6.22. A phase closure checking $\Delta\Phi_{ij} = \Delta\Phi_{ik} + \Delta\Phi_{kj}$ is also carried out, and is shown in Fig. 6.21.

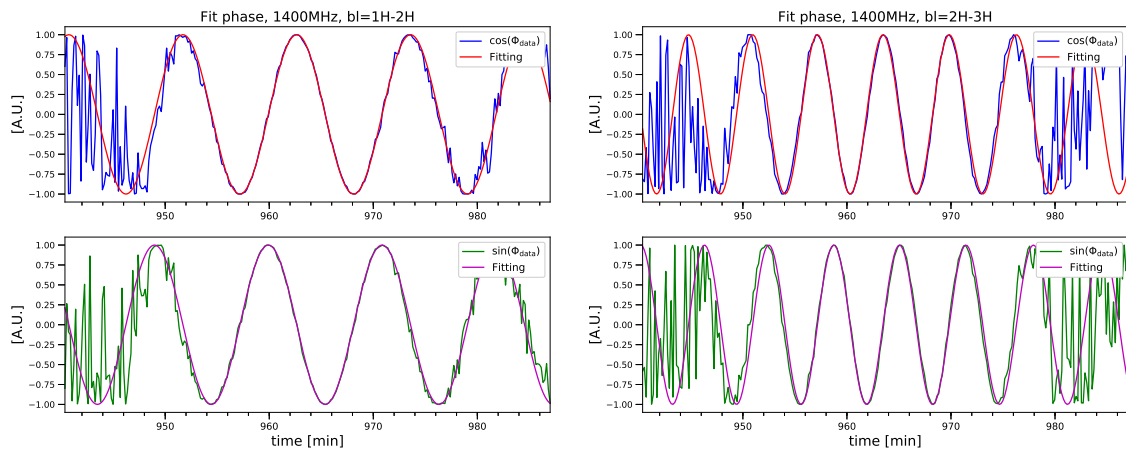


Fig. 6.17 Fitting the complex phase by the trigonometric function of $\cos(\Phi_{ij}) + i\sin(\Phi_{ij})$.

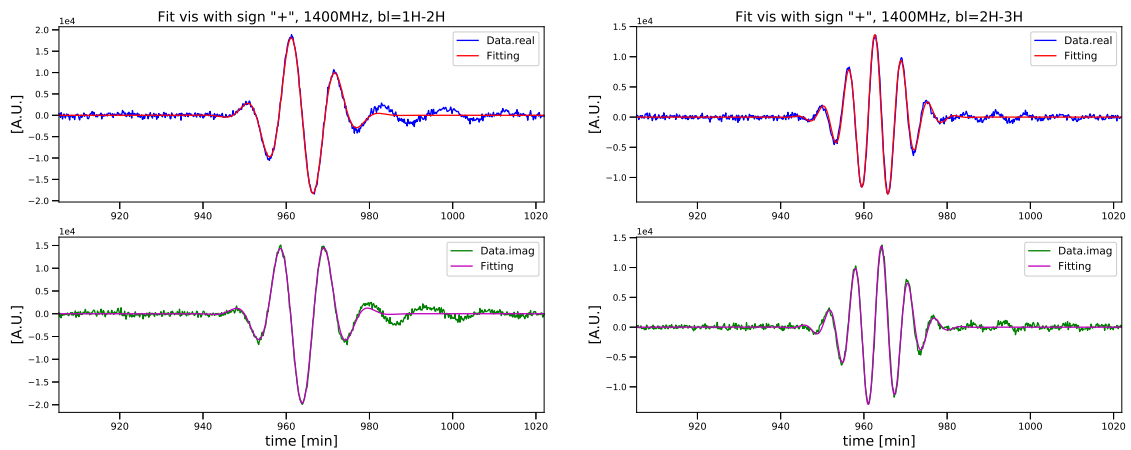


Fig. 6.18 Fitting directly the real (top) and imaginary (bottom) part of the time dependent visibility $V_{ij}(t)$, at 1400 MHz. Baseline 1H-2H (left) and 2H-3H (right) are shown as an example.

Based on the extra phase fitted, the equivalent length difference of the cables can be computed. If the velocity of propagation of electrical signal in the cable (or wire) is v_s , the slope k_s of $\Delta\Phi_{ij}$ is related to the difference of cable lengths by

$$k_s \cdot v = \frac{2\pi v}{v_s} \Delta L_{ij} \quad \Rightarrow \quad \Delta L_{ij} = \frac{k_s v_s}{2\pi} \quad (6.24)$$

where $\Delta L_{ij} = L_j - L_i$ is the length difference of cables of two channels, $\Delta L_{ij} > 0$ means the length of i -th cable is longer than the j -th. The velocity factor, which is the ratio of the velocity of propagation in the medium to the speed of light in a vacuum, is typically between 0.5 to 0.8 for the cable. However, we should note that the digital delay between different FPGA's may be responsible for most of the observed delays. For PAON-4, the delay is usually 2–8 ns.

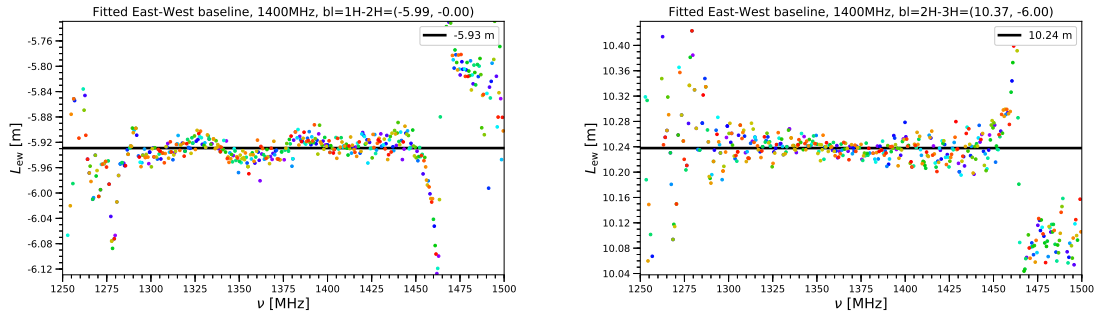


Fig. 6.19 The fitted lengths of East-West baselines, as a function of frequency, for 1H-2H (left) and 2H-3H (right) baselines.

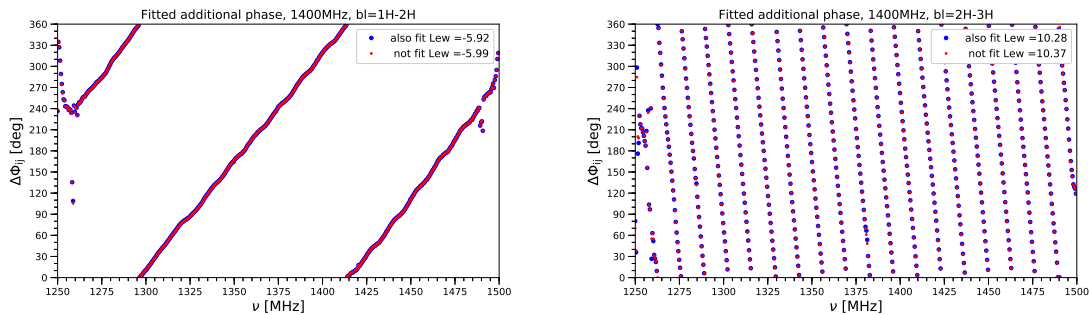


Fig. 6.20 The fitted extra phase as a function of frequency.

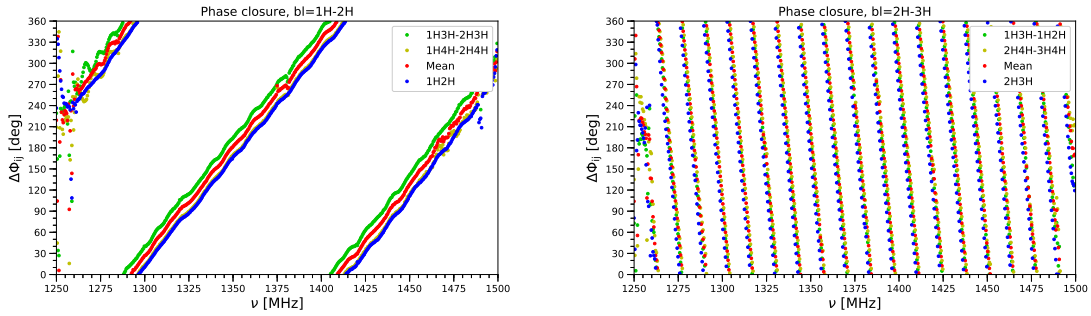


Fig. 6.21 Phase closure checking.

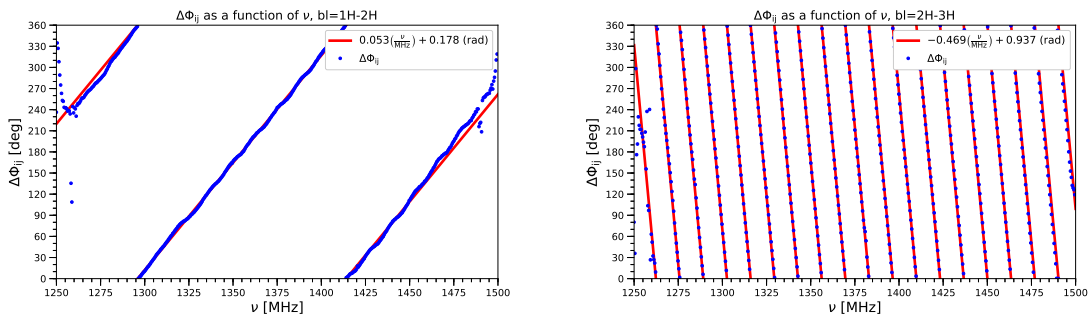


Fig. 6.22 Linear variation of the instrumental phase $\Delta\Phi_{ij}$ with frequency, for 1H-2H (left) and 2H-3H (right) baselines.

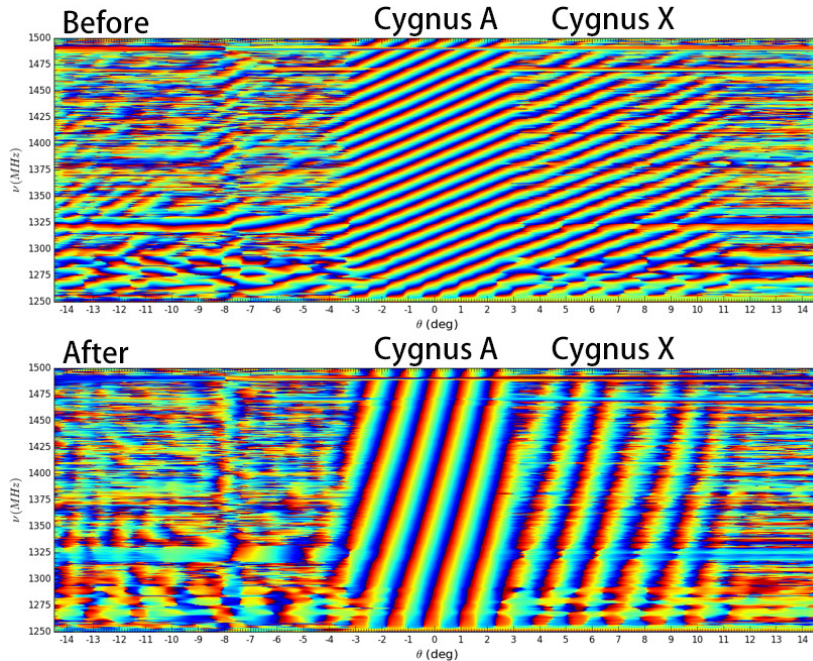


Fig. 6.23 The phase before (top) and after (bottom) the calibration. Two sources in the image have strong cross-correlation, one is Cygnus A, the other is Cygnus X which is a active star-forming region near Cygnus A.

6.7 Flux calibration

6.7.1 Standard calibrator

The widely used standard calibrators at \sim GHz bands are the strong radio sources Cassiopeia A, Cygnus A, Taurus A (Crab Nebula) and Virgo A listed in [22], with an absolute accuracy of about 5%. However, Cassiopeia A and Taurus A are supernova remnants that are still expanding and the flux fading. Cassiopeia A had an average fading rate of $0.97(\pm 0.04) - 0.30(\pm 0.04) \log \frac{\nu}{\text{GHz}}$ %/yr in the frequency range of 20 MHz to 30 GHz according to the observations between 1949 and 1976 [22, 92]. More recent observations (until 2010s) shows that Cassiopeia A faded at an average rate of 0.670 ± 0.019 %/yr in L band (\sim GHz) and Taurus A 0.102 ± 0.042 %/yr [246, 207]. Thus, Cygnus A, which is a radio galaxy 600 Mly away with two incredible jets emanating from an AGN, is more often cited for the calibration [22].

However, the above four sources have angular sizes of several arcminutes, making them not suitable for the modern interferometer with high resolution. Some compact sources, such as 3C196, 3C286 and 3C295, have been used as the calibrators for VLA (Very Large Array)⁵ [188, 189], from 50 MHz to 50 GHz.

For PAON-4, given the lower resolution of an order of degree and that the sensitivity is not very high, and the observational region is centered at Dec $\sim 40^\circ$, we select the Cygnus A as our flux calibrator. Fig. 6.24 shows the flux density of the three standard calibrators varying with the frequency [22], with fading for Cas A and Tau A, and Tab. 6.2 shows the flux densities of the standard calibrators at some frequencies predicted by the polynomial fitting.

ν [MHz]	Cassiopeia A [Jy]	Cygnus A [Jy]	Taurus A [Jy]
10	22340	13335	5088
408	5658	5208	1260
750	3504	2913	1109
1400	2085	1590	933
1420	2063	1569	931
2300	1438	930	778
10000	427	221	526

Table 6.2 The flux densities of Cygnus A, Cassiopeia A and Taurus A at some frequencies predicted by the polynomial fitting.

⁵<https://science.nrao.edu/facilities/vla/observing/callist>

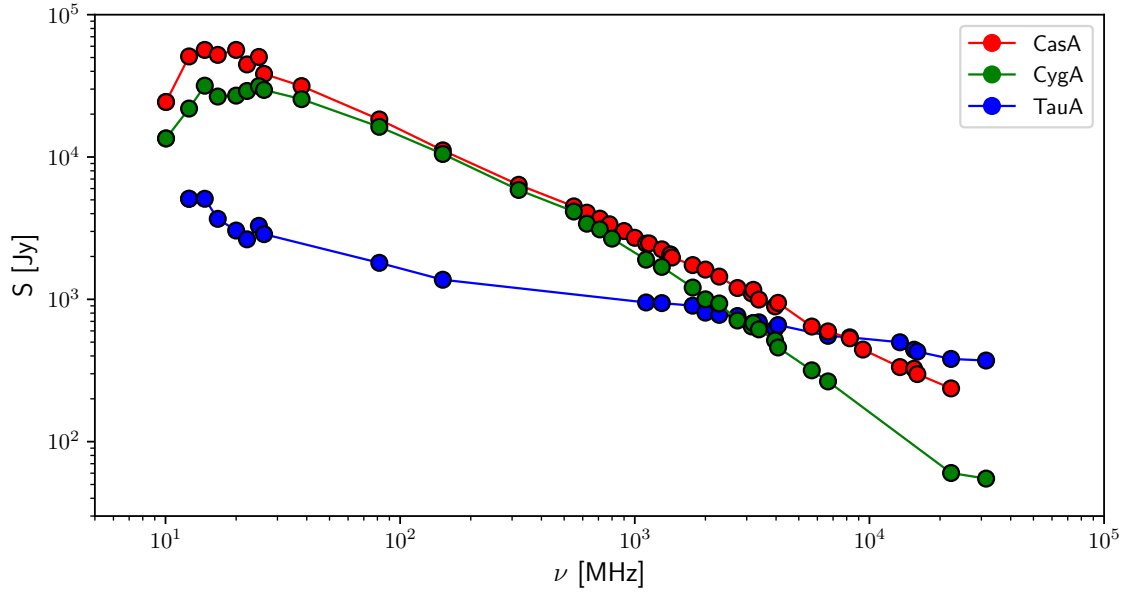


Fig. 6.24 Flux densities of Cassiopeia A (red), Cygnus A (green) and Taurus A (blue) as a function of frequency, adapted from reference [22], with fading for Cas A and Tau A.

The brightness temperature of a radio source can be calculated if the antenna beam is known. Considering a Gaussian beam (Eq. 3.2), the solid angle can be computed by

$$\Omega(\theta_{\text{fwhm}}) = 2\pi \int_0^\pi e^{-4\ln 2 \left(\frac{\theta}{\theta_{\text{fwhm}}}\right)^2} \sin \theta \, d\theta \approx 1.133\theta_{\text{fwhm}}^2 \quad (6.25)$$

and the result is shown in Fig. 6.25.

For a blackbody, the intensity is expressed by Planck's law [45]

$$I_\nu = \frac{2h\nu^3}{c^2} \frac{1}{e^{\frac{h\nu}{k_B T}} - 1} \quad (6.26)$$

In radio band, i.e. $h\nu \ll k_B T$, $I(\nu)$ can be approximately expressed by Rayleigh-Jeans law [192]

$$I_\nu = \frac{2\nu^2 k_B T}{c^2} \quad (6.27)$$

Since the angular size of radio source is much smaller than the antenna beam (point source assumption), an approximate relationship can be obtained

$$I_\nu \equiv \frac{\partial S_\nu}{\partial \Omega} \approx \frac{S_\nu}{\Omega} \quad (6.28)$$

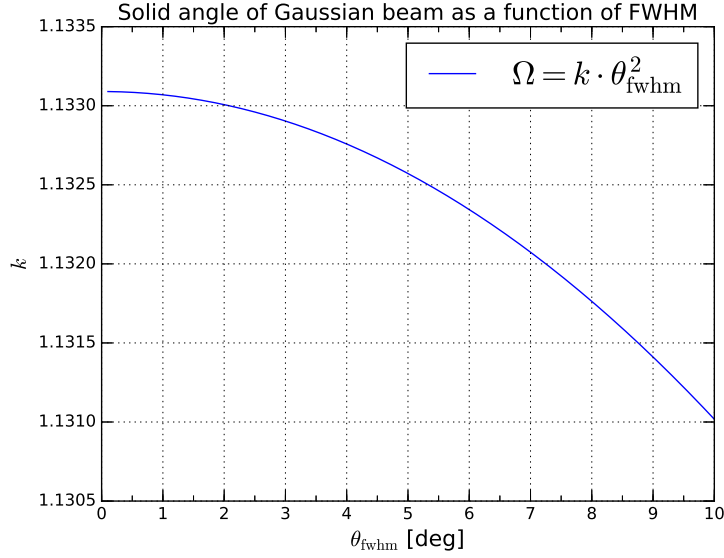


Fig. 6.25 The solid angle of Gaussian beam as a function of FWHM resolution.

For a Gaussian beam, the relationship between the flux density and the bright temperature is

$$\frac{T_b}{\text{K}} \approx 3.1 \times 10^{-4} \left(\frac{S_v}{\text{Jy}} \right) \left(\frac{D_{\text{eff}}}{\text{m}} \right)^2 \quad (6.29)$$

For PAON-4 with effective diameter of $D_{\text{eff}} = 4.2$ m, the brightness temperature can be estimated by

$$\frac{T_b^{\text{PAON4}}}{\text{K}} = 5.4 \times 10^{-3} \frac{S_v}{\text{Jy}} \quad (6.30)$$

For example, for Cygnus A with 1590 Jy at 1400 MHz, one could get a maximum antenna temperature increase ~ 8.6 K.

6.7.2 Data noise

The relationship between the variances of noise of auto-correlation data and cross-correlation data can be used to perform the amplitude calibration. Here we simply introduce the conclusion, for the detail, please see Appendix B.

Assuming the input noises of two channels are white Gaussian noise X and Y and in the auto-correlation data, the auto-correlations of the input noises are \mathbf{A}_X and \mathbf{A}_Y , respectively. In cross-correlation data of these two channels, the cross-correlation of the input noises is

C_{XY} . The noise of auto-correlation data is a random variable of A_X with a standard deviation of σ_{A_X} . Similarly, the standard deviation of the noise of cross-correlation data is $\sigma_{C_{XY}}$.

The relationship between σ_{A_X} and $\sigma_{C_{XY}}$ is (see Appendix B for detail)

$$2\sigma_{C_{XY}}^2 = \sigma_{A_X} \sigma_{A_Y} = 2\sigma_X^2 \sigma_Y^2 / n \quad (6.31)$$

where n is the number of elements of the random variable.

Fig. 6.26 shows the ratio of $\frac{\sigma_{A_X} \sigma_{A_Y}}{2\sigma_{C_{XY}}^2}$ of the PAON-4 data. It can be seen that the ratios of each channel pairs are close to 1, which is consistent with Eq. (6.31).

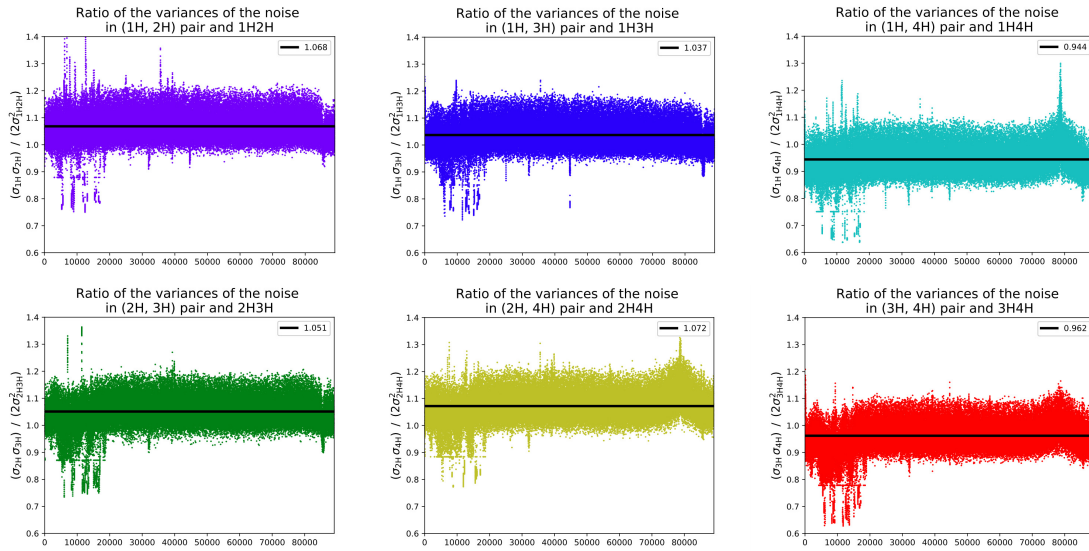


Fig. 6.26 The ratio of $\frac{\sigma_{A_X} \sigma_{A_Y}}{2\sigma_{C_{XY}}^2}$ of PAON-4 data, which is close to 1.

As we can see in Sec. 6.2 and Sec. 6.5, the diffuse emission affects in a much weaker level the cross correlation than the auto-correlation during a bright source transit. Therefore, once the amplitude of cross-correlation data is calibrated using the standard calibrators, based on the relationship described in Eq. (6.31), the amplitude of auto-correlation data can be then calibrated. In addition, if auto-correlation data and cross-correlation data are calibrated independently, Eq. (6.31) can be used to check the calibration results.

6.7.3 Flux calibration on cross-correlation

We use Cygnus A to calibrate the flux of cross-correlation of PAON-4 data. We have estimated the effective diameters of each channels in Sec. 6.5.2, and the expected flux densities of Cygnus A at different frequencies can be found in Sec. 6.7.1; According to the conversion

formula of Eq. (6.29) from flux density to brightness temperature, the brightness temperature of Cygnus A for PAON-4 amplitude calibration for each channels is listed in Tab. 6.3 (here only list the frequencies of 1400 MHz and 1420.4 MHz as an example). Due to the different effective diameters of each reflector, we obtain different values for the expected brightness temperatures of Cygnus A for each baseline (feed pair).

	1400 MHz	1420.4 MHz
1H2H	8.61 K	8.51
1H3H	8.86	8.75
1H4H	9.12	9.00
2H3H	8.61	8.51
2H4H	8.91	8.80
3H4H	9.16	9.05

Table 6.3 The brightness temperature of Cygnus A at two frequencies of 1.4 GHz and 1420.4 MHz. Due to the different effective diameters of each channels, the brightness temperatures of Cygnus A in each channels are different in the unit of Kelvin.

Fig. 6.27 shows the amplitude calibrated cross-correlation data of PAON-4 (at 1400 MHz as an example).

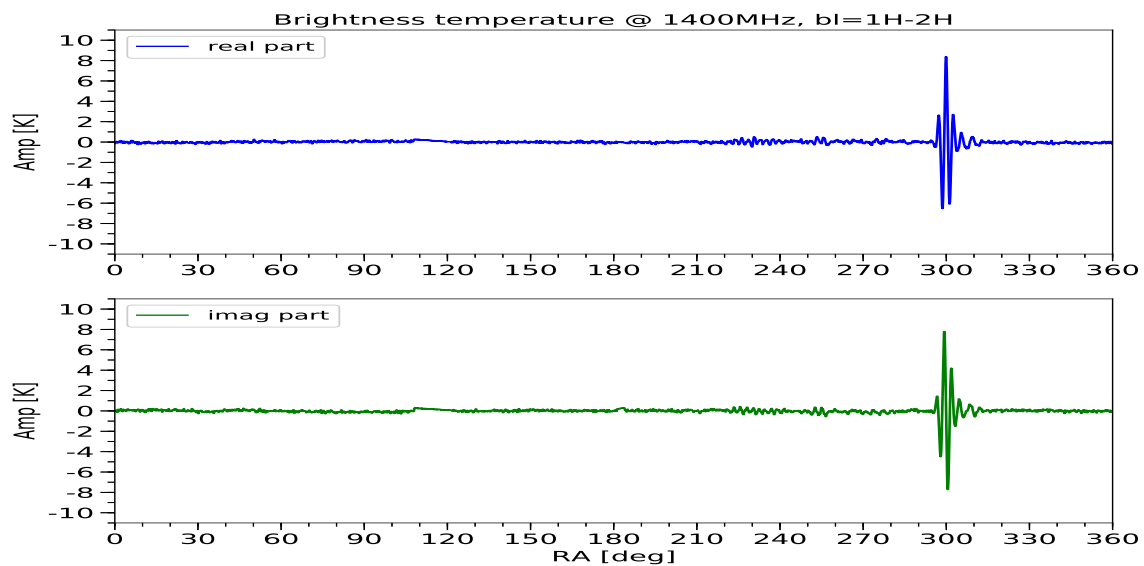


Fig. 6.27 Cross-correlation data of channel 1H-2H at 1400 MHz after amplitude calibration, Horizontal axis correspond to time converted into right ascension, and vertical axis in the brightness temperature in Kelvin. Top and bottom panels are for real part and imaginary part, respectively.

6.7.4 Flux calibration on auto-correlation

In auto-correlation data, the sky radiation around the bright source is nonuniform, the lower PAON-4 angular resolution makes the bright source signal less significant. In addition, the image of the bright source is distorted by the radiation of the surrounding sky in auto-correlation, which is no longer the shape of the antenna beam, leading to difficulty calibrating the amplitude of auto-correlation data.

Here we use two methods to calibrate the amplitude of auto-correlation signals, one is based on the observed Galactic 21-cm emission from the LAB survey (Leiden/Argentine/Bonn Survey [141]) and the radio sky model described in Sec. 3; the other is based on the data noise properties described above in Sec. 6.7.2.

Using sky maps

For the simulation sky map, we use our SSM (Self-consistent Sky Model) [130], which is a model available from 10 MHz to 2.3 GHz. SSM can generate a whole sky map, containing diffuse (synchrotron + free-free) emission and radio sources, at a high-resolution up to 1 arcminute. Refer to Sec. 3 for a detailed description of SSM.

For the Galactic neutral hydrogen 21-cm emission at 1420.4 MHz, we use the LAB survey data [141]. The LAB survey obtained the entire sky map by merging the Leiden/Dwingeloo Survey (LDS) of the sky north of -30° [123] with the Instituto Argentino de Radioastronomia Survey (IAR) of the sky south of -25° [14, 23]. The angular resolution of the LAB data is $\sim 0.6^\circ$ and with a spectral resolution of 1.3 km/s.

Due to the angular resolution of single dish of PAON-4 at 1400–1420.4 MHz is $\sim 3^\circ$, the angular resolutions of the sky maps of SSM and LAB are reduced to match the PAON-4, the corresponding sky maps are shown in Fig. 6.28.

PAON-4 is a drift scan interferometer scanning the sky as the Earth rotating. The scan at the latitude of Dec = $+40.733^\circ$ which Cygnus A locates at is first calibrated. Here we assume that the calibration is stable over a few days, then the calibration results can be applied to the other PAON-4 data collected in several close days.

Fig 6.29 shows the scans of SSM+LAB which are used to calibrate the PAON-4 auto-correlation data, at the latitude of Dec = $+40.733^\circ$. Here only the figures at 1400 MHz and 1420.4 MHz are shown as an example, the corresponding frequency resolution is 0.488 MHz and FWHM resolution is $\sim 3^\circ$. The calibrated PAON-4 auto-correlation data is shown in Fig. 6.30.

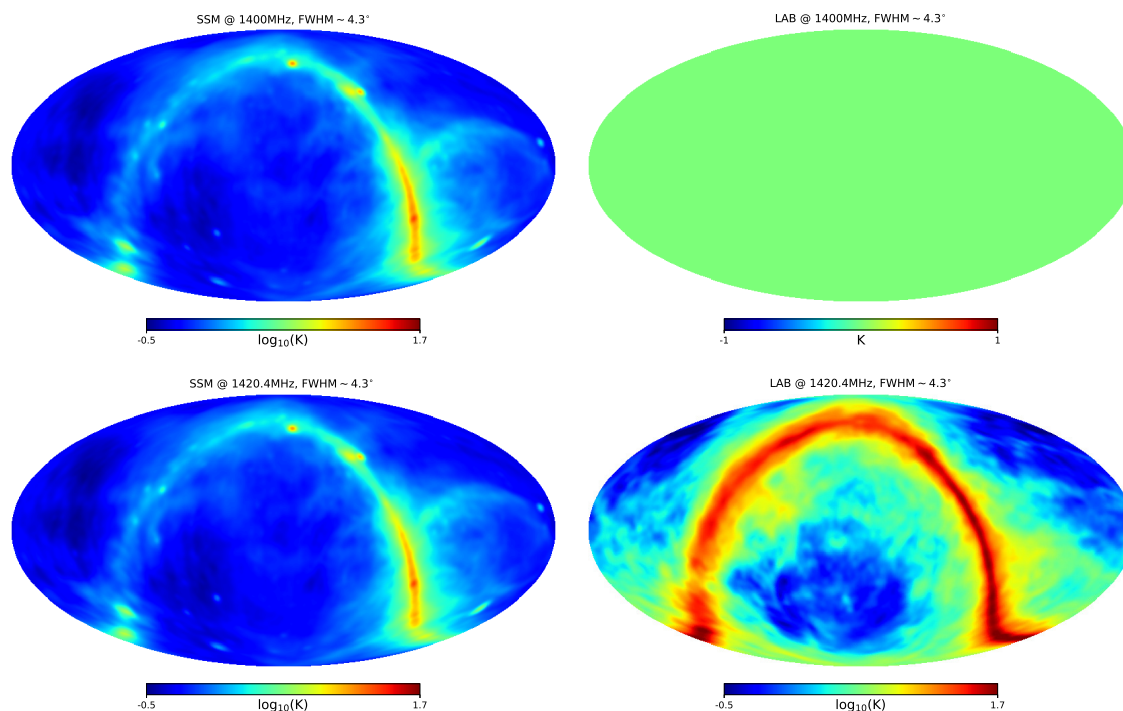


Fig. 6.28 Left and right columns are the maps of SSM and LAB, up and down panels are at 1400 MHz and 1420.4 MHz, respectively. The angular resolutions of the maps are $\sim 3^\circ$.

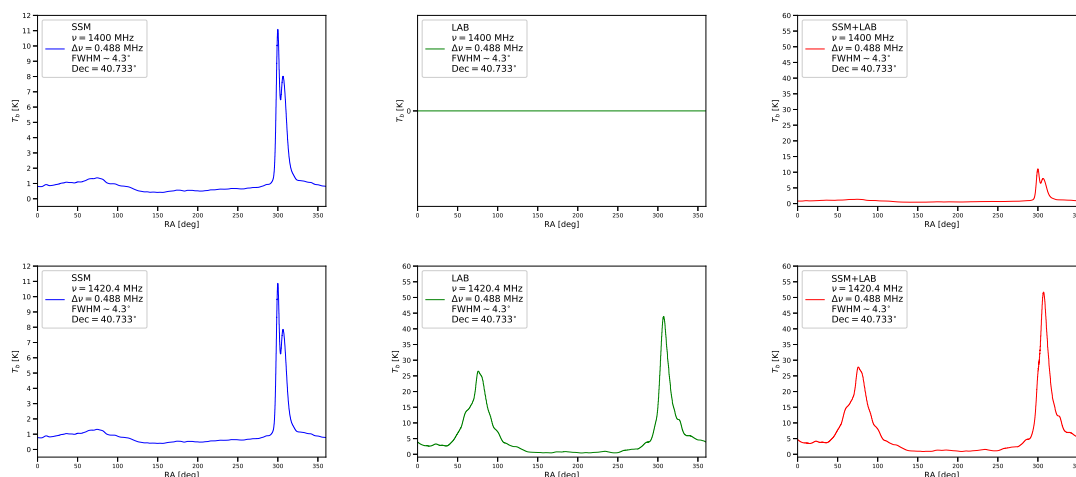


Fig. 6.29 The scans of SSM+LAB which are used to calibrate the PAON-4 auto-correlation data, at the declination $\delta = +40.733^\circ$, with a frequency resolution of 0.488 MHz and an angular resolution of $\sim 4.3^\circ$. Up and down panels are the scans at 1400 MHz and 1420.4 MHz respectively. From left to right columns are SSM, LAB, SSM+LAB (total temperature). Horizontal axis is RA from 0° to 360° , vertical axis is brightness temperature, 0 to 12 K for the left panels, and 0 to 60 K for the center and right panels.

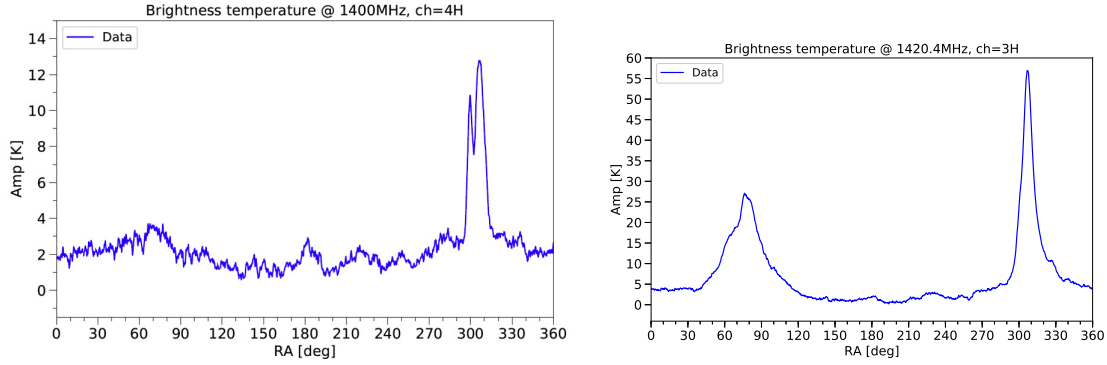


Fig. 6.30 The calibrated PAON-4 auto-correlation data for the scan at declination $\delta = +40.733^\circ$. Left and right figures are at 1400 MHz and 1420.4 MHz, respectively.

Using data noise

As we have described in Sec. 6.7.2, the computed visibility data fluctuation variances due to the noise is used for the following three goals:

1. Calibrating auto-correlation signals: after calibrating the cross-correlation amplitudes using the standard calibrators (CygnusA here), we use Eq. (6.31) to calibrate the auto-correlation data. This equation describes the relationship between the variances of noise in auto-correlation data and cross-correlation data.
2. If the auto-correlation data is calibrated by using the sky maps described in Sec. 6.7.4, Eq. (6.31) can be used to check the amplitude calibration results between the auto- and cross-correlation, as the cross-correlation data is calibrated in a different way from the auto-correlation.
3. The data noise can also be used to estimate the system temperature, based on the assumption that the noise is almost Gaussian. Please see Sec. 6.8 for more information.

The data noise of each auto-correlation channel can be obtained by solving the equation system. The system of equations of the standard deviation of noise in each cross-correlation data and the corresponding auto-correlation data is set up as follows:

$$\begin{cases} \sigma_1 \sigma_2 = 2\sigma_{12}^2 \\ \sigma_1 \sigma_3 = 2\sigma_{13}^2 \\ \sigma_1 \sigma_4 = 2\sigma_{14}^2 \\ \sigma_2 \sigma_3 = 2\sigma_{23}^2 \\ \sigma_2 \sigma_4 = 2\sigma_{24}^2 \\ \sigma_3 \sigma_4 = 2\sigma_{34}^2 \end{cases} \quad (6.32)$$

where σ_i denotes the standard deviation of noise in auto-correlation data of i -th channel, where σ_{ij} denotes the standard deviation of noise in cross-correlation data of i -th and j -th channels.

Eq. (6.32) can be written in a matrix formalism

$$\mathbf{A}\mathbf{x} = 0 \quad (6.33)$$

where the vector $\mathbf{x} = [\sigma_1, \sigma_2, \sigma_3, \sigma_4]^T$, and matrix \mathbf{A} is

$$\mathbf{A} = \begin{bmatrix} 0 & 0 & \sigma_{14}^2 & -\sigma_{13}^2 \\ 0 & 0 & \sigma_{24}^2 & -\sigma_{23}^2 \\ 0 & \sigma_{13}^2 & -\sigma_{12}^2 & 0 \\ 0 & \sigma_{14}^2 & 0 & -\sigma_{12}^2 \\ 0 & \sigma_{34}^2 & 0 & -\sigma_{23}^2 \\ 0 & \sigma_{34}^2 & -\sigma_{24}^2 & 0 \\ \sigma_{23}^2 & 0 & -\sigma_{12}^2 & 0 \\ \sigma_{23}^2 & -\sigma_{13}^2 & 0 & 0 \\ \sigma_{24}^2 & 0 & 0 & -\sigma_{12}^2 \\ \sigma_{24}^2 & -\sigma_{14}^2 & 0 & 0 \\ \sigma_{34}^2 & 0 & 0 & -\sigma_{13}^2 \\ \sigma_{34}^2 & 0 & -\sigma_{14}^2 & 0 \end{bmatrix} \quad (6.34)$$

An obvious solution of Eq. (6.33) is $\mathbf{x} = 0$, i.e. $\sigma_1 = \sigma_2 = \sigma_3 = \sigma_4 = 0$. But based on the cross-correlation data calibrated in Sec. 6.7.3, the standard deviation of noise in cross-correlation data $\sigma_{C_{XY}}$ is calculated and listed in Tab. 6.4, which is shown that none of σ_i ($i = 1, 2, 3, 4$) is zero. So by solving Eq. (6.33), the nonzero standard deviations of noise in each auto-correlation channels can be obtained, as listed in Tab. 6.5.

	1400 MHz	1420.4 MHz
1H2H	0.153 K	0.155
1H3H	0.168	0.156
1H4H	0.187	0.186
2H3H	0.181	0.174
2H4H	0.186	0.192
3H4H	0.187	0.177

Table 6.4 The standard deviation of noise in cross-correlation data in Kelvin, with frequency resolution of 0.488 MHz and integration time of 0.4s, at frequencies of 1.4 GHz and 1420.4 MHz as an example.

	1400 MHz	1420.4 MHz
1H	0.233 K	0.228
2H	0.232	0.242
3H	0.277	0.245
4H	0.273	0.277

Table 6.5 The standard deviation of noise in auto-correlation data in Kelvin, with frequency resolution of 0.488 MHz and integration time of 0.4s, at frequencies of 1.4 GHz and 1420.4 MHz as an example.

6.8 System temperature

The system temperature can be estimated from the noise in auto-correlation or cross-correlation data. Assuming the noise is Gaussian, in auto-correlation, the system temperature can be obtained by

$$T_{\text{sys}}^i = \sigma_i \sqrt{\Delta t \cdot \Delta \nu} \quad (6.35)$$

where Δt is the integration time, $\Delta \nu$ is the channel width of a frequency bin, σ_i is the standard deviation of noise in auto-correlation data of i -th channel (Tab. 6.5), T_{sys}^i is the system temperature of i -th channel. In cross-correlation, the system temperature can be obtained by

$$T_{\text{sys}}^{ij} = \sigma_{ij} \sqrt{2 \Delta t \cdot \Delta \nu} \quad (6.36)$$

where the factor $\sqrt{2}$ is from Eq. (6.32) for a pair of channel, σ_{ij} is the standard deviation of noise in cross-correlation data of the channel pair of i -th and j -th (Tab. 6.4).

Fig. 6.31 and Fig. 6.32 are system temperatures estimated from auto-correlation data and cross-correlation data, respectively. The system temperatures of each channels are different. For the PAON-4, the average system temperature is 110 K.

As the gain drops below 1275 MHz and above 1475 MHz (Fig. 6.10), the results of two edges of the frequency band are unreliable. In addition, RFI from satellites affects strongly the frequency band below 1300 MHz.

6.9 Map-making

6.9.1 PAON-4 scan

PAON-4 is a drift scan radio interferometer. The observation strategy consists of obtaining visibility data for a set of right ascension (RA) scans at fixed declinations. All antennae are pointed toward the same, common declination. Visibility signals are recorded as the sky

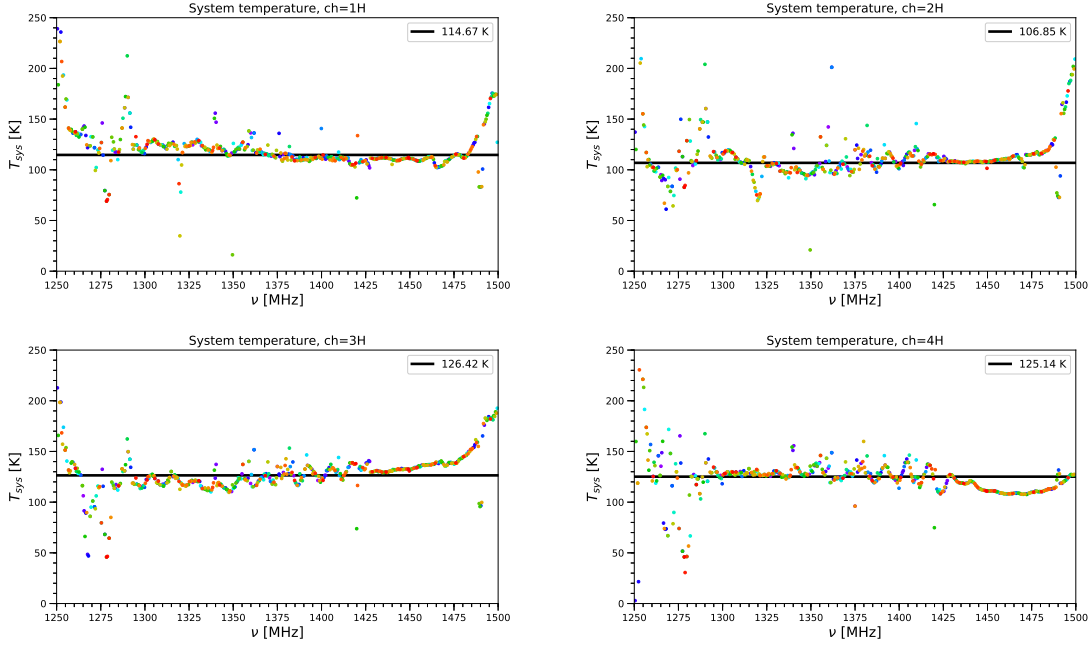


Fig. 6.31 System temperatures T_{sys} as a function of frequency, estimated from auto-correlation signals, calibrated using sky maps (SSM + LAB). From left to right, top to bottom, 1H, 2H, 3H, 4H.

drifts in front of the antennae, due to the Earth rotation. Once a scan at a given declination is done, typically after a duration multiple of 24 hours, the antennae are pointed toward a new declination direction. By repeating this process, visibility data from a large region of sky, a band in declination covering the full right ascension range is obtained.

The datasets used to reconstruct the sky map presented in this section are listed in Tab. 6.6, and cover a sky region around the Cygnus A declination, from $\delta = +35.7^\circ$ to $+45.7^\circ$, and 360° in RA.

6.9.2 Algorithm

For telescope operating in drift scan mode, the m -mode algorithm can be used to image visibility data. Here we briefly introduce this algorithm, for detail, please see [223, 264].

Generally the visibility can be written as Eq. 2.44 or Eq. 2.57. For the drift scan interferometric array, different time corresponds to different right ascensions α on the sky. For a complete scan of 360° in right ascension, Fourier transform can be performed on the visibility as a function of right ascension $V_{ij}(\alpha)$ [223]:

$$V_{ij}(\alpha) = \sum \mathbf{v}_m e^{im\alpha} dm \quad (6.37)$$

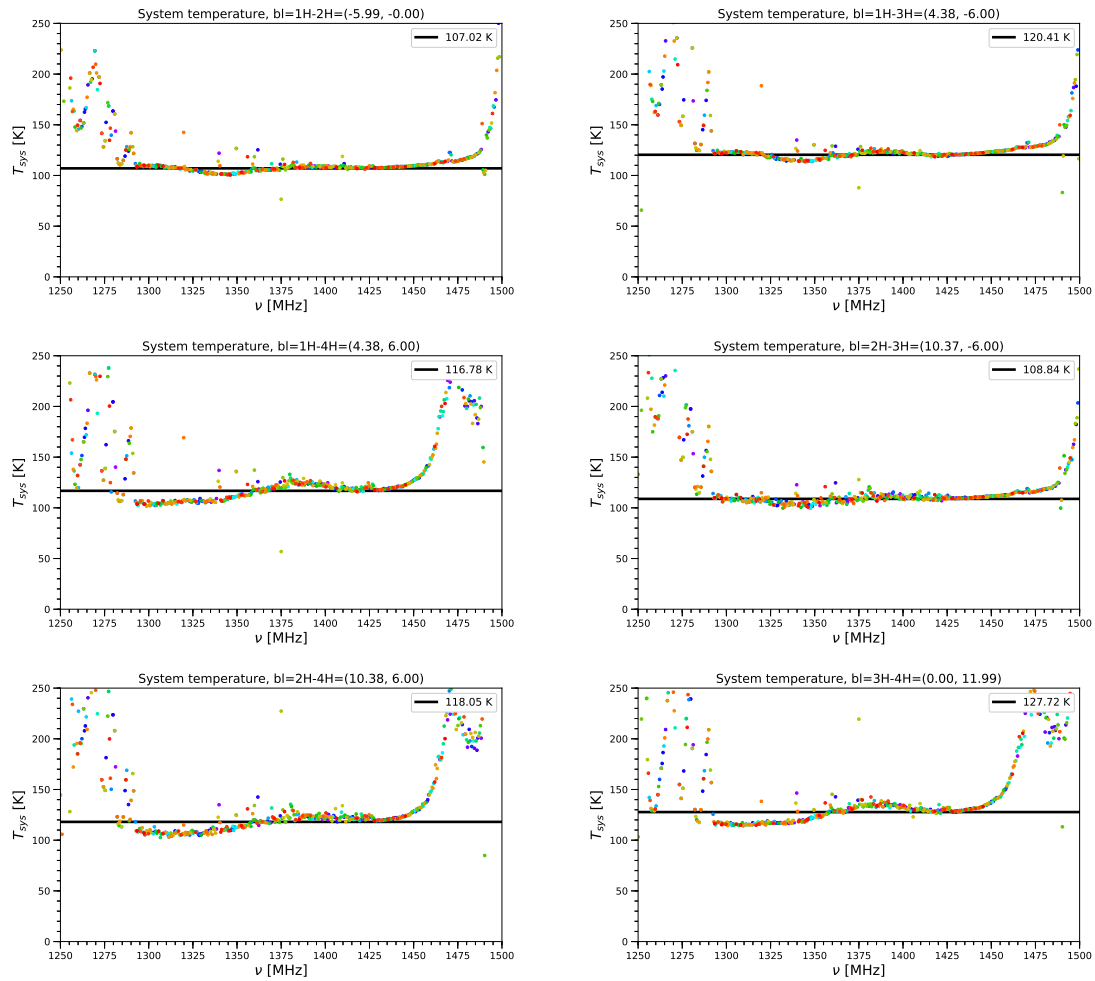


Fig. 6.32 System temperatures T_{sys} as a function of frequency, estimated from cross-correlation signals, calibrated using the Cygnus A source transit. From left to right, top to bottom, the six plots show the system temperature for the six baselines, 1H-2H, 1H-3H, 1H-4H, 2H-3H, 2H-4H, 3H-4H.

Dataset	Dec.	Freq. [MHz]	Begin (UTC)	Duration (Sidereal time)
CygA17nov16	+40.733°	1250–1500	13:30	24 h
CygA18nov16	+41.733°	1250–1500	14:00	24 h
CygA19nov16	+39.733°	1250–1500	14:45	24 h
CygA21nov16	+42.733°	1250–1500	10:00	24 h
CygA22nov16	+38.733°	1250–1500	10:30	24 h
CygA23nov16	+43.733°	1250–1500	11:00	24 h
CygA24nov16	+37.733°	1250–1500	11:30	24 h
CygA25nov16	+44.733°	1250–1500	12:00	24 h
CygA26nov16	+36.733°	1250–1500	12:30	24 h
CygA27nov16	+45.733°	1250–1500	13:00	24 h
CygA1dec16	+35.733°	1250–1500	13:30	24 h

Table 6.6 PAON-4 November 2016 dataset used in this section, which covers the declination range $\delta = +35.7^\circ$ to $+45.7^\circ$, around Cygnus A at $\delta = +40.7^\circ$.

As m is a discrete (integer) index, a Fourier sum is applied instead of integral in Eq. (6.37).

Performing the spherical harmonic expansion on the sky temperature and the complex beam

$$T(\theta, \varphi) = \sum_{l=0}^{+\infty} \sum_{m=-l}^l \mathcal{T}_{lm} Y_{lm}(\theta, \varphi) \quad (6.38)$$

$$\begin{aligned} B(\theta, \varphi, \alpha) &= D_i(\theta, \varphi, \alpha) D_j^*(\theta, \varphi, \alpha) e^{i\vec{k}(\vec{r}_j - \vec{r}_i)} \\ &= \sum_{l=0}^{+\infty} \sum_{m=-l}^l \mathcal{B}_{lm}(\alpha) Y_{lm}(\theta, \varphi) = \sum_{l=0}^{+\infty} \sum_{m=-l}^l \mathcal{B}_{l,-m}(\alpha) Y_{l,-m}(\theta, \varphi) \\ &= \sum_{l=0}^{+\infty} \sum_{m=-l}^l \mathcal{B}_{l,-m}(\alpha) (-1)^m Y_{lm}^*(\theta, \varphi) \end{aligned} \quad (6.39)$$

note that here we hide the baseline indices ij for the complex beam B and its spherical harmonic expansion coefficient \mathcal{B} for simplicity, but keep in mind that B and \mathcal{B} are baseline

dependent. Then it is obtained

$$\begin{aligned}
\sum_{m=-\infty}^{+\infty} \mathcal{V}_m e^{im\alpha} &= \int \left(\sum_{l=0}^{+\infty} \sum_{m=-l}^l \mathcal{B}_{l,-m}(\alpha) (-1)^m Y_{lm}^*(\theta, \varphi) \right) \left(\sum_{l=0}^{+\infty} \sum_{m=-l}^l \mathcal{T}_{lm} Y_{lm}(\theta, \varphi) \right) d\Omega \\
&= \sum_{m=-\infty}^{+\infty} \sum_{l=|m|}^{+\infty} (-1)^m \mathcal{B}_{l,-m}(\alpha) \mathcal{T}_{lm} \int Y_{lm}(\theta, \varphi) Y_{lm}^*(\theta, \varphi) d\Omega \\
&= \sum_{m=-\infty}^{+\infty} \sum_{l=|m|}^{+\infty} (-1)^m \mathcal{B}_{l,-m}(\alpha) \mathcal{T}_{lm}
\end{aligned} \tag{6.40}$$

Note that l and m in the last term of Eq. (6.40) are swapped (m first, and then l).

For a reference direction of $\alpha = 0$, the spherical harmonic coefficients of antenna response $\mathcal{B}_{lm}(\alpha)$ is written as

$$\mathcal{B}_{lm}(\alpha) = \mathcal{B}_{lm}(\alpha = 0) e^{im\alpha} \tag{6.41}$$

For brevity, use the label \mathcal{B}_{lm} instead of $\mathcal{B}_{lm}(\alpha = 0)$, but keep in mind that \mathcal{B}_{lm} is a function of α . Summing Eq. (6.40) up to a certain l_{\max} , it is obtained

$$\mathcal{V}_m = \sum_{l=|m|}^{l_{\max}} (-1)^m \mathcal{B}_{l,-m} \mathcal{T}_{lm} \tag{6.42}$$

As the brightness temperature of the sky is real, its complex conjugation is itself, then

$$\begin{aligned}
T^*(\theta, \varphi) &= T(\theta, \varphi) = \sum_{l=0}^{+\infty} \sum_{m=-l}^l \mathcal{T}_{lm}^* Y_{lm}(\theta, \varphi)^* = \sum_{l=0}^{+\infty} \sum_{m=-l}^l \mathcal{T}_{lm}^* (-1)^m Y_{l,-m}(\theta, \varphi) \\
&= \sum_{l=0}^{+\infty} \sum_{m=-l}^l \mathcal{T}_{l,-m}^* (-1)^m Y_{l,m}(\theta, \varphi)
\end{aligned} \tag{6.43}$$

Combine Eq. (6.38) and Eq. (6.38) and get

$$\mathcal{T}_{l,-m}^* = (-1)^m \mathcal{T}_{lm} \tag{6.44}$$

Then wen can obtain

$$\mathcal{V}_{-m}^* = \sum_{l=|m|}^{l_{\max}} \mathcal{B}_{lm}^* \mathcal{T}_{lm} \tag{6.45}$$

Paper [264] showed that as long as the pixel size of the image is less than the resolution of synthetic aperture, the quality of the reconstructed map is independent of larger l_{\max} and larger n_{inside} (a parameter of HEALPix). For PAON-4, $D_{\text{array}} \sim 18$ m and $\lambda \sim 0.2$ m, the

resolution of synthetic aperture ~ 40 arcmin. So selecting $n_{\text{side}} = 256$ (pixel size ~ 13 arcmin) and $l_{\text{max}} \gtrsim \frac{2\pi D_{\text{array}}}{\lambda} \sim 600$ is enough for PAON-4.

Rewrite Eq. (6.42) and Eq. (6.45) to a matrix formalism

$$\begin{bmatrix} \mathcal{V}(m_0) \\ \mathcal{V}(m_1) \\ \dots \\ \mathcal{V}(m_{\text{max}}) \end{bmatrix} = \begin{bmatrix} \mathcal{B}(m_0, l) & & & \\ & \mathcal{B}(m_1, l) & & \\ & & \dots & \\ & & & \mathcal{B}(m_{\text{max}}, l) \end{bmatrix} \begin{bmatrix} \mathcal{T}(l, m_0) \\ \mathcal{T}(l, m_1) \\ \dots \\ \mathcal{T}(l, m_{\text{max}}) \end{bmatrix} \quad (6.46)$$

Note that for the matrix $\mathcal{B}(m_i, l)$, row is m and column is l , while for the matrix $\mathcal{T}(l, m_i)$, row is l and column is m . It can be seen that each m -mode is independent. Therefore, by imaging each m -mode, a large matrix operation can be transformed to a series of small matrix operations, the imaging efficiency can be greatly improved.

For simplicity, Eq. (6.46) can be rewrote to be

$$[\mathcal{V}]_m = [\mathcal{B}(l)]_m [\mathcal{T}(l)]_m + [\mathbf{N}]_m \quad (6.47)$$

where $[\bullet]$ are used to denote vectors, $[\mathbf{N}]_m$ is the covariance matrix of the noise. For a likelihood function as

$$p([\mathcal{V}]_m | [\mathcal{T}(l)]_m) \propto \exp \left[-\frac{1}{2} ([\mathcal{V}]_m - [\mathcal{B}(l)]_m [\mathcal{T}(l)]_m)^T [\mathbf{N}]_m^{-1} ([\mathcal{V}]_m - [\mathcal{B}(l)]_m [\mathcal{T}(l)]_m) \right] \quad (6.48)$$

The maximum likelihood estimator of $[\hat{\mathcal{T}}(l)]_m$ is

$$[\hat{\mathcal{T}}(l)]_m = ([\mathcal{B}(l)]_m^\dagger [\mathbf{N}]_m^{-1} [\mathcal{B}(l)]_m)^{-1} [\mathcal{B}(l)]_m^\dagger [\mathbf{N}]_m^{-1} [\mathcal{V}]_m \quad (6.49)$$

The noise of different baselines is considered to be independent and random, so the covariance matrix of each m -mode is a diagonal matrix, then Eq. (6.49) can be reduced to

$$[\hat{\mathcal{T}}]_m = \left([\mathbf{N}]_m^{-\frac{1}{2}} [\mathcal{B}(l)]_m \right)^{-1} [\mathbf{N}]_m^{-\frac{1}{2}} [\mathcal{V}]_m \quad (6.50)$$

Finally, the reconstructed sky map can be obtained by performing an inverse spherical harnomic transformation on the estimated $[\hat{\mathcal{T}}]_m$.

6.9.3 PAON-4 reconstructed map

Eleven datasets are used to reconstruct the sky map in this chapter, the central declinations are $+35.733^\circ$, $+36.733^\circ$, $+37.733^\circ$, $+38.733^\circ$, $+39.733^\circ$, $+40.733^\circ$, $+41.733^\circ$, $+42.733^\circ$, $+43.733^\circ$, $+44.733^\circ$ and $+45.733^\circ$, from $+35.7^\circ$ to $+45.7^\circ$ (see Sec. 6.9.1).

In order to verify the correctness of the calibration and imaging methods, both the observation data of PAON4 and the corresponding simulation data (see Sec. 6.7.4) are imaged.

The top panel in Fig. 6.33 is the reconstructed sky map of the calibrated PAON-4 data at 1.4 GHz, Cygnus A and the Galactic plane can be seen clearly. As a reference for comparison, the middle panel in Fig. 6.33 is the reconstructed sky map of simulation data in the same sky region and at the same frequency. The bottom panel shows a zoom over the area around Cygnus A. The left hand side image shows the PAON-4 reconstructed map at 1400 MHz, while the right hand side is the reconstructed map from simulated visibility time streams.

6.10 Brief summary

In this chapter, the PAON-4 data is calibrated and imaged. Due to the RFI has a great influence on the calibration accuracy, it is firstly removed by the SumThreshold method. The system gain is calibrated both in frequency domain and time domain, it is found that the amplifying ability of LNA, which is exposed to air, is sensitive to the air temperature, the system gain decreases as the air temperature increases. The pointing of each antenna is calibrated and the effective diameter is estimated, the average diameter of PAON-4 is 4.2 m, and the pointing is in an accuracy of 1° . The extra phase in the data is calibrated. Due to the difference of the cable length and the electronic system, an extra phase is introduced to the visibility data, which varies linearly with the frequency. We have also use the phase closure to check the result. For the amplitude calibration, the cross-correlation data is first calibrated using the standard calibrators. For auto-correlation data, because the sky radiation distribution is not uniform and the resolution of PAON-4 antenna is not high enough, it is difficult to use the standard calibrators. Thus, we use the simulation sky map from SSM and observational sky map of LAB, as well as the relationship between the noises in cross- and auto-correlation data to calibrate the auto-correlation data. The system temperature of PAON-4 is also estimated, which is about 110 K. Finally, the m -mode algorithm is used to image the calibrated PAON-4 data in the spherical harmonic domain, and the comparison of reconstructed map between the PAON-4 data and simulation data is performed. Observations with PAON-4 have been continued throughout 2018 and 2019, and, at the time of finishing this manuscript, a publication on design, operation and performance of the instrument is

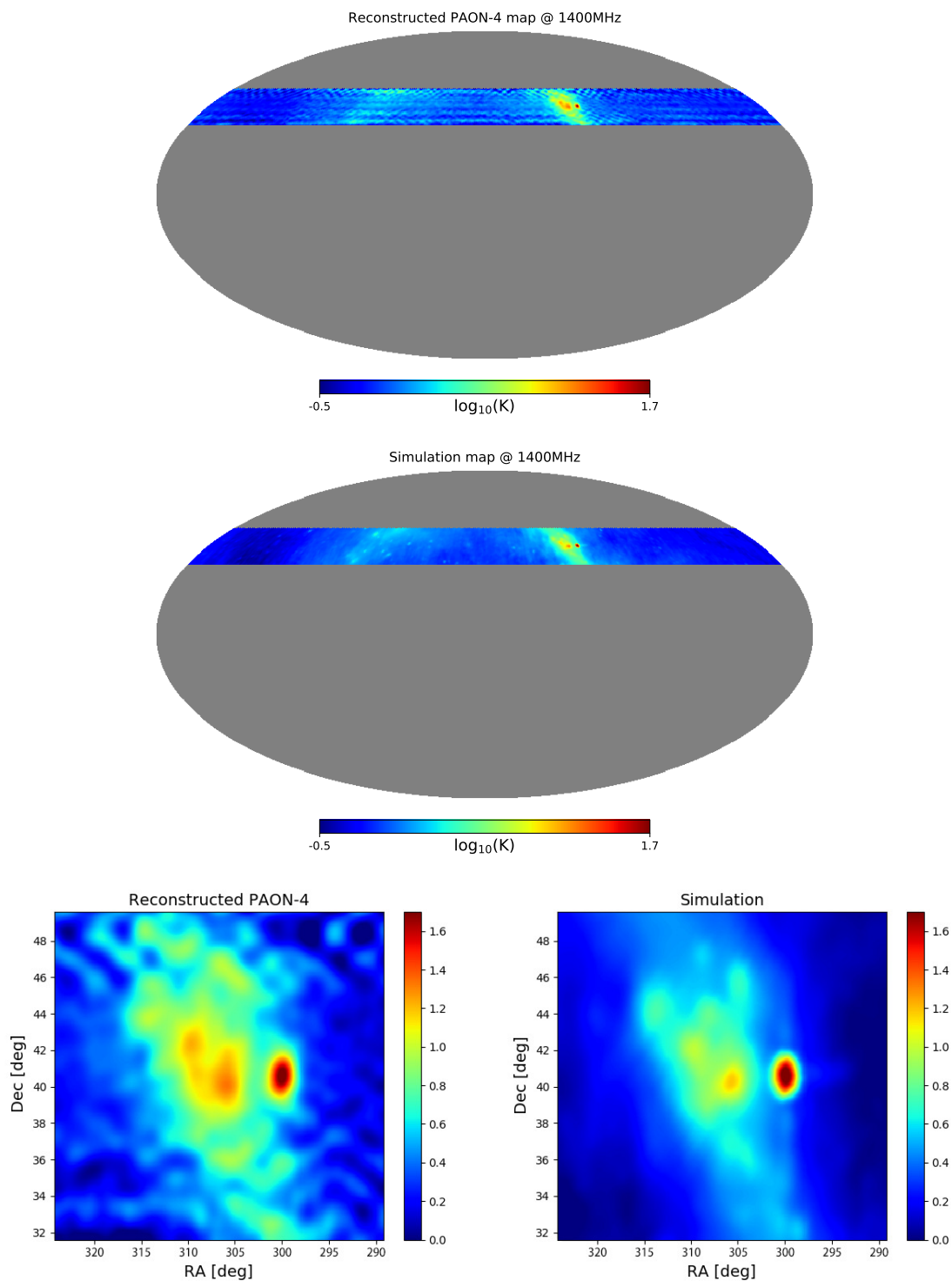


Fig. 6.33 PAON-4 reconstructed sky maps using the m -mode decomposition in spherical harmonics algorithm [223, 264]. Top panel shows the reconstructed sky map from the calibrated PAON-4 November 2016 data at 1.4 GHz, Cygnus A and the Galactic plane can be seen clearly. For comparison, the middle panel shows the reconstructed sky map from simulated visibility data in the same sky region and at the same frequency. Bottom panel: the zoom-in around Cygnus A, RA from 290° to 325° and Dec from $+32^\circ$ to $+50^\circ$, the reconstructed map from PAON-4 observations is shown on the left, while the right hand side shows the map reconstructed from simulated visibilities.

being finalised [11]. The analysis described in this article extends the one presented in this chapter and shows that the calibration strategy described here is indeed effective, with a good stability over long observation periods. The analysis presented here, and in [11] need however to be refined in order to reach the milli-Kelvin sensitivity levels through much larger integration times, required for intensity mapping. This work is also being done with similar methods and concepts with the Tianlai dish array data [87].

Chapter 7

Summary and Outlooks

In this dissertation, some problems of cosmological 21-cm signal detection and mid- and low-frequency radio data processing have been studied theoretically and experimentally, including the high-resolution self-consistent foreground modelling, cosmological 21-cm signal extraction, lunar orbit satellite interferometric imaging with time-varying all-sky response and non-coplanar baseline, and actual ground radio interferometric data calibration and imaging.

A high-resolution self-consistent foreground model has been constructed, which is divided into two parts: point source model and diffuse emission model. For point sources, it is further divided into bright sources and faint sources. To model the bright sources, NVSS and SUMSS surveys are used as the sky coverage of these two surveys is almost the whole sky. A complete sample from NVSS+SUMSS is selected, and the same number surface density of source is kept when merging the two surveys. More than 7500 overlapping sources in the overlapping regions of the two survey data are identified, and their flux density spectral indices are computed which is extrapolated to other frequencies. To model the faint sources, the radio luminosity function is first calculated, and the radio differential count is computed, then using the Rayleigh-Lévy random walk to generate the all-sky distribution of the faint point source. In addition, the confusion limits of telescopes in different resolutions are also calculated.

The cosmological 21-cm signal extraction method based on frequency and angular domain filtering is introduced. First, we compute the cosmological 21-cm power spectrum by linear biasing the dark matter power spectrum which is calculated by CAMB, assuming the HI distribution traces the dark matter. Then we generate a Gaussian random density field of HI and multiplying the 21-cm bright temperature to get the 21-cm simulated sky map. Foreground maps are computed using the foreground model developed here. We then use a cascade of two different Wiener filters, filtering both in frequency domain and angular

domain, making use of the difference in properties among the 21-cm signal, the foreground and the noise: in frequency domain, along the direction of one line of sight, the foreground is usually considered to be smooth while the 21-cm signal and noise are highly variable. The smooth foreground can be filtered out from the data in frequency domain. In angular domain, i.e. in time domain, the receiver noise is uncorrelated while the cosmological 21-cm signal exhibits correlations at different scales as HI traces the large-scale structure of the Universe and 21-cm signal is convoluted by the telescope beam during observation. So the noise can be filtered out from the 21-cm signal in angular domain.

Imaging is a significant problem for lunar orbit satellite interferometers with time-varying response and non-coplanar baselines. A satellite interferometer in the orbit around the Moon can make an excellent observation on the frequency band below 30 MHz, because the satellite is beyond the Earth's atmosphere and the moon can shield the strong RFI from the Earth. However, because the beam of the electric-short antenna carried by the satellite is very wide (almost all-sky), the imaging of a fixed orbital plane encounters the symmetry problem. In addition, the sky region blocked by the Moon changes with the motion of the satellite, resulting in a time-varying instrument response. This time-varying response and time-varying non-coplanar baseline distribution make widely used large field-of-view imaging methods such as W-Projection and W-Stacking not suitable for data imaging. Aiming at the above problems, precession of the orbital plane is used to solve the mirror symmetry problem, two imaging algorithms in pixel domain and spherical harmonic domain are introduced to image the orbital interferometric data with all-sky time-varying response and time-varying non-coplanar baselines. In addition, the effects of a variety of asymmetric baseline distributions on imaging are also discussed.

Finally, we analyze the data of the radio antenna array PAON-4. From the raw data, RFI is removed using the SumThreshold method. We then correct the temperature dependent electronic gain variations. The directions of each antennae are also determined as there is a slight pointing error below 1° , due to mechanical and alignment unperfection. Meanwhile, the efficiency of antenna receiving area is computed to be about 70%. Then the phase and amplitude of the data are calibrated using the standard point source calibrators as well as simulated data, and the system temperature is calculated to be about 110 K. In addition, the calibrated data is used to reconstruct sky maps applying the m -mode decomposition method in spherical harmonic domain.

This dissertation presents several studies in radio astronomy, from phenomenological modeling to actual observation analysis, from ground experiments to space missions. Many simplifying assumptions have been included in these studies and a number of refinements are still needed to make the models closer to reality and results more reliable. For example, the

celestial radiation is usually polarised, while we have considered unpolarised radiation in our studies. The receiver noises should be slightly correlated due to the $1/f$ noise, however we have assumed them uncorrelated. The Moon's blockages on the sky for each satellites would be different because of the different positions of each satellites to the Moon, but has been consider identical in our study and the differences in the orbits of each satellites have not been taken into account. The emission in the radio bands of the Sun and other planets, such as Jupiter are time variables, as are their positions in the sky, leading to a time variable sky emission, while we have considered a static sky in our study of the lunar orbit interferometer imaging. The radio waves are reflected and diffracted by the Moon, and the rugged terrain on the Moon affects the radio signals received by the satellite array. Here again, we have considered the Moon as an ideal sphere, neglecting radio wave reflection and diffraction by its surface. These effects need to be taken into account in future studies.

The data analysis methods and their application to PAON-4 presented in chapter 6 have been extended and refined in subsequent analysis of PAON-4 data, with a much larger set of of observations carried in 2018 and 2019. Similar technics are also being applied to the Tianlai 16 dish array, which is observing the sky at lower frequencies, around 750 MHz. The results which we have obtained, as instrument performance, calibration strategy and stability are quite encouraging, at least at the level of sensitivities currently reached. These methods, including the map making methods need still to be refined and applied to the full PAON-4 and Tianlai data sets. It should be also stressed that the Tianlai dish array polar cap transit survey being carried out has specificities, compared to mid-latitude surveys discussed here which need to be addressed. Finally, the foreground model developed in chapter 3 would be a valuable tool for PAON-4 and Tianlai analysis.

References

- [1] Abedi, H. and Abbassi, A. M. (2017). Primordial perturbations in multi-scalar inflation. *J. Cosmology Astropart. Phys.*, 7:049.
- [2] Abel, T., Bryan, G. L., and Norman, M. L. (2002). The Formation of the First Star in the Universe. *Science*, 295:93–98.
- [3] Ackermann, M., Ajello, M., Atwood, W. B., Baldini, L., Ballet, J., Barbiellini, G., Bastieri, D., Baughman, B. M., Bechtol, K., Bellardi, F., Bellazzini, R., Belli, F., Ylinen, T., and Ziegler, M. (2010). Fermi LAT observations of cosmic-ray electrons from 7 GeV to 1 TeV. *Phys. Rev. D*, 82(9):092004.
- [4] Adams, F. C., Bond, J. R., Freese, K., Frieman, J. A., and Olinto, A. V. (1993). Natural inflation: Particle physics models, power-law spectra for large-scale structure, and constraints from the Cosmic Background Explorer. *Phys. Rev. D*, 47:426–455.
- [5] Akeret, J., Seehars, S., Chang, C., Monstein, C., Amara, A., and Refregier, A. (2017). HIDE SEEK: End-to-end packages to simulate and process radio survey data. *Astronomy and Computing*, 18:8–17.
- [6] Albrecht, A., Bernstein, G., Cahn, R., Freedman, W. L., Hewitt, J., Hu, W., Huth, J., Kamionkowski, M., Kolb, E. W., Knox, L., Mather, J. C., Staggs, S., and Suntzeff, N. B. (2006). Report of the Dark Energy Task Force. *arXiv Astrophysics e-prints*.
- [7] Alexander, J. K., Kaiser, M. L., Novaco, J. C., Grena, F. R., and Weber, R. R. (1975). Scientific instrumentation of the Radio-Astronomy-Explorer-2 satellite. *A&A*, 40:365–371.
- [8] Alexander, J. K. and Novaco, J. C. (1974). Survey of the galactic background radiation at 3.93 and 6.55 MHz. *AJ*, 79:777.
- [9] Alonso, D., Bueno Beloso, A., Sánchez, F. J., García-Bellido, J., and Sánchez, E. (2014). Measuring the transition to homogeneity with photometric redshift surveys. *MNRAS*, 440:10–23.
- [10] Alonso, D., Bull, P., Ferreira, P. G., and Santos, M. G. (2015). Blind foreground subtraction for intensity mapping experiments. *MNRAS*, 447:400–416.
- [11] Ansari, R., Campagne, J. E., Charlet, D., Moniez, M., Pailler, C., Perdureau, O., Taurigna, M., Martin, J. M., Rigaud, F., Colom, P., Abbon, P., Magneville, C., Pezzani, J., Viou, C., Torchinsky, S. A., Huang, Q., and Zhang, J. (2019). Design, operation and performance of the PAON4 prototype transit interferometer. *arXiv e-prints*.

- [12] Ansari, R., Campagne, J. E., Colom, P., Ferrari, C., Magneville, C., Martin, J. M., Moniez, M., and Torrentó, A. S. (2016). On sky characterization of the BAORadio wide band digital backend. Search for H_I emission in Abell85, Abell1205 and Abell2440 galaxy clusters. *Experimental Astronomy*, 41:117–144.
- [13] Ansari, R., Campagne, J. E., Colom, P., Le Goff, J. M., Magneville, C., Martin, J. M., Moniez, M., Rich, J., and Yèche, C. (2012). 21 cm observation of large-scale structures at $z \sim 1$. Instrument sensitivity and foreground subtraction. *A&A*, 540:A129.
- [14] Arnal, E. M., Bajaja, E., Larrarte, J. J., Morras, R., and Pöppel, W. G. L. (2000). A high sensitivity HI survey of the sky at $\delta = -25^\circ$. *A&AS*, 142:35–40.
- [15] Asad, K. M. B., Koopmans, L. V. E., Jelić, V., de Bruyn, A. G., Pandey, V. N., and Gehlot, B. K. (2018). Polarization leakage in epoch of reionization windows - III. Wide-field effects of narrow-field arrays. *MNRAS*, 476:3051–3062.
- [16] Asad, K. M. B., Koopmans, L. V. E., Jelić, V., Ghosh, A., Abdalla, F. B., Brentjens, M. A., de Bruyn, A. G., Ciardi, B., Gehlot, B. K., Iliev, I. T., Mevius, M., Pandey, V. N., Yatawatta, S., and Zaroubi, S. (2016). Polarization leakage in epoch of reionization windows - II. Primary beam model and direction-dependent calibration. *MNRAS*, 462:4482–4494.
- [17] Asad, K. M. B., Koopmans, L. V. E., Jelić, V., Pandey, V. N., Ghosh, A., Abdalla, F. B., Bernardi, G., Brentjens, M. A., de Bruyn, A. G., Bus, S., Ciardi, B., Chapman, E., Daiboo, S., Fernandez, E. R., Harker, G., Iliev, I. T., Jensen, H., Martinez-Rubi, O., Mellema, G., Mevius, M., Offringa, A. R., Patil, A. H., Schaye, J., Thomas, R. M., van der Tol, S., Vedantham, H. K., Yatawatta, S., and Zaroubi, S. (2015). Polarization leakage in epoch of reionization windows - I. Low Frequency Array observations of the 3C196 field. *MNRAS*, 451:3709–3727.
- [18] Athreya, R. (2009). A New Approach to Mitigation of Radio Frequency Interference in Interferometric Data. *ApJ*, 696:885–890.
- [19] Aubourg, É., Bailey, S., Bautista, J. E., Beutler, F., Bhardwaj, V., Bizyaev, D., Blanton, M., Blomqvist, M., Bolton, A. S., Bovy, J., Brewington, H., Yèche, C., Zehavi, I., Zhao, G.-B., and BOSS Collaboration (2015). Cosmological implications of baryon acoustic oscillation measurements. *Phys. Rev. D*, 92(12):123516.
- [20] Aver, E., Olive, K. A., and Skillman, E. D. (2015). The effects of He I $\lambda 10830$ on helium abundance determinations. *J. Cosmology Astropart. Phys.*, 7:011.
- [21] Baan, W. A., Fridman, P. A., and Millenaar, R. P. (2004). Radio Frequency Interference Mitigation at the Westerbork Synthesis Radio Telescope: Algorithms, Test Observations, and System Implementation. *AJ*, 128:933–949.
- [22] Baars, J. W. M., Genzel, R., Pauliny-Toth, I. I. K., and Witzel, A. (1977). The absolute spectrum of CAS A - an accurate flux density scale and a set of secondary calibrators. *A&A*, 61:99–106.
- [23] Bajaja, E., Arnal, E. M., Larrarte, J. J., Morras, R., Pöppel, W. G. L., and Kalberla, P. M. W. (2005). A high sensitivity HI survey of the sky at $\delta = -25^\circ$. Final data release. *A&A*, 440:767–773.

- [24] Banday, A. J. and Wolfendale, A. W. (1991). Fluctuations in the galactic synchrotron radiation. I - Implications for searches for fluctuations of cosmological origin. *MNRAS*, 248:705–714.
- [25] Bandura, K., Addison, G. E., Amiri, M., Bond, J. R., Campbell-Wilson, D., Connor, L., Cliche, J.-F., Davis, G., Deng, M., Denman, N., Dobbs, M., Fandino, M., Gibbs, K., Gilbert, A., Halpern, M., Hanna, D., Hincks, A. D., Hinshaw, G., Höfer, C., Klages, P., Landecker, T. L., Masui, K., Mena Parra, J., Newburgh, L. B., Pen, U.-I., Peterson, J. B., Recnik, A., Shaw, J. R., Sigurdson, K., Sitwell, M., Smecher, G., Smegal, R., Vanderlinde, K., and Wiebe, D. (2014). Canadian Hydrogen Intensity Mapping Experiment (CHIME) pathfinder. In *Ground-based and Airborne Telescopes V*, volume 9145 of *procspie*, page 914522.
- [26] Bania, T. M., Rood, R. T., and Balsler, D. S. (2002). The cosmological density of baryons from observations of $^3\text{He}^+$ in the Milky Way. *Nature*, 415:54–57.
- [27] Barkana, R. and Loeb, A. (2001). In the beginning: the first sources of light and the reionization of the universe. *Phys. Rep.*, 349:125–238.
- [28] Barnbaum, C. and Bradley, R. F. (1998). A New Approach to Interference Excision in Radio Astronomy: Real-Time Adaptive Cancellation. *AJ*, 116:2598–2614.
- [29] Basart, J. P. and Burns, J. O. (1992). Low frequency astronomy from lunar orbit. In Sadeh, W. Z., Sture, S., and Miller, R. J., editors, *Engineering, Construction, and Operations in space - III: Space '92*, volume 2, pages 1913–1924.
- [30] Bassett, B. and Hlozek, R. (2010). *Baryon acoustic oscillations*, page 246. Ruiz-Lapuente, P.
- [31] Battye, R. A., Browne, I. W. A., Dickinson, C., Heron, G., Maffei, B., and Pourtsidou, A. (2013). H I intensity mapping: a single dish approach. *MNRAS*, 434:1239–1256.
- [32] Bennett, C. L., Hill, R. S., Hinshaw, G., Nolta, M. R., Odegard, N., Page, L., Spergel, D. N., Weiland, J. L., Wright, E. L., Halpern, M., Jarosik, N., Kogut, A., Limon, M., Meyer, S. S., Tucker, G. S., and Wollack, E. (2003). First-Year Wilkinson Microwave Anisotropy Probe (WMAP) Observations: Foreground Emission. *ApJS*, 148:97–117.
- [33] Bennett, C. L., Larson, D., Weiland, J. L., Jarosik, N., Hinshaw, G., Odegard, N., Smith, K. M., Hill, R. S., Gold, B., Halpern, M., Komatsu, E., Nolta, M. R., Page, L., Spergel, D. N., Wollack, E., Dunkley, J., Kogut, A., Limon, M., Meyer, S. S., Tucker, G. S., and Wright, E. L. (2013). Nine-year Wilkinson Microwave Anisotropy Probe (WMAP) Observations: Final Maps and Results. *ApJS*, 208:20.
- [34] Bergman, J. E. S., Blott, R. J., Forbes, A. B., Humphreys, D. A., Robinson, D. W., and Stavrinidis, C. (2009). FIRST Explorer – An innovative low-cost passive formation-flying system. *ArXiv e-prints*.
- [35] Bertulani, C. A., Fuqua, J., and Hussein, M. S. (2013). Big Bang Nucleosynthesis with a Non-Maxwellian Distribution. *ApJ*, 767:67.

- [36] Beutler, F., Blake, C., Colless, M., Jones, D. H., Staveley-Smith, L., Campbell, L., Parker, Q., Saunders, W., and Watson, F. (2011). Constant The 6dF Galaxy Survey: baryon acoustic oscillations and the local Hubble constant. *MNRAS*, 416:3017–3032.
- [37] Bigot-Sazy, M.-A., Dickinson, C., Battye, R. A., Browne, I. W. A., Ma, Y.-Z., Maffei, B., Novello, F., Remazeilles, M., and Wilkinson, P. N. (2015). Simulations for single-dish intensity mapping experiments. *MNRAS*, 454:3240–3253.
- [38] Blott, R. J., Baan, I. W. A., Boonstra, A.-J., Bergman, J., Robinson, D., Liddle, D., Navarathinam, N., Eves, S., Bridges, C., Gao, S., Bentum, M., Forbes, A., Humphreys, D., and Harroch, C.-G. (2013). Space-based ultra-long wavelength radio observatory (low cost) - SURO-LC. *European Planetary Science Congress*, 8:EPSC2013–279.
- [39] Bock, D. C.-J., Large, M. I., and Sadler, E. M. (1999). SUMSS: A Wide-Field Radio Imaging Survey of the Southern Sky. I. Science Goals, Survey Design, and Instrumentation. *AJ*, 117:1578–1593.
- [40] Bonaldi, A., Bonato, M., Galluzzi, V., Harrison, I., Massardi, M., Kay, S., De Zotti, G., and Brown, M. L. (2019). The Tiered Radio Extragalactic Continuum Simulation (T-RECS). *MNRAS*, 482:2–19.
- [41] Bondyopadhyay, P. K. (1998). Sir J.C. Bose diode detector received Marconi’s first transatlantic wireless signal of December 1901 (the "Italian Navy Coherer" Scandal Revisited). *PROCEEDINGS OF THE IEEE*, 86:1–27.
- [42] Boonstra, A. J., Garrett, M., Kruithof, G., Wise, M., van Ardenne, A., Yan, J., Wu, J., Zheng, J., Gill, E. K. A., Guo, J., Bentum, M., Girard, J. N., Hong, X., An, T., Falcke, H., Klein-Wolt, M., Wu, S., Chen, W., Koopmans, L., Rothkaehl, H., Chen, X., Huang, M., Chen, L., Gurvits, L., Zarka, P., Cecconi, B., and de Haan, H. (2016). Discovering the sky at the longest wavelengths (dsl). In *2016 IEEE Aerospace Conference*, pages 1–20.
- [43] Boonstra, A.-J., Saks, N., Falcke, H., Klein-Wolt, M., Bentum, A., Thilak Rajan, R., Wijnholds, I. S. J., Arts, M., van-T Klooster, K., and Belien, F. (2010). A Low-Frequency Distributed Aperture Array for Radio Astronomy in Space. In *38th COSPAR Scientific Assembly*, volume 38 of *COSPAR Meeting*, page 11.
- [44] Bouman, K. L., Johnson, M. D., Zoran, D., Fish, V. L., Doleman, S. S., and Freeman, W. T. (2016). Computational Imaging for VLBI Image Reconstruction. In *The IEEE Conference on Computer Vision and Pattern Recognition (CVPR)*.
- [45] Boya, L. J. (2004). The Thermal Radiation Formula of Planck (1900). *arXiv Physics e-prints*.
- [46] Braden, J., Kofman, L., and Barnaby, N. (2010). Reheating the universe after multi-field inflation. *J. Cosmology Astropart. Phys.*, 7:016.
- [47] Bridle, A. H. (1967). The spectrum of the radio background between 13 and 404 MHz. *MNRAS*, 136:219.
- [48] Bridle, A. H. and Purton, C. R. (1968). Observations of radio sources at 10.03 MHz. *AJ*, 73:717–726.

- [49] Briggs, F. H., Bell, J. F., and Kesteven, M. J. (2000). Removing Radio Interference from Contaminated Astronomical Spectra Using an Independent Reference Signal and Closure Relations. *AJ*, 120:3351–3361.
- [50] Bromm, V., Coppi, P. S., and Larson, R. B. (2002). The Formation of the First Stars. I. The Primordial Star-forming Cloud. *ApJ*, 564:23–51.
- [51] Bromm, V. and Larson, R. B. (2004). The First Stars. *ARA&A*, 42:79–118.
- [52] Brown, L. W. (1973). The Galactic Radio Spectrum Between 130 and 2600kHz. *ApJ*, 180:359–370.
- [53] Cane, H. V. (1978). A 30 MHz map of the whole sky. *Australian Journal of Physics*, 31:561.
- [54] Cane, H. V. (1979). Spectra of the non-thermal radio radiation from the galactic polar regions. *MNRAS*, 189:465–478.
- [55] Cane, H. V. and Whitham, P. S. (1977). Observations of the southern sky at five frequencies in the range 2-20 MHz. *MNRAS*, 179:21–29.
- [56] Caswell, J. L. (1976). A map of the northern sky at 10 MHz. *MNRAS*, 177:601–616.
- [57] Cendes, Y., Prasad, P., Rowlinson, A., Wijers, R. A. M. J., Swinbank, J. D., Law, C. J., van der Horst, A. J., Carbone, D., Broderick, J. W., Staley, T. D., Stewart, A. J., Huizinga, F., Molenaar, G., Alexov, A., Bell, M. E., Coenen, T., Corbel, S., Eislöffel, J., Fender, R., Grießmeier, J.-M., Jonker, P., Kramer, M., Kuniyoshi, M., Pietka, M., Stappers, B., Wise, M., and Zarka, P. (2018). RFI flagging implications for short-duration transients. *Astronomy and Computing*, 23:103.
- [58] Chang, T.-C., Pen, U.-L., Bandura, K., and Peterson, J. B. (2010). An intensity map of hydrogen 21-cm emission at redshift z 0.8. *Nature*, 466:463–465.
- [59] Chang, T.-C., Pen, U.-L., Peterson, J. B., and McDonald, P. (2008). Baryon Acoustic Oscillation Intensity Mapping of Dark Energy. *Physical Review Letters*, 100(9):091303.
- [60] Chapman, E., Abdalla, F. B., Bobin, J., Starck, J.-L., Harker, G., Jelić, V., Labropoulos, P., Zaroubi, S., Brentjens, M. A., de Bruyn, A. G., and Koopmans, L. V. E. (2013). The scale of the problem: recovering images of reionization with Generalized Morphological Component Analysis. *MNRAS*, 429:165–176.
- [61] Chapman, E., Abdalla, F. B., Harker, G., Jelić, V., Labropoulos, P., Zaroubi, S., Brentjens, M. A., de Bruyn, A. G., and Koopmans, L. V. E. (2012). Foreground removal using FASTICA: a showcase of LOFAR-EoR. *MNRAS*, 423:2518–2532.
- [62] Chen, X. (2005). Some thoughts on developing our country’s space-based low frequency radio astronomy. In *Proceedings of the second academic annual meeting of the deep space exploration branch of the Chinese Aerospace Society*, page 49.
- [63] Chen, X. (2011). Radio detection of dark energy the Tianlai project. *Scientia Sinica Physica, Mechanica Astronomica*, 41:1358.

- [64] Chen, X. (2012). The Tianlai Project: a 21CM Cosmology Experiment. In *International Journal of Modern Physics Conference Series*, volume 12 of *International Journal of Modern Physics Conference Series*, pages 256–263.
- [65] Chen, X. (2015). The Tianlai 21cm intensity mapping experiment. *IAU General Assembly*, 22:2252187.
- [66] Chen, X., Burns, J., Koopmans, L., Rothkaehi, H., Silk, J., Wu, J., Boonstra, A.-J., Cecconi, B., Chiang, C. H., Chen, L., Deng, L., Falanga, M., Falcke, H., Fan, Q., Fang, G., Fialkov, A., Gurvits, L., Ji, Y., Kasper, J. C., Li, K., Mao, Y., Mckinley, B., Monsalve, R., Peterson, J. B., Ping, J., Subrahmanyam, R., Vedantham, H., Klein Wolt, M., Wu, F., Xu, Y., Yan, J., and Yue, B. (2019). Discovering the Sky at the Longest Wavelengths with Small Satellite Constellations. *arXiv e-prints*.
- [67] Chen, X. and Miralda-Escudé, J. (2008). The 21 cm Signature of the First Stars. *ApJ*, 684:18–33.
- [68] Ciardi, B. and Ferrara, A. (2005). The First Cosmic Structures and Their Effects. *Space Sci. Rev.*, 116:625–705.
- [69] Ciardi, B. and Madau, P. (2003). Probing beyond the Epoch of Hydrogen Reionization with 21 Centimeter Radiation. *ApJ*, 596:1–8.
- [70] Clesse, S. (2011). *Hybrid Inflation: Multi-field Dynamics and Cosmological Constraints*. PhD thesis, PhD Thesis, 2011.
- [71] Coc, A., Goriely, S., Xu, Y., Saimpert, M., and Vangioni, E. (2012). Standard Big Bang Nucleosynthesis up to CNO with an Improved Extended Nuclear Network. *ApJ*, 744:158.
- [72] Coc, A., Petitjean, P., Uzan, J.-P., Vangioni, E., Descouvemont, P., Iliadis, C., and Longland, R. (2015). New reaction rates for improved primordial D/H calculation and the cosmic evolution of deuterium. *Phys. Rev. D*, 92(12):123526.
- [73] Coc, A. and Vangioni, E. (2017). Primordial nucleosynthesis. *International Journal of Modern Physics E*, 26:1741002.
- [74] Cohen, A. S., Lane, W. M., Cotton, W. D., Kassim, N. E., Lazio, T. J. W., Perley, R. A., Condon, J. J., and Erickson, W. C. (2007). The VLA Low-Frequency Sky Survey. *AJ*, 134:1245–1262.
- [75] Colombi, S., Bouchet, F. R., and Schaeffer, R. (1995). A count probability cookbook: Spurious effects and the scaling model. *ApJS*, 96:401–428.
- [76] Condon, J. J. (1984). Cosmological evolution of radio sources found at 1.4 GHz. *ApJ*, 284:44–53.
- [77] Condon, J. J. (1989). The 1.4 gigahertz luminosity function and its evolution. *ApJ*, 338:13–23.
- [78] Condon, J. J., Cotton, W. D., Fomalont, E. B., Kellermann, K. I., Miller, N., Perley, R. A., Scott, D., Vernstrom, T., and Wall, J. V. (2012). Resolving the Radio Source Background: Deeper Understanding through Confusion. *ApJ*, 758:23.

- [79] Condon, J. J., Cotton, W. D., Greisen, E. W., Yin, Q. F., Perley, R. A., Taylor, G. B., and Broderick, J. J. (1998). The NRAO VLA Sky Survey. *AJ*, 115:1693–1716.
- [80] Cooke, R. J., Pettini, M., Jorgenson, R. A., Murphy, M. T., and Steidel, C. C. (2014). Precision Measures of the Primordial Abundance of Deuterium. *ApJ*, 781:31.
- [81] Cornwell, T. J., Golap, K., and Bhatnagar, S. (2005). W Projection: A New Algorithm for Wide Field Imaging with Radio Synthesis Arrays. In Shopbell, P., Britton, M., and Ebert, R., editors, *Astronomical Data Analysis Software and Systems XIV*, volume 347 of *Astronomical Society of the Pacific Conference Series*, page 86.
- [82] Cornwell, T. J., Golap, K., and Bhatnagar, S. (2008). The Noncoplanar Baselines Effect in Radio Interferometry: The W-Projection Algorithm. *IEEE Journal of Selected Topics in Signal Processing*, 2:647–657.
- [83] Cornwell, T. J. and Perley, R. A. (1992). Radio-interferometric imaging of very large fields - The problem of non-coplanar arrays. *A&A*, 261:353–364.
- [84] Crosby, B. D., O’Shea, B. W., Smith, B. D., Turk, M. J., and Hahn, O. (2013). Population III Star Formation in Large Cosmological Volumes. I. Halo Temporal and Physical Environment. *ApJ*, 773:108.
- [85] Cyburt, R. H., Fields, B. D., Olive, K. A., and Yeh, T.-H. (2016). Big bang nucleosynthesis: Present status. *Reviews of Modern Physics*, 88(1):015004.
- [86] Czerny, M., Higaki, T., and Takahashi, F. (2014). Multi-natural inflation in supergravity and BICEP2. *Physics Letters B*, 734:167–172.
- [87] Das, S., Anderson, C. J., Ansari, R., Campagne, J.-E., Charlet, D., Chen, X., Chen, Z., Cianciara, A. J., Colom, P., Cong, Y., Gayley, K. G., Geng, J., Hao, J., Huang, Q., Keith, C. S., Li, C., Li, J., Li, Y., Liu, C., Liu, T., Magneville, C., Marriner, J. P., Martin, J.-M., Moniez, M., Oxholm, T. M., Pen, U.-l., Perdureau, O., Peterson, J. B., Shi, H., Shu, L., Stebbins, A., Sun, S., Timbie, P. T., Torchinsky, S., Tucker, G. S., Wang, G., Wang, R., Wang, X., Wang, Y., Wu, F., Xu, Y., Yu, K., Zhang, J., Zhang, J., Zhang, L., Zhu, J., and Zuo, S. (2018). Progress in the construction and testing of the Tianlai radio interferometers. In *Millimeter, Submillimeter, and Far-Infrared Detectors and Instrumentation for Astronomy IX*, volume 10708 of *Society of Photo-Optical Instrumentation Engineers (SPIE) Conference Series*, page 1070836.
- [88] de la Fuente, A., Saraswat, P., and Sundrum, R. (2015). Natural Inflation and Quantum Gravity. *Physical Review Letters*, 114(15):151303.
- [89] de Oliveira-Costa, A., Tegmark, M., Gaensler, B. M., Jonas, J., Landecker, T. L., and Reich, P. (2008). A model of diffuse Galactic radio emission from 10 MHz to 100 GHz. *MNRAS*, 388:247–260.
- [90] de Oliveira-Costa, A., Tegmark, M., Gaensler, B. M., Jonas, J., Landecker, T. L., and Reich, P. (2008). A model of diffuse Galactic Radio Emission from 10 MHz to 100 GHz. *Mon. Not. Roy. Astron. Soc.*, 388:247.

- [91] DeBoer, D. R., Parsons, A. R., Aguirre, J. E., Alexander, P., Ali, Z. S., Beardsley, A. P., Bernardi, G., Bowman, J. D., Bradley, R. F., Carilli, C. L., Cheng, C., de Lera Acedo, E., Dillon, J. S., Ewall-Wice, A., Fadana, G., Fagnoni, N., Fritz, R., Furlanetto, S. R., Glendenning, B., Greig, B., Grobbelaar, J., Hazelton, B. J., Hewitt, J. N., Hickish, J., Jacobs, D. C., Julius, A., Kariseb, M., Kohn, S. A., Lekalake, T., Liu, A., Loots, A., MacMahon, D., Malan, L., Malgas, C., Maree, M., Martinot, Z., Mathison, N., Matsetela, E., Mesinger, A., Morales, M. F., Neben, A. R., Patra, N., Pieterse, S., Pober, J. C., Razavi-Ghods, N., Ringuette, J., Robnett, J., Rosie, K., Sell, R., Smith, C., Syce, A., Tegmark, M., Thyagarajan, N., Williams, P. K. G., and Zheng, H. (2017). Hydrogen Epoch of Reionization Array (HERA). *PASP*, 129(4):045001.
- [92] Dent, W. A., Aller, H. D., and Olsen, E. T. (1974). The Evolution of the Radio Spectrum of Cassiopeia a. *ApJL*, 188:L11.
- [93] Di Matteo, T., Ciardi, B., and Miniati, F. (2004). The 21-cm emission from the reionization epoch: extended and point source foregrounds. *MNRAS*, 355:1053–1065.
- [94] Di Matteo, T., Perna, R., Abel, T., and Rees, M. J. (2002). Radio Foregrounds for the 21 Centimeter Tomography of the Neutral Intergalactic Medium at High Redshifts. *ApJ*, 564:576–580.
- [95] Dickinson, C. (2014). BINGO - A novel method to detect BAOs using a total-power radio telescope. *ArXiv e-prints*.
- [96] Dijkstra, M., Haiman, Z., and Spaans, M. (2006). Ly α Radiation from Collapsing Protogalaxies. I. Characteristics of the Emergent Spectrum. *ApJ*, 649:14–36.
- [97] Dine, M. and Stephenson-Haskins, L. (2015). Hybrid inflation with Planck scale fields. *Journal of High Energy Physics*, 9:208.
- [98] Drinkwater, M. J., Jurek, R. J., Blake, C., Woods, D., Pimblet, K. A., Glazebrook, K., Sharp, R., Pracy, M. B., Brough, S., Colless, M., Couch, W. J., Croom, S. M., Davis, T. M., Forbes, D., Forster, K., Gilbank, D. G., Gladders, M., Jelliffe, B., Jones, N., Li, I.-H., Madore, B., Martin, D. C., Poole, G. B., Small, T., Wisnioski, E., Wyder, T., and Yee, H. K. C. (2010). The WiggleZ Dark Energy Survey: survey design and first data release. *MNRAS*, 401:1429–1452.
- [99] Dunkley, J., Komatsu, E., Nolte, M. R., Spergel, D. N., Larson, D., Hinshaw, G., Page, L., Bennett, C. L., Gold, B., Jarosik, N., Weiland, J. L., Halpern, M., Hill, R. S., Kogut, A., Limon, M., Meyer, S. S., Tucker, G. S., Wollack, E., and Wright, E. L. (2009). Five-Year Wilkinson Microwave Anisotropy Probe Observations: Likelihoods and Parameters from the WMAP Data. *ApJS*, 180:306–329.
- [100] Eisenstein, D. J. (2005). Dark energy and cosmic sound [review article]. *New Astron. Rev.*, 49:360–365.
- [101] Ekers, R. and Bell, J. (2000). Radio Frequency Interference. *arXiv Astrophysics e-prints*.
- [102] Ellingson, S. W. and Hampson, G. A. (2002). A subspace-tracking approach to interference nulling for phased array-based radio telescopes. *IEEE Transactions on Antennas and Propagation*, 50:25–30.

- [103] Fan, X., Carilli, C. L., and Keating, B. (2006). Observational Constraints on Cosmic Reionization. *ARA&A*, 44:415–462.
- [104] Feldman, H. A., Kaiser, N., and Peacock, J. A. (1994). Power-spectrum analysis of three-dimensional redshift surveys. *ApJ*, 426:23–37.
- [105] Field, G. B. (1958). Excitation of the Hydrogen 21-CM Line. *Proceedings of the IRE*, 46:240–250.
- [106] Fischer, H. (2011). *A history of the central limit theorem. From classical to modern probability theory.*
- [107] Foley, M., Sasankan, N., Kusakabe, M., and Mathews, G. J. (2017). Revised uncertainties in Big Bang Nucleosynthesis. *International Journal of Modern Physics E*, 26:1741008.
- [108] Freese, K., Frieman, J. A., and Olinto, A. V. (1990). Natural inflation with pseudo Nambu-Goldstone bosons. *Physical Review Letters*, 65:3233–3236.
- [109] Freese, K. and Kinney, W. H. (2015). Natural inflation: consistency with cosmic microwave background observations of Planck and BICEP2. *J. Cosmology Astropart. Phys.*, 3:044.
- [110] Furlanetto, S. R., Oh, S. P., and Briggs, F. H. (2006). Cosmology at low frequencies: The 21 cm transition and the high-redshift Universe. *Phys. Rep.*, 433:181–301.
- [111] Gal, R. R., de Carvalho, R. R., Lopes, P. A. A., Djorgovski, S. G., Brunner, R. J., Mahabal, A., and Odewahn, S. C. (2003). The Northern Sky Optical Cluster Survey. II. An Objective Cluster Catalog for 5800 Square Degrees. *AJ*, 125:2064–2084.
- [112] Gao, X., Li, T., and Shukla, P. (2014). Cosmological observables in multi-field inflation with a non-flat field space. *J. Cosmology Astropart. Phys.*, 10:008.
- [113] Gleser, L., Nusser, A., and Benson, A. J. (2008). Decontamination of cosmological 21-cm maps. *MNRAS*, 391:383–398.
- [114] Gong, J.-O. (2017). Multi-field inflation and cosmological perturbations. *International Journal of Modern Physics D*, 26:1740003.
- [115] Gong, Y., Chen, X., Silva, M., Cooray, A., and Santos, M. G. (2011). The OH Line Contamination of 21 cm Intensity Fluctuation Measurements for $z = 1-4$. *ApJL*, 740:L20.
- [116] Górski, K. M., Hivon, E., Banday, A. J., Wandelt, B. D., Hansen, F. K., Reinecke, M., and Bartelmann, M. (2005). HEALPix: A Framework for High-Resolution Discretization and Fast Analysis of Data Distributed on the Sphere. *ApJ*, 622:759–771.
- [117] Griffiths, D. J. (1982). Hyperfine splitting in the ground state of hydrogen. *American Journal of Physics*, 50:698–703.
- [118] Guzmán, A. E., May, J., Alvarez, H., and Maeda, K. (2011). All-sky Galactic radiation at 45 MHz and spectral index between 45 and 408 MHz. *A&A*, 525:A138.

- [119] Haiman, Z., Spaans, M., and Quataert, E. (2000). *Lya* Cooling Radiation from High-Redshift Halos. *ApJL*, 537:L5–L8.
- [120] Hamaker, J. P. (2000). Understanding radio polarimetry. IV. The full-coherency analogue of scalar self-calibration: Self-alignment, dynamic range and polarimetric fidelity. *A&AS*, 143:515–534.
- [121] Hamilton, A. J. S. (1988). On hierarchical solutions to the BBGKY hierarchy. *ApJ*, 332:67–74.
- [122] Hamilton, A. J. S. and Gott, III, J. R. (1988). Cluster-cluster correlations and constraints on the correlation hierarchy. *ApJ*, 331:641–647.
- [123] Hartmann, D. and Burton, W. B. (1997). *Atlas of Galactic Neutral Hydrogen*.
- [124] Haslam, C. G. T., Salter, C. J., Stoffel, H., and Wilson, W. E. (1982a). A 408 MHz all-sky continuum survey. II - The atlas of contour maps. *A&AS*, 47:1.
- [125] Haslam, C. G. T., Salter, C. J., Stoffel, H., and Wilson, W. E. (1982b). A 408 MHz all-sky continuum survey. II - The atlas of contour maps. *A&AS*, 47:1.
- [126] Haverkorn, M., Katgert, P., and de Bruyn, A. G. (2003). Multi-frequency polarimetry of the Galactic radio background around 350 MHz. I. A region in Auriga around $l = 161$ deg, $b = 16$ deg. *A&A*, 403:1031–1044.
- [127] Högbom, J. A. (1974). Aperture Synthesis with a Non-Regular Distribution of Interferometer Baselines. *A&AS*, 15:417.
- [128] Hou, S. Q., He, J. J., Parikh, A., Kahl, D., Bertulani, C. A., Kajino, T., Mathews, G. J., and Zhao, G. (2017). Non-extensive Statistics to the Cosmological Lithium Problem. *ApJ*, 834:165.
- [129] Huang, Q., Sun, S., Zuo, S., Wu, F., Xu, Y., Yue, B., Ansari, R., and Chen, X. (2018a). An Imaging Algorithm for a Lunar Orbit Interferometer Array. *AJ*, 156:43.
- [130] Huang, Q., Wu, F., and Chen, X. (2019). A high-resolution self-consistent whole sky foreground model. *Science China Physics, Mechanics, and Astronomy*, 62:989511.
- [131] Huang, Q.-Z., Wu, F.-Q., Ansari, R., and Chen, X. (2018b). Extracting 21 cm signal by frequency and angular filtering. *Research in Astronomy and Astrophysics*, 18:114.
- [132] Huynh, M. and Lazio, J. (2013). An Overview of the Square Kilometre Array. *ArXiv e-prints*.
- [133] Iliev, I. T., Shapiro, P. R., Ferrara, A., and Martel, H. (2002). On the Direct Detectability of the Cosmic Dark Ages: 21 Centimeter Emission from Minihalos. *ApJL*, 572:L123–L126.
- [134] Iocco, F., Mangano, G., Miele, G., Pisanti, O., and Serpico, P. D. (2009). Primordial nucleosynthesis: From precision cosmology to fundamental physics. *Phys. Rep.*, 472:1–76.

- [135] Jackson, C. (2005). The Extragalactic Radio Sky at Faint Flux Densities. *pasa*, 22:36–48.
- [136] Jansky, K. G. (1933). Radio Waves from Outside the Solar System. *Nature*, 132:66.
- [137] Jelić, V., Zaroubi, S., Labropoulos, P., Bernardi, G., de Bruyn, A. G., and Koopmans, L. V. E. (2010). Realistic simulations of the Galactic polarized foreground: consequences for 21-cm reionization detection experiments. *MNRAS*, 409:1647–1659.
- [138] Jelić, V., Zaroubi, S., Labropoulos, P., Thomas, R. M., Bernardi, G., Brentjens, M. A., de Bruyn, A. G., Ciardi, B., Harker, G., Koopmans, L. V. E., Pandey, V. N., Schaye, J., and Yatawatta, S. (2008). Foreground simulations for the LOFAR-epoch of reionization experiment. *MNRAS*, 389:1319–1335.
- [139] Jester, S. and Falcke, H. (2009). Science with a lunar low-frequency array: From the dark ages of the Universe to nearby exoplanets. *New Astron. Rev.*, 53:1–26.
- [140] Jones, D. L., Weiler, K. W., Allen, R. J., Desch, M. M., Erickson, W. C., Kaiser, M. L., Kassim, N. E., Kuiper, T. B. H., Mahoney, M. J., Marsh, K. A., Perley, R. A., Preston, R. A., and Stone, R. G. (1998). The Astronomical Low-Frequency Array (ALFA). In Zensus, J. A., Taylor, G. B., and Wrobel, J. M., editors, *IAU Colloq. 164: Radio Emission from Galactic and Extragalactic Compact Sources*, volume 144 of *Astronomical Society of the Pacific Conference Series*, page 393.
- [141] Kalberla, P. M. W., Burton, W. B., Hartmann, D., Arnal, E. M., Bajaja, E., Morras, R., and Pöppel, W. G. L. (2005). The Leiden/Argentine/Bonn (LAB) Survey of Galactic HI. Final data release of the combined LDS and IAR surveys with improved stray-radiation corrections. *A&A*, 440:775–782.
- [142] Kanno, S., Soda, J., and Watanabe, M.-a. (2010). Anisotropic power-law inflation. *J. Cosmology Astropart. Phys.*, 12:024.
- [143] Kassim, N. E., Polisensky, E. J., Clarke, T. E., Hicks, B. C., Crane, P. C., Stewart, K. P., Ray, P. S., Weiler, K. W., Rickard, L. J., Lazio, T. J. W., Lane, W. M., Cohen, A. S., Nord, M. E., Erickson, W. C., and Perley, R. A. (2005). The Long Wavelength Array. In Kassim, N., Perez, M., Junor, W., and Henning, P., editors, *From Clark Lake to the Long Wavelength Array: Bill Erickson's Radio Science*, volume 345 of *Astronomical Society of the Pacific Conference Series*, page 392.
- [144] Kawasaki, M., Kohri, K., Moroi, T., and Takaesu, Y. (2018). Revisiting big-bang nucleosynthesis constraints on long-lived decaying particles. *Phys. Rev. D*, 97(2):023502.
- [145] Kazemi, S., Yatawatta, S., Zaroubi, S., Lampropoulos, P., de Bruyn, A. G., Koopmans, L. V. E., and Noordam, J. (2011). Radio interferometric calibration using the SAGE algorithm. *MNRAS*, 414:1656–1666.
- [146] Keshet, U., Waxman, E., and Loeb, A. (2004). Imprint of Intergalactic Shocks on the Radio Sky. *ApJ*, 617:281–302.
- [147] Kobayashi, T. and Seto, O. (2015). Beginning of Universe through large field hybrid inflation. *Modern Physics Letters A*, 30:1550106.

- [148] Komori, Y. (2011). Cosmic-ray electron spectrum estimated from synchrotron emissions. *International Cosmic Ray Conference*, 6:263.
- [149] Kuiper, T. B. H. and Jones, D. (2000). Lunar Surface Arrays. *Washington DC American Geophysical Union Geophysical Monograph Series*, 119:351–357.
- [150] Landecker, T. L. and Wielebinski, R. (1970). The Galactic Metre Wave Radiation: A two-frequency survey between declinations $+25^\circ$ and -25° and the preparation of a map of the whole sky. *Australian Journal of Physics Astrophysical Supplement*, 16:1.
- [151] Langlois, D. (2008). Cosmological perturbations from multi-field inflation. In *Journal of Physics Conference Series*, volume 140 of *Journal of Physics Conference Series*, page 012004.
- [152] Lawson, K. D., Mayer, C. J., Osborne, J. L., and Parkinson, M. L. (1987). Variations in the Spectral Index of the Galactic Radio Continuum Emission in the Northern Hemisphere. *MNRAS*, 225:307.
- [153] Lazio, J., Kasper, J., Maksimovic, M., Alibay, F., Amiri, N., Bastian, T., Cohen, C., Landi, E., Manchester, W., Reinard, A., Schwadron, N., Cecconi, B., Hallinan, G., Hegedus, A., Krupar, V., and Zaslavsky, A. (2017). The Sun Radio Imaging Space Experiment (SunRISE) Mission. In *EGU General Assembly Conference Abstracts*, volume 19 of *EGU General Assembly Conference Abstracts*, page 5580.
- [154] Leshem, A., van der Veen, A.-J., and Boonstra, A.-J. (2000). Multichannel Interference Mitigation Techniques in Radio Astronomy. *ApJS*, 131:355–373.
- [155] Lewis, A., Challinor, A., and Lasenby, A. (2000). Efficient Computation of Cosmic Microwave Background Anisotropies in Closed Friedmann-Robertson-Walker Models. *ApJ*, 538:473–476.
- [156] Liu, A. and Tegmark, M. (2012). How well can we measure and understand foregrounds with 21-cm experiments? *MNRAS*, 419:3491–3504.
- [157] Loeb, A. and Barkana, R. (2001). The Reionization of the Universe by the First Stars and Quasars. *ARA&A*, 39:19–66.
- [158] Loeb, A. and Zaldarriaga, M. (2004). Measuring the small - scale power spectrum of cosmic density fluctuations through 21 cm tomography prior to the epoch of structure formation. *Phys. Rev. Lett.*, 92:211301.
- [159] Loeb, A. and Zaldarriaga, M. (2004). Measuring the Small-Scale Power Spectrum of Cosmic Density Fluctuations through 21cm Tomography Prior to the Epoch of Structure Formation. *Physical Review Letters*, 92(21):211301.
- [160] Lucchin, F. and Matarrese, S. (1985). Power-law inflation. *Phys. Rev. D*, 32:1316–1322.
- [161] Madau, P., Meiksin, A., and Rees, M. J. (1997). 21 Centimeter Tomography of the Intergalactic Medium at High Redshift. *ApJ*, 475:429–444.

- [162] Mandelbrot, B. (1975). On a decomposable model of a hierarchical universe - Derivation of galactic correlations on the celestial sphere. *Academie des Sciences Paris Comptes Rendus Serie Sciences Mathematiques*, 280:1551–1554.
- [163] Mao, Y., Tegmark, M., McQuinn, M., Zaldarriaga, M., and Zahn, O. (2008). How accurately can 21cm tomography constrain cosmology? *Phys. Rev. D*, 78(2):023529.
- [164] Masui, K. W., Switzer, E. R., Banavar, N., Bandura, K., Blake, C., Calin, L.-M., Chang, T.-C., Chen, X., Li, Y.-C., Liao, Y.-W., Natarajan, A., Pen, U.-L., Peterson, J. B., Shaw, J. R., and Voytek, T. C. (2013). Measurement of 21 cm Brightness Fluctuations at $z \approx 0.8$ in Cross-correlation. *ApJL*, 763:L20.
- [165] Mauch, T., Murphy, T., Buttery, H. J., Curran, J., Hunstead, R. W., Piestrzynski, B., Robertson, J. G., and Sadler, E. M. (2003). SUMSS: a wide-field radio imaging survey of the southern sky - II. The source catalogue. *MNRAS*, 342:1117–1130.
- [166] Mauch, T. and Sadler, E. M. (2007). Radio sources in the 6dFGS: local luminosity functions at 1.4GHz for star-forming galaxies and radio-loud AGN. *MNRAS*, 375:931–950.
- [167] Mimoun, D., Wieczorek, M. A., Alkalai, L., Banerdt, W. B., Baratoux, D., Bougeret, J.-L., Bouley, S., Cecconi, B., Falcke, H., Flohrer, J., Garcia, R. F., Grimm, R., Grott, M., Gurvits, L., Jaumann, R., Johnson, C. L., Knapmeyer, M., Kobayashi, N., Konovalenko, A., Lawrence, D., Le Feuvre, M., Lognonné, P., Neal, C., Oberst, J., Olsen, N., Röttgering, H., Spohn, T., Vennerstrom, S., Woan, G., and Zarka, P. (2012). Farside explorer: unique science from a mission to the farside of the moon. *Experimental Astronomy*, 33:529–585.
- [168] Morales, M. F. and Matejek, M. (2009). Software holography: interferometric data analysis for the challenges of next generation observatories. *MNRAS*, 400:1814–1820.
- [169] Morales, M. F. and Wyithe, J. S. B. (2010). Reionization and Cosmology with 21-cm Fluctuations. *ARA&A*, 48:127–171.
- [170] Mosiane, O., Oozeer, N., Aniyani, A., and Bassett, B. A. (2017). Radio Frequency Interference Detection using Machine Learning. In *Materials Science and Engineering Conference Series*, volume 198 of *Materials Science and Engineering Conference Series*, page 012012.
- [171] Murdoch, H. S., Crawford, D. F., and Jauncey, D. L. (1973). Maximum-Likelihood Estimation of the Number-Flux Distribution of Radio Sources in the Presence of Noise and Confusion. *ApJ*, 183:1–14.
- [172] Nakayama, K., Takahashi, F., and Yanagida, T. T. (2013). Polynomial chaotic inflation in the Planck era. *Physics Letters B*, 725:111–114.
- [173] Nan, R., Li, D., Jin, C., Wang, Q., Zhu, L., Zhu, W., Zhang, H., Yue, Y., and Qian, L. (2011). The Five-Hundred Aperture Spherical Radio Telescope (fast) Project. *International Journal of Modern Physics D*, 20:989–1024.
- [174] Newburgh, L. B., Bandura, K., Bucher, M. A., Chang, T.-C., Chiang, H. C., Cliche, J. F., Davé, R., Dobbs, M., Clarkson, C., Ganga, K. M., Gogo, T., Gumba, A., Gupta, N., Hilton, M., Johnstone, B., Karastergiou, A., Kunz, M., Lokhorst, D., Maartens, R.,

- Macpherson, S., Mdlalose, M., Moodley, K., Ngwenya, L., Parra, J. M., Peterson, J., Recnik, O., Saliwanchik, B., Santos, M. G., Sievers, J. L., Smirnov, O., Stronkhorst, P., Taylor, R., Vanderlinde, K., Van Vuuren, G., Weltman, A., and Witzemann, A. (2016). HIRAX: a probe of dark energy and radio transients. In *Ground-based and Airborne Telescopes VI*, volume 9906 of *procspie*, page 99065X.
- [175] Norris, R. P., Hopkins, A. M., Afonso, J., Brown, S., Condon, J. J., Dunne, L., Feain, I., Hollow, R., Jarvis, M., Johnston-Hollitt, M., Lenc, E., Middelberg, E., Padovani, P., Prandoni, I., Rudnick, L., and Seymour, N. (2011). EMU: Evolutionary Map of the Universe. *Publ. Astron. Soc. Australia*, 28:215–248.
- [176] Novaco, J. C. and Brown, L. W. (1978). Nonthermal galactic emission below 10 megahertz. *ApJ*, 221:114–123.
- [177] Nyquist, H. (1928). Thermal Agitation of Electric Charge in Conductors. *Physical Review*, 32:110–113.
- [178] Offringa, A. R., de Bruyn, A. G., Biehl, M., Zaroubi, S., Bernardi, G., and Pandey, V. N. (2010a). Post-correlation radio frequency interference classification methods. *MNRAS*, 405:155–167.
- [179] Offringa, A. R., de Bruyn, A. G., Zaroubi, S., and Biehl, M. (2010b). A LOFAR RFI detection pipeline and its first results. *arXiv e-prints*.
- [180] Offringa, A. R., McKinley, B., Hurley-Walker, N., Briggs, F. H., Wayth, R. B., Kaplan, D. L., Bell, M. E., Feng, L., Neben, A. R., Hughes, J. D., Rhee, J., Murphy, T., Bhat, N. D. R., Bernardi, G., Bowman, J. D., Cappallo, R. J., Corey, B. E., Deshpande, A. A., Emrich, D., Ewall-Wice, A., Gaensler, B. M., Goetze, R., Greenhill, L. J., Hazelton, B. J., Hindson, L., Johnston-Hollitt, M., Jacobs, D. C., Kasper, J. C., Kratzenberg, E., Lenc, E., Lonsdale, C. J., Lynch, M. J., McWhirter, S. R., Mitchell, D. A., Morales, M. F., Morgan, E., Kudryavtseva, N., Oberoi, D., Ord, S. M., Pindor, B., Procopio, P., Prabu, T., Riding, J., Roshi, D. A., Shankar, N. U., Srivani, K. S., Subrahmanyan, R., Tingay, S. J., Waterson, M., Webster, R. L., Whitney, A. R., Williams, A., and Williams, C. L. (2014). WSCLEAN: an implementation of a fast, generic wide-field imager for radio astronomy. *MNRAS*, 444:606–619.
- [181] Otte, B., Gallagher, III, J. S., and Reynolds, R. J. (2002). Emission-Line Ratios and Variations in Temperature and Ionization State in the Diffuse Ionized Gas of Five Edge-on Galaxies. *ApJ*, 572:823–837.
- [182] Overzier, R. A., Röttgering, H. J. A., Rengelink, R. B., and Wilman, R. J. (2003). The spatial clustering of radio sources in NVSS and FIRST; implications for galaxy clustering evolution. *A&A*, 405:53–72.
- [183] Ozsoy, O. (2018). On synthetic gravitational waves from multi-field inflation. *J. Cosmology Astropart. Phys.*, 4:062.
- [184] Paciga, G., Chang, T.-C., Gupta, Y., Nityanada, R., Odegova, J., Pen, U.-L., Peterson, J. B., Roy, J., and Sigurdson, K. (2011). The GMRT Epoch of Reionization experiment: a new upper limit on the neutral hydrogen power spectrum at z 8.6. *MNRAS*, 413:1174–1183.

- [185] Parsons, A. R., Backer, D. C., Foster, G. S., Wright, M. C. H., Bradley, R. F., Gugliucci, N. E., Parashare, C. R., Benoit, E. E., Aguirre, J. E., Jacobs, D. C., Carilli, C. L., Herne, D., Lynch, M. J., Manley, J. R., and Werthimer, D. J. (2010). The Precision Array for Probing the Epoch of Re-ionization: Eight Station Results. *AJ*, 139:1468–1480.
- [186] Peck, L. W. and Fenech, D. M. (2013). SERPent: Automated reduction and RFI-mitigation software for e-MERLIN. *Astronomy and Computing*, 2:54–66.
- [187] Perley, R. A. (1999). Imaging with Non-Coplanar Arrays. In Taylor, G. B., Carilli, C. L., and Perley, R. A., editors, *Synthesis Imaging in Radio Astronomy II*, volume 180 of *Astronomical Society of the Pacific Conference Series*, page 383.
- [188] Perley, R. A. and Butler, B. J. (2013). An Accurate Flux Density Scale from 1 to 50 GHz. *ApJS*, 204:19.
- [189] Perley, R. A. and Butler, B. J. (2017). An Accurate Flux Density Scale from 50 MHz to 50 GHz. *ApJS*, 230:7.
- [190] Peterson, J. B., Aleksan, R., Ansari, R., Bandura, K., Bond, D., Bunton, J., Carlson, K., Chang, T.-C., DeJongh, F., Dobbs, M., Dodelson, S., Darhmaoui, H., Gnedin, N., Halpern, M., Hogan, C., Le Goff, J.-M., Liu, T. T., Legrouri, A., Loeb, A., Loudiyi, K., Magneville, C., Marriner, J., McGinnis, D. P., McWilliams, B., Moniez, M., Palanque-Delabruille, N., Pasquinelli, R. J., Pen, U.-L., Rich, J., Scarpine, V., Seo, H.-J., Sigurdson, K., Seljak, U., Stebbins, A., Steffen, J. H., Stoughton, C., Timbie, P. T., Vallinotto, A., and Teche, C. (2009). 21-cm Intensity Mapping. In *astro2010: The Astronomy and Astrophysics Decadal Survey*, volume 2010 of *Astronomy*.
- [191] Peterson, J. B., Pen, U. L., and Wu, X. P. (2004). The Primeval Structure Telescope. In *American Astronomical Society Meeting Abstracts*, volume 36 of *Bulletin of the American Astronomical Society*, page 1560.
- [192] Planck, M. and Braun, C. (1992). The theory of heat radiation. *Applied Optics - APPL OPT*, 31:01.
- [193] Planck Collaboration, Adam, R., Ade, P. A. R., Aghanim, N., Arnaud, M., Ashdown, M., Aumont, J., Baccigalupi, C., Banday, A. J., Barreiro, R. B., and et al. (2016a). Planck 2015 results. IX. Diffuse component separation: CMB maps. *A&A*, 594:A9.
- [194] Planck Collaboration, Ade, P. A. R., Aghanim, N., Alves, M. I. R., Arnaud, M., Ashdown, M., Aumont, J., Baccigalupi, C., Banday, A. J., Barreiro, R. B., and et al. (2016b). Planck 2015 results. XXV. Diffuse low-frequency Galactic foregrounds. *A&A*, 594:A25.
- [195] Planck Collaboration, Ade, P. A. R., Aghanim, N., Arnaud, M., Ashdown, M., Aumont, J., Baccigalupi, C., Banday, A. J., Barreiro, R. B., Bartlett, J. G., and et al. (2016c). Planck 2015 results. XIII. Cosmological parameters. *A&A*, 594:A13.
- [196] Planck Collaboration, Aghanim, N., Akrami, Y., Ashdown, M., Aumont, J., Baccigalupi, C., Ballardini, M., Banday, A. J., Barreiro, R. B., Bartolo, N., Basak, S., Battye, R., Benabed, K., Bernard, J.-P., Bersanelli, M., Bielewicz, P., Bock, J. J., and Bond, J. R. (2018a). Planck 2018 results. VI. Cosmological parameters. *arXiv e-prints*.

- [197] Planck Collaboration, Akrami, Y., Ashdown, M., Aumont, J., Baccigalupi, C., Ballardini, M., Banday, A. J., Barreiro, R. B., Bartolo, N., Basak, S., Benabed, K., Bersanelli, M., Bielewicz, P., Bond, J. R., Borrill, J., Bouchet, F. R., Boulanger, F., Bucher, M., Burigana, C., Calabrese, E., and Cardoso, J.-F. (2018b). Planck 2018 results. IV. Diffuse component separation. *arXiv e-prints*.
- [198] Platania, P., Bensadoun, M., Bersanelli, M., De Amici, G., Kogut, A., Levin, S., Maino, D., and Smoot, G. F. (1998). A Determination of the Spectral Index of Galactic Synchrotron Emission in the 1-10 GHz Range. *ApJ*, 505:473–483.
- [199] Platania, P., Burigana, C., Maino, D., Caserini, E., Bersanelli, M., Cappellini, B., and Mennella, A. (2003). Full sky study of diffuse Galactic emission at decimeter wavelengths. *A&A*, 410:847–863.
- [200] Plice, L., Galal, K., and Burns, J. O. (2017). DARE Mission Design: Low RFI Observations from a Low-Altitude Frozen Lunar Orbit. *ArXiv e-prints*.
- [201] Pritchard, J. R. and Loeb, A. (2008). Evolution of the 21cm signal throughout cosmic history. *Phys. Rev. D*, 78(10):103511.
- [202] Pritchard, J. R. and Loeb, A. (2012). 21 cm cosmology in the 21st century. *Reports on Progress in Physics*, 75(8):086901.
- [203] Reber, G. (1944). Cosmic Static. *ApJ*, 100:279.
- [204] Reber, G. (1994). Hectometer Radio Astronomy. *J. R. Astron. Soc. Canada*, 88:297.
- [205] Reich, P. and Reich, W. (1988). A map of spectral indices of the Galactic radio continuum emission between 408 MHz and 1420 MHz for the entire northern sky. *A&AS*, 74:7–20.
- [206] Reich, P., Testori, J. C., and Reich, W. (2001). A radio continuum survey of the southern sky at 1420 MHz. The atlas of contour maps. *A&A*, 376:861–877.
- [207] Reichart, D. E. and Stephens, A. W. (2000). The Fading of Supernova Remnant Cassiopeia A from 38 MHz to 16.5 GHz from 1949 to 1999 with New Observations at 1405 MHz. *ApJ*, 537:904–908.
- [208] Remazeilles, M., Dickinson, C., Banday, A. J., Bigot-Sazy, M.-A., and Ghosh, T. (2015). An improved source-subtracted and destriped 408-MHz all-sky map. *MNRAS*, 451:4311–4327.
- [209] Roger, R. S., Costain, C. H., Landecker, T. L., and Swerdlyk, C. M. (1999). The radio emission from the Galaxy at 22 MHz. *A&AS*, 137:7–19.
- [210] Rottgering, H. J. A., Braun, R., Barthel, P. D., van Haarlem, M. P., Miley, G. K., Morganti, R., and Snellen, I. (2006). LOFAR - Opening up a new window on the Universe. In *Conference on Cosmology, Galaxy Formation and Astro-Particle Physics on the Pathway to the SKA Oxford, England, April 10-12, 2006*.
- [211] Ryle, M. and Vonberg, D. D. (1946). Solar Radiation on 175 Mc./s. *Nature*, 158:339–340.

- [212] Sadler, E. M., Jackson, C. A., Cannon, R. D., McIntyre, V. J., Murphy, T., Bland-Hawthorn, J., Bridges, T., Cole, S., Colless, M., Collins, C., Couch, W., Dalton, G., De Propris, R., Driver, S. P., Efstathiou, G., Ellis, R. S., Frenk, C. S., Glazebrook, K., Lahav, O., Lewis, I., Lumsden, S., Maddox, S., Madgwick, D., Norberg, P., Peacock, J. A., Peterson, B. A., Sutherland, W., and Taylor, K. (2002). Radio sources in the 2dF Galaxy Redshift Survey - II. Local radio luminosity functions for AGN and star-forming galaxies at 1.4 GHz. *MNRAS*, 329:227–245.
- [213] Salvini, S. and Wijnholds, S. J. (2014). Fast gain calibration in radio astronomy using alternating direction implicit methods: Analysis and applications. *A&A*, 571:A97.
- [214] Sandage, A., Tammann, G. A., and Yahil, A. (1979). The velocity field of bright nearby galaxies. I - The variation of mean absolute magnitude with redshift for galaxies in a magnitude-limited sample. *ApJ*, 232:352–364.
- [215] Santos, M. G., Cooray, A., and Knox, L. (2005). Multifrequency Analysis of 21 Centimeter Fluctuations from the Era of Reionization. *ApJ*, 625:575–587.
- [216] Sault, R. J., Hamaker, J. P., and Bregman, J. D. (1996). Understanding radio polarimetry. II. Instrumental calibration of an interferometer array. *A&AS*, 117:149–159.
- [217] Sault, R. J. and Oosterloo, T. A. (2007). Imaging algorithms in radio interferometry. *ArXiv Astrophysics e-prints*.
- [218] Saunders, W., Rowan-Robinson, M., Lawrence, A., Efstathiou, G., Kaiser, N., Ellis, R. S., and Frenk, C. S. (1990). The 60-micron and far-infrared luminosity functions of IRAS galaxies. *MNRAS*, 242:318–337.
- [219] Sbordone, L., Bonifacio, P., Caffau, E., Ludwig, H.-G., Behara, N. T., González Hernández, J. I., Steffen, M., Cayrel, R., Freytag, B., van't Veer, C., Molaro, P., Plez, B., Sivarani, T., Spite, M., Spite, F., Beers, T. C., Christlieb, N., François, P., and Hill, V. (2010). The metal-poor end of the Spite plateau. I. Stellar parameters, metallicities, and lithium abundances. *A&A*, 522:A26.
- [220] Scott, D. and Rees, M. J. (1990). The 21-cm line at high redshift: a diagnostic for the origin of large scale structure. *MNRAS*, 247:510.
- [221] Seo, H.-J., Dodelson, S., Marriner, J., McGinnis, D., Stebbins, A., Stoughton, C., and Vallinotto, A. (2010). A Ground-based 21 cm Baryon Acoustic Oscillation Survey. *ApJ*, 721:164–173.
- [222] Shaver, P. A., Windhorst, R. A., Madau, P., and de Bruyn, A. G. (1999). Can the reionization epoch be detected as a global signature in the cosmic background? *A&A*, 345:380–390.
- [223] Shaw, J. R., Sigurdson, K., Pen, U.-L., Stebbins, A., and Sitwell, M. (2014). All-sky Interferometry with Spherical Harmonic Transit Telescopes. *ApJ*, 781:57.
- [224] Shaw, J. R., Sigurdson, K., Sitwell, M., Stebbins, A., and Pen, U.-L. (2015). Coaxing cosmic 21 cm fluctuations from the polarized sky using m-mode analysis. *Phys. Rev. D*, 91(8):083514.

- [225] Sironi, G. (1974). The spectrum of the galactic non-thermal background radiation-1. Observations at 151-5 and 408 MHz. *MNRAS*, 166:345–354.
- [226] Smirnov, O. M. (2011). Revisiting the radio interferometer measurement equation. II. Calibration and direction-dependent effects. *A&A*, 527:A107.
- [227] Smirnov, O. M. and Tasse, C. (2015). Radio interferometric gain calibration as a complex optimization problem. *MNRAS*, 449:2668–2684.
- [228] Spergel, D. N., Bean, R., Doré, O., Nolta, M. R., Bennett, C. L., Dunkley, J., Hinshaw, G., Jarosik, N., Komatsu, E., Page, L., Peiris, H. V., Verde, L., Halpern, M., Hill, R. S., Kogut, A., Limon, M., Meyer, S. S., Odegard, N., Tucker, G. S., Weiland, J. L., Wollack, E., and Wright, E. L. (2007). Three-Year Wilkinson Microwave Anisotropy Probe (WMAP) Observations: Implications for Cosmology. *ApJS*, 170:377–408.
- [229] Spinelli, M., Bernardi, G., and Santos, M. G. (2018). Simulations of Galactic polarized synchrotron emission for Epoch of Reionization observations. *MNRAS*, 479:275–283.
- [230] Sramek, R. A. and Schwab, F. R. (1989). Imaging. In Perley, R. A., Schwab, F. R., and Bridle, A. H., editors, *Synthesis Imaging in Radio Astronomy*, volume 6 of *Astronomical Society of the Pacific Conference Series*, page 83.
- [231] Steigman, G. (2007). Primordial Nucleosynthesis in the Precision Cosmology Era. *Annual Review of Nuclear and Particle Science*, 57:463–491.
- [232] Strong, A. W., Moskalenko, I. V., and Ptuskin, V. S. (2007). Cosmic-Ray Propagation and Interactions in the Galaxy. *Annual Review of Nuclear and Particle Science*, 57:285–327.
- [233] Strong, A. W., Orlando, E., and Jaffe, T. R. (2011). The interstellar cosmic-ray electron spectrum from synchrotron radiation and direct measurements. *A&A*, 534:A54.
- [234] Subrahmanyan, R. and Ekers, R. D. (2002). CMB observations using the SKA. *arXiv Astrophysics e-prints*.
- [235] Switzer, E. R., Chang, T.-C., Masui, K. W., Pen, U.-L., and Voytek, T. C. (2015). Interpreting the Unresolved Intensity of Cosmologically Redshifted Line Radiation. *ApJ*, 815:51.
- [236] Switzer, E. R., Masui, K. W., Bandura, K., Calin, L.-M., Chang, T.-C., Chen, X.-L., Li, Y.-C., Liao, Y.-W., Natarajan, A., Pen, U.-L., Peterson, J. B., Shaw, J. R., and Voytek, T. C. (2013). Determination of z 0.8 neutral hydrogen fluctuations using the 21 cm intensity mapping autocorrelation. *MNRAS*, 434:L46–L50.
- [237] Tasse, C., van der Tol, S., van Zwieten, J., van Diepen, G., and Bhatnagar, S. (2013). Applying full polarization A-Projection to very wide field of view instruments: An imager for LOFAR. *A&A*, 553:A105.
- [238] Tegmark, M. (1997). How to Make Maps from Cosmic Microwave Background Data without Losing Information. *ApJL*, 480:L87–L90.

- [239] Tegmark, M., Eisenstein, D. J., Strauss, M. A., Weinberg, D. H., Blanton, M. R., Frieman, J. A., Fukugita, M., Gunn, J. E., Hamilton, A. J. S., Knapp, G. R., Nichol, R. C., Ostriker, J. P., Padmanabhan, N., Percival, W. J., Schlegel, D. J., Schneider, D. P., Scoccimarro, R., and Seljak, U. (2006). Cosmological constraints from the SDSS luminous red galaxies. *Phys. Rev. D*, 74(12):123507.
- [240] Tello, C., Villela, T., Torres, S., Bersanelli, M., Smoot, G. F., Ferreira, I. S., Cingoz, A., Lamb, J., Barbosa, D., Perez-Becker, D., Ricciardi, S., Currivan, J. A., Platania, P., and Maino, D. (2013). VizieR Online Data Catalog: The 2.3GHz continuum survey of the GEM project (Tello+, 2013). *VizieR Online Data Catalog*, 355.
- [241] Testori, J. C., Reich, P., Bava, J. A., Colomb, F. R., Hurrel, E. E., Larrarte, J. J., Reich, W., and Sanz, A. J. (2001). A radio continuum survey of the southern sky at 1420 MHz. Observations and data reduction. *A&A*, 368:1123–1132.
- [242] Thompson, A. R., Gergely, T. E., and vanden Bout, P. A. (1991). Interference and radioastronomy. *Physics Today*, 44:41–49.
- [243] Thompson, A. R., Moran, J. M., and Swenson, G. W. (1986). *Interferometry and synthesis in radio astronomy*.
- [244] Tingay, S. J., Goeke, R., Bowman, J. D., Emrich, D., Ord, S. M., Mitchell, D. A., Morales, M. F., Booler, T., Crosse, B., Wayth, R. B., Lonsdale, C. J., Tremblay, S., Pallot, D., Colegate, T., Wicenc, A., Kudryavtseva, N., Arcus, W., Barnes, D., Bernardi, G., Briggs, F., Burns, S., Bunton, J. D., Cappallo, R. J., Corey, B. E., Deshpande, A., Desouza, L., Gaensler, B. M., Greenhill, L. J., Hall, P. J., Hazelton, B. J., Herne, D., Hewitt, J. N., Johnston-Hollitt, M., Kaplan, D. L., Kasper, J. C., Kincaid, B. B., Koenig, R., Kratzenberg, E., Lynch, M. J., Mckinley, B., Mcwhirter, S. R., Morgan, E., Oberoi, D., Pathikulangara, J., Prabu, T., Remillard, R. A., Rogers, A. E. E., Roshi, A., Salah, J. E., Sault, R. J., Udaya-Shankar, N., Schlagenhauser, F., Srivani, K. S., Stevens, J., Subrahmanyam, R., Waterson, M., Webster, R. L., Whitney, A. R., Williams, A., Williams, C. L., and Wyithe, J. S. B. (2013). The Murchison Widefield Array: The Square Kilometre Array Precursor at Low Radio Frequencies. *PASA*, 30:7.
- [245] Toffolatti, L., Franceschini, A., Danese, L., and de Zotti, G. (1987). The local radio luminosity function of galaxies. *A&A*, 184:7–15.
- [246] Trotter, A. S., Reichart, D. E., Egger, R. E., Stýblová, J., Paggén, M. L., Martin, J. R., Dutton, D. A., Reichart, J. E., Kumar, N. D., Maples, M. P., Barlow, B. N., Berger, T. A., Foster, A. C., Frank, N. R., Ghigo, F. D., Haislip, J. B., Heatherly, S. A., Kouprianov, V. V., LaCluyzé, A. P., Moffett, D. A., Moore, J. P., Stanley, J. L., and White, S. (2017). The fading of Cassiopeia A, and improved models for the absolute spectrum of primary radio calibration sources. *MNRAS*, 469:1299–1313.
- [247] Väisänen, P., Tollestrup, E. V., and Fazio, G. G. (2001). Confusion limit resulting from galaxies: using the Infrared Array Camera on board SIRTf. *MNRAS*, 325:1241–1252.
- [248] Van Eck, C. L., Haverkorn, M., Alves, M. I. R., Beck, R., Best, P., Carretti, E., Chyży, K. T., Farnes, J. S., Ferrière, K., Hardcastle, M. J., Heald, G., Horellou, C., Iacobelli, M., Jelić, V., Mulcahy, D. D., O’Sullivan, S. P., Polderman, I. M., Reich, W., Riseley, C. J., Röttgering, H., Schnitzeler, D. H. F. M., Shimwell, T. W., Vacca, V., Vink, J., and

- White, G. J. (2018). Polarized point sources in the LOFAR Two-meter Sky Survey: A preliminary catalog. *A&A*, 613:A58.
- [249] Van Eck, C. L., Haverkorn, M., Alves, M. I. R., Beck, R., de Bruyn, A. G., Enßlin, T., Farnes, J. S., Ferrière, K., Heald, G., Horellou, C., Horneffer, A., Iacobelli, M., Jelić, V., Martí-Vidal, I., Mulcahy, D. D., Reich, W., Röttgering, H. J. A., Scaife, A. M. M., Schnitzeler, D. H. F. M., Sobey, C., and Sridhar, S. S. (2017). Faraday tomography of the local interstellar medium with LOFAR: Galactic foregrounds towards IC 342. *A&A*, 597:A98.
- [250] van Haarlem, M. P., Wise, M. W., Gunst, A. W., Heald, G., McKean, J. P., and Hessels, J. W. T. (2013). LOFAR: The LOw-Frequency ARray. *A&A*, 556:A2.
- [251] van Weeren, R. J., Williams, W. L., Hardcastle, M. J., Shimwell, T. W., Rafferty, D. A., Sabater, J., Heald, G., Sridhar, S. S., Dijkema, T. J., Brunetti, G., Brüggén, M., Andrade-Santos, F., and Ogrean, G. A. (2016). LOFAR Facet Calibration. *ApJS*, 223:2.
- [252] Vedantham, H., Udaya Shankar, N., and Subrahmanyam, R. (2012). Imaging the Epoch of Reionization: Limitations from Foreground Confusion and Imaging Algorithms. *ApJ*, 745:176.
- [253] Wagoner, R. V. (1973). Big-Bang Nucleosynthesis Revisited. *ApJ*, 179:343–360.
- [254] Wang, Q. and Liu, J. (2016). A Chang'e-4 mission concept and vision of future Chinese lunar exploration activities. *Acta Astronautica*, 127:678–683.
- [255] Wang, X., Tegmark, M., Santos, M. G., and Knox, L. (2006). 21 cm Tomography with Foregrounds. *ApJ*, 650:529–537.
- [256] Weber, R., Faye, C., Biraud, F., and Dansou, J. (1997). Spectral detector for interference time blanking using quantized correlator. *A&AS*, 126:161–167.
- [257] Webster, A. S. (1974). The spectrum of the galactic non-thermal background radiational Observations at 408, 610 and 1407 MHz. *MNRAS*, 166:355–372.
- [258] White, M. (2005). Baryon oscillations. *Astroparticle Physics*, 24:334–344.
- [259] Wiener, N. (1949). *Extrapolation, Interpolation, and Smoothing of Stationary Time Series*.
- [260] Winkel, B., Kerp, J., and Stanko, S. (2007). RFI detection by automated feature extraction and statistical analysis. *Astronomische Nachrichten*, 328:68–79.
- [261] Wolz, L., Abdalla, F. B., Blake, C., Shaw, J. R., Chapman, E., and Rawlings, S. (2014). The effect of foreground subtraction on cosmological measurements from intensity mapping. *MNRAS*, 441:3271–3283.
- [262] Xu, Y., Wang, X., and Chen, X. (2015). Forecasts on the Dark Energy and Primordial Non-Gaussianity Observations with the Tianlai Cylinder Array. *ApJ*, 798:40.

- [263] Zarka, P., Bougeret, J.-L., Briand, C., Cecconi, B., Falcke, H., Girard, J., Griebmeier, J.-M., Hess, S., Klein-Wolt, M., Konovalenko, A., Lamy, L., Mimoun, D., and Aminaei, A. (2012). Planetary and exoplanetary low frequency radio observations from the Moon. *Planet. Space Sci.*, 74:156–166.
- [264] Zhang, J., Ansari, R., Chen, X., Campagne, J.-E., Magneville, C., and Wu, F. (2016a). Sky reconstruction from transit visibilities: PAON-4 and Tianlai dish array. *MNRAS*, 461:1950–1966.
- [265] Zhang, J., Ansari, R., Chen, X., Campagne, J.-E., Magneville, C., and Wu, F. (2016b). Sky reconstruction from transit visibilities: PAON-4 and Tianlai dish array. *MNRAS*, 461:1950–1966.
- [266] Zhang, J., Zuo, S., Ansari, R., Chen, X., Li, Y., Wu, F., Campagne, J.-E., and Magneville, C. (2016c). Sky reconstruction for the Tianlai cylinder array. *arXiv e-prints*.
- [267] Zhang, J., Zuo, S.-F., Ansari, R., Chen, X., Li, Y.-C., Wu, F.-Q., Campagne, J.-E., and Magneville, C. (2016d). Sky reconstruction for the Tianlai cylinder array. *Research in Astronomy and Astrophysics*, 16:158.
- [268] Zhang, J. X., Chen, X. L., Cao, X. B., and An, J. S. (2017). Formation Flying Around Lunar for Ultra-Long Wave Radio Interferometer Mission. *Journal of Deep Space Exploration*, 4:158.
- [269] Zhao, J., Zou, X., and Weng, F. (2013). WindSat Radio-Frequency Interference Signature and Its Identification Over Greenland and Antarctic. *IEEE Transactions on Geoscience and Remote Sensing*, 51:4830–4839.
- [270] Zheng, H., Tegmark, M., Dillon, J. S., Kim, D. A., Liu, A., Neben, A. R., Jonas, J., Reich, P., and Reich, W. (2017a). An improved model of diffuse galactic radio emission from 10 MHz to 5 THz. *MNRAS*, 464:3486–3497.
- [271] Zheng, H., Tegmark, M., Dillon, J. S., Liu, A., Neben, A. R., Tribiano, S. M., Bradley, R. F., Buza, V., Ewall-Wice, A., Gharibyan, H., Hickish, J., Kunz, E., Losh, J., Lutomirski, A., Morgan, E., Narayanan, S., Perko, A., Rosner, D., Sanchez, N., Schutz, K., Valdez, M., Villasenor, J., Yang, H., Zarb Adami, K., Zelko, I., and Zheng, K. (2017b). Brute-force mapmaking with compact interferometers: a MITEoR northern sky map from 128 to 175 MHz. *MNRAS*, 465:2901–2915.
- [272] Zheng, Q., Wu, X.-P., Johnston-Hollitt, M., Gu, J.-h., and Xu, H. (2016). Radio Sources in the NCP Region Observed with the 21 Centimeter Array. *ApJ*, 832:190.
- [273] Zuo, S., Chen, X., Ansari, R., and Lu, Y. (2019). 21 cm Signal Recovery via Robust Principal Component Analysis. *AJ*, 157:4.

Appendix A

Radio source count

A.1 Radio luminosity function

Two types of radio luminosity functions are generally used

- $\rho(L, z)$: the comoving number density of radio sources in luminosity range from L to $L + dL$ at redshift z ;
- $\rho_m(L, z) d[\log_m(L)]$: the comoving number density of radio sources in luminosity range from $\log_m(L)$ to $\log_m(L) + d[\log_m(L)]$ at redshift z .

The relation between two types is

$$\rho_m(L, z) = \ln(m) L \rho(L, z) \quad (\text{A.1})$$

Also, there are two methods to compute the local luminosity function. One is the maximum volume V_m method [76, 77, 245], the other is the STY maximum likelihood method [214]. In this work, the maximum volume method is used.

Move the target source forward and backward along the redshift, to obtain the maximum volume which the source can still be observed

$$\rho_m(L) = \sum_{i=1}^N \left(\frac{1}{V_m} \right)_i \quad (\text{A.2})$$

where N is the number of the sources.

Using the data from [166], and the cosmological parameters from Planck 2015 [195]. For the data fitting, two cases are taken into account. One case is the late-type galaxies

(star-forming), the empirical formula of the luminosity is [218]

$$\rho_m(L) = C \left[\frac{L}{L_*} \right]^{1-a} \exp \left\{ -\frac{1}{2} \left[\frac{\log_{10} \left(1 + \frac{L}{L_*} \right)}{\sigma} \right]^2 \right\} \quad (\text{A.3})$$

The best-fit parameters are

$$\begin{aligned} C &= 10^{-2.883} \text{mag}^{-1} \text{Mpc}^{-1} \\ L_* &= 10^{21.22} \text{WHz}^{-1} \\ a &= 1.040 \\ \sigma &= 0.608 \end{aligned} \quad (\text{A.4})$$

The other case is the radio loud active galactic nucleus, the empirical formula of the luminosity is [77]

$$\log_{10}(\rho_m) = Y - \frac{3}{2} \log_{10}(L) - \sqrt{B^2 + \left[\frac{\log_{10}(L) - X}{W} \right]^2} \quad (\text{A.5})$$

The best-fit parameters are

$$\begin{aligned} Y &= 33.889 \\ B &= 2.265 \\ X &= 25.961 \\ W &= 0.848 \end{aligned} \quad (\text{A.6})$$

The local radio luminosity function is shown in Fig. A.1.

A.2 radio normalized differential count

To compute the differential count, the cosmological model which is used is Λ CDM model, and the cosmological parameters is from Plank 2015 [195]. Assume there is a isotropy radio source at redshift z at frequency ν , the flux density spectral index is $\alpha \equiv -d[\ln(S)]/d[\ln(\nu)]$.

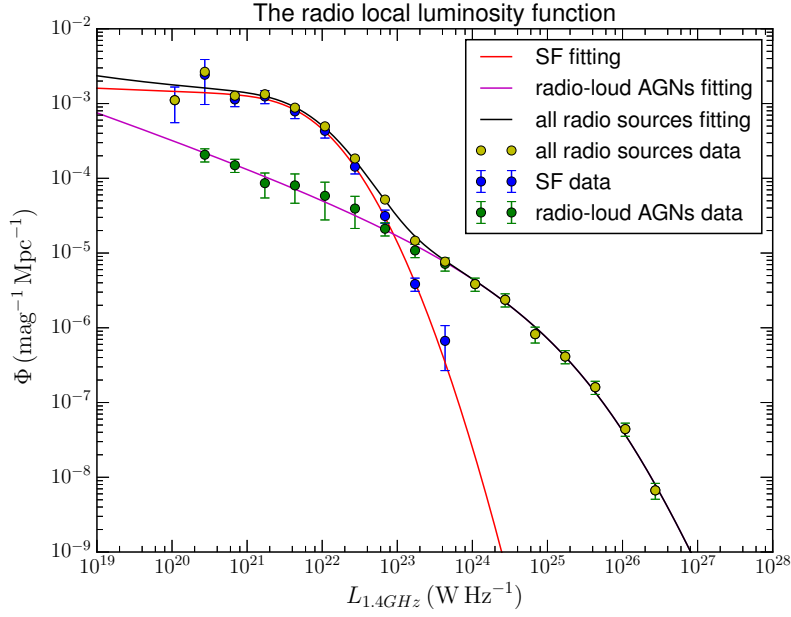


Fig. A.1 The local radio luminosity function at 1.4 GHz. Blue, green and yellow points are the late-type galaxies, radio loud active galactic nucleus and their sum respectively. Red, purple and blank curves are the fitting curves of late-type galaxies, radio loud active galactic nucleus and their sum respectively.

For the Λ CDM universe, if ignoring the radiation density, the luminosity distance of this source is

$$D_L = \frac{c(1+z)}{H_0} \int_0^z \frac{dz'}{\sqrt{\Omega_\Lambda + \Omega_m(1+z')^3}} \quad (\text{A.7})$$

The relationship between the flux density S and the luminosity L is [76]

$$S = \frac{L}{4\pi D_L^2(1+z)^{1+\alpha}} = \frac{L}{A(1+z)^{1+\alpha}} \quad (\text{A.8})$$

and then obtain

$$\frac{dL}{dS} = A(1+z)^{1+\alpha} \quad (\text{A.9})$$

In the comoving distance range of r to $r + dr$, the number of sources which have the luminosity range of L to $L + dL$ is $\rho_m(L, z)dLAdr$. This is equal to $\eta(S, z)dSdz$ which is the number of sources in the flux density range of S to $S + dS$ at redshift range of z to $z + dz$.

The comoving distance is

$$dr = \frac{cdz}{H} = \frac{cdz}{H_0 \sqrt{\Omega_\Lambda + \Omega_m(1+z)^3}} \quad (\text{A.10})$$

Let $\eta(S, z)dSdz = \rho_m(L, z)dLAdr$, where $\eta(S, z)$ is the number of sources in unit flux density and unit redshift

$$\eta(S, z) = \rho(L, z)A \frac{dL dr}{dS dz} = \frac{cA^2(1+z)^{1+\alpha}\rho(L, z)}{H_0 \sqrt{\Omega_\Lambda + \Omega_m(1+z)^3}} \quad (\text{A.11})$$

The normalized differential count is defined as [76]

$$S^{5/2}n(S) \equiv \frac{1}{4\pi} \int_0^\infty S^{5/2}\eta(S, z)dz \quad (\text{A.12})$$

where $n(S)$ is the number of radio source per steradian per flux density, the weight $S^{5/2}$ is for the traditional “static Euclidean” normalization [79].

The radio luminosity function ρ_m is a function of redshift, and can be separated into two independent parts, one is the “pure” luminosity evolution, the other is the “pure” density evolution [76]:

$$\rho_m(L, z) = g(z) \rho_m\left(\frac{L}{f(z)}, 0\right) \quad (\text{A.13})$$

where $f(z)$ and $g(z)$ are power-laws, and $g(z)$ also has a cutoff

$$f(z) = (1+z)^x, \quad g(z) = (1+z)^y e^{-\left(\frac{z}{z_c}\right)^q} \quad (\text{A.14})$$

Using the complete sample of NVSS+SUMSS (Sec. 3.3.1) to fit the luminosity evolution function, the best-fit parameters are

$$\begin{aligned} x &= 6.676 \\ y &= -8.335 \\ z_c &= 2.397 \\ q &= 2.526 \end{aligned} \quad (\text{A.15})$$

Finally, $n(S)$ is computed and shown in Fig. 3.7.

Appendix B

The relationship between auto- and cross-correlation of noise

Assuming the input noises of two channels are white Gaussian noise X and Y and in the auto-correlation data, the auto-correlations of the input noises are \mathbf{A}_X and \mathbf{A}_Y , respectively. In cross-correlation data of these two channels, the cross-correlation of the input noises is \mathbf{C}_{XY} . The noise of auto-correlation data is a random variable of \mathbf{A}_X with a standard deviation of $\sigma_{\mathbf{A}_X}$. Similarly, the standard deviation of the noise of cross-correlation data is $\sigma_{\mathbf{C}_{XY}}$.

To derive Eq. (6.31) in Sec. 6.7.2, three distributions are used:

- Chi-square Distribution with k degrees of freedom: For k independent Gaussian random variables with zero mean and variance of σ^2 , i.e. $X_i \sim N(0, \sigma^2)$ where $i = 1, 2, \dots, k$, the sum of the squares of these random variables $Y = \sum_{i=1}^k X_i^2$ has a probability density of

$$f(y) = \frac{1}{2^{k/2} \Gamma(k/2) \sigma^2} \left(\frac{y}{\sigma^2} \right)^{k/2-1} e^{-\frac{y}{2\sigma^2}} \quad (\text{B.1})$$

where $\Gamma(x)$ is a Gamma function. The expectation and variance are

$$\mathbf{E}(Y) = k\sigma^2, \quad \mathbf{Var}(Y) = 2k\sigma^4 \quad (\text{B.2})$$

- Normal Product Distribution: Two independent Gaussian random variables with zero mean and variances of σ_1^2 and σ_2^2 respectively, i.e. $X_1 \sim N(0, \sigma_1^2)$ and $X_2 \sim N(0, \sigma_2^2)$, the product of these two random variables $Y = X_1 \cdot X_2$ has a probability density of

$$f(y) = \frac{1}{\pi \sigma_1 \sigma_2} K_0\left(\frac{|y|}{\sigma_1 \sigma_2}\right) \quad (\text{B.3})$$

where $K_0(x)$ is the modified Bessel function of the second kind. The expectation and variance are

$$\mathbf{E}(Y) = 0, \quad \mathbf{Var}(Y) = \sigma_1^2 \sigma_2^2 \quad (\text{B.4})$$

- Central Limit Theorem: For n independent and same-distributed random variables X_1, X_2, \dots, X_n , with the same and limited expectations μ and variance σ^2 , their sum $Y = \sum_{i=1}^n X_i$ tends to be a Gaussian distribution, Y is closer to the Gaussian distribution $N(n\mu, n\sigma^2)$ as n is larger.

In an realistic observation, the thermal noise of the whole system mainly comes from the first level of LNA, due to the thermal noise from the first level of LNA becomes larger and larger by step-by-step amplifying by the following LNAs. Assuming the thermal noise is Gaussian random noise, with zero mean and variance of σ_i^2 (the lower-right label i denotes the i -th feed).

Using X and Y to denote the signals from i -th and j -th feeds. According to the Chi-square Distribution and the Central Limit Theorem, the auto-correlations of X and Y are \mathbf{A}_X and \mathbf{A}_Y of

$$\mathbf{A}_X = \langle XX^* \rangle \sim N\left(\mu_{\mathbf{A}_X} = \sigma_1^2, \sigma_{\mathbf{A}_X}^2 = \frac{2\sigma_1^4}{n}\right) \quad (\text{B.5})$$

$$\mathbf{A}_Y = \langle YY^* \rangle \sim N\left(\mu_{\mathbf{A}_Y} = \sigma_2^2, \sigma_{\mathbf{A}_Y}^2 = \frac{2\sigma_2^4}{n}\right) \quad (\text{B.6})$$

where n is the number of the data points.

According to the Normal Product Distribution and the Central Limit Theorem, the cross-correlation between them \mathbf{C}_{XY} is

$$\mathbf{C}_{XY} = \langle XY^* \rangle \sim N\left(\mu_{\mathbf{C}_{XY}} = 0, \frac{\sigma_1^2 \sigma_2^2}{n}\right) \quad (\text{B.7})$$

Finally, Eq. (6.31) in Sec. 6.7.2 is obtain

$$2\sigma_{\mathbf{C}_{XY}}^2 = \sigma_{\mathbf{A}_X} \sigma_{\mathbf{A}_Y} = 2\sigma_1^2 \sigma_2^2 / n \quad (\text{B.8})$$

Appendix C

My publications

Three articles have been published in AJ (the Astronomical Journal), SCIENCE CHINA Physics, Mechanics & Astronomy and RAA (Research in Astronomy and Astrophysics), based on the works presented in chapter 5, 3 and 4 of this dissertation, respectively. At the time of finishing this dissertation, a fourth article is being finalised and will be submitted to MNRAS (Monthly Notices of the Royal Astronomical Society), on PAON-4 design and first analysis. The analysis in this article extends the one presented in chapter 6 of this dissertation.

- An Imaging algorithm for a lunar orbit interferometer array¹ [129]
- A high-resolution self-consistent whole sky foreground model² [130]
- Extracting 21-cm signal by frequency and angular filtering³ [131]
- Design, operation and performance of the PAON4 prototype transit interferometer⁴

[11]

The first pages of each publications, with the list of authors and the abstracts are inserted below.

¹<https://iopscience.iop.org/article/10.3847/1538-3881/aac6c6>

²<http://engine.scichina.com/publisher/scp/journal/SCPMA/62/8/10.1007/s11433-018-9333-1?slug=abstract>

³<http://www.raa-journal.org/raa/index.php/raa/article/view/4173>

⁴<https://arxiv.org/abs/1910.07956>



An Imaging Algorithm for a Lunar Orbit Interferometer Array

Qizhi Huang^{1,2,3}, Shijie Sun¹, Shifan Zuo^{1,2}, Fengquan Wu¹, Yidong Xu¹ , Bin Yue¹ , Reza Ansari³, and Xuelei Chen^{1,2,4}

¹ Key Laboratory of Computational Astrophysics, National Astronomical Observatories, Chinese Academy of Sciences, Beijing 100101, People's Republic of China
xuelei@cosmology.bao.ac.cn

² School of Astronomy and Space Science, University of Chinese Academy of Sciences, Beijing 100049, People's Republic of China

³ Université Paris-Sud, LAL, UMR 8607, F-91898 Orsay Cedex, France & CNRS/IN2P3, F-91405 Orsay, France

⁴ Center for High Energy Physics, Peking University, Beijing 100871, People's Republic of China

Received 2018 April 2; revised 2018 May 16; accepted 2018 May 19; published 2018 July 5

Abstract

Radio astronomical observations below 30 MHz are hampered by the refraction and absorption of the ionosphere as well as the radio frequency interference (RFI), and thus, high angular resolution sky intensity map is not yet available. An interferometer array on lunar orbit provides a perfect observatory in this frequency band: it is out of the ionosphere, and the Moon helps to block the RFIs from the Earth. The satellites can make observations on the far side of the Moon and then send back the data on the near-side part of the orbit. However, for such arrays, the traditional imaging algorithm is not applicable: the field of view is very wide (almost whole-sky), and for baselines distributed on a plane, there is a mirror symmetry between the two sides of the plane. A further complication is that for each baseline, the Moon blocks part of the sky, but as the satellites orbit the Moon, both the direction of the baseline and the blocked sky change, so even imaging algorithms that can deal with a noncoplanar baseline may not work in this case. Here, we present an imaging algorithm based on solving the linear mapping equations relating the sky intensity to the visibilities. We show that the mirror symmetry can be broken by the three-dimensional baseline distribution generated naturally by the precession of the orbital plane of the satellites. The algorithm is applicable and good maps can be reconstructed, even though the sky blocking by the Moon is different for each baseline. We also investigate how the map-making is affected by inhomogeneous baseline distributions.

Key words: dark ages, reionization, first stars – instrumentation: interferometers – methods: data analysis – radio continuum: general – space vehicles: instruments – techniques: interferometric

1. Introduction

Radio astronomy began at low frequency with the observation by Karl Jansky at 20.5 MHz (Jansky 1933), and Grote Reber made many low-frequency observations down to hectometer waveband over the years (Reber 1994). However, ground-based low-frequency radio observation suffers from strong ionosphere refraction below 30 MHz and absorption below 10 MHz. Furthermore, human-generated radio frequency interference (RFI) at low frequency is almost omnipresent on the Earth due to reflection from the ionosphere. Except for strong emissions from solar radio bursts and planetary radio activities, there were only very few observations at the frequency below 30 MHz, and the sky radiation in this frequency range is poorly known (Bridle & Purton 1968; Cane & Whitham 1977; Cane 1978). In recent years, interest in low-frequency radio astronomy has been renewed, prompted especially by the observation of the redshifted 21 cm line from the Epoch of Reionization, cosmic dawn, and the dark ages (Pritchard & Loeb 2012). Some ground-based experiments, such as the low-frequency array (LOFAR; van Haarlem et al. 2013) and Long Wavelength Array (Clarke et al. 2011) have bandwidth coverage below 30 MHz. Nevertheless, most observations of these new arrays are made at higher frequencies; the lower band is mainly used for observation of the Sun and planets. It is therefore highly desirable to make low-frequency astronomical observations from space.

In the 1970s, the *IMP-6* (Brown 1973), *Radio Astronomy Explore (RAE)-1* (Alexander & Novaco 1974), and *RAE-2* (Alexander et al. 1975) satellites made some low-frequency radio observations from space. The data collected by these satellites showed that the Earth has strong radio emissions at

the relevant band but that the Moon can shield the spacecraft from these emissions; thus, the far side of the Moon provides an ideal environment for low-frequency radio observation. However, limited by the technology available at that time, the sky map constructed from the *RAE* missions is of poor angular resolution (Novaco & Brown 1978). Additionally, there are substantial differences in the spectrum measured by these missions (Keshet et al. 2004).

Since the 1980s, a number of dedicated low-frequency radio space mission concepts have been proposed (see, e.g., Kassim & Weiler 1990; Basart et al. 1997; Kaiser & Weiler 2000 for a review of the early studies), though so far none have been realized. However, some low-frequency observations were made by instruments on board spacecrafts such as *WIND* (Bougeret et al. 1995) and *CASSINI* (Gurnett et al. 2004).

A mission on the Earth orbit (e.g., the solar radio mission *SunRISE* Lazio et al. 2017) is economical and relatively simple in terms of technology, but the RFI from the Earth would be a major concern for imaging the sky or even probing the dark ages. An array on the Sun–Earth L2 point, e.g., *ALFA* (Jones et al. 1998), *FIRST* (Bergman et al. 2009), *SURO-LC* (Blott et al. 2013), allows all-time monitoring of the whole sky, but it is also constantly exposed to the radio emission from the Earth, though reduced in magnitude by the distance. Launching the satellites and maintaining the array configuration around the unstable L2 point, determining their relative positions, and transmitting the data back all require a lot of research and development as well as a substantial amount of resources both on board the satellite and on the ground. Radio observation from the far-side lunar surface is another option (see reviews in Kuiper & Jones 2000; Jester & Falcke 2009; Mimoun et al. 2012; Zarka et al. 2012). A first

A high-resolution self-consistent whole sky foreground model

QiZhi Huang^{1,2}, FengQuan Wu¹, and XueLei Chen^{1,3,4*}

¹Key Laboratory of Computational Astrophysics, National Astronomical Observatories, Chinese Academy of Sciences, Beijing 100101, China;

²Université Paris-Sud, LAL, UMR 8607, F-91898 Orsay Cedex, France & CNRS/IN2P3, Orsay F-91405, France;

³School of Astronomy and Space Science, University of Chinese Academy of Sciences, Beijing 100049, China;

⁴Center for High Energy Physics, Peking University, Beijing 100871, China

Received September 30, 2018; accepted November 26, 2018; published online April 25, 2019

The neutral hydrogen 21 cm line is potentially a very powerful probe of the observable universe, and a number of on-going experiments are trying to detect it at cosmological distances. However, the presence of strong foreground radiations such as the galactic synchrotron radiation, galactic free-free emission and extragalactic radio sources make it a very challenging task. For the design of 21 cm experiments and analysis of their data, simulation is an essential tool, and good sky foreground model is needed. With existing data the whole sky maps are available only in low angular resolutions or for limited patches of sky, which is inadequate in the simulation of these new 21 cm experiments. In this paper, we present the method of constructing a high resolution self-consistent sky model at low frequencies, which incorporates both diffuse foreground and point sources. Our diffuse map is constructed by generating physical foreground components including the galactic synchrotron emission and galactic free-free emission. The point source sample is generated using the actual data from the NRAO VLA Sky Survey (NVSS) and the Sydney University Molonglo Sky Survey (SUMSS) where they are available and complete in flux limit, and mock point sources according to statistical distributions. The entire model is made self-consistent by removing the integrated flux of the point sources from the diffuse map so that this part of radiation is not double counted. We show that with the point sources added, a significant angular power is introduced in the mock sky map, which may be important for foreground subtraction simulations. Our sky maps and point source catalogues are available to download.

neutral hydrogen, 21 cm line, foreground model, whole sky map, simulation

PACS number(s): 95.80.+p, 95.85.Bh, 98.70.Dk, 95.75.Mn, 95.75.Pq

Citation: Q. Z. Huang, F. Q. Wu, and X. L. Chen, A high-resolution self-consistent whole sky foreground model, *Sci. China-Phys. Mech. Astron.* **62**, 989511 (2019), <https://doi.org/10.1007/s11433-018-9333-1>

1 Introduction

Tomographic observation of the redshifted 21 cm signal from neutral hydrogen will allow us to study the Epoch of Reionization (EoR) [1, 2] and the Cosmic Dawn [3], to trace the evolution of the large scale structure of our universe and constrain the cosmological parameters including the equation of state of dark energy [4, 5], and even to probe the cosmic dark age [6]. A number of telescopes have been developed

to detect the cosmological 21 cm signal, including the EoR experiments such as LOFAR [7], MWA [8], PAPER [9], and HERA [10]; and the dark energy experiments such as Tianlai [11] and CHIME [12]; and the next generation telescopes such as SKA [13] which are expected to provide considerably more accurate power spectrum and directly map the large scale structures.

However, detecting the cosmological 21 cm signal is very difficult due to the presence of foregrounds which are several orders of magnitude stronger. At low frequencies the main astrophysical foregrounds include the galactic synchrotron

*Corresponding author (email: xuelei@cosmology.bao.ac.cn)

RAA 2018 Vol. 18 No. 9, 114(12pp) doi: 10.1088/1674-4527/18/9/114

© 2018 National Astronomical Observatories, CAS and IOP Publishing Ltd.

<http://www.raa-journal.org> <http://iopscience.iop.org/raa>

*Research in
Astronomy and
Astrophysics*

Extracting 21 cm signal by frequency and angular filtering

Qi-Zhi Huang^{1,2,3}, Feng-Quan Wu¹, Reza Ansari³ and Xuelei Chen^{1,2,4}

¹ Key Laboratory of Computational Astrophysics, National Astronomical Observatories, Chinese Academy of Sciences, Beijing 100101, China; xuelei@bao.ac.cn

² School of Astronomy and Space Science, University of Chinese Academy of Sciences, Beijing 100049, China

³ Université Paris-Sud, LAL, UMR 8607, F-91898 Orsay Cedex, France & CNRS/IN2P3, F-91405 Orsay, France

⁴ Center for High Energy Physics, Peking University, Beijing 100871, China

Received 2018 April 20; accepted 2018 April 28

Abstract Extracting the neutral hydrogen (HI) signal is a great challenge for cosmological 21 cm experiments; both the astrophysical foregrounds and receiver noise are typically several orders of magnitude greater than the 21 cm signal. However, the different properties of the 21 cm signal, foreground and noise can be exploited to separate these components. The foregrounds are generally smooth or correlated over the frequency space along a line of sight (LoS), while both the 21 cm signal and noise vary stochastically along the same LoS. The foreground can be removed by filtering out the smooth component in frequency space. The receiver noise is basically uncorrelated for observations at different times, hence for surveys it is also uncorrelated in different directions, while the 21 cm signal, which traces the large scale structure, is correlated up to certain scales. In this exercise, we apply Wiener filters in frequency and angular space to extract the 21 cm signals. We found that the method works well. Inaccurate knowledge about the beam could degrade the reconstruction, but the overall result is still good, showing that the method is fairly robust.

Key words: methods: data analysis — (cosmology:) dark ages, reionization, first stars — cosmology: observations

1 INTRODUCTION

The neutral hydrogen 21 cm line is one of the most promising tools to study the observable Universe. Tomographic observation of the redshifted 21 cm line could be used to reveal the evolution of the intergalactic medium (IGM) throughout the Epoch of Reionization (EoR) (Madau et al. 1997; Ciardi & Madau 2003), and to map out the large scale structure and constrain cosmological parameters including the dark energy equation of state (Chang et al. 2008; Mao et al. 2008). In principle, it could even probe the cosmic dark age (Loeb & Zaldarriaga 2004). Compared with the cosmic microwave background (CMB), which images the Universe at the last scattering surface during the EoR, one advantage of the redshifted 21 cm tomography signal as a cosmological probe is that it provides a three dimensional

(3D) map of the Universe at different redshifts, giving more information and also showing how the Universe evolved.

In recent years, a number of experiments set observation of 21 cm as one of their main scientific goals, for example experiments with existing telescopes such as the Green Bank Telescope (GBT; Chang et al. 2010; Masui et al. 2013; Switzer et al. 2013), Giant Metrewave Radio Telescope (GMRT; Paciga et al. 2011) and telescopes that are newly built or being built, such as the 21 CentiMeter Array (21CMA; Zheng et al. 2016), Tianlai (Chen 2012), Baryon acoustic oscillations In Neutral Gas Observations (BINGO; Battye et al. 2013), Low-Frequency ARray (LOFAR; van Haarlem et al. 2013), Murchison Widefield Array (MWA; Tingay et al. 2013), Precision Array for Probing the Epoch of Re-ionization (PAPER; Parsons et al. 2010), Canadian Hydrogen

Design, operation and performance of the PAON4 prototype transit interferometer

R. Ansari¹, J.E Campagne^{1*}, D. Charlet¹, M. Moniez¹, C. Paillet¹, O. Perdereau¹, M. Taurigna¹, J.M. Martin², F. Rigaud², P. Colom³, Ph. Abbon⁴, Ch. Magneville⁴, J. Pezzani⁵, C. Viou⁵, S.A. Torchinsky⁶, Q. Huang^{8,1}, and J. Zhang^{7,1,8}

¹LAL, Univ. Paris-Sud, CNRS/IN2P3, Université Paris-Saclay, 91105 Orsay, France

²GEPI, UMR 8111, Observatoire de Paris, 61 Av. de l'Observatoire, 75014 Paris, France

³LESIA, UMR 8109, Observatoire de Paris, 5 place Jules Janssen, 92195 Meudon Cedex, France

⁴CEA, DSM/IRFU, Centre d'Etudes de Saclay, 91191 Gif-sur-Yvette, France

⁵Station de Radioastronomie de Nançay, Observatoire de Paris, PSL Research University, CNRS, Université d'Orléans, 18330 Nançay, France

⁶APC, Université Paris Diderot, CNRS/IN2P3, CEA/Irfu, Observatoire de Paris, Sorbonne Paris Cité, 75205 Paris Cedex 13, France

⁷College of Physics and Electronic Engineering, Shanxi University, Shanxi 030006, China

⁸National Astronomical Observatories, Chinese Academy of Sciences, Beijing 100012, China

Accepted XXX. Received YYY; in original form ZZZ

ABSTRACT

PAON4 is an L-band (1250-1500 MHz) small interferometer operating in transit mode deployed at the Nançay observatory in France, designed as a prototype instrument for Intensity Mapping. It features four 5 meter diameter dishes in a compact triangular configuration, with a total geometric collecting area of $\sim 75\text{m}^2$, and equipped with dual polarisation receivers. A total of 36 visibilities are computed from the 8 independent RF signals by the software correlator over the full 250 MHz RF band. The array operates in transit mode, with the dishes pointed toward a fixed declination, while the sky drifts in front of the instrument. Sky maps for each frequency channel are then reconstructed by combining the time-dependent visibilities from the different baselines observed at different declinations. This paper presents an overview of the PAON4 instrument design and goals, as a prototype for dish arrays to map the Large Scale Structure in radio, using intensity mapping of the atomic hydrogen 21 cm line. We have operated PAON4 over several years and we have used data from observations in different periods to assess the array performances. We present preliminary analysis of a large fraction of this data and discuss crucial issues for this type of instrument, such as the calibration strategy, instrument response stability and noise behaviour.

Key words: Radio telescopes and instrumentation, Intensity Mapping, wide band interferometry, extragalactic H_I

1 INTRODUCTION

Despite the tremendous success of the Λ CDM cosmological model and the wealth of information provided by the analysis of CMB anisotropies (Hinshaw et al. 2013; Planck Collaboration et al. 2016, 2018), SNIa luminosities (Betoule et al. 2014) and optical surveys (see e.g. Salazar-Albornoz et al. 2017; Abbott et al. 2018; DES Collaboration et al. 2018),

the nature of Dark Matter and Dark Energy remain elusive (Bull et al. 2016) and a number of fundamental physics questions still need clarification. The Large Scale Structure (LSS) and its Baryon Acoustic Oscillation (BAO) feature are among the most powerful probes to constrain the cosmological model and Dark Energy and Modified gravity models (Amendola et al. 2013). The matter distribution at large scale in the universe is usually mapped through optical photometric and spectroscopic surveys.

The 21 cm line emission/absorption at 1.42 GHz due

* Email: campagne@lal.in2p3.fr

Titre : Quelques sujets en cosmologie à 21-cm: modèles d'avant plans et leur soustraction, reconstruction de cartes pour les interféromètres à grand champ de vue et l'analyse des données de PAON-4

Mots clés : Cosmologie, Énergie Noire, Emission 21cm (HI), Interférométrie Radio

Résumé : Certains aspects de l'extraction du signal cosmologique à 21 cm à partir des observations radio, ainsi que le traitement des données interférométriques pour des observations depuis le sol et depuis l'espace ont été étudiés et sont présentés dans cette thèse.

J'ai développé un modèle cohérent et à haute résolution du ciel en radio, qui peut fournir une carte complète et précise du ciel, dans la gamme de fréquence 10 MHz à 2,3 GHz, avec une résolution pouvant atteindre une minute d'arc. Le modèle inclut plusieurs sources de rayonnement diffus, en particulier le synchrotron Galactique, les sources radio brillantes du ciel, ainsi qu'un modèle des sources faibles.

J'ai également mis au point une méthode pour extraire le signal 21 cm cosmologique, fortement contaminé par les émissions d'avant-plan et le bruit des récepteurs. La méthode utilise une cascade de deux filtres de Wiener, dans l'espace des fréquences d'abord, et ensuite, dans le domaine angulaire. Le premier filtre exploite les variations lentes des émissions d'avant-plan selon la fréquence, tandis que le second filtre exploite les corrélations angulaires du signal cosmologique pour filtrer le bruit des récepteurs, considéré non corrélé entre deux directions différentes.

J'ai développé un nouvel algorithme d'imagerie pour les interféromètres en orbite lunaire. Un tel instrument serait idéal pour cartographier le ciel en dessous de 30 MHz; il ne

serait en effet pas soumis aux perturbations ionosphériques et serait protégé des interférences électromagnétiques dues aux émissions terrestres. J'ai montré que l'utilisation de la précession du plan orbital du satellite permet de résoudre le problème de la symétrie miroir. La méthode exploite la relation de projection linéaire entre la carte du ciel et les visibilité mesurées, tant dans l'espace angulaire que dans l'espace des harmoniques sphériques pour reconstruire la carte du ciel. L'algorithme d'imagerie gère la complication due à l'ombre de la Lune se déplaçant avec le temps sur le champ de vue des antennes couvrant tout le ciel. Notons que ces effets ne sont pas pris en charge par les algorithmes d'imagerie existants tels que la W-Projection et la W-Stacking.

Enfin, j'ai effectué une première analyse des données de l'interféromètre de transit PAON-4. J'ai évalué la performance globale du réseau en termes de température de bruit et de la réponse des antennes. J'ai pu étalonner avec succès les visibilité, en déterminant à la fois l'amplitude et la phase des termes de gain complexes, tout en corrigeant les décalages de pointage des antennes de PAON4. J'ai ensuite reconstruit la carte du ciel pour une bande de 10 degrés autour de la déclinaison de la source brillante Cygnus A, à partir du flot de données PAON-4 calibré et nettoyé, en appliquant l'algorithme de décomposition en mode m dans l'espace des harmoniques sphériques.

Title : Topics in 21-cm cosmology: Foreground models and their subtraction, map reconstruction for wide field of view interferometers and PAON-4 data analysis

Keywords : Cosmology, Dark Energy, 21cm emission (HI), Radio Interferometry

Abstract : Some aspects of extracting cosmological 21cm signal from radio observations, as well as processing of interferometric data for ground based or space born instruments have been studied and discussed in this dissertation.

I have developed a high-resolution self-consistent radio whole sky model, which provides an accurate full sky maps in the frequency range from 10 MHz to 2.3 GHz, with angular resolution up to 1 arcmin. It includes bright and faint radio sources, Galactic synchrotron and Galactic free-free emissions.

I have also developed a method to extract the faint cosmological 21-cm signal, heavily contaminated by foreground emissions and receiver noise. The method uses a cascade of two Wiener filters, in frequency domain and then, in angular domain. The first filter exploits the smoothness of the foreground emissions along the frequency, while the second filter exploits the angular correlations of the cosmological signal, due to the receiver noise is considered to be nearly uncorrelated between different directions.

I have developed a studied the performance of a new imaging algorithm for lunar orbit interferometers. Such an

instrument would be ideal for mapping the radio sky below 30 MHz, as it would be free from ionospheric perturbations, as well as electromagnetic interferences due to terrestrial emissions. I have shown that we make use of the precession of satellite orbital plane to solve the mirror symmetry problem, and exploit the linear mapping between the sky map and the measured visibility, both in angular space and spherical harmonic space to reconstruct the sky map. The imaging algorithm handles the time-varying Moon's blockage over the whole sky field of view, which are not handled by existing imaging algorithms such as the W-Projection and the W-Stacking.

Finally, I have carried out a first analysis of the observational visibility data from the PAON-4 transit interferometer. I have evaluated the overall performance of the array in terms of system temperature and antenna response, and successfully calibrated the visibility, determining both amplitude and phase of the complex gain terms, while correcting PAON-4 antennae pointing offsets. I have then reconstructed the sky map for a 10 degree strip around Cygnus A declination, from the cleaned calibrated PAON-4 data streams, applying the m-mode decomposition map-making algorithm in spherical harmonic space.

